

Towards a precise measurement of the cosmic-ray positron fraction

Der Fakultät für Mathematik, Informatik und Naturwissenschaften der
RWTH Aachen University
vorgelegte Dissertation zur Erlangung des akademischen Grades eines
Doktors der Naturwissenschaften

von

Diplom-Physiker
Henning Gast

aus Düsseldorf

Abstract

This thesis deals with detector concepts aiming at a precise measurement of the cosmic-ray positron fraction extending to an as yet unreached range of energy. The indirect search for dark matter is the main motivation for this endeavour.

The evolution and large-scale structure of the Universe is described by the Hot Big Bang model which is well supported by observational evidence. In this model, roughly a quarter of the energy density of the Universe must be made up of the elusive dark matter. Evidence for its existence comes from, for example, the observation of galactic rotation curves, dynamics of clusters of galaxies, and the pattern of anisotropies in the cosmic microwave background. While the nature of dark matter is as yet unknown, the most popular candidate for its constituents is the neutralino included in supersymmetric extensions to the standard model of particle physics. Neutralinos annihilating in the Galactic halo are considered as a potential primary source of cosmic-ray positrons. For the calculation of the expected secondary background of positrons, a common cosmic-ray propagation model has been adopted and its uncertainties have been assessed. The cosmic-ray positron fraction data available so far indicate an excess over the expectation for purely secondary production, a trend recently confirmed and intensified by measurements of the PAMELA satellite detector. The AMS-02 detector will be ready for installation on the International Space Station in 2010 and is designed to perform precision spectroscopy of many different cosmic-ray species including positrons.

Here, a design concept for a new detector, called Positron Electron Balloon Spectrometer (PEBS), is presented. Intended for a measurement of the cosmic-ray positron fraction on one or more flights at high altitude using a long-duration balloon, PEBS will have an unprecedentedly high acceptance of almost $0.4 \text{ m}^2 \text{ sr}$. A first launch could take place in 2012. Using a superconducting magnet to create a mean magnetic field of 0.8 T and a scintillating fibre tracker with silicon photomultiplier readout, it will allow reliable charge-sign and momentum measurements up to at least 100 GeV. The enormous challenge of reliably identifying positrons in front of the vast proton background is tackled by a combination of two independent subdetectors for particle identification. The first one is an electromagnetic calorimeter which will consist of layers of tungsten absorber interleaved with scintillator bars, read out by silicon photomultipliers. The second one is a transition radiation detector (TRD) similar to the one built for AMS-02, made of an irregular fleece radiator followed by thin-walled detection tubes.

A detailed Monte Carlo simulation of PEBS, based on Geant4, was created to study the expected performance of the detector, along with a reconstruction and analysis suite. The simulation predicts a momentum resolution of 18 % for 100 GeV positrons. For the same energy, the calorimeter is predicted to have an energy resolution of 6 % and a proton rejection of 3000 at 80 % positron efficiency. The transition radiation detector will provide an additional rejection factor of 700, again with 80 % positron efficiency. Using testbeam data acquired with a prototype for the AMS-02-TRD, the accuracy of the simulation of transition radiation and ionisation losses provided by Geant4 was studied. Excellent agreement was found between the transition radiation spectra in data and simulation. Small discrepancies at the 25 %-level are present in the tails of the proton energy loss spectra but this makes the predicted proton rejections uncertain by a factor of two.

In a series of testbeam measurements, the proof of principle was established for the scintillating fibre tracker with silicon photomultiplier readout. The intrinsic spatial resolution achieved at the current level of design is $70\ \mu\text{m}$.

Neutralino dark matter was studied in the minimal supergravity grand unification (mSUGRA) model. Assuming that neutralino annihilations are enhanced by boost factors taken from best fits to the positron fraction data published so far, both PEBS and AMS-02 will be capable of substantially constraining mSUGRA parameter space. It is shown that a moderately good fit to the high-energy PAMELA data can be obtained in the mSUGRA model as well. At the same time, the low-energy PAMELA data may hint at charge-sign dependent solar modulation effects.

Zusammenfassung

In dieser Arbeit werden Detektorkonzepte vorgestellt, die eine präzise Vermessung des Positronenanteils in der kosmischen Strahlung bis hin zu bislang unerreichten Energiebereichen zum Ziel haben.

Die Entwicklung und die großräumige Struktur des Universums werden von dem Urknallmodell beschrieben, das durch vielfältige Beobachtungen gestützt wird. In diesem Modell macht die rätselhafte dunkle Materie etwa ein Viertel der gesamten Energiedichte des Universums aus. Hinweise auf ihre Existenz finden sich zum Beispiel in galaktischen Rotationskurven, der Dynamik von Galaxienhaufen und dem Muster der Anisotropien in der kosmischen Hintergrundstrahlung. Obwohl die Natur der dunklen Materie nach wie vor unbekannt ist, sind die in supersymmetrischen Erweiterungen des Standardmodells der Teilchenphysik enthaltenen Neutralinos der beliebteste Kandidat. Neutralinos, die im galaktischen Halo zerstrahlen, werden hier als mögliche primäre Quellen für Positronen in der kosmischen Strahlung betrachtet. Für die Berechnung des erwarteten sekundären Untergrundes wurde ein gebräuchliches Modell für die Propagation kosmischer Strahlung angenommen und seine Unsicherheiten abgeschätzt. Die bisher zum Positronenanteil in der kosmischen Strahlung vorliegenden Daten zeigen einen Überschuss im Vergleich zu der Erwartung aus rein sekundärer Erzeugung, ein Trend, der kürzlich durch Messungen des satellitengestützten Detektors PAMELA bestätigt und verstärkt wurde. Der Detektor AMS-02 wird im Jahre 2010 für die Befestigung an der internationalen Raumstation bereit stehen. Er wurde für die Präzisionsspektroskopie vieler verschiedener Teilchensorten in der kosmischen Strahlung einschließlich Positronen entwickelt.

In dieser Arbeit wird ein Entwicklungskonzept für einen neuen Detektor vorgestellt, genannt Positron Electron Balloon Spectrometer (PEBS). PEBS hat eine Messung des Positronenanteils in der kosmischen Strahlung bei einem oder mehreren Flügen mit einem Langzeit-Höhenballon in großer Flughöhe zum Ziel, mit einer bisher unerreicht großen Apertur von $0,4 \text{ m}^2 \text{ sr}$. Der erste Start könnte im Jahr 2012 stattfinden. Durch Benutzung eines supraleitenden Magneten, der ein mittleres Feld von $0,8 \text{ T}$ erzeugt, und einem aus szintillierenden Fasern, die von Silizium-Photovervielfachern ausgelesen werden, bestehenden Spurdetektor wird PEBS verlässliche Messungen von Impuls und Ladungsvorzeichen bis mindestens 100 GeV ermöglichen. Die enorme Herausforderung, die darin besteht, Positronen vor dem überwältigenden Untergrund an Protonen verlässlich zu identifizieren, wird mit einer Kombination zweier Subdetektoren zur Teilchenidentifikation angegangen. Der erste ist ein elektromagnetisches Kalorimeter, das aus Wolframlagen bestehen wird, die von Szintillatorbarren gefolgt werden, die mit Silizium-Photovervielfachern ausgelesen werden. Der zweite ist ein Übergangsstrahlungsdetektor (TRD), der dem für AMS-02 gebauten ähnelt und aus einem irregulären Faserradiator besteht, der von dünnwandigen Detektorröhrchen gefolgt wird.

Eine detaillierte Monte Carlo-Simulation von PEBS wurde erschaffen, ebenso wie ein Programmpaket für Rekonstruktion und Analyse. Die Simulation basiert auf Geant4 und ermöglicht es, die zu erwartende Leistungsfähigkeit von PEBS zu studieren. Sie sagt eine Impulsauflösung von 18% für 100 GeV Positronen vorher. Für das Kalorimeter wird dabei eine Energieauflösung von 6% und eine Protonenunterdrückung um 3000 bei einer Positron-Effizienz von 80% vorhergesagt. Der Übergangsstrahlungsdetektor wird einen weiteren Faktor 700 beitragen, ebenso mit 80% Positron-Effizienz. Mit Hilfe von Teststrahldaten, die mit einem Prototypen für den AMS-02-TRD aufgenommen wurden, wurde die Genauigkeit der Simulation von Übergangsstrahlung

und Ionisationsverlusten mit Geant4 studiert. Hervorragende Übereinstimmung zwischen Daten und Simulation wurde für die Spektren der Übergangsstrahlung gefunden. Kleine Abweichungen auf dem Niveau von 25 % treten in den Ausläufern der Energieverlustspektren von Protonen zu Tage und führen zu einer Unsicherheit der vorhergesagten Protonunterdrückungsfaktoren von etwa einem Faktor zwei.

In einer Reihe von Teststrahlungsmessungen wurde die Machbarkeit des Spurdetektors aus szintillierenden Fasern, die von Silizium-Photovervielfachern ausgelesen werden, gezeigt. Die intrinsische Ortsauflösung, die auf dem derzeitigen Entwicklungsstand erreicht wird, beträgt $70 \mu\text{m}$.

Aus Neutralinos bestehende dunkle Materie wurde im Rahmen des mSUGRA (minimal supergravity grand unification)-Modells studiert. Unter der Annahme, dass die Zerstrahlung von Neutralinos um einen Faktor erhöht ist, der sich aus besten Anpassungen an die bisher veröffentlichten Positrondaten ergibt, werden sowohl AMS-02 als auch PEBS in der Lage sein, den Parameterraum des mSUGRA-Modells beträchtlich einzuschränken. Es wird gezeigt, dass im mSUGRA-Modell eine einigermaßen gute Beschreibung der PAMELA-Daten zu hohen Energien möglich ist. Gleichzeitig könnten die PAMELA-Daten bei niedrigen Energien Hinweise auf ladungsabhängige solare Modulationseffekte geben.

Contents

1	Introduction	1
2	Cosmic rays and dark matter	5
2.1	Big Bang cosmology	5
2.2	Evidence for the existence of dark matter	8
2.3	Dark matter candidates	10
2.4	Dark matter in the mSUGRA model	11
2.5	Production and propagation of cosmic rays	14
2.5.1	Basic facts about cosmic rays	15
2.5.2	Sources of cosmic rays	15
2.5.3	Propagation of cosmic rays in the Galaxy	16
2.5.4	Solar modulation	19
2.5.5	Effect of the geomagnetic field	19
2.5.6	Measurements of cosmic rays	20
2.5.7	Atmospheric backgrounds	21
2.6	Model for cosmic-ray propagation	21
2.7	A hint of charge-sign dependent solar modulation in the low-energy PAMELA data	31
3	Detectors to measure the cosmic-ray positron fraction	35
3.1	PAMELA	35
3.2	AMS-02	36
3.3	PEBS	36
3.3.1	Design overview	36
3.3.2	Carrier system	40
3.3.3	Secondary targets	40
4	Design study for PEBS based on Monte Carlo simulations	43
4.1	Working principle of the Monte Carlo simulation	44
4.2	Design study for PEBS and implementation in the Monte Carlo simulation	45
4.2.1	Magnet	45
4.2.2	Tracker	46
4.2.3	Silicon photomultipliers for scintillating fibre readout	49
4.2.4	Time-of-flight system	52
4.2.5	Electromagnetic calorimeter	52
4.2.6	Transition radiation detector	57
4.2.7	Physics processes	61

4.2.8	Adjustment of parameters for the simulation of transition radiation with testbeam data	62
4.3	Event reconstruction	72
4.4	Projected performance	77
4.4.1	Momentum resolution	77
4.4.2	Angular resolution	81
4.4.3	Impact of SiPM noise	82
4.4.4	Impact of module thickness	83
4.4.5	ECAL energy resolution	83
4.4.6	ECAL rejection and efficiency analysis	87
4.4.7	TRD rejection	91
4.4.8	Acceptance calculation	92
5	PEBS tracker prototype testbeam campaign	99
5.1	First testbeam 2006	99
5.1.1	Setup description	99
5.1.2	Analysis procedure	102
5.1.3	Prototype performance and comparison to Monte Carlo study . . .	111
5.2	Second testbeam 2008	113
5.2.1	Setup description	113
5.2.2	Data analysis	116
6	Constraining supersymmetry with cosmic-ray data	131
6.1	Model description	131
6.1.1	mSUGRA and observables	131
6.1.2	Cosmic rays	136
6.2	Constraints on mSUGRA parameter space from currently available data . .	138
6.3	Projected improvements with PEBS	146
6.4	Comparison to AMS-02	149
6.5	mSUGRA dark matter in the light of PAMELA data	150
7	Conclusions and outlook	157

1 Introduction

What are the constituents of matter and how do they interact? Is the Universe static, or else, how did it evolve into its current state? These two questions arguably stand out as especially fascinating among the problems that fundamental science seeks to solve.

After a long series of experiments, including those conducted with enormous detectors used to analyse the debris from collisions of particles smashed together at breakneck speeds at huge accelerators, the discipline of particle physics has emerged with a theory – simply called the standard model – describing the interactions of elementary particles in the framework of quantum field theory. So far, its predictions have been found to be of exquisite precision. Electrons and quarks make up the atoms that our planet and every living being on it are made of, neutrinos help to maintain the equilibrium inside our star over billions of years, and photons, gluons, and the W and Z bosons mediate the interactions of these building blocks of matter, as dictated by a set of simple mathematical symmetries.

At the same time, based on a host of precise astronomical observations covering many different wavelengths, cosmology has come a long way from the old picture that saw Earth at the centre of a static universe. Instead, the evolution of the Universe has been traced back to within the tiniest fraction of a second from its coming into being in the so-called Big Bang. It must have started from an initially hot, dense, and almost perfectly homogeneous state and then cooled down and expanded over the eons until stars, galaxies, and eventually planets could form. The expansion of the Universe is governed by its matter and energy content as described in the framework of General Relativity.

But there are problems. Imprinted on the ubiquitous microwave radiation filling the cosmos is a snapshot of the acoustic oscillations in the early Universe, yet their pattern hints at the presence of additional matter interacting with the plasma only by gravitational interaction. The structure of the Universe on large scales could only have formed in gravitational wells much deeper than calculated from the distribution of the matter that astronomers can see. The observed motions of stars and gas around galaxies cannot be explained by the laws of gravity taking only the attraction of the luminous matter into account. These observations, among others, have led to the conclusion that there must be large amounts of non-luminous, only weakly interacting, matter out there in the Universe which only betrays itself by its own mass. Its energy density today must exceed that of ordinary baryonic matter by roughly a factor of six. This is known as the dark matter problem. The existence of dark matter seems well established by now, but its nature remains elusive.

The hunt for dark matter is on. At the Large Hadron Collider now commissioned near Geneva, physicists hope to create dark matter particles from energy. In laboratories deep under ground, extremely sensitive detectors are employed to look for collisions of dark matter particles with nuclei. In the third approach, the indirect search for dark matter,

1 Introduction

one tries to identify the remnants of pairwise annihilations of dark matter particles taking place across the Galaxy and its halo. Antiparticles of high energy are expected to be created in these collisions and as they have no known primary source in the Galaxy, they can be used as messengers of possible dark matter annihilations. Positrons are especially promising as they are stable and thus able to bridge vast distances in the Galaxy and typically carry away a significant fraction of the dark matter particles' mass. As a consequence, they stand out from the astrophysical backgrounds more easily. After diffusing through the Galactic medium, they may reach Earth as a small admixture to the cosmic rays.

Cosmic rays are a stream of energetic elementary particles and nuclei reaching our planet from the skies. Apart from maybe shedding some light on the grand questions outlined above, their study allows us to draw conclusions about our cosmic surroundings. For example, the spectra and composition of cosmic rays are sensitive to the structure of the Galaxy and the interactions with the solar wind and magnetic fields. In addition, the study of cosmic rays has had a big influence on particle physics as many elementary particles were first identified in the cosmic rays. As all but the most high-energetic cosmic rays are absorbed by Earth's atmosphere long before they can reach the ground, an instrument trying to measure cosmic rays must be deployed either in space or on a high-altitude balloon circling at the outskirts of the atmosphere.

This thesis deals with detector concepts aiming at a precise measurement of the cosmic-ray positron fraction extending to an as yet unreached range of energy. The first steps have been made by a series of small detectors flying on high-altitude balloons over the past decades. Their results have sparked excitement because they indicate an excess in the relative positron flux over what is expected from purely secondary production in collisions of protons and nuclei with interstellar matter. It has been speculated that this excess might be due to dark matter annihilations. Now, the PAMELA detector is orbiting Earth and taking data, while the AMS-02 detector is nearing completion and waiting for a flight to the International Space Station. The PAMELA positron fraction data have recently become available and confirm the trend of the earlier measurements.

The main focus of this work is a design study for a new experiment, called Positron-Electron Balloon Spectrometer (PEBS), specifically designed to measure the cosmic-ray positron fraction in the energy range from a few hundred MeV up to 100 GeV and more. The main motivation is derived from the indirect search for dark matter, but as briefly touched upon above, the range of topics profiting from a precise measurement is much wider. As a balloon-borne detector, PEBS could be realised at a fraction of the cost of a space experiment the same size. In addition, it could be salvaged after the flight, allowing for post-flight calibration and checks, and possibly be flown multiple times. Various space agencies around the globe have been operating high-altitude balloon programmes reaching flight durations of up to forty days. The remaining atmosphere would make the data somewhat harder to interpret compared to a space experiment, but the necessary corrections turn out to be small and are well understood.

Several obstacles have to be overcome before a precise measurement of the cosmic-ray positron fraction, i.e. the ratio of the positron flux to the total electron flux, becomes fea-

sible. First of all, the fluxes of electrons and positrons are low and drop steeply towards higher energies so that a precise measurement requires a large geometric acceptance or long exposures. On the other hand, the size of the detector and its measurement time are limited by the constraints that the carrier system imposes on the weight budget and hence the amount of consumables that can be carried. Moreover, the proton flux exceeds the electron and positron fluxes by many orders of magnitude. To reliably identify positrons and electrons in front of this enormous background, both AMS-02 and PEBS rely on the combination of two independent subdetectors, a transition radiation detector and an electromagnetic calorimeter. The separation of electrons and positrons requires a clean measurement of the particle momentum. To that end, the two experiments employ a superconducting magnet inside a helium cryostat and a tracking device. While a conventional silicon tracker is used in AMS-02, PEBS features an innovative scintillating fibre tracker with silicon photomultiplier readout that is currently under development. Silicon photomultipliers are novel devices promising single-photon detection combined with desirable properties such as high gain, compactness, auto-calibration and insensitivity to magnetic fields. The key asset of such a tracking device is its conceptual simplicity that comes along with low weight and low material budget.

In the design of a new particle detector, Monte Carlo simulations are of utmost importance allowing one to study the expected behaviour of the individual components and the entire detector by simulating it on the computer before even the first prototype is built. As the design progresses, prototype measurements in test beams are necessary to verify the simulations and to demonstrate the proof of principle for the detector design.

This thesis is organised as follows. Chapter 2 contains a brief review of Big Bang cosmology and the evidence for the existence of dark matter. The most popular candidates are presented and one candidate, the neutralino of the mSUGRA model, is described in some more detail. After a short description of the physics of cosmic rays and an explanation of the effects important for their detection on Earth, the particular propagation model used to study the projected performance of AMS-02 and PEBS is elaborated on and its uncertainties are assessed. In chapter 3, the designs of PAMELA, AMS-02, and PEBS are sketched, with a focus on the latter.

Chapter 4 contains a detailed description of the design study for PEBS based on Monte Carlo simulations as well as the reconstruction and analysis techniques used to extract the projected performance of the detector, presented at the end of the chapter. Several module prototypes for the scintillating fibre tracker for PEBS have been subjected to a proton testbeam at CERN over the past three years and these measurements are described in chapter 5. They provide important input to the Monte Carlo simulations. The capability of PEBS and AMS-02 to constrain model parameters in the case of a discovery is studied in chapter 6 for the example of the mSUGRA model. This is contrasted with the ability of the presently available cosmic-ray data to constrain this model. Some concluding remarks and an outlook are given in chapter 7.

1 Introduction

2 Cosmic rays and dark matter

In this chapter, one of the biggest questions in modern physics, the nature of dark matter, is explained and it is shown how cosmic-ray physics might help to solve it. First, the standard model of cosmology is reviewed. This is vital to understand how certain candidates for dark matter could have come into existence and populate the Galaxy today. It is then shown that observations at very different cosmological scales demonstrate that some form of dark matter must exist in the Universe today and theories for the most popular candidates are briefly reviewed. The neutralino is a candidate predicted by supersymmetric extensions to the standard model of particle physics. As it was chosen to study the projected performance of PEBS for the case that the mSUGRA model is realised in nature, this model and its dark matter candidate are described next. Then, the cosmic-ray physics needed in the context of the PEBS mission is introduced and in particular, the propagation model used for the treatment of the secondary background is examined. Finally, a possible hint at charge-sign dependent solar modulation of cosmic rays in the recently published PAMELA data is explored.

2.1 Big Bang cosmology

From a fruitful interplay of astronomical observations and theoretical developments over the past decades, a quantitative understanding of the history of the Universe has emerged [1, 2, 3]. The standard model of cosmology is the Hot Big Bang model according to which the Universe came into existence roughly 14 billion years ago and started from a very compressed and therefore very hot state. The expansion of the Universe caused the temperature to decrease. At first, the energy density was divided among matter – in the form of the known elementary particles and dark matter – and radiation – in the form of photons and neutrinos – and an exotic form of energy called dark energy, which plays the role of a fluid with negative pressure. Matter and radiation were in thermal equilibrium, with the radiation dominating the expansion initially. Around 10^{-6} s after the Big Bang, the temperature dropped to 10^{13} K, corresponding to an energy scale of 1 GeV, and thus, protons and neutrons formed from the quark-gluon plasma. After 1 s the temperature reached the level of the nuclear binding energy, 1 MeV. During the era of nucleosynthesis that began now, the light elements ^2H , ^3He , ^4He , and ^7Li were produced. The next important era was reached roughly 300 000 years into the expansion, when the temperature dropped to the level of the atomic binding energies, around 1 eV. At that point, protons and electrons combined to form hydrogen atoms and the Universe became transparent. The radiation emitted from the surface of last scattering permeates the Universe today and is known as the cosmic microwave background. It can be observed today to follow an almost perfect black-body spectrum, at the redshifted temperature of 2.7 K. The Universe then started to be matter-dominated, and eventually, the baryonic matter began

2 Cosmic rays and dark matter

to form complex structures, stars and galaxies and clusters of galaxies that dominate the large-scale structure of the Universe today. It is believed that dark matter has played an important role in the structure formation, building the potential wells that the baryonic matter would then collapse into. Later, emission from the first generation of stars and supernovae seems to have reionised the Universe temporarily. While the gravitational pull of matter led to a deceleration of the expansion during these stages, we are now in an era where the energy density is dominated by the dark energy, which tends to cause a cosmic acceleration.

The observational evidence for the Hot Big Bang Model is overwhelming. The first hint that the Universe is not static came from Edwin Hubble's observation that most galaxies are receding away from us. The velocity v of a given galaxy is on average proportional to its distance d , $v = Hd$. The constant of proportionality is called Hubble constant and has a value of $H = 100 h \text{ km s}^{-1} \text{ Mpc}^{-1}$ and $h = 0.73 \pm 0.03$ [5]. The expansion can be understood in the framework of General Relativity. The Einstein equations relate the energy-momentum tensor to the properties of space-time. When the matter content of the Universe is modelled as a perfect fluid, the Friedmann equation relates the energy density ρ of the Universe to the time development of its scale factor R :

$$H^2 = \left(\frac{\dot{R}}{R} \right)^2 = \frac{8\pi G\rho}{3} - \frac{k}{R^2} + \frac{\Lambda}{3} \quad (2.1)$$

where G is the gravitational constant, $k = 0, \pm 1$ describes the curvature of space on large scales, and the cosmological constant Λ is connected to dark energy.

The cosmic microwave background was first observed by Penzias and Wilson in 1965 [4]. Its existence had already been predicted for a Hot Big Bang Model by Gamow more than 20 years in advance. Before recombination, radiation and matter were coupled via the reaction $H + \gamma \leftrightarrow p + e^-$. When the temperature dropped well below the ionisation energy of hydrogen, due to the expansion of the Universe, the Universe became transparent, the photons decoupled from matter and are travelling on geodesics ever since. These photons permeate the Universe today.

The relative abundance of light elements in the Universe agrees accurately with what would be synthesised in an initially hot, expanding universe. While it is generally accepted that the heavier elements are produced in stars towards the final stages of their lifetimes, this mechanism cannot explain the fact that the mass fraction of ^4He is about 24%. In contrast to this, taking into account the age of the Galaxy, its luminosity and the energy yield of hydrogen fusion, it is found that hydrogen burning can only account for a helium abundance of roughly 1%. The theory of Big Bang nucleosynthesis predicts the abundances of the light nuclei ^2H , ^3He , ^4He , and ^7Li , synthesised at the end of the first three minutes of the Universe, as a function of the baryon-to-photon ratio η_B . The observed abundances agree with the predicted ones, from the number ratio $^4\text{He}/\text{H} \sim 0.08$ down to $^7\text{Li}/\text{H} \sim 10^{-10}$ [5].

Lastly, the oldest objects found in the Universe – globular clusters of stars and some radioactive isotopes – do not seem to exceed an age of around 13 billion years. This indicates that the Universe is of finite age and is consistent with the age of the Universe

as found in the standard model of cosmology.

The contribution of a given component i with energy density ρ_i to the total energy density of the Universe is usually given as a fraction of the critical density $\rho_c = 3H_0^2/8\pi G$ that leads to a Universe whose expansion comes to a halt asymptotically and that is flat on large scales:

$$\Omega_i = \frac{\rho_i}{\rho_c} \quad (2.2)$$

From a combination of observations of the anisotropy in the cosmic microwave background by the WMAP experiment [6], the luminosity distances to type Ia supernovae [7], and the baryon acoustic oscillations in the distribution of galaxies [8], the key parameters of the Hot Big Bang Model are determined to be [9, 10] $\Omega_B = 0.0462 \pm 0.0015$ for the baryon density, $\Omega_{\text{dm}} = 0.233 \pm 0.013$ for the dark matter density, $\Omega_\Lambda = 0.721 \pm 0.015$ for the dark energy density and $H_0 = (70.1 \pm 1.3) \text{ km s}^{-1} \text{ Mpc}^{-1}$ for the Hubble constant. The total density is found to be $\Omega_{\text{tot}} = 1.0052 \pm 0.0064$, consistent with the critical value.

An important aspect of the Hot Big Bang model is the freeze-out of heavy particles. Assuming that a massive particle species of mass m never left thermal equilibrium, the number of particles N in a comoving volume is $N \sim (m/T)^{3/2} \exp(-m/T)$ and therefore negligible today if $m/T \gg 1$. However, a so-called relic density of massive particles can remain if their interaction rate Γ drops below the expansion rate H of the Universe at some point in the expansion history. As an example, a weakly interacting species χ that is annihilated and created in the reaction $\chi + \bar{\chi} \leftrightarrow X + \bar{X}$ is considered. The X particles are taken to be strongly interacting compared to the χ 's and therefore are kept in thermal equilibrium. The time evolution of the number density n_χ in the comoving frame is then governed by the Boltzmann equation that can be derived to be

$$\frac{dn_\chi}{dt} = -3Hn_\chi - \langle\sigma|\mathbf{v}|\rangle(n_\chi^2 - (n_\chi^{\text{EQ}})^2) \quad (2.3)$$

The first term on the right-hand side expresses a decrease in number density that is due to the expansion of the Universe. The second term describes annihilation of χ particles, proportional to $\langle\sigma|\mathbf{v}|\rangle n_\chi^2$ and creation in the back-reaction, proportional to $\langle\sigma|\mathbf{v}|\rangle (n_\chi^{\text{EQ}})^2$. Here, $\langle\sigma|\mathbf{v}|\rangle$ denotes the thermally averaged annihilation cross section for the reaction $\chi + \bar{\chi} \rightarrow X + \bar{X}$ and n_χ^{EQ} is the equilibrium number density of χ 's. Normalising n_χ to the entropy density s , which can be shown to be conserved in a volume of $R^3(t)$, and introducing $Y_\chi \equiv n_\chi/s$ and $x \equiv m_\chi/T$, (2.3) can be rewritten in the form

$$\frac{x}{Y_\chi^{\text{EQ}}} \frac{dY}{dx} = -\frac{\Gamma_A}{H} \left(\left(\frac{Y_\chi}{Y_\chi^{\text{EQ}}} \right)^2 - 1 \right) \quad (2.4)$$

where $\Gamma_A = n_\chi^{\text{EQ}} \langle\sigma|\mathbf{v}|\rangle$. This shows that the evolution is governed by the factor Γ_A/H . Equation (2.4) can be solved numerically and the solution describes the freeze-out of a massive particle species. At some value $x_f = m_\chi/T_f$ for the freeze-out temperature T_f , the abundance Y_χ leaves the equilibrium curve. The relic abundance will be higher the

smaller the annihilation cross section is. Generically, an order-of-magnitude estimate is given by [11]

$$\Omega_\chi h^2 \approx \frac{3 \cdot 10^{-27} \text{ cm}^3 \text{ s}^{-1}}{\langle \sigma v \rangle} \quad (2.5)$$

2.2 Evidence for the existence of dark matter

A variety of observations, both direct and indirect, from galactic to cosmological scales, lead to the conclusion that a yet unknown form of matter must exist which contributes significantly to the energy density in the Universe. Although hints for its existence are manifold, it has not been identified yet. This is known as the dark matter problem. Any candidate for dark matter must be only weakly interacting since it could not have evaded our attention otherwise. It must be stable on cosmological timescales or it would have disappeared from the cosmic stage long ago. In the following, the evidence for the existence of dark matter in the Universe will be reviewed briefly [5, 11].

The most direct evidence for the existence of dark matter can be obtained at the galactic scale. Dark matter betrays itself in practically all rotation curves of galaxies measured so far. The rotation curve describes the rotational velocity $v(r)$ of objects at a distance r from the galactic centre around the centre. It is based on measurements of the Doppler shift of suitable emission or absorption lines. Most importantly, the observations can be extended beyond the visible disk by looking at the CO and HI(21 cm) line emissions of gas clouds. If all matter in a galaxy were located in the luminous disk, one would expect a rotation curve $v \propto r^{-1/2}$ outside the disk according to Kepler's third law. Contrary to this, flat rotation curves are observed, $v = \text{const}$, consistent with a mass distribution of $\rho \propto r^{-2}$ that extends beyond the visible disk. It is assumed that this is due to dark matter forming halos around the disks of galaxies.

On larger scales, observations of clusters of galaxies provide hints for the existence of dark matter. This includes studies of weak gravitational lensing of background galaxies by a cluster which depends on the mass distribution inside the cluster. In addition, in a virialized cluster, the peculiar velocities of the galaxies allow one to trace the gravitational potential. The same is true for measurements of the x-ray emissions of the hot gas in the cluster. The mass-to-light ratios so obtained exceed the one measured in the solar neighbourhood by more than an order of magnitude which implies the presence of additional non-luminous matter.

On the cosmological scale, the discovery of tiny anisotropies in the cosmic microwave background opened the door to a new era of precision cosmology. According to the standard paradigm, small random density fluctuations in the early Universe caused gravitational instabilities which formed the seeds of the large-scale structures observed today. The observed anisotropies then are a combination of a snapshot of the density distribution at the time of decoupling and the subsequent gravitational red- and blueshifting of photons leaving over- or underdense regions. The sky map of the anisotropies in the cosmic microwave background has been measured, e.g. by the WMAP experiment over a period of five years (fig. 2.1 *left*).

The basic idea for the understanding of the anisotropies at smaller scales is the realisa-

2.2 Evidence for the existence of dark matter

tion that the early Universe must have resounded with acoustic oscillations. They are created when fluctuations in density cause photons and matter to fall into potential wells. The infall will be slowed and eventually reversed by radiation pressure, and the process will repeat to form an oscillation. The properties of the oscillations will depend on the fractional contributions of the various forms of energy to the overall energy content of the Universe, and hence on the cosmological parameters. The anisotropies can be characterised by their angular scales. For example, the size of a causally connected region at the time of decoupling is given by $H(z = z_{\text{rec}})^{-1}$, where z_{rec} is the redshift at recombination. The angle subtended by such a region today is given by $\theta = 1/d_A H(z = z_{\text{rec}})$ and defines the position of the so-called first acoustic peak. The angular size distance d_A depends on the expansion history of the Universe and thus on the cosmological parameters. More specifically, the anisotropy is decomposed in spherical harmonics,

$$\frac{\delta T(\hat{\mathbf{n}})}{T} = \sum_{l=2}^{\infty} \sum_{m=-l}^l a_{lm} Y_{lm}(\theta, \phi) \quad (2.6)$$

A term of index l corresponds to fluctuations with typical angular scale π/l . Information about the cosmological parameters can then be obtained from the power spectrum (fig. 2.1

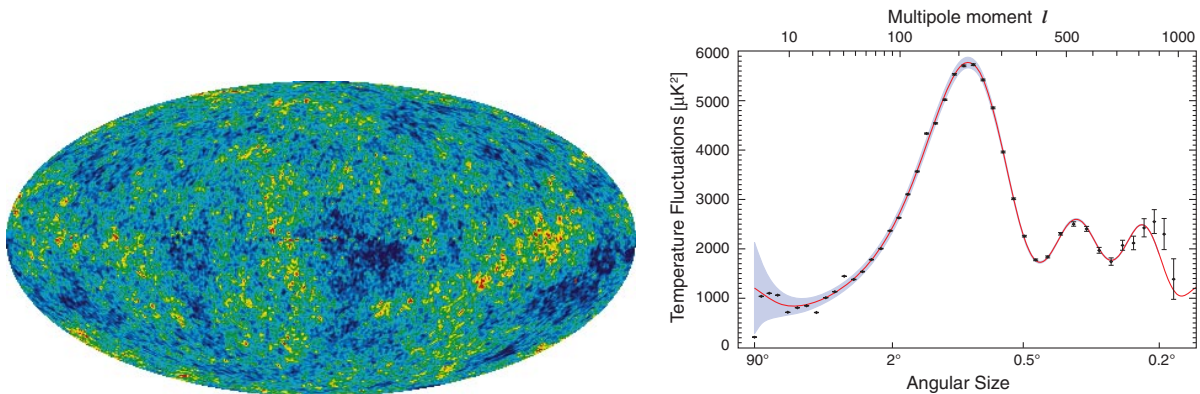


Fig. 2.1: *Left:* Sky map of the temperature anisotropies in the cosmic microwave background measured by the WMAP experiment in five years. Red regions are warmer and blue regions are colder by about $200 \mu\text{K}$. *Right:* Corresponding power spectrum. Credit for both pictures: NASA/WMAP Science Team [9].

right) given in terms of the angular averages

$$C_l = \langle a_{lm} a_{lm}^* \rangle = \frac{1}{2l+1} \sum_{m=-l}^l a_{lm} a_{lm}^* \quad (2.7)$$

The cosmological parameters extracted in this way have already been quoted in section 2.1. In particular, the discrepancy between the baryon density Ω_B and the matter density $\Omega_M = \Omega_B + \Omega_{\text{dm}}$ clearly shows the need for a dark matter component.

In addition, Big Bang nucleosynthesis, as discussed in section 2.1, predicts the value of

$\Omega_B h^2$ to be in the range $0.017 \leq \Omega_B h^2 \leq 0.024$ at 95% confidence level [5], and this is consistent with the value obtained from the WMAP data.

2.3 Dark matter candidates

Having established the existence of dark matter, the question of its nature arises. In this section, the most important candidates will be reviewed briefly [11].

The most widely studied candidate is provided by supersymmetric extensions to the standard model of particle physics. This will be discussed in more detail in section 2.4.

Standard model neutrinos Standard model neutrinos have been considered as candidates for dark matter in the past. They only interact by the weak force and they are known to be massive from the observation of neutrino oscillations. Among the candidates presented here, they are special because their existence is not hypothetical but has been well established. However, assuming that neutrinos do not overclose the Universe, their relic density can be calculated to be

$$\Omega_\nu h^2 = \frac{\sum m_\nu}{93 \text{ eV}} \quad (2.8)$$

However, because of their low mass, neutrinos are relativistic and therefore a candidate for so-called hot dark matter. Data on the large-scale structure of the Universe, combined with anisotropies in the cosmic microwave background and other cosmological probes can be used to set an upper limit of 0.17 eV (95% confidence level) on the neutrino masses [12], implying a relic density of not more than $\Omega_\nu h^2 < 0.006$, not enough for neutrinos to be the dominant form of dark matter.

Kaluza-Klein dark matter In theories of universal extra dimensions, it is assumed that there exist dimensions in addition to the known four-dimensional space-time. The additional dimensions have not been observed yet, so they have to be compactified which introduces some characteristic scale R . This leads to the appearance of a so-called tower of new particle states in the effective four-dimensional theory, with the mass of the n -th Kaluza-Klein (KK) mode given by

$$m^{(n)} = \sqrt{(n/R)^2 + m^2} \quad (2.9)$$

for a standard-model particle of mass m . Assuming a symmetry called KK parity, the lightest KK state (LKP) can be stable and therefore constitutes a candidate for dark matter [13, 14]. It is likely to be associated with the first excitation of the hypercharge gauge boson, the $B^{(1)}$. A calculation of the relic density shows that the LKP can explain the observed relic density Ω_{dm} of dark matter if its mass is on the order of 1000 GeV. The $B^{(1)}$ as a dark matter candidate has the attractive feature of dominantly producing charged leptons in its annihilation. This would provide a source of hard positrons in the cosmic rays.

Axions The axion [15] was proposed as a solution to the strong CP problem that arises in the standard model of particle physics. In general, the action density of the standard model includes a term

$$\mathcal{L}_{\text{SM}} = \dots + \frac{\theta g^2}{32\pi^2} G_{\mu\nu}^a \tilde{G}^{a\mu\nu} \quad (2.10)$$

where $G_{\mu\nu}^a$ are the QCD field strengths, g is the QCD coupling constant, and θ is a parameter. The observed physics depends on the value $\bar{\theta} \equiv \theta - \arg \det m_q$ where m_q is the quark mass matrix. While the term in (2.10) violates the C and CP symmetries, as do the weak interactions in the standard model, the experimental upper bound on the electric dipole moment of the neutron limits $|\bar{\theta}| < 10^{-10}$ [15] and the question arises why $\bar{\theta}$ is so small when it can be expected to be an arbitrary number. It was shown that the introduction of an additional field $A(x)$, called the axion, can naturally explain why $\bar{\theta}$ is zero. The corresponding term in the action is

$$\mathcal{L}_{\text{axion}} = \frac{1}{2} \partial_\mu A \partial^\mu A + \frac{g^2}{32\pi^2} \frac{A(x)}{f_A} G_{\mu\nu}^a \tilde{G}^{a\mu\nu} \quad (2.11)$$

f_A is a constant with dimension of energy, and the mass and couplings of the axion can be expressed in terms of this constant, $m_A, g_{Aii} \propto f_A^{-1}$. The allowed axion mass range is limited from below by cosmological bounds and from above by the physics of stellar evolution to lie in the range $10^{-6} \sim 10^{-3}$ eV. Nevertheless, the axion is a viable candidate for cold dark matter, with relic density $\Omega_A \propto m_A^{-7/6}$, because cold, non-thermal axions may have been produced during the QCD phase transition in the early Universe. Searches for cosmological and solar axions are underway, but they have eluded discovery so far.

Other candidates Some other candidates [11] include sterile neutrinos, gravitinos and axinos. Positrons from annihilation of light scalar dark matter have been proposed to cause the 511 keV-line observed in the direction of the Galactic bulge. Little Higgs models, introduced as an alternative mechanism to supersymmetry to stabilise the weak scale, may contain a dark matter candidate, too. Superheavy dark matter particles, so called wimpzillas, would be interesting also because of their contribution to the phenomenology of ultra-high energy cosmic rays. Many more exotic proposals exist. It should be noted that it is entirely possible that dark matter is made up of more than one species.

2.4 Dark matter in the mSUGRA model

Although the standard model of particle physics has so far been enormously successful at describing the interactions of matter at the most fundamental level, it has a number of shortcomings from a theoretical point of view. Two examples are the hierarchy problem and the problem of unification of the gauge couplings. The former is related to the question why the Higgs mass is so small. While the mass scale of the standard model is set by the vacuum expectation value of the Higgs $v \approx 246$ GeV, divergent quadratic loop corrections to the Higgs mass occur, $\delta m_H^2 \sim \Lambda^2$, where Λ is a cut-off scale at which the standard model must be modified to remain valid. This is usually associated with the Planck scale, $M_P = (G_N)^{-1/2} \approx 1.2 \cdot 10^{19}$ GeV, which means that the mass parameter

2 Cosmic rays and dark matter

μ in the Higgs potential $V = -\mu^2\phi^\dagger\phi + \lambda/4(\phi^\dagger\phi)^2$ must be of a similar amplitude to cancel the divergence. This large fine-tuning, where two large mass scales almost cancel to produce the observed masses of the standard model, seems unnatural and is known as the hierarchy problem.

The second example revolves around the unification of gauge couplings. The running of the gauge couplings in the standard model as a function of the energy scale is described by the renormalisation group equations (RGEs). The inverse gauge couplings $\alpha_1^{-1}(Q^2)$, $\alpha_2^{-1}(Q^2)$, and $\alpha_3^{-1}(Q^2)$ fail to meet at high $Q^2 \sim (10^{16} \text{ GeV})^2$ though they come close to doing so. A unification of the gauge couplings is a highly desirable property of a fundamental theory.

In fact, these and other problems can be overcome in supersymmetric extensions to the standard model [11, 16, 17, 18]. The operators Q of supersymmetry (SUSY) satisfy the algebraic relation

$$\{Q_a, \bar{Q}_b\} = 2\gamma_{ab}^\mu P_\mu \quad \text{where} \quad \bar{Q}_a \equiv (Q^\dagger \gamma_0)_a \quad (2.12)$$

and transform bosons into fermions and vice versa,

$$Q_a |J\rangle = |J \pm 1/2\rangle \quad (2.13)$$

Two remarkable features of a supersymmetric theory can be seen from (2.12) and (2.13). The link between the SUSY operators and the 4-momentum operator demonstrates that the concept of space-time has to be extended to include additional degrees of freedom, acted upon by the Q 's. The second consequence is the prediction of additional particles, superpartners to the standard model fields, with identical quantum numbers but different spin. As none of the superpartners has been discovered yet, their masses must be different from the standard model ones, meaning that supersymmetry must be broken. The supersymmetric model that includes the smallest number of additional particles necessary to give rise to all fields of the standard model is called the Minimal Supersymmetric Standard Model (MSSM). Its field content is summarised in table 2.1.

The MSSM can be formulated such that a multiplicative quantum number, called R -parity and defined as

$$R \equiv (-1)^{3B+L+2S} \quad (2.14)$$

is conserved. Standard model particles have $R = 1$ and the superpartners (sparticles) have $R = -1$. Originally introduced to prevent rapid proton decay, R -parity conservation implies that the lightest sparticle (called the LSP) is stable and can only be destroyed by pair annihilation. In many MSSM scenarios, the LSP is the lightest neutralino $\chi \equiv \tilde{\chi}_1^0$ and this is the best motivated candidate for dark matter known so far. Because of their properties, neutralinos are among the group of candidates called weakly-interacting massive particles (WIMPs).

In general, the neutralino is a linear combination of the superpartners of the B and W_3 gauge bosons and of the neutral Higgses,

$$\chi = N_{11}\tilde{B} + N_{12}\tilde{W}_3 + N_{13}\tilde{H}_1^0 + N_{14}\tilde{H}_2^0 \quad (2.15)$$

2.4 Dark matter in the mSUGRA model

Standard Model particles and fields		Supersymmetric partners			
Symbol	Name	Interaction eigenstates Symbol	Interaction eigenstates Name	Mass eigenstates Symbol	Mass eigenstates Name
$q = d, c, b, u, s, t$	quark	\tilde{q}_L, \tilde{q}_R	squark	\tilde{q}_1, \tilde{q}_2	squark
$l = e, \mu, \tau$	lepton	\tilde{l}_L, \tilde{l}_R	slepton	\tilde{l}_1, \tilde{l}_2	slepton
$\nu = \nu_e, \nu_\mu, \nu_\tau$	neutrino	$\tilde{\nu}$	sneutrino	$\tilde{\nu}$	sneutrino
g	gluon	\tilde{g}	gluino	\tilde{g}	gluino
W^\pm	W -boson	\tilde{W}^\pm	wino	} $\tilde{\chi}_{1,2}^\pm$	chargino
H^-	Higgs boson	\tilde{H}_1^-	higgsino		
H^+	Higgs boson	\tilde{H}_2^+	higgsino		
B	B -field	\tilde{B}	bino	} $\tilde{\chi}_{1,2,3,4}^0$	neutralino
W^3	W^3 -field	\tilde{W}^3	wino		
H_1^0	Higgs boson	\tilde{H}_1^0	higgsino		
H_2^0	Higgs boson	\tilde{H}_2^0	higgsino		
H_3^0	Higgs boson				

Tab. 2.1: Standard Model particles and their superpartners in the MSSM [23].

The gaugino and higgsino fractions f_G and f_H are then defined as

$$f_G = N_{11}^2 + N_{12}^2 \quad \text{and} \quad f_H = N_{13}^2 + N_{14}^2 \quad (2.16)$$

respectively.

The MSSM is based on the same gauge group as the standard model. The R -parity conserving superpotential, in the notation of [16], is given by

$$W = h_{ij}^U \hat{Q}_i \hat{H}_u \hat{u}_j^c + h_{ij}^D \hat{Q}_i \hat{H}_d \hat{d}_j^c + h_{ij}^E \hat{L}_i \hat{H}_d \hat{e}_j^c + \mu \hat{H}_d \hat{H}_u \quad (2.17)$$

Here \hat{Q} and \hat{L} represent the quark and lepton SU(2) doublet superfields, \hat{u}^c , \hat{d}^c , \hat{e}^c the corresponding SU(2) singlets, and \hat{H}_u , \hat{H}_d the Higgs superfields whose scalar components give mass to up- and down-type quarks and/or leptons, respectively. Generational indices have been shown explicitly, but group indices have been dropped. The allowed soft SUSY-breaking terms are given by

$$\begin{aligned} -\mathcal{L}_{\text{soft}} = & \left(A_{(ij)}^U h_{ij}^U \tilde{Q}_i H_u \tilde{u}_j^c + A_{(ij)}^D h_{ij}^D \tilde{Q}_i H_d \tilde{d}_j^c + A_{(ij)}^E h_{ij}^E \tilde{L}_i H_d \tilde{e}_j^c + \text{h.c.} \right) + B\mu(H_d H_u + \text{h.c.}) \\ & + m_{H_d}^2 |H_d|^2 + m_{H_u}^2 |H_u|^2 + m_{\tilde{L}}^2 |\tilde{L}|^2 + m_{\tilde{e}^c}^2 |\tilde{e}^c|^2 + m_{\tilde{Q}}^2 |\tilde{Q}|^2 + m_{\tilde{u}^c}^2 |\tilde{u}^c|^2 + m_{\tilde{d}^c}^2 |\tilde{d}^c|^2 \\ & + \frac{1}{2} (M_1 \bar{\psi}_B \psi_B + M_2 \bar{\psi}_W^a \psi_W^a + m_{\tilde{g}} \bar{\psi}_g^a \psi_g^a + \text{h.c.}) \end{aligned} \quad (2.18)$$

Here the tilded fields are the scalar partners of the quark and lepton fields, while the ψ_i are the spin-1/2 partners of the $i = U(1)_Y, SU(2)_L, SU(3)_c$ gauge bosons. The $A_{(ij)}$ and B are mass parameters.

A study of the phenomenology of the MSSM is made difficult by its large number of free

2 Cosmic rays and dark matter

parameters of more than 100, mostly masses and mixing angles. This number is greatly reduced in the constrained MSSM – also called mSUGRA – model [19, 20, 21, 22] where the MSSM is coupled to minimal supergravity from which the following set of assumptions emerges, inspired by the unification of gauge couplings at some high unification scale M_X [16]:

- Common gaugino mass $m_{1/2}$. The soft SUSY-breaking gaugino mass terms are equal to $m_{1/2}$ at M_X :

$$M_1(M_X) = M_2(M_X) = m_{\tilde{g}}(M_X) \equiv m_{1/2} \quad (2.19)$$

- Common scalar mass m_0 . The soft SUSY-breaking scalar mass terms contributing to the squark, slepton, and Higgs boson masses are equal to m_0 at M_X :

$$m_{\tilde{Q}}^2(M_X) = m_{\tilde{u}^c}^2 = \dots = m_{H_d}^2(M_X) = m_{H_u}^2(M_X) \equiv m_0 \quad (2.20)$$

- Common trilinear scalar coupling A_0 . The soft trilinear SUSY-breaking terms are all equal to A_0 at M_X :

$$A_t(M_X) = A_b(M_X) = A_\tau(M_X) = \dots \equiv A_0 \quad (2.21)$$

Requiring radiative electroweak symmetry breaking to occur, $\mu^2(m_Z)$ can be eliminated as a free parameter in favour of m_Z , but the sign of μ remains free. Similarly, $B(m_Z)$ can be eliminated in favour of $\tan \beta(m_Z)$, where $\tan \beta \equiv v_u/v_d$ is the ratio of the Higgs vacuum expectation values. In the end, the five free parameters

$$m_0, m_{1/2}, A_0, \tan \beta, \text{sgn } \mu \quad (2.22)$$

remain. A study of the mSUGRA model in connection with the indirect search for dark matter will be the subject of chapter 6.

2.5 Production and propagation of cosmic rays

For centuries, mankind has used the light reaching us from distant celestial objects to gather information about the Universe surrounding us. Nowadays, in the field of astronomy, the emission in a large part of the electromagnetic spectrum and from very different sources is examined by a multitude of observatories. In 1912, cosmic rays [24, 25, 26, 27] were discovered by Victor Hess during a series of balloon flights over Austria, Bohemia and Prussia [28] who found an increase in the discharge rate of an electrometer with increasing altitude. They constitute another source of knowledge about the workings of nature, and the interplay between their study and conventional particle physics has created the field of astroparticle physics. A number of important discoveries in particle physics have been made in cosmic rays. For example, the positron [29], the muon [30, 31], the pion [32] and the kaon [33], among others, were first observed in experiments studying cosmic rays. On the other hand, particle physics plays a vital role in the understanding of cosmic-ray production and propagation mechanisms.

2.5.1 Basic facts about cosmic rays

Cosmic rays mainly consist of nuclei. Roughly 90% of them are protons, 9% are α -particles, and heavier nuclei make up the rest. Electrons, positrons and antiprotons are found in small quantities. In general, the relative abundances of the individual elements follow the abundances found in the solar system. This indicates that the production mechanism is the same in both cases, namely fusion of lighter nuclei in the cores of stars near the end of their life cycle. But there are also important differences. On the one hand, protons are much more abundant than nuclei with $Z > 1$ in the solar system than in the cosmic rays. This could have something to do with the fact that hydrogen is relatively hard to ionise for injection into the acceleration process, or it could reflect a genuine difference in composition at the source. On the other hand, the elements Li, Be, B and Sc, Ti, V, Cr, Mn are much more abundant in the cosmic rays than in solar system material. While they are essentially absent as end products in stellar nucleosynthesis, they are produced in spallation processes during interactions of carbon and oxygen or iron with interstellar matter, respectively. This mechanism can be used for an understanding of the propagation process.

Starting in the GeV-range, the number density of cosmic rays as a function of energy follows a power law up to very high energies,

$$\frac{dN}{dE} \propto E^{-\gamma} \quad (2.23)$$

Up to roughly 10^{15} eV, one finds $\gamma \approx 2.7$. At higher energies, the spectral index γ increases, that is the slope of the spectrum becomes steeper, and this is known as the *knee* of the spectrum. This decrease may indicate that some of the acceleration mechanisms reach a maximal energy here. Around 10^{19} eV, the spectral index decreases again, the particles observed in this range are believed to be of extragalactic origin, especially as their Larmor radius exceeds the size of the Galaxy. In fact, the Pierre Auger collaboration has reported a tentative correlation between the arrival directions of cosmic rays above $6 \cdot 10^{19}$ eV and the position of active galactic nuclei within ~ 75 Mpc [34]. Events with energies above 10^{20} eV have even been observed, corresponding to macroscopic energies of a few Joules.

2.5.2 Sources of cosmic rays

In this section, the widely accepted theory of cosmic-ray acceleration shall be briefly discussed, limited to the energy range of interest for this study, below the knee in the cosmic-ray spectrum [25]. While it has been observed that particles are accelerated to GeV energies in solar flares, a different mechanism is needed to explain acceleration up to the TeV range.

From the energy density of cosmic rays, $\rho_E \approx 1 \text{ eV/cm}^3$, a timescale for diffusion out of the Galaxy of $\tau \sim 2 \cdot 10^7$ a, a galactic radius of 15 kpc and a disk height of 800 pc, the power needed to keep up the cosmic-ray energy density is roughly estimated by

$$P_{\text{CR}} = \frac{V \rho_E}{\tau} \sim 4 \cdot 10^{33} \text{ J/s} \quad (2.24)$$

2 Cosmic rays and dark matter

Supernovae are the most likely source for that power. Given a typical energy release of 10^{44} J and a mean rate of one supernova every 30 years, the power released is 10^{35} J/s so that an efficiency of a few percent would suffice. First-order Fermi acceleration at a strong shock describes how a particle diffusing through the turbulent magnetic fields carried along with a moving plasma gains energy proportional to v/c during each cycle of passage through the shock front, where v is the velocity of the shock front. Since there is a certain possibility in each cycle for the particle to be lost from the acceleration region, this process naturally leads to the observed power law of the cosmic-ray spectrum. This picture is now supported by observational evidence. An example is shown in figure 2.2

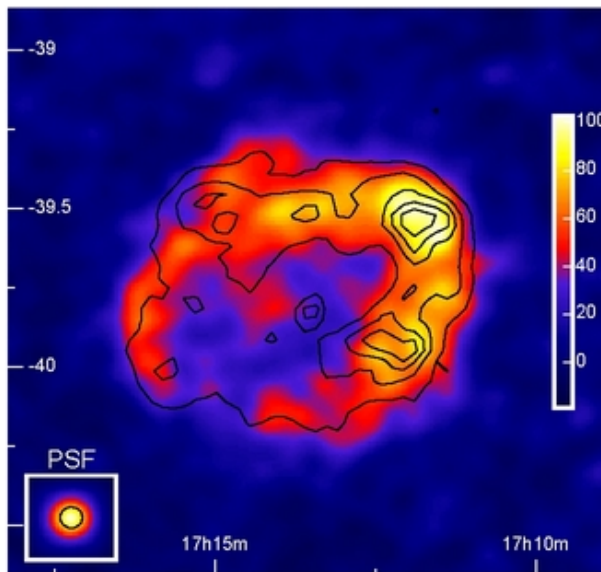


Fig. 2.2: γ -radiation from supernova remnant RX 1713.7-3946 as measured by HESS [35]. The contour lines trace the x-ray emission and the inset in the lower left corner shows the point spread function of HESS. Reproduced with permission by the authors.

depicting the γ -radiation emitted by the supernova remnant RX 1713.7-3946, as measured by the HESS telescope. This shows the internal structure of a source of TeV- γ -rays. The γ -ray spectrum follows a power law with spectral index of about 2 and extends up to roughly 10 TeV. This implies the presence of protons accelerated to even higher energies than that, producing the observed γ -rays in collisions with matter present in the vicinity of the supernova remnant.

2.5.3 Propagation of cosmic rays in the Galaxy

On the way of cosmic rays through the Galaxy, their spectra are altered and their composition is changed by a variety of physical processes. Hadronic interactions of protons and nuclei with interstellar matter create secondary charged particles, as well as γ -rays by π^0 -production. Electrons lose energy by bremsstrahlung processes due to the interstellar matter, synchrotron radiation in the Galactic magnetic field, and inverse Compton scattering on photons of the cosmic microwave background and of starlight. Radioactive

isotopes decay in flight.

As opposed to γ -rays, charged cosmic-ray particles do not follow straight lines, but they are scattered on magnetohydrodynamic waves and discontinuities. As we have no information about the microscopic structure of the magnetic field in the Galaxy, charged particles will in effect perform a random walk, and therefore, a diffusion model is the appropriate description of the propagation process. This also explains the high level of isotropy found in cosmic rays and the fact that the Galaxy can store cosmic rays up to high energies. Intuitively, it is clear that the diffusion coefficient must have a tendency to increase with energy because the trajectory of a particle will be more rigid with regard to a magnetic field at higher energies.

The study of cosmic-ray propagation is vital for an indirect search for dark matter because all the signal particles – positrons, antiprotons and γ -rays – are produced as secondaries in the interactions of primary cosmic rays with the interstellar matter. This means that propagation effects constitute the background that has to be disentangled from any supposed signal. For example, pions and kaons produced in collisions of protons with interstellar matter decay to muons and these subsequently decay to positrons and electrons.

While several analytical or semi-analytical approaches to the description of cosmic-ray propagation exist [36], it was chosen to use the numerical model described by the Galprop code [37, 38, 39, 40, 41], version 50p, which was created with the aims of enabling simultaneous predictions of all relevant observations, overcoming the limitations of analytical models and incorporating as much current information as possible, for example on galactic structure and source distributions. The propagation equation is written in the form

$$\frac{\partial \psi}{\partial t} = q(\vec{r}, t) + \vec{\nabla} \cdot (D_{xx} \vec{\nabla} \psi - \vec{V} \psi) + \frac{\partial}{\partial p} p^2 D_{pp} \frac{\partial}{\partial p} \frac{1}{p^2} \psi - \frac{\partial}{\partial p} \left(\dot{p} \psi - \frac{p}{3} (\vec{\nabla} \cdot \vec{V}) \psi \right) - \frac{1}{\tau_f} \psi - \frac{1}{\tau_r} \psi \quad (2.25)$$

Here, $\psi = \psi(\vec{r}, p, t)$ is the density per unit of total particle momentum and $\psi(p) dp = 4\pi p^2 f(\vec{p})$ in terms of phase-space density $f(\vec{p})$. The terms on the right hand side of the propagation equation can be understood as follows:

- $q(\vec{r}, t)$ is the source term. The injection spectrum of nucleons is assumed to be a power law in momentum, $dq(p)/dp \propto p^{-\gamma}$, and the distribution of cosmic-ray sources is chosen as

$$q(R, z) = q_0 \left(\frac{R}{R_\odot} \right)^\alpha \exp \left(-\beta \frac{R - R_\odot}{R_\odot} - \frac{|z|}{0.2 \text{ kpc}} \right) \quad (2.26)$$

where q_0 is a normalisation constant and the parameters here are chosen to be $\alpha = 1/2$ and $\beta = 1$. $R_\odot = 8.5 \text{ kpc}$ is the distance of the solar system from the Galactic centre.

- D_{xx} is the spatial diffusion coefficient. It depends on rigidity R as $D_{xx} = D_0 \beta^\lambda (R/R_0)^\alpha$, where $\beta = v/c$, D_0 is a constant and λ influences the behaviour at low rigidities. Typical values of the diffusion coefficient are $D_{xx} \sim (3 - 5) \cdot 10^{28} \text{ cm}^2 \text{ s}^{-1}$ at $\sim 1 \text{ GeV}/n$, and a is in the range 0.3 to 0.6.

2 Cosmic rays and dark matter

- Galactic winds lead to a convective transport of cosmic rays and are described by the convection velocity $V(z)$. $V(z)$ is assumed to increase linearly with distance from the Galactic plane. This implies a constant adiabatic energy loss.
- In addition to spatial diffusion, the scattering of cosmic-ray particles on randomly moving magnetohydrodynamic waves leads to stochastic reacceleration, described in the transport equation as diffusion in momentum space with the diffusion coefficient D_{pp} . It is related to D_{xx} by

$$D_{pp}D_{xx} = \frac{4p^2v_A^2}{3a(4-a^2)(4-a)w} \quad (2.27)$$

where w characterises the level of turbulence. The main free parameter in this relation is the Alfvén speed v_A , which is a characteristic velocity of weak disturbances propagating in a magnetic field. As only v_A^2/w is relevant here, one can set $w = 1$.

- \dot{p} is the momentum loss rate, and the term involving $\vec{\nabla} \cdot \vec{V}$ represents adiabatic momentum gain or loss in the nonuniform flow of gas, with a frozen-in magnetic field whose inhomogeneities scatter the cosmic rays.
- τ_f and τ_r are the timescales for loss by fragmentation and radioactive decay, respectively.

The structure of the Galaxy is included in the form of the gas content, which is important for secondary production, and the interstellar radiation field (ISRF) and magnetic field, which strongly affect electron energy losses. The distribution of atomic hydrogen is reasonably well known from 21-cm surveys, but the distribution of molecular hydrogen can only be estimated using the CO tracer [41]. The Galactic magnetic field can be determined from pulsar rotation and dispersion measurements combined with a model for the distribution of ionised gas. The ISRF comes from the cosmic microwave background and from stars of all types and is modified by absorption and reemission by interstellar dust.

Interactions and production of secondary particles are governed by the cross sections for energy losses of nuclei and electrons, bremsstrahlung and synchrotron radiation, inverse Compton emission and pion production of γ -rays, electrons and positrons.

Equation (2.25) is solved numerically in two dimensions, assuming cylindrical symmetry, with spatial boundary conditions assuming free particle escape, and the time dependence is followed until the steady state is reached. The propagation equation has to be considered for all relevant particle species, and the resulting reaction network is solved starting at the heaviest nucleus, ^{64}Ni . Equation (2.25) is solved, computing all the resulting secondary source functions, and then the process is repeated for the nuclei with $A - 1$.

Before studying the predictions of the Galprop model in some detail, one first has to consider how interactions of cosmic-ray particles with the solar wind and the geomagnetic field affect the particle spectra measured at the top of the Earth's atmosphere.

2.5.4 Solar modulation

Arriving at the outskirts of the solar system, the fluxes of cosmic-ray particles are modulated due to interactions with the solar wind [26]. The first hints at this effect came from observations of an anticorrelation between neutron monitor counts and the sunspot number, the latter being an indicator of the level of solar activity [27]. The solar wind consists mostly of protons, with a typical kinetic energy of 500 eV, velocities of 350 km/s, flux of $1.5 \cdot 10^{12} \text{m}^{-2} \text{s}^{-1}$ and a temperature of 10^6 K. It originates from the corona of the Sun. A magnetic field, rooted in the Sun, is frozen into the solar wind plasma, and the Sun's rotation leads to the creation of the large-scale structure known as the Archimedes spiral. Cosmic-ray particles are scattered on the magnetic fields. Gleeson and Axford [42] model the solar modulation by taking into account cosmic-ray diffusion through this magnetic field, convection by the outward motion of the solar wind, and adiabatic deceleration of the cosmic rays in this flow. In the force-field approximation, that is used in the remainder of this thesis, the effect of solar modulation can be described by a single parameter ϕ that depends on the solar wind speed V and the diffusion coefficient κ as

$$\phi = \frac{E + m}{E} \frac{T}{3} \int_{r_E}^{r_b} \frac{V(x, t)}{\kappa(x, E, t)} dx \quad (2.28)$$

where E , T and m are the total, kinetic and rest energy of a cosmic-ray particle, respectively. The integral is taken from the location of the Earth to the boundary of the heliosphere. The interstellar cosmic-ray flux J_{IS} is then modulated to yield the locally observed one J as

$$J(E) = \frac{E^2 - m^2}{(E + |z|\phi)^2 - m^2} \cdot J_{IS}(E + |z|\phi) \quad (2.29)$$

where z is the particle charge. The modulation parameter ϕ has the dimension of a rigidity and is of the order of 500 MV but it changes with time in accordance with the solar cycle. It must be stressed that the modulation parameter is not a model-independent quantity. Because the interstellar flux J_{IS} appears in (2.29), a value of ϕ can only be quoted in the context of a given propagation model.

2.5.5 Effect of the geomagnetic field

The magnetic field of the Earth is the final barrier for cosmic-ray particles to overcome before they can finally be detected in the atmosphere or a low orbit. Particles with low rigidities will follow spiral trajectories around the field lines and eventually lose their energy. The minimal rigidity that a particle must have in order to reach Earth through its magnetic field is called the cutoff rigidity R_S . In the vicinity of the Earth, the magnetic field can be approximated by a dipole field. For this case, a formula for the cutoff rigidity for vertically approaching particles can be derived as [26]

$$R_S \geq 14.9 \text{ GV} \cdot \cos^4 \lambda \quad (2.30)$$

2 Cosmic rays and dark matter

The cutoff depends on the latitude λ of the observer, as measured with respect to the equatorial plane of the dipole. It is lowest near the magnetic poles. For particles arriving from any given direction, the cutoff depends on the azimuthal angle as well. This leads to the so called east-west effect: For positively charged particles at the same zenith angle the cutoff is higher from the east direction and vice versa for negatively charged particles [27]. In reality, the field is not a perfect dipole and interactions with the solar wind lead to additional distortions. Therefore, an accurate determination of the geomagnetic cutoff requires a detailed model of the geomagnetic field and proceeds by backtracing individual particles with a given position, time, and rigidity through the magnetic field by integrating the equation of motion, to see if the particle reaches outer space.

The cutoff effect due to the geomagnetic field leads to a distortion of the spectrum $\Phi(R)$ of a given cosmic-ray species. For the purposes of this work, it can be described as [43]

$$\Phi^{\text{mod,geo}}(R) = \Phi(R) \cdot \frac{1}{1 + \left(\frac{R}{R_c}\right)^{-\gamma_c}} \quad (2.31)$$

where R_c is a cutoff rigidity and γ_c describes the steepness of the modulation. Typically, γ_c is on the order of unity.

2.5.6 Measurements of cosmic rays

Measurements of cosmic rays can be divided into two groups. Below 10^{14} eV, a direct measurement is possible. For this purpose, instruments known from particle physics, such as emulsion chambers, scintillators, tracking devices, calorimeters, Cherenkov counters or transition radiation detectors, are combined in a suitable way to measure mass, momentum, energy or charge sign of a particle. The PEBS and AMS-02 detectors belong to this category. Since the thickness of Earth's atmosphere at sea level amounts to twenty radiation lengths or eight hadronic interaction lengths, cosmic rays in the energy range of interest here are absorbed long before reaching the surface of the Earth. Therefore, a detector measuring primary cosmic rays has to be flown on a balloon at as high an altitude as possible or in space.

Above 10^{14} eV, another path has to be taken to obtain acceptable counting rates because of the steep decline in flux as given in (2.23). In this region of indirect measurements, Earth's atmosphere is used as a giant calorimeter to look for extended air showers created in the wake of an interaction of the primary particle in the upper layers of the atmosphere. The energy of the primary can be derived from the size and shape of the shower. Above primary energies of roughly 10^{15} eV, the shower particles can reach the surface of the Earth and be detected there. For that purpose, an appropriately sized area is instrumented with detector units, such as scintillators or water Cherenkov counters. In addition, one can observe the Cherenkov radiation emitted by the shower particles moving at velocities that exceed the speed of light in air or the fluorescence light. The latter is emitted after the excitation of nitrogen molecules in the air by passing shower particles, and with wavelengths in the range from 300 to 400 nm. As an example, the Pierre Auger observatory in Argentina employs a hybrid detection technique with great success [44].

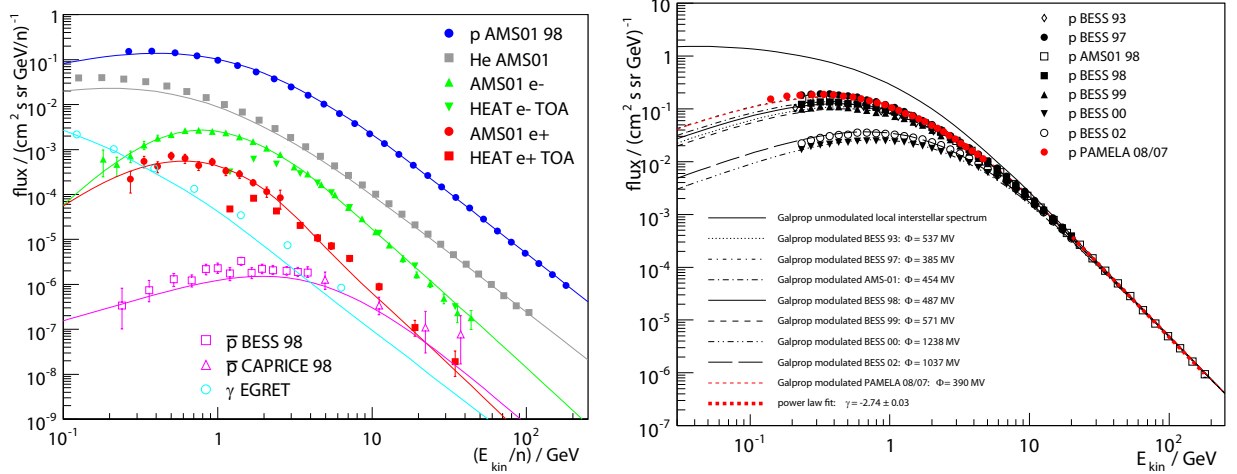


Fig. 2.3: *Left:* Measured fluxes of protons [46], helium [47], electrons and positrons [48, 49], antiprotons [50, 51], and diffuse γ -rays from the Galactic centre region [52]. The solar modulated predictions by the conventional Galprop model for each species are included. *Right:* Cosmic-ray proton spectrum as measured by BESS [53, 54], AMS01 [46] and PAMELA [55], together with the prediction by the Galprop conventional model. The effect of solar modulation in the data is clearly seen. The unmodulated model flux is plotted, as well as the modulated ones, using the best-fit modulation parameter ϕ for each data set.

2.5.7 Atmospheric backgrounds

For balloon-based measurements of cosmic rays, the remaining atmosphere between the flight altitude and outer space additionally modifies particle fluxes. Most important for the purposes of this work are positrons created in the decay chains following hadronic interactions of protons with the atoms in the upper layers of the atmosphere. A grammage of approximately 3.7 g/cm^2 has to be overcome at an altitude of 40 km in the polar regions during summer. Reference [45] deals with a Monte Carlo study of the necessary corrections in great detail. It arrives at the conclusion that they will be of the order of 10% for positrons above 1 GeV.

2.6 Model for cosmic-ray propagation

As already stated in section 2.5.3, Galprop is used as the propagation model. There are two sets of propagation parameters for Galprop that have been found to give a good description of a wide range of available cosmic-ray data. They are summarised in [40]. The first standard Galprop model, called plain diffusion model, is based solely on diffusive transport of cosmic rays, with neither convection nor reacceleration. The prices to pay for this simplicity are an ad-hoc break in the rigidity dependence of the diffusion coefficient and an additional factor of β^{-3} that need to be introduced to match the B/C-ratio at low energies. Specifically, in this model $D = \beta^{-2} D_0 (R/R_0)^a$ with $a = 0$ below and $a = 0.6$ above the reference rigidity $R_0 = 3 \text{ GV}$ and $D_0 = 2.2 \cdot 10^{28} \text{ cm}^2 \text{ s}^{-1}$. The spectral index for the nucleon source term is $\gamma_s = 2.3$ below a break rigidity of 40 GV and $\gamma_s = 2.15$ above.

2 Cosmic rays and dark matter

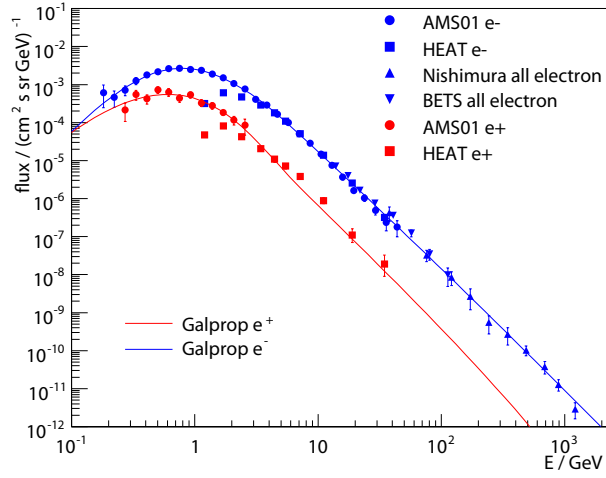


Fig. 2.4: Electron spectrum as measured by HEAT [48], AMS01 [49], all electron spectrum as measured by Nishimura et al. [56] and BETS [57], and positron spectrum as measured by HEAT [48] and AMS01 [49], together with the respective predictions of the Galprop conventional model. Modelling of the solar and geomagnetic modulation is performed for the AMS01 fluxes here. The same solar modulation parameter of $\phi = 442$ MV was used for electrons and positrons, while the parameters for geomagnetic modulation according to eq. (2.31) are $R_{c,e^-} = 0.72$ GV, $R_{c,e^+} = 1.59$ GV, $\gamma_{c,e^-} = 1.87$, and $\gamma_{c,e^+} = 1.02$.

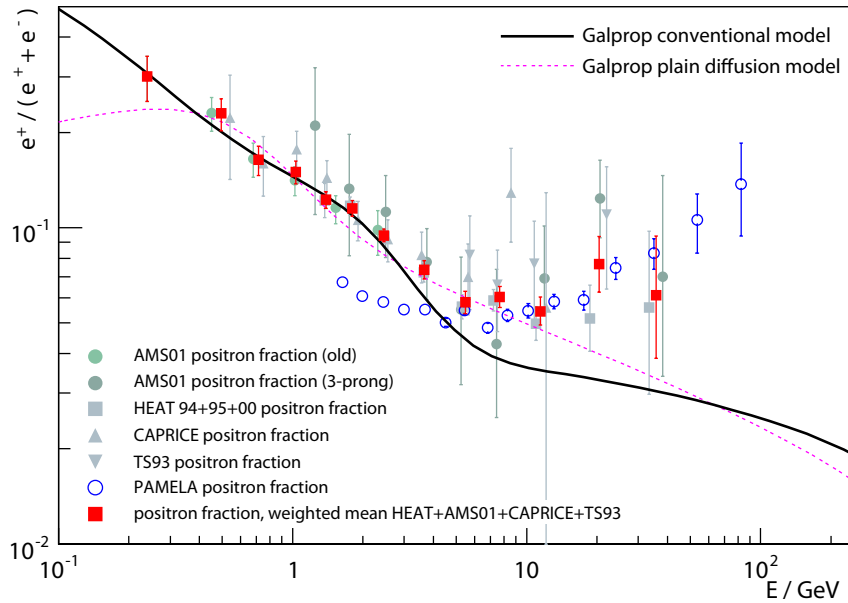


Fig. 2.5: Positron fraction data from AMS01 [49, 58], HEAT [59], CAPRICE [60], and TS93 [61], and the weighted mean of these data [62], together with the secondary background as predicted by Galprop's conventional and plain diffusion models. Recent data from PAMELA [63] are included, too.

2.6 Model for cosmic-ray propagation

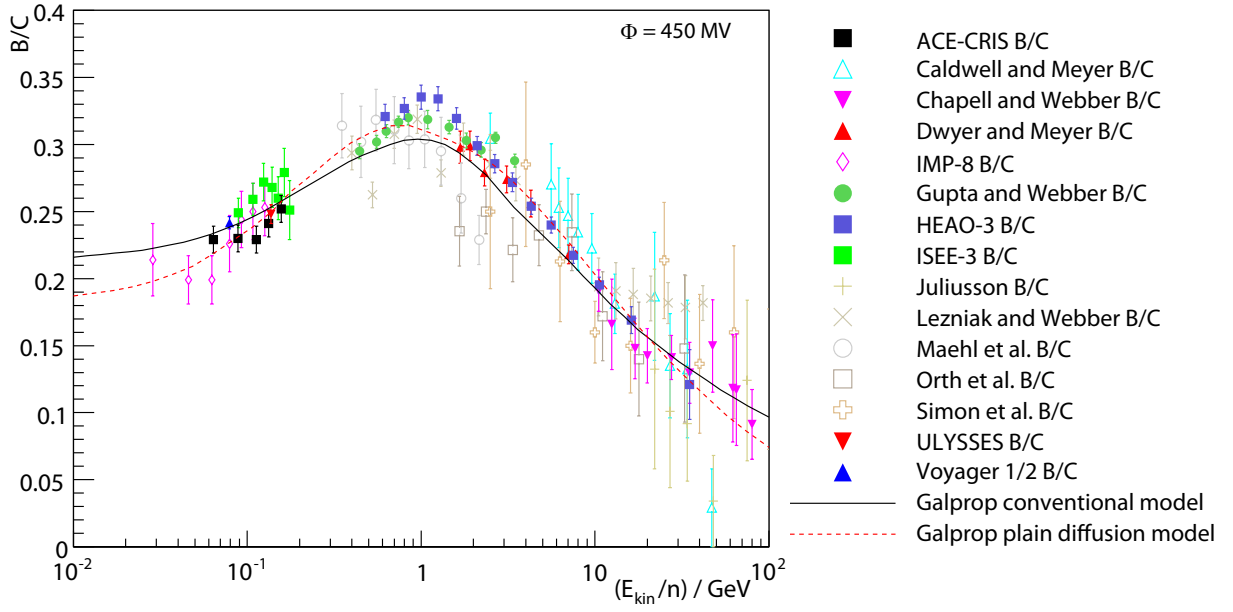


Fig. 2.6: Cosmic-ray B/C-ratio as a function of kinetic energy per nucleon, compared to Galprop’s conventional and plain diffusion models. Data are from ACE-CRIS [64], Caldwell and Meyer [65], Chapell and Webber [66], Dwyer and Meyer [67], IMP-8 [68], Gupta and Webber [69], HEAO-3 [70], ISEE-3 [71], Juliusson [72], Lezniak and Webber [73], Maehl et al. [74], Orth et al. [75], Simon et al. [76], ULYSSES [77], and Voyager [78].

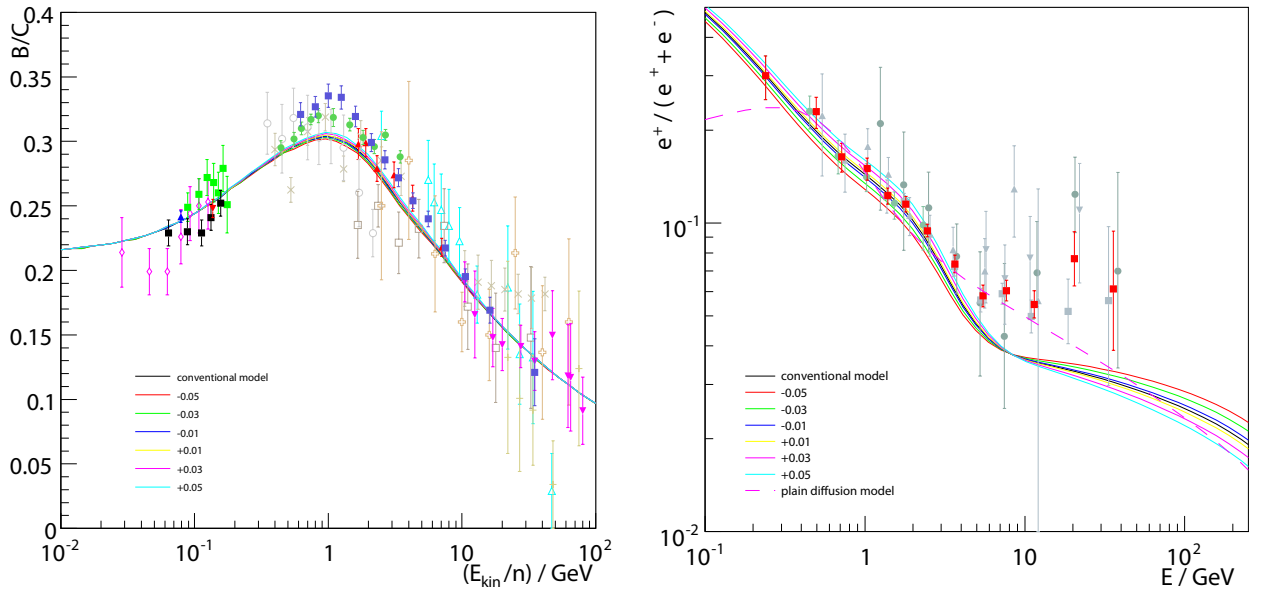


Fig. 2.7: Effect of variation of the nuclear injection spectral indices on B/C ratio (*left*) and positron fraction (*right*).

2 Cosmic rays and dark matter

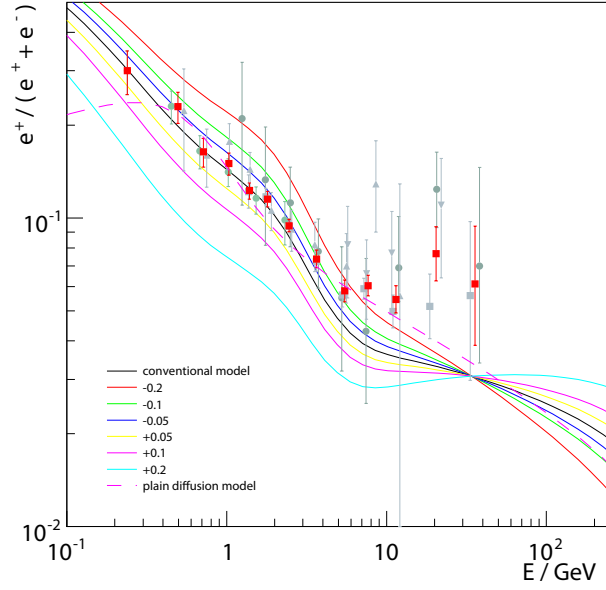


Fig. 2.8: Effect of variation of the electron injection spectral indices on the positron fraction. The B/C ratio remains unchanged.

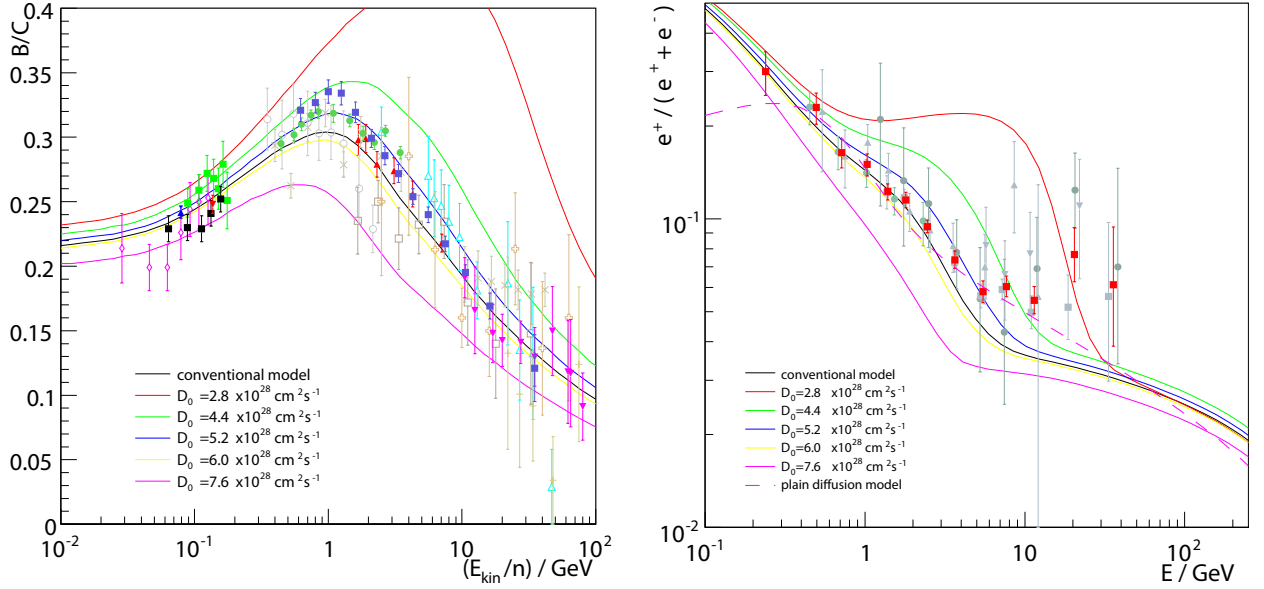


Fig. 2.9: Effect of variation of the diffusion coefficient on B/C ratio (*left*) and positron fraction (*right*).

2.6 Model for cosmic-ray propagation

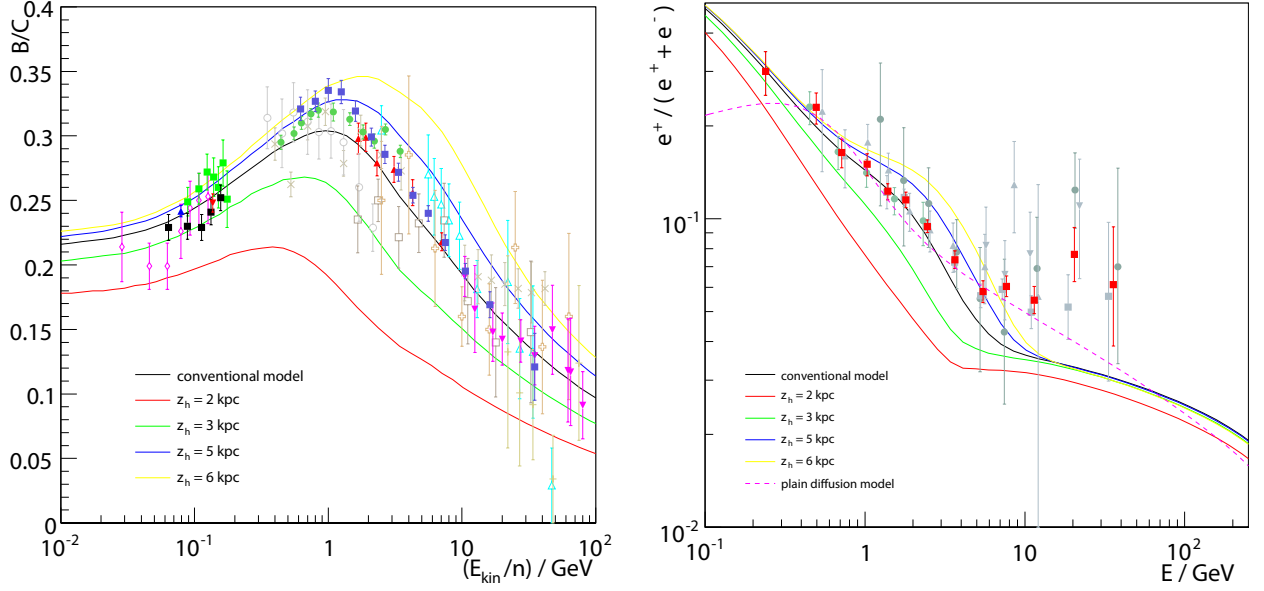


Fig. 2.10: Effect of variation of the halo size on B/C ratio (*left*) and positron fraction (*right*).

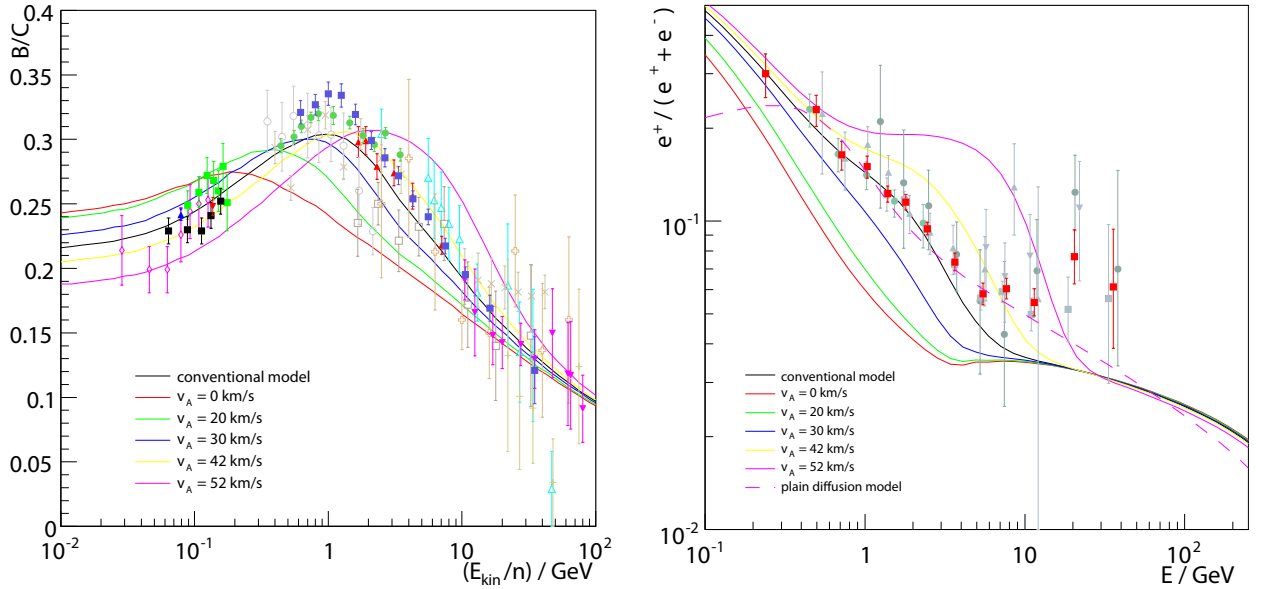


Fig. 2.11: Effect of variation of the Alfvén speed on B/C ratio (*left*) and positron fraction (*right*).

2 Cosmic rays and dark matter

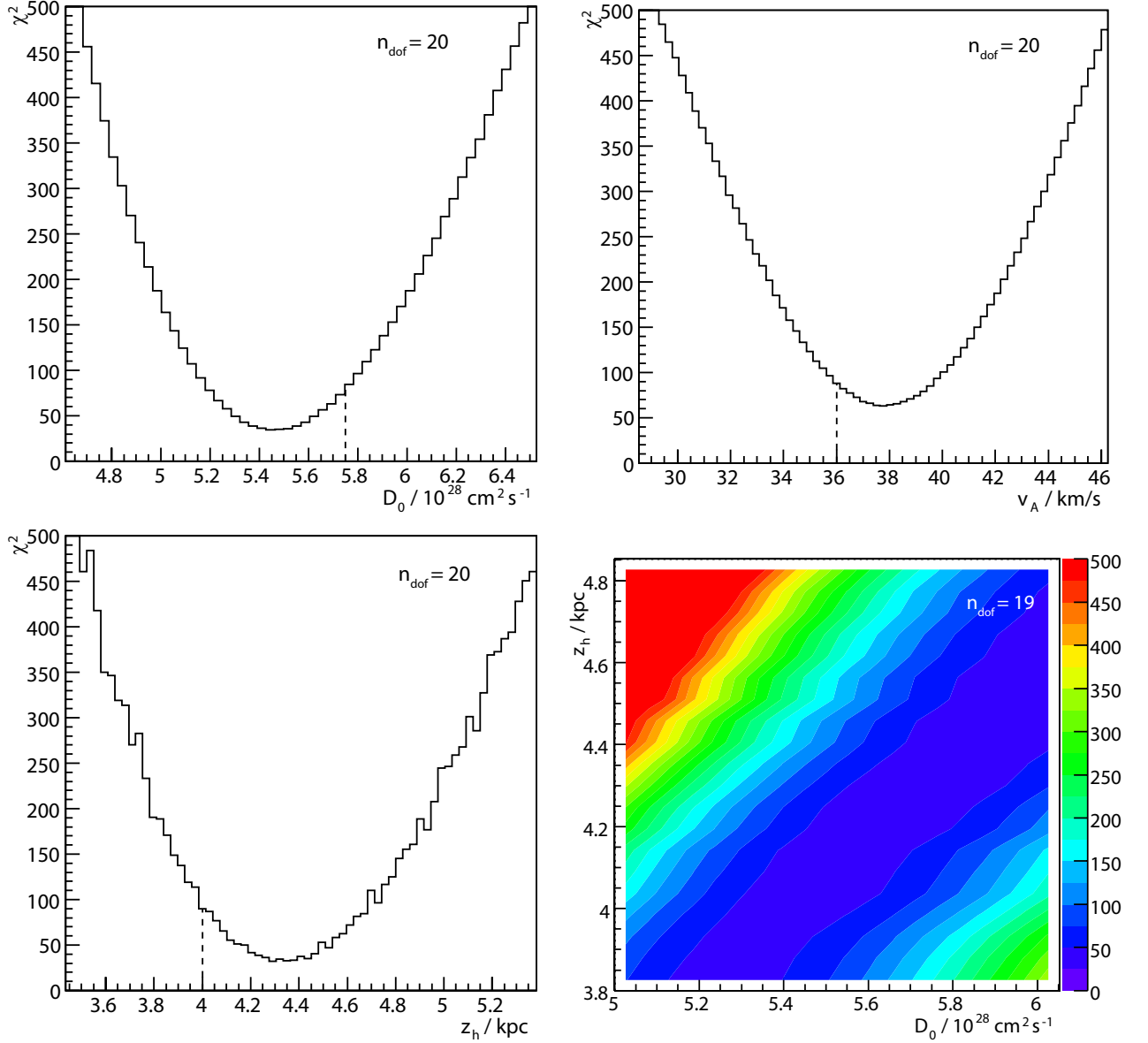


Fig. 2.12: Combined χ^2 values, as defined in the text, for variations of the diffusion coefficient, Alfvén speed, and halo size, and in the z_h - D_0 -plane. The respective nominal parameter values in the conventional Galprop models are marked by dashed lines.

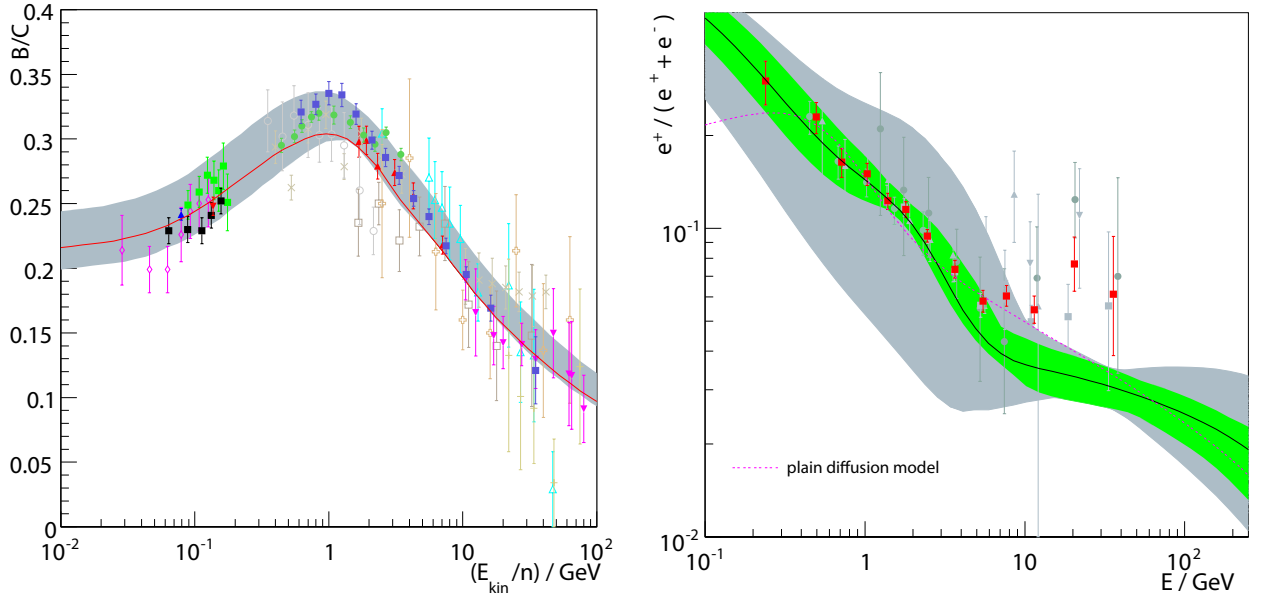


Fig. 2.13: *Left:* Wild scan results for models giving a description of the B/C data with equal or better $\chi^2_{\text{HEAO-3}}$ than the conventional Galprop model fall within the grey band. The red line shows the prediction of the conventional Galprop model itself. *Right:* The corresponding predictions for the positron fraction fall within the grey band. Models additionally giving $\chi^2_{e^+/(e^++e^-)} < 20.8$ for the data points below 3 GeV, i.e. outside the signal region, yield the green uncertainty band.

For the electron source term, the spectral index remains constant at $\gamma_e = 2.4$. On the other hand, the diffusive reacceleration – or conventional – model includes reacceleration, characterised by an Alfvén velocity of $v_A = 36 \text{ km s}^{-1}$. Here, the spectral indices for the nucleon source term are $\gamma_s = 1.82$ and $\gamma_s = 2.36$ below and above a break rigidity of 9 GV while for the electron source term, they are $\gamma_e = 1.6$ below 4 GV and $\gamma_e = 2.5$ above. The diffusion coefficient has the well motivated form $D = \beta D_0 (R/R_0)^a$ with $a = 1/3$ and $D_0 = 5.2 \cdot 10^{28} \text{ cm}^2 \text{ s}^{-1}$. The halo half-height is $z_h = 4 \text{ kpc}$ in both models. An overview of the predictions of the conventional model for various particle species is given in figure 2.3 (*left*).

It should be noted that statements about propagation parameters must always be considered in the context of a given model, for example the Kolmogorov spectrum ($a = 1/3$) is ruled out in the semi-analytic model studied in [36].

The cosmic-ray proton spectrum obtained in the conventional Galprop model is shown in figure 2.3 (*right*). Before it can be compared to data, solar modulation according to eq. (2.29) is applied, the modulation parameter being extracted by a fit to the data. The data shown were taken by space-borne or balloon detectors, during several flights across a period of almost a decade, corresponding to more than half of a solar cycle. The effect of solar modulation at lower energies is clearly visible. A significant change of its amplitude is apparent on the timescale of one year.

2 Cosmic rays and dark matter

The most precise data on the electron and positron fluxes currently available are compiled in figure 2.4. In the low-energy regime, the solar modulation effect has to be modelled to get a good description of the data. While the electrons used to determine the AMS-01 electron flux have been selected for low geomagnetic cutoffs, the dip towards the lowest energies that is evident in fig. 2.4 can only be reproduced if a correction for geomagnetic effects, according to (2.31), is applied as well. In the high-energy regime, the electron spectrum follows a power law that is well reproduced by the Galprop models. The overall normalisation of the spectra is a parameter of the model. The solar modulation parameter found for the AMS-01 proton flux as $\phi = (454 \pm 7)$ MV is consistent with the value obtained from the AMS-01 electron spectrum, which is $\phi = (442 \pm 40)$ MV.

The positron flux has not been measured reliably above 50 GeV, and there is an excess over the background expectation which will be discussed in more detail in chapter 6.

Instead of the absolute positron flux, experiments often quote the positron fraction, that is the flux ratio $\Phi(e^+)/(\Phi(e^+) + \Phi(e^-))$, because certain systematic uncertainties, such as uncertainties in the detector acceptance and trigger live-time, cancel in this case. The effect of solar modulation is also reduced, but not completely eliminated, as can be seen from eq. (2.29). Positron fraction data from space and balloon experiments, gathered over the past two decades, are assembled in figure 2.5. They are shown together with the prediction of the secondary background as obtained in the conventional and plain diffusion models of Galprop. For easy comparison, the weighted mean of the data from HEAT, AMS-01, CAPRICE and TS93 is included. The positron fraction data measured by the PAMELA detector have recently become available in a pre-print [63] and are shown in the figure, too. Towards high energies, the trend of an increasing positron fraction as seen by the earlier experiments is confirmed. The PAMELA data extend to higher energies and have smaller statistical errors than all previous data. At low energies, the PAMELA data points are lower than those of the earlier measurements and the prediction of the propagation model. These new data will be put aside for the moment. Their low-energy behaviour will be investigated in section 2.7, and a possible exotic signal will be discussed in section 6.5.

It is evident from the figure that the existing data are still limited both in terms of statistical uncertainties and energy range. This is caused by the steep decrease of the positron flux with energy and the increasing difficulty in the experimental determination of the charge sign for a high-energetic particle. There is a significant difference in the predicted secondary positron fraction between the conventional model and the plain diffusion one, but the change in slope of the positron fraction towards high energies apparent in the data can be reproduced in neither case.

The figure already hints at the fact that the positron data may not only be used to look for signals of new physics but is also vital for our understanding of the propagation mechanism of cosmic rays. This statement will be corroborated in the remainder of this section by looking at the dependence of the positron fraction on the most important parameters in the propagation model used here. Naturally, this study will also give an idea about the stability of the positron excess with respect to uncertainties in the background model.

Any comprehensive cosmic-ray model should describe not only the spectra of primary particles, but also those of as many secondary particles as possible. For instance, the

abundance of boron in cosmic rays is higher than its abundance in the solar system by orders of magnitude. It was realised long ago that this is due to the fact that boron is produced in spallation reactions of carbon on interstellar matter. The amount of boron produced in this way depends on the amount of matter traversed. Therefore, the correct description of the ratio B/C of boron to carbon is a standard test for any propagation model, although the detailed explanation of the observed spectral shape remains a challenge. This can be seen in figure 2.6. Both Galprop models do a good job at describing the overall shape of the B/C ratio, but the peak around $1 \text{ GeV}/n$ is not as pronounced as in the data.

In the following, the key parameters of the conventional model will be varied to see the corresponding changes in the B/C ratio, which is used to fix the model parameters, and the secondary positron fraction, which constitutes the background for a possible exotic primary component. The key parameters are the spectral indices γ_s for nuclei and γ_e for electrons at injection, the diffusion coefficient D_0 , the Alfvén velocity v_A , and the halo size z_h . The solar modulation parameters are kept fixed in the process. During variation of one parameter, the remaining parameters are fixed at their nominal values (table 2.2). The effect of variation of the spectral indices at injection is illustrated in figures 2.7 and 2.8 for the nuclear and electron injection spectra, respectively. At high energies, where solar modulation effects do not distort the spectra, a harder proton injection spectrum leads to a higher number of – secondarily produced – positrons. In the same vein, a harder electron spectrum will naturally lead to a higher number of primary electrons at high energies thus reducing the fraction of positrons.

The diffusion coefficient D_0 strongly influences the production of secondaries, positrons and boron among others (fig. 2.9). The time needed to cross a distance x in a diffusive process scales as $t \sim x^2/2D$. Therefore, particles spend a longer time in the interstellar matter and thus produce more secondaries for a smaller diffusion coefficient.

A similar effect is caused by a variation of the halo size z_h (fig. 2.10). In a larger halo, more secondaries are produced. The comparison of figures 2.9 and 2.10 already shows that a degeneracy exists between the parameters of the propagation model. This underlines the necessity of comparing the model to as many different sets of data as possible to develop a consistent picture of cosmic-ray propagation.

Lastly, figure 2.11 shows how the Alfvén velocity influences the position of the peak in the B/C-ratio and that reacceleration must be included in order to describe the B/C-ratio without an ad-hoc break in the diffusion coefficient. On the other hand, the effect of variation of v_A on the positron fraction is similar to what is found when the diffusion coefficient is varied.

As a last step, the uncertainty on the secondary positron fraction as predicted in the conventional Galprop model needs to be estimated. To that end, the parameters described in this section have been varied around their nominal values. In a first approach, χ^2 -plots for the parameters primarily affecting the spectra of secondary species, namely the diffusion coefficient D_0 , Alfvén velocity v_A , and halo size z_h , are prepared (fig. 2.12). The χ^2 plotted is a combined value, defined to quantify the deviation for both B/C data and

2 Cosmic rays and dark matter

the positron fraction as

$$\chi^2 \equiv \chi_{\text{HEAO-3}}^2 + \chi_{e^+/(e^++e^-), \leq 3 \text{ GeV}}^2 \quad (2.32)$$

An acceptable model is defined as giving an acceptable χ^2 -value with respect to the B/C-data. More specifically, the HEAO-3 data were chosen as comparison because they represent a precise measurement that extends over the largest energy interval. A solar modulation parameter of $\phi = 450$ MV was used.

Due to the rather good precision in the energy range up to a few GeV, the positron fraction could in principle be used to further constrain the parameter space of the propagation model. In practice, solar modulation and geomagnetic effects at low energies complicate the picture, and in addition, an energy range that is presumed to be free from any primary signal needs to be defined. In the most conservative approach, only models yielding too *many* positrons can be excluded. Nevertheless, for a fixed set of modulation parameters, one can use the low-energy positron fraction data below 3 GeV to further constrain propagation models. The corresponding χ^2 is therefore added to the one from the B/C-data to form the combined χ^2 defined in (2.32).

The χ^2 -plots for the one-dimensional lines in the parameter space must be viewed with caution, however. A somewhat clearer picture emerges from correlation plots. As an example, the partial degeneracy of the parameters z_h and D_0 is demonstrated in figure 2.12, too.

Still, the complete picture could only be obtained from a complete scan of the Galprop parameter space. However, because the number of parameters is quite large, a wild scan technique was employed to estimate the uncertainty coming with the conventional Galprop model, tuned with the intention to describe as wide a variety of primary and secondary data as possible. 1000 models were randomly generated with parameter values randomly drawn according to a uniform distribution in the ranges given in table 2.2. For the injection indices, the bounds were adapted to the errors obtained from power-law fits

parameter	nominal value	lower bound	upper bound
γ_s	1.82/2.36	1.77/2.31	1.87/2.41
γ_e	1.6/2.5	1.4/2.3	1.8/2.7
$D_0/\text{cm}^2/\text{s}$	$5.75 \cdot 10^{28}$	$4.4 \cdot 10^{28}$	$7.2 \cdot 10^{28}$
$v_A/\text{km}/\text{s}$	36	26	46
z_h/kpc	4	3.2	5.5

Tab. 2.2: Range of parameter variation for wild scan of the parameter space of the conventional Galprop model. Slashes separate values below and above the respective break rigidities quoted in the text.

to the high-energy proton and electron spectra. The other parameters were conservatively bounded such that the deviation from the measured B/C-ratio became noticeable. The respective ranges can be read off figures 2.9 to 2.11.

For those models giving a description of the B/C data equal to or better than the conventional model ($\chi_{\text{HEAO-3}}^2 \leq 79$, $n_{\text{dof}} = 9$), the corresponding positron fraction was then plotted (figure 2.13). Though the resulting band of models is quite large compared to

2.7 A hint of charge-sign dependent solar modulation in the low-energy PAMELA data

the measurement errors, the overall spectral shape remains the same, a power law trend that becomes harder around 10 GeV. It should be noted that the difference between the conventional and the plain diffusion models is comparable to that between two models at the outer ends of the wild scan uncertainty band. However, none of the models compatible with the B/C data can explain the excess seen in the positron fraction. The final uncertainty band is then constructed from models in agreement with the positron fraction below 3 GeV, requiring a $\chi^2_{e^+/(e^++e^-)} < 20.8 = 5.7 + 15.1$ with respect to the weighted mean of the positron fraction data. The conventional model has $\chi^2 = 5.7$, and the statistical error at 99% confidence level for $n = 5$ parameters is then formally obtained by looking for a χ^2 variation of 15.1 [79]. The suitable models are drawn using green colour in figure 2.13. The exact value of the cut seems arbitrary, especially taking the above mentioned effects into account, but the magnitude of the resulting uncertainty band remains unaffected. It will therefore be employed again in chapter 6.

2.7 A hint of charge-sign dependent solar modulation in the low-energy PAMELA data

At first glance, the positron fraction measured by PAMELA at low energies, below 10 GeV, seems puzzling. While the other measurements taken in recent years agree well in this energy range, the PAMELA data points indicate significantly fewer positrons (fig. 2.5). If the pronounced rise at high energies apparent in the PAMELA data is to be taken seriously, it must first be shown that this observation does not point to a systematic error in the response of the PAMELA apparatus nor the data analysis. In this section, it is argued that charge-sign dependent solar modulation [80] is a possible way to explain all measurements quoted above.

The amplitude of solar modulation varies along with the solar cycle, with its well known half-period of eleven years. A good measure for the activity of the sun is the sunspot number, which has been observed almost continuously for the last centuries. Although the magnetic field of the sun is complex, it is nearly always dominated by the dipole term. The projection of this dipole on the solar rotation axis can be either positive or negative and these two states are referred to as A^+ and A^- , respectively. The dipole reverses direction at each sunspot maximum, leading to alternating magnetic polarity in successive solar cycles [81].

It can be expected that solar modulation depends on the charge sign of a particle, affecting positrons and electrons differently. As a simple extension of the force-field approximation used so far, it can be assumed that the modulation parameter ϕ in (2.29) is charge-dependent and takes different values ϕ^+ and ϕ^- for positively and negatively charged particles, respectively.

Allowing for different values of ϕ^+ and ϕ^- , a fit of the local interstellar positron fraction calculated in the conventional Galprop model to the PAMELA positron fraction data below 4 GeV yields values of $\phi^+ = 438$ MV and $\phi^- = 2$ MV with statistical uncertainties of 4 MV (fig. 2.14 *left*). These values mean that electrons can reach the Earth almost

2 Cosmic rays and dark matter

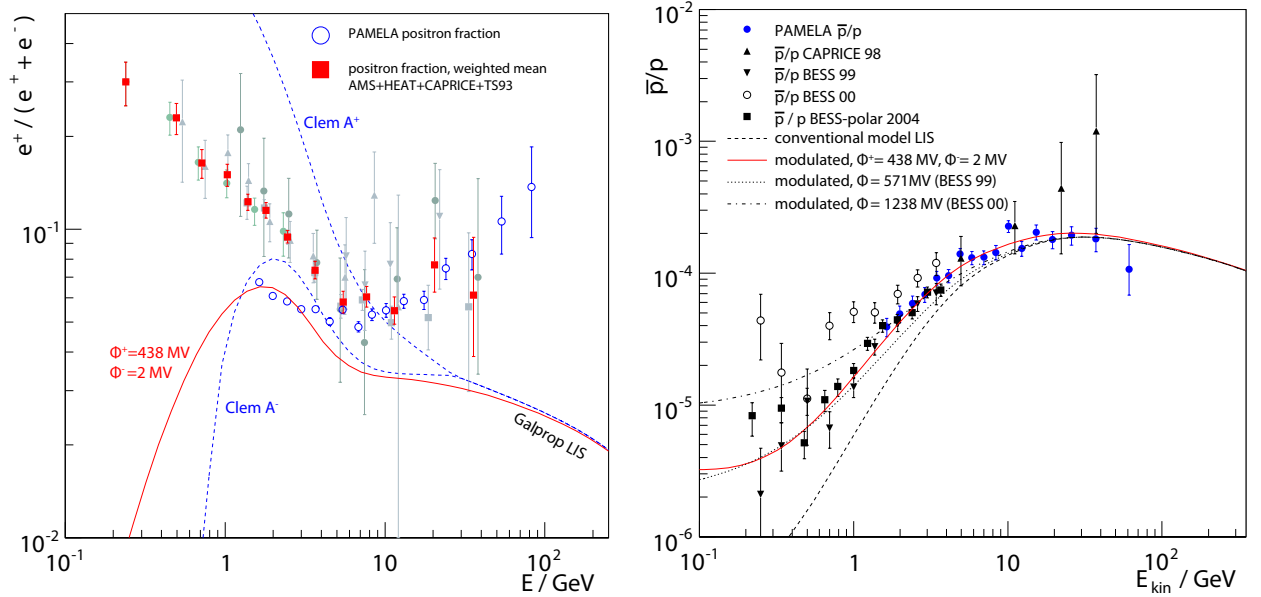


Fig. 2.14: *Left:* Positron fraction data compared to predictions for the low-energy behaviour, based on the local interstellar spectrum (LIS) obtained in the conventional Galprop model. The solid red line is based on charge-sign dependent modulation parameters in the force-field approximation formula (2.29), the dashed blue lines are obtained in the empirical model of Clem et al. [80], as described in the text. Data are marked as in fig. 2.5. *Right:* Antiproton-to-proton ratio measured by PAMELA [85] compared to the prediction obtained by applying the same charge-sign dependent solar modulation to the secondary flux predicted by the propagation model as to the positron fraction. Data from BESS-polar [86], taken in the same A^- -cycle, are included, too. Some data taken in the previous A^+ -cycle, by BESS [87] and CAPRICE [51], are compared to predictions in the charge-symmetric case, with parameters obtained from fits to the corresponding proton spectra.

unhindered by the solar wind while positrons are moderately suppressed so that the fraction of positrons is reduced with respect to the charge-symmetric case.

In an empirical model of charge-dependent solar modulation, Clem et al. [80] assumed that the flux J_E of a given species with charge sign q measured at Earth is related to the interstellar flux J_{IS} by

$$J_E(R, \hat{\phi}, qA) = C(qA, R) \cdot M(R, \hat{\phi}) \cdot J_{IS}(R) \quad (2.33)$$

where R is rigidity, A is the solar magnetic polarity, and $\hat{\phi}$ is the phase of the solar cycle. C and M are two modulation factors, and $\hat{\phi}$ is associated to the modulation parameter considered before. This simple model neglects the adiabatic deceleration present in (2.29), but it has the advantage that J_E can be expressed in terms of just J_{IS} and $\varrho(R)$, the ratio of the total electron fluxes in the A^+ -cycle to the total electron fluxes in the A^- -cycle. The empirical data on $\varrho(R)$ as assembled by Clem et al. can be parameterised as

$$\varrho(R) = 0.166 \log(R/\text{GeV}) + 0.452 \quad (2.34)$$

2.7 A hint of charge-sign dependent solar modulation in the low-energy PAMELA data

It can then be shown that J_E is given by

$$J_E = \frac{J_{IS}^2(R+1) - RJ_{IS}}{2J_{IS} - 1} \quad \text{for } A^- \quad (2.35)$$

and

$$J_E = \frac{J_{IS}^2(R+1) - J_{IS}}{R(2J_{IS} - 1)} \quad \text{for } A^+ \quad (2.36)$$

The resulting curves are included in fig. 2.14. It can be seen that the trend predicted for the A^- cycle, during which the PAMELA data were taken, is rather similar to the curve predicted in the ϕ^\pm -model presented above.

The antiproton-to-proton ratio measured by PAMELA [85] can be used to cross-check the ϕ^\pm -model. In fact, using the same ϕ^\pm -values as for the positron fraction, the \bar{p}/p -ratio can be reproduced well (2.14 *right*). To put this result into perspective, some data taken in the previous A^+ -cycle are compared to predictions in the charge-symmetric case, with parameters obtained from fits to the corresponding proton spectra. The BESS data taken at solar maximum show some discrepancy with respect to the prediction obtained in the charge-symmetric case. It is unclear however if this points to a problem in the modulation model, the propagation model providing the interstellar fluxes, or both.

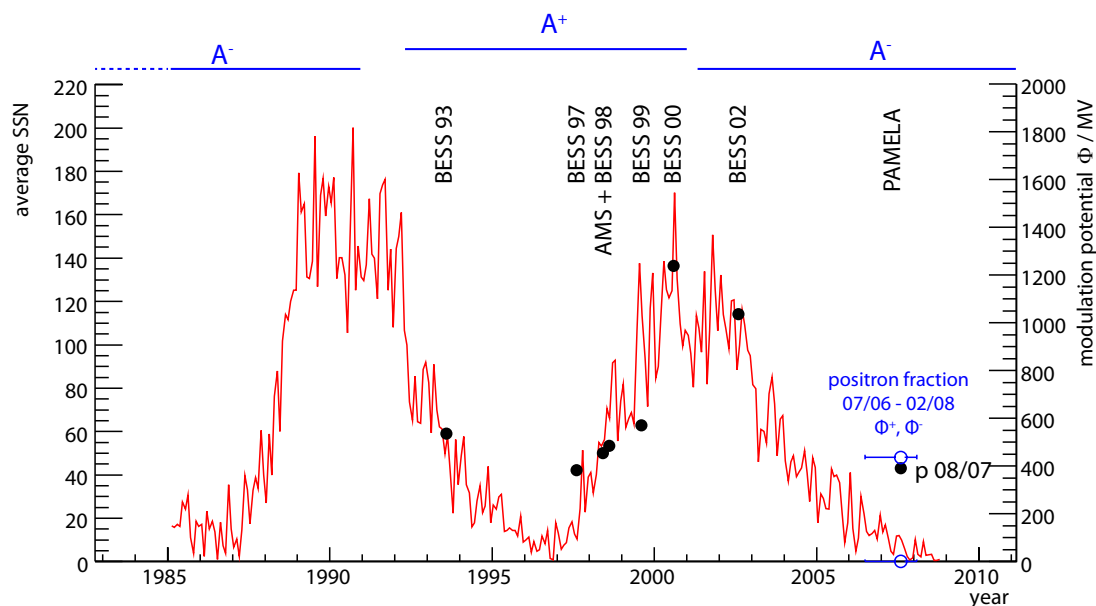


Fig. 2.15: Monthly average of the observed sunspot numbers [82] since 1985, compared to the values of the modulation parameter extracted from the fits to the proton spectra included in fig. 2.3. The charge-sign dependent parameters used to describe the low-energy positron fraction measured by PAMELA are depicted, too. The cycle of the solar magnetic polarity is indicated by the bars at the top of the figure, with the approximate start and end dates taken from [83] and [84].

2 Cosmic rays and dark matter

Looking at the correlation of the solar activity, expressed in terms of the sunspot number, with the modulation potential obtained from fits to the proton spectra taken in recent years (2.15), a good match is found in general. The value for the PAMELA protons is somewhat higher than expected from the trend implied by the solar data, by a margin comparable to the difference in the values of ϕ^+ and ϕ^- quoted above.

A prediction of this model of charge-dependent solar modulation is an unexpected and rather drastic decrease of the positron fraction at the lowest energies, below 1 GeV (fig. 2.14). A new measurement at these energies during the current solar cycle is therefore highly desirable.

Using the model of solar modulation presented in this section and the local interstellar positron and electron spectra calculated in the Galprop conventional model, both the previously published data and the new PAMELA positron fraction data can be corrected for the solar modulation effects to obtain estimates of the interstellar amplitudes (fig. 2.16). The result shows that in this model, the PAMELA data are in very good agreement with

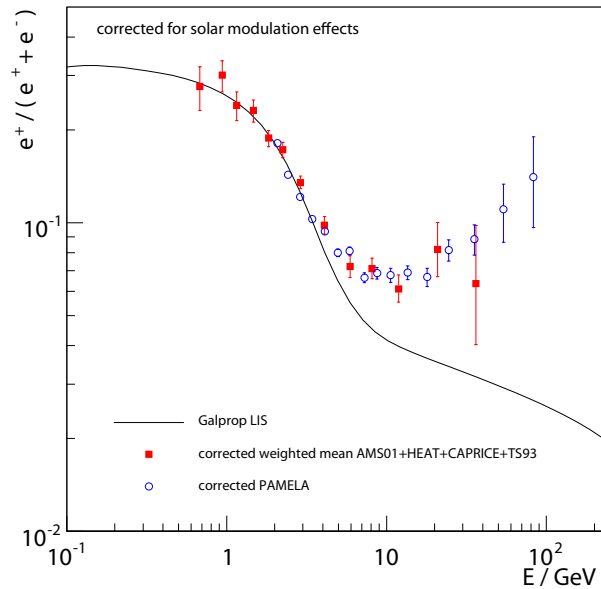


Fig. 2.16: Positron fraction data corrected for solar modulation effects according to the Galprop conventional model. PAMELA data have been corrected based on the charge-sign dependent model, the weighted mean of the previously published data has been corrected based on a charge-symmetric model using $\phi = 442$ MV.

the weighted mean of the data from AMS-01, HEAT, CAPRICE, and TS93.

3 Detectors to measure the cosmic-ray positron fraction

In this chapter, first the two contemporary players in the field of indirect dark matter search using the cosmic-ray positron fraction, AMS-02 and PAMELA, will be presented briefly. Then, an overview of the design concept for the new PEBS detector [88, 89, 90] will be given. It is shown which detector components are needed in order to fulfil the mission objectives and how these components will work together. Details of their working principles, implementation in the simulation software, and the projected performance will be treated in chapter 4.

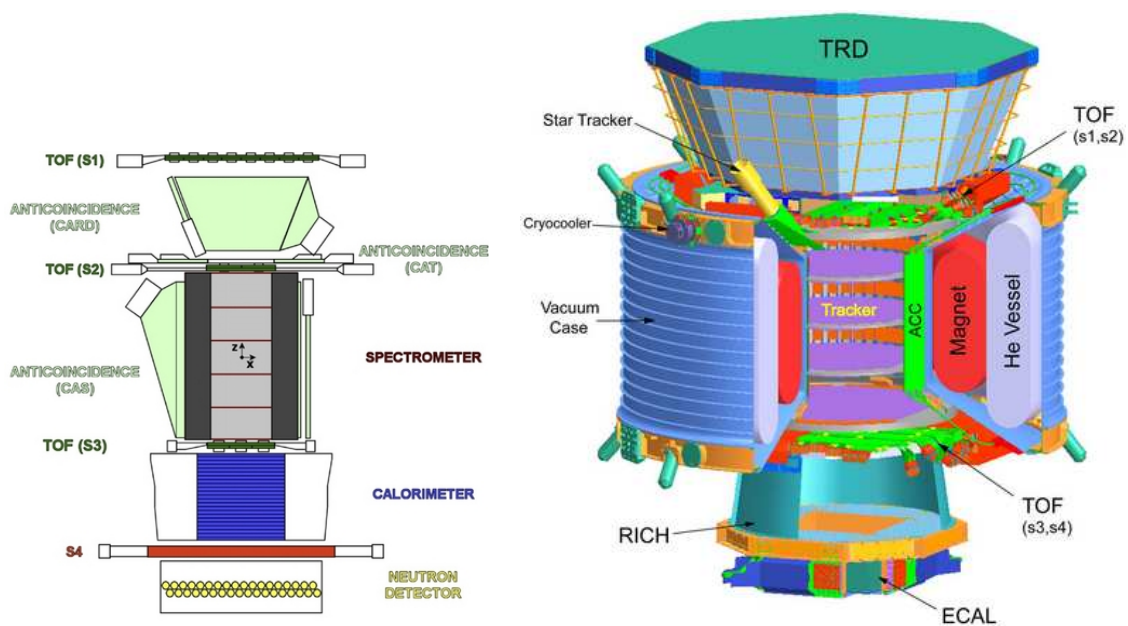


Fig. 3.1: Schematic drawings of the PAMELA (*left*) and AMS-02 detectors (*right*). PAMELA drawing reprinted from [91], Copyright 2006, with permission from Elsevier.

3.1 PAMELA

The PAMELA experiment [91] (fig. 3.1 *left*) is a satellite-borne detector designed to study charged particles in the cosmic radiation with a particular focus on antiparticles. It was launched in June 2006 [92] and some preliminary results on in-flight performance [93] and the abundances of light nuclei and isotopes [94] have been published. First results on positron [63] and antiproton [85] data have also been made available. The PAMELA

3 Detectors to measure the cosmic-ray positron fraction

apparatus measures roughly 1.3 m in height, weighs 470 kg and has a power consumption of 355 W. The overall acceptance is $21.5 \text{ cm}^2 \text{ sr}$. Its magnetic spectrometer consists of a 0.43 T permanent magnet and six $300 \mu\text{m}$ thick silicon detector planes yielding a spatial resolution of $3 \mu\text{m}$ in the bending plane and $11.5 \mu\text{m}$ in the non-bending plane [95]. The sampling electromagnetic calorimeter [96] comprises 44 single-sided silicon sensor planes interleaved with 22 plates of tungsten absorber, each having a thickness of 0.26 cm, giving a total depth of $16.3 X_0$. It reaches a proton rejection factor of about 10^5 at 90 % positron efficiency. A neutron detector complements the electron-proton discrimination capabilities of the calorimeter. The detector is completed by the time-of-flight and anticoincidence systems.

3.2 AMS-02

AMS-02 [97] (fig. 3.1 *right*) is a particle detector designed for installation on the International Space Station and a mission duration of three years. It contains eight main components. A superconducting magnet, cooled by superfluid helium, creates a strong magnetic field, for a total bending power of $BL^2 = 0.8 \text{ Tm}^2$. A silicon tracker consisting of eight layers of double-sided sensors measures the intersection points of particle tracks with a precision of $10 \mu\text{m}$ and $30 \mu\text{m}$ in the bending and non-bending planes, respectively. It provides a proton rigidity resolution of 20 % at 500 GeV and is able to determine the charge of nuclei up to iron ($Z = 26$). A laser alignment system is used to measure the positions of the tracker ladders with a precision of $5 \mu\text{m}$. A 20-layer transition radiation detector identifies electrons and positrons with a rejection factor against protons of 10^3 at 1.5 GeV to 10^2 at 300 GeV. A sandwich of lead and scintillating fibres serves as the electromagnetic calorimeter. It allows three-dimensional shower reconstruction and has a thickness of $16.7 X_0$. A proton rejection of 10^4 is reached in the range between 1.5 GeV and 1 TeV and the energy resolution is parameterised as $\sigma(E)/E = 10.2\%/\sqrt{E/\text{GeV}} \oplus 2.3\%$. Four layers of time-of-flight hodoscopes provide precision time measurements with a resolution of 120 ps and dE/dx measurements. A ring-imaging Cherenkov counter measures the velocity, to a precision of 0.1 %, and the charge of nuclei. A system of anticoincidence counters rejects particles passing outside the magnet aperture. A system of two star trackers allows the precise reconstruction of the origin of high-energy γ -rays. The overall acceptance of AMS-02 was calculated to be roughly $875 \text{ cm}^2 \text{ sr}$ by a Monte Carlo integration (sec. 4.4.8).

3.3 PEBS

3.3.1 Design overview

The primary mission goal of the PEBS detector is a precise and reliable measurement of the cosmic-ray positron fraction, i.e. the ratio of the positron flux Φ_{e^+} to the total electron flux $\Phi_{e^+} + \Phi_{e^-}$, in an energy range extending from the GeV-region up to 100 GeV and above. The main motivation for this endeavour is drawn from the observation of an excess in the positron fraction data available so far which seems to be hard to explain from

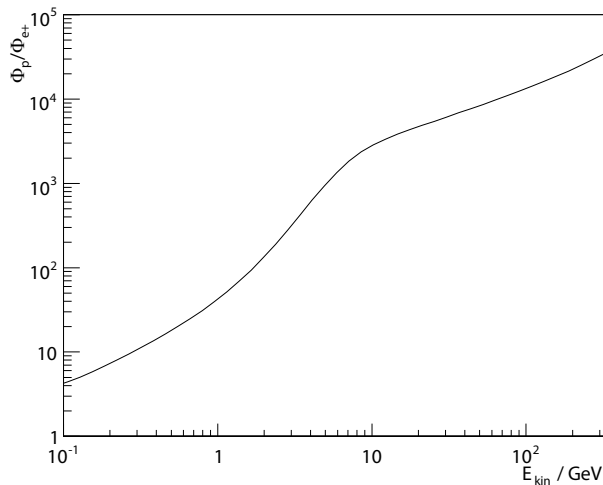


Fig. 3.2: Local interstellar ratio of proton to positron flux, as a function of energy, calculated in the conventional Galprop model.

secondary production alone (sec. 2.6) but may arise from the annihilation of long-sought dark matter particles with masses of the order of 100 GeV, for example in the scenario treated in chapter 6. For such a measurement to become feasible, four main obstacles need to be overcome:

1. The positron flux in the cosmic rays decreases steeply with energy (fig. 2.3). Therefore a detector needs a very high geometric acceptance in order to obtain sufficient statistics in the high-energy regime.
2. Positrons constitute only a small fraction of the overall composition of cosmic rays. They are vastly outnumbered by protons which therefore are the main background for this measurement. The flux ratio Φ_p/Φ_{e^+} as a function of energy (fig. 3.2) reaches a value of 10^4 and even more at energies above 100 GeV. This means that one may not misidentify more than 1 in 1,000,000 protons for a clean positron sample with a remaining proton contamination of 1%. As outlined below, this will be achieved by the combination of an electromagnetic calorimeter (ECAL, sec. 4.2.5) and a transition radiation detector (TRD, sec. 4.2.6), each providing roughly a factor 1000 to the proton rejection.
3. A reliable determination of the charge sign is needed in order to separate electrons from positrons. As the positron flux is expected to be of the order of 1 to 10% of the electron flux, the fraction of events with incorrectly reconstructed charge sign must not be above the per mille level. The magnet and tracker (sec. 4.2.2) are designed with this goal in mind.
4. Earth's atmosphere with its thickness of roughly twenty radiation lengths prohibits a measurement of cosmic rays within the energy range of interest here from the ground. An attractive alternative to a space-based measurement is found in high-altitude balloons as explained in section 3.3.2. Such a platform entails strong constraints on

3 Detectors to measure the cosmic-ray positron fraction

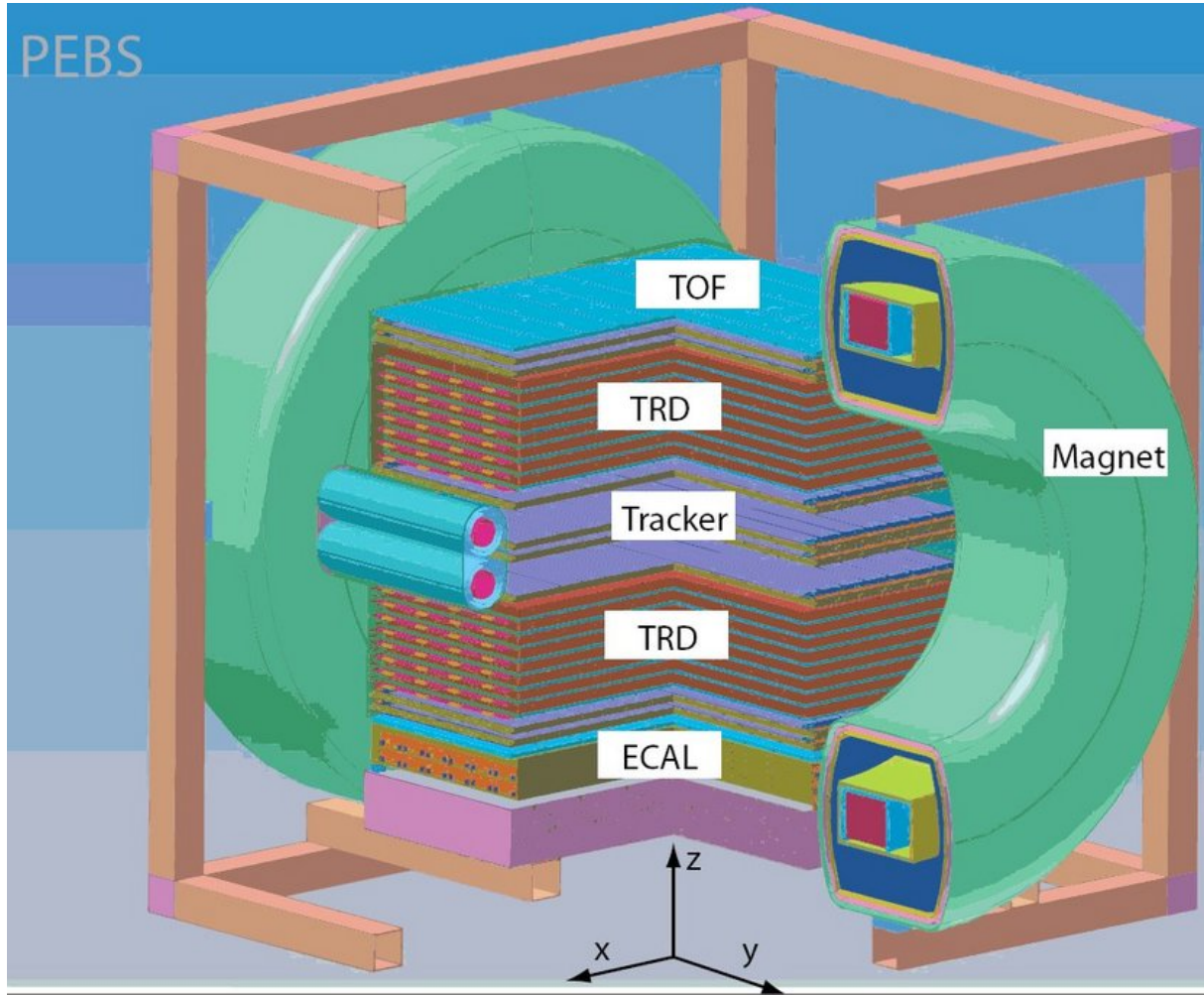


Fig. 3.3: Cutaway three-dimensional view of the PEBS detector. The magnet coils and support are visible enclosing the inner detector consisting of the time-of-flight system (TOF), tracker, transition radiation detector (TRD) and electromagnetic calorimeter (ECAL). A cylinder of solar panels enclosing the structure shown here will be used for power generation. Carbon fibre and aluminium support structures are shown, too.

weight and power consumption that have to be taken into account during the design of the detector. As briefly mentioned in section 2.5.7, the remaining atmosphere at flight altitude will require small corrections to extrapolate to the top-of-atmosphere fluxes, too.

Figures 3.3 and 3.4 show drawings of the PEBS design. The detector resides between two Helmholtz coils. The coils are made of superconducting Al-stabilised Niobium filaments and are located inside a helium cryostat. This superconducting magnet (sec. 4.2.1) will be able to create a magnetic field with a mean flux density of $B = 0.8\text{ T}$ and mean $BL^2 = 0.63\text{ Tm}^2$ for a period of 20-40 days until the helium is evaporated. The field created by the superconducting magnet will be used by the tracker [98, 99] to measure the curvature of the tracks of charged cosmic rays and hence their momentum and charge

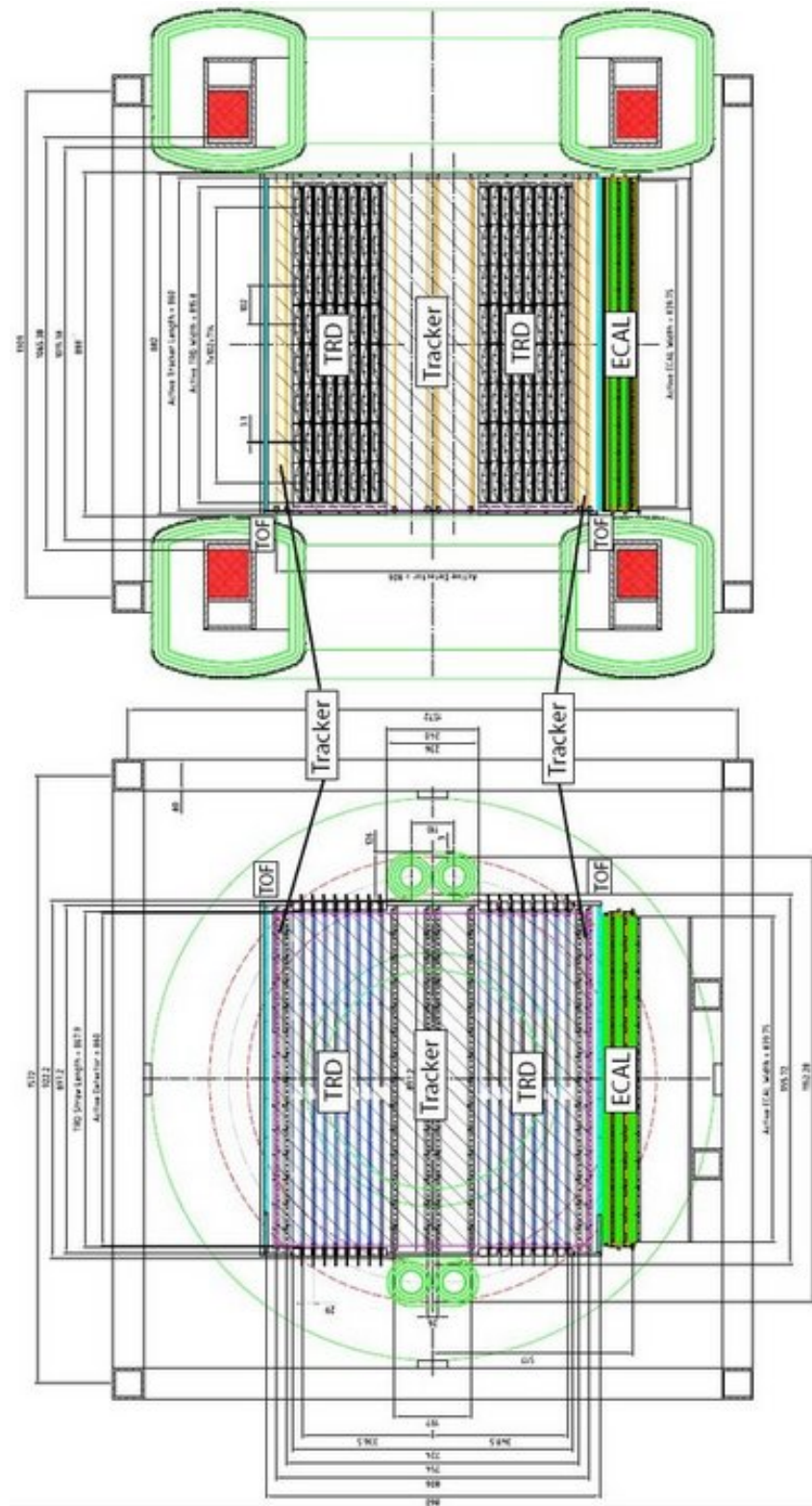


Fig. 3.4: Schematic drawing of PEBS, including the dimensions (in mm). The bending plane (xz) and non-bending plane (yz) views are shown in the lower and upper parts of the figure, respectively.

3 Detectors to measure the cosmic-ray positron fraction

sign. The tracker (sec. 4.2.2) consists of eight rows of double-layered modules of scintillating fibres of $250\ \mu\text{m}$ diameter which are read out by linear silicon photomultiplier (SiPM, sec. 4.2.3) arrays. A momentum resolution of 18% is expected for positrons of 100 GeV. For proton suppression, two independent subdetectors, an electromagnetic calorimeter (sec. 4.2.5) and a transition radiation detector (sec. 4.2.6), are used. The calorimeter (ECAL) employs a sandwich of tungsten absorber plates and scintillator bars, again read out by SiPMs, to determine the energy and the shape of an electromagnetic shower induced by electrons and positrons. At an energy of 100 GeV, an energy resolution of 6% is predicted by the Monte Carlo simulation. The corresponding proton rejection is 3×10^3 at 80% positron efficiency.

The design of the transition radiation detector (TRD) is based on the one used in the AMS-02 experiment. The x-ray transition radiation photons created in radiator fleece layers are detected by straw-tube proportional counters filled with a mixture of xenon and CO_2 . The expected proton rejection at 100 GeV is 700 at 80% positron efficiency.

The time-of-flight (ToF) system will consist of scintillator panels of 5 mm thickness mounted above and below the tracker. Both upper and lower ToF will have one or two layers of scintillator panels rotated by 90 degrees with respect to each other. Each layer is built out of nine scintillator panels with SiPM readout on both ends.

3.3.2 Carrier system

While space experiments have the undisputed virtue of being able to measure the spectra of cosmic rays completely undisturbed by Earth's atmosphere, scientific high-altitude balloons constitute an interesting alternative for several reasons. The experiment can be salvaged after the flight and be recalibrated, refitted and eventually repeated for the gradual improvement of the statistical accuracy, and it can be conducted at a much lower cost.

High-altitude scientific balloons reach an altitude of 40 km and carry a payload of up to 3 tons. Their skin has a thickness of $20\ \mu\text{m}$ and expands to a volume of $10^6\ \text{m}^3$. During summer stable weather conditions develop at Earth's poles including circumpolar winds that can carry a balloon on a more or less predictable trajectory around the North or South Pole. The record in flight duration is held by the CREAM [100] experiment which was flown above Antarctica circumnavigating the South Pole three times for a total of 42 days in December 2004. Launch sites in the Northern hemisphere include Kiruna, Sweden, and the Svalbard archipelago. Other experiments successfully flown with balloons include ATIC [101], BESS [102], CAPRICE [103], HEAT [104] TRACER [105], and ISOMAX [106], which was equipped with a superconducting magnet similar to the one foreseen for PEBS.

Table 3.1 contains a power and weight budget for the PEBS gondola, partially based on the figures for CREAM.

3.3.3 Secondary targets

In addition to a measurement of the cosmic-ray positron fraction, other interesting questions may be tackled with the PEBS detector. Low-energetic antiprotons are of interest

	weight / kg	power / W
flight control and flight train	50	0
control and data handling	38	60
telecommunications	66	84
electrical power	250	107
mechanical structure	110	0
altitude control	75	4
system cabling	85	2
sub total	674	257
science	1600	343
total	2274	600

Tab. 3.1: Power and weight budget for the PEBS gondola.

because they might also contain clues to additional primary sources of cosmic rays. In addition, as with other low-energetic particles, their continued measurement over a series of years promises a better understanding of heliospheric physics including solar modulation, as well as geomagnetic effects. A measurement of the $^3\text{He}/^4\text{He}$ and B/C ratios is of great interest for an improved understanding of cosmic-ray propagation. Detailed studies of the feasibility of these ideas need to be conducted in the future.

3 Detectors to measure the cosmic-ray positron fraction

4 Design study for PEBS based on Monte Carlo simulations

The design and construction of PEBS are complex tasks. An essential tool in this process is a simulation of the detector that can be used to study its performance in a fast and inexpensive way, without having to resort to a lengthy series of prototype building.

The passage of a particle through the detector is governed by the principle of chance at the most fundamental level. This is completely counter-intuitive and demonstrates the quantum nature of the physical processes involved. For example, a proton passing the calorimeter may do so almost completely unhindered, leaving only a few clouds of ionisation along its track. The next time, though flying on exactly the same path, an interaction with a nucleus of the calorimeter material may occur leading to the disintegration of the two particles and the creation of a bunch of new ones. A neutral pion might be among those, and its decay to two photons will lead to an electromagnetic shower in the calorimeter and thus a radically different event topology.

When a particle crosses a detector element, made of a certain material, every interaction process occurs with a certain probability. This is encoded in the cross section σ of a process relating the mean number dN of interactions to the number density n of targets and thickness dx of the material traversed by

$$dN = \sigma n dx \tag{4.1}$$

From the discussion above, it is clear that the correct approach to predicting the detector performance is a Monte Carlo simulation. The toolkit best suited and most widely used for this task is GEANT4 [107]. It has widespread applications in high-energy physics, space and radiation physics and medical physics, among others.

A full simulation of PEBS based on GEANT4 has been created. This simulation can be used to predict the overall behaviour of the detector, vary design parameters and study the change in detector performance, test reconstruction algorithms, develop analysis techniques, and many more. In section 4.1, the working principle of the simulation is explained. The detector design and its implementation in the simulation are described in section 4.2. This section also contains information about the various process activated for the simulation as well as the modelling of the response of the different subdetectors to passing particles. Part of these models use input from testbeam data, and the extraction of the required information is detailed in section 4.2.8 as well as in chapter 5.

The simulation alone is not sufficient to get a realistic picture of the detector performance. The events it produces contain raw information that is arranged in a similar way as is expected from the real detector. The task of the reconstruction program presented in section 4.3 is to transform the raw data of the individual subdetectors into higher-

level objects. This includes track finding and fitting in the tracker and the TRD, and reconstruction of a possible electromagnetic shower in the calorimeter.

Results for the most important figures of merit for PEBS will be presented in the final section 4.4 of this chapter.

4.1 Working principle of the Monte Carlo simulation

For every GEANT4 application, the user must provide a description of the detector geometry, a list of the interaction processes to be used, and instructions for generating the primary particle entering the detector. The program will then calculate the energy deposition in those elements of the detector marked as sensitive by the user. This information can subsequently be used to model the response of the detector and create so called simulated events - a picture of the passing particle as taken by the detector.

For a given particle, the simulation proceeds by transporting it through its current material in small steps. First, a proposed step length is randomly generated for every process activated for the particle species, based on the process cross section for the current material. If the shortest step length is shorter than the distance to the boundary to the next material, the corresponding process will be set to be invoked after the step. Before that, all continuous processes, such as ionisation energy loss, are invoked and the energy, position and time of the particle are updated according to the step taken. During evaluation of the continuous processes or the chosen process, the particle may be destroyed and/or additional particles may be created. If the range of a particle created in an interaction inside a given material exceeds a certain cut value, the particle will be added to the list of secondaries to be propagated. Otherwise, the corresponding energy loss is added at the place of the interaction. Increasing this range cut will reduce the computing time needed at the possible expense of simulation accuracy.

Transportation during the step takes the given magnetic field into account. After completion of a step, the procedure starts anew, and when the particle reaches the boundary of the simulated volume or is destroyed, any secondary particles are tracked in the same way, possibly creating additional new particles. The event is finished when no secondaries are left to be tracked.

Particles can be generated from a fixed point or uniformly generated on a surface, with fixed or random momentum, and with perpendicular incidence or from an angular distribution corresponding to an isotropic flux, projected onto a plane, i.e. drawn from uniformly distributed $\cos^2 \theta$ and ϕ . To increase efficiency in the early test stages, initial trajectories can be forced to approximately lie inside the detector acceptance, so that the number of events with particles traversing the magnet is minimised and CPU time is saved.

The PEBS simulation was designed with two main goals in mind. First, the performance to be expected from PEBS should be projected as accurately as possible. This requires that the key detector components be modelled to a high degree of detail. At the same time, the user should be as flexible as possible to vary the main design parameters of the detector which is important for the design optimisation process. The latter is accomplished by

4.2 Design study for PEBS and implementation in the Monte Carlo simulation

using Geant4's command language enabling the user to control many different aspects of the simulation with macro files. For example, the tracker fibre diameter or the number of layers in the ECAL and its absorber material can be modified in this way.

4.2 Design study for PEBS and implementation in the Monte Carlo simulation

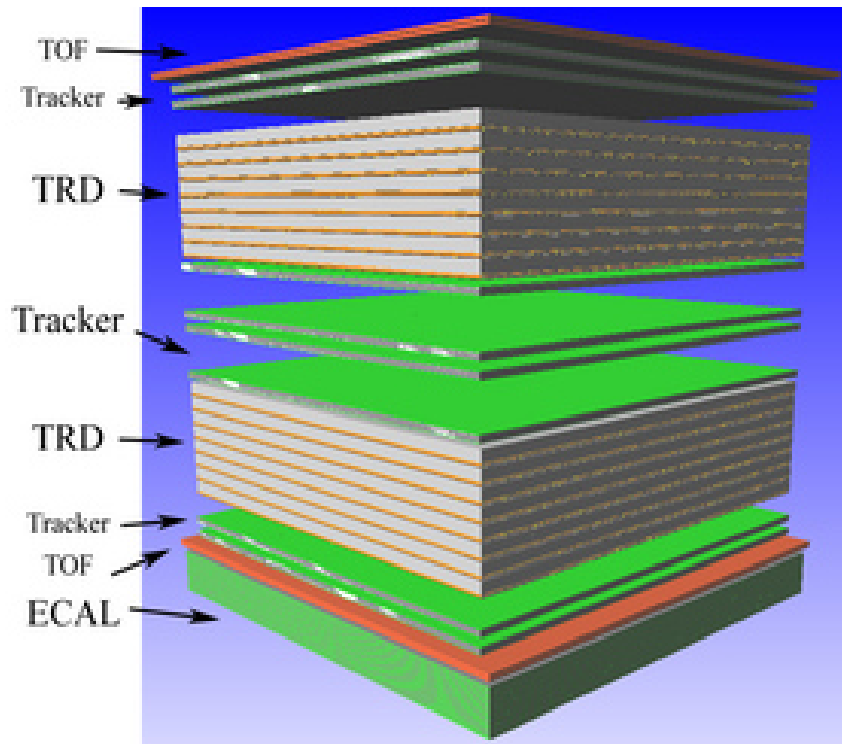


Fig. 4.1: View of the inner detector as modelled in the Geant4 simulation. The scintillating fibres of the tracker, not individually resolved on this scale, are painted in light green, and the foam in between is dark grey. The TRD radiator is drawn in grey, with the TRD straw tubes in brown sitting in between. The TOF panels are dark orange and the ECAL at the bottom has absorber plates in grey and fibre bars in green.

In the following, the working principles of the individual subdetectors and their current designs are presented. The implementation of their geometry in the simulation (fig. 4.1) is shown, too.

4.2.1 Magnet

The magnet design foresees a pair of superconducting Helmholtz coils of 1150 mm diameter creating a mean flux density of 0.8 T inside the tracker volume. The coils will be located inside a helium cryostat and the amount of helium to be carried will allow flight durations

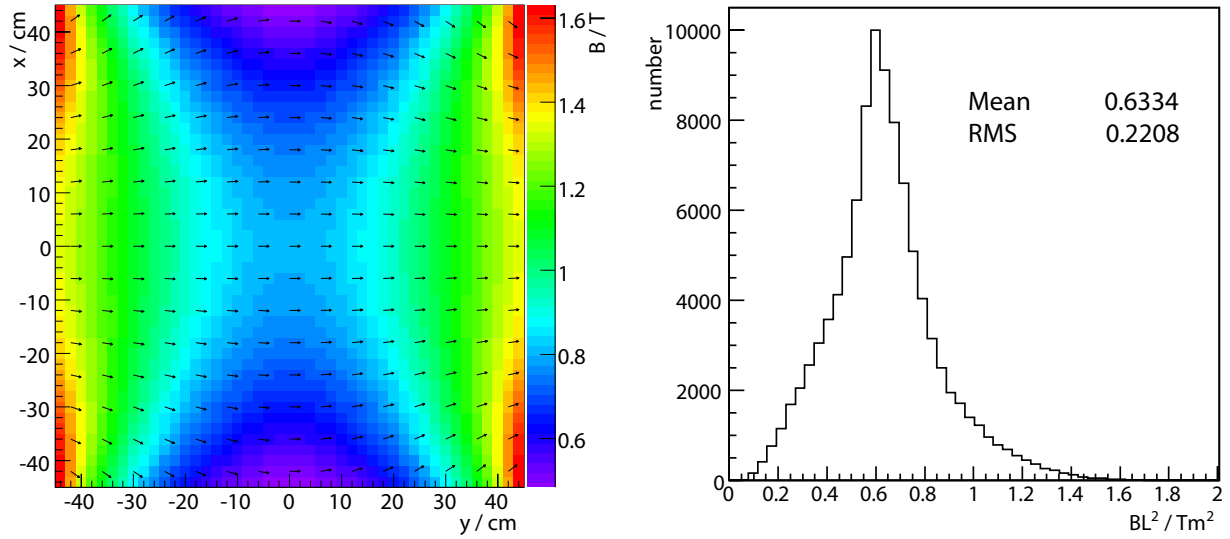


Fig. 4.2: *Left:* Magnetic field amplitude $|\vec{B}|$ at $z = 0$. The magnet coils are located to the left and right. *Right:* Distribution of BL^2 as defined in the text, for tracks within the acceptance of PEBS.

of 20-40 days. The opening aperture of the magnet measures $882 \times 882 \text{ mm}^2$. Figure 4.2 shows the magnetic field map in a plane containing the centre of the detector. The mean bending power of the magnet is found to be $BL^2 = 0.63 \text{ Tm}^2$. Here, BL^2 is defined by

$$BL^2 \equiv \int B_{\perp}(\ell) d\ell \cdot L \quad (4.2)$$

so that two field configurations with the same BL^2 will lead to the same angular deflection of a charged particle.

In the simulation, a homogeneous magnetic field of 0.8 T is used inside the tracker volume, to simplify the tracking and reconstruction algorithms for the time being and because the magnet design is still in a state of flux anyway. The corresponding $BL^2 = 0.57 \text{ Tm}^2$ is somewhat lower than in the current design and the resulting estimates for the detector performance will therefore be conservative.

The insensitive material parts surrounding the tracker, such as the magnet coils and cryostat, solar panels, electronics crates, and so on, are not included in the simulation yet.

4.2.2 Tracker

Working principle

The purpose of the tracker is to measure the momentum and thus the charge sign of an incoming particle. The measurement exploits the fact that the path followed by a particle of momentum p and charge z in a constant magnetic field \vec{B} is a helix. While the TRD is used to measure its pitch angle λ , the tracker is used to determine the radius R of

4.2 Design study for PEBS and implementation in the Monte Carlo simulation

curvature of the helix which is related to the momentum by [5]

$$\frac{p}{\text{GeV}} \cos \lambda = 0.3 z \frac{B}{\text{T}} \frac{R}{\text{m}} \quad (4.3)$$

The uncertainties in a measurement of momentum are best discussed in terms of the errors of the curvature $k \equiv 1/R$ because the distribution of this quantity is approximately Gaussian. The overall error σ_k on the curvature measurement has contributions from the position error as well as from multiple scattering and may be approximated by

$$\sigma_k^2 = \sigma_{k,\text{res}}^2 + \sigma_{k,\text{msc}}^2 \quad (4.4)$$

The term due to multiple scattering is only important for low momenta and is approximately given by

$$\sigma_{k,\text{msc}} = \frac{0.016 \text{ GeV}/c \cdot |z|}{L/\text{m} p \beta \cos^2 \lambda} \sqrt{\frac{L}{X_0}} \quad (4.5)$$

where L is the total track length and X_0 is the radiation length defined in section 4.2.5. The contribution from the limited spatial resolution of the individual tracker elements is given by [108]

$$\sigma_{k,\text{res}} = \frac{\sigma}{L'^2} \sqrt{\frac{720}{N+4}} \quad (4.6)$$

if N independent measurements are taken at equal distances with resolution σ perpendicular to the trajectory for a total length L' measured in the projection to the bending plane.

This uncertainty can be reduced in the so-called optimised spacing of detection planes, where $N/4$ measurements are taken at the entry and exit of the tracker each, and $N/2$ at the centre. The curvature error then becomes

$$\sigma_{k,\text{res}} = \frac{\sigma}{L'^2} \sqrt{\frac{256}{N}} \quad (4.7)$$

Design and implementation in the simulation

The tracker is constructed from modules like the one depicted in figure 4.3. Particles traversing the module deposit energy in two stacks of scintillating fibres, creating scintillation photons. The scintillation light is then guided by total internal reflection to the fibre ends where it is detected by novel silicon photomultiplier (SiPM) arrays [109] (sec. 4.2.3). Each fibre stack consists of five layers of 128 round fibres of 250 μm diameter and 860 mm length, positioned with a horizontal pitch of 275 μm and glued together. The distance between the individual channels on an SiPM array matches this fibre pitch. The vertical fibre spacing is taken to be 5 μm . The stacks are produced by threading the fibres on a rotating barrel with premachined grooves. These grooves have to be somewhat further apart than the diameter of the fibres to allow for inhomogeneities in the fibre diameter. The stacks are supported by spacers consisting of two carbon-fibre skins of 100 μm thickness with 10 mm of Rohacell foam in between. The performance of such a fibre module in a proton testbeam is studied in section 5.2.

4 Design study for PEBS based on Monte Carlo simulations

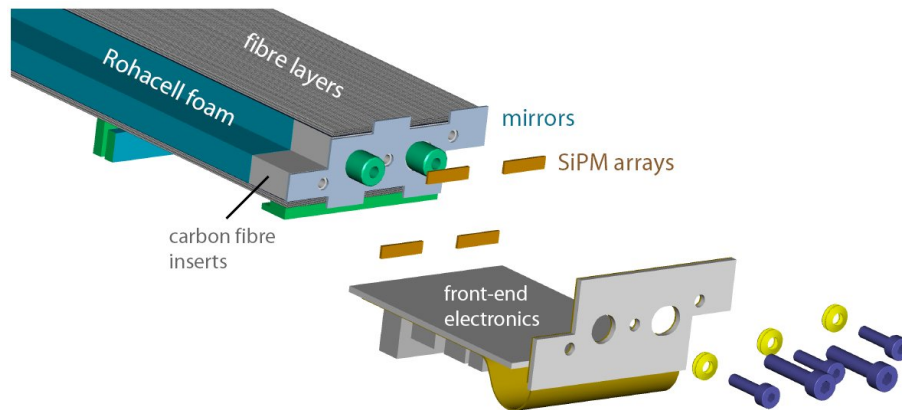


Fig. 4.3: Exploded view of a PEBS tracker module. Two stacks of scintillating fibres are carried by Rohacell foam with carbon fibre inserts at the ends. Plates equipped with reflective foils and silicon photomultiplier arrays are screwed to the sides of the module. The large screws will be used to mount the module to the tracker walls.

The SiPM arrays are located on ceramic plates mounted to both fibre ends which also contain highly reflective mirroring foils. The SiPM arrays and mirrors are arranged in such a way that each fibre is covered by a mirror on one end and by an SiPM array channel on the other. This compact module design allows the construction of a tracker sensitive to particles almost across its entire aperture. The modules will be grouped into eight layers, with two layers each located at the top and bottom of the tracker and four layers around the centre. In this configuration, the momentum resolution is optimised (eq. (4.7)) and space is created for the TRD. For the simulation, a somewhat simpler module shape is used at the moment (fig. 4.4).

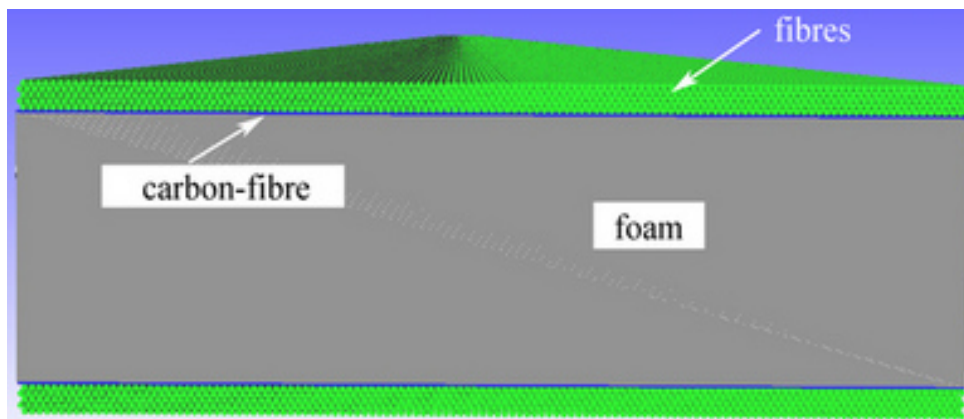


Fig. 4.4: Visualisation of a tracker module in the Geant4 simulation. The fibres, carbon-fibre spacers and Rohacell foam are visible.

4.2.3 Silicon photomultipliers for scintillating fibre readout

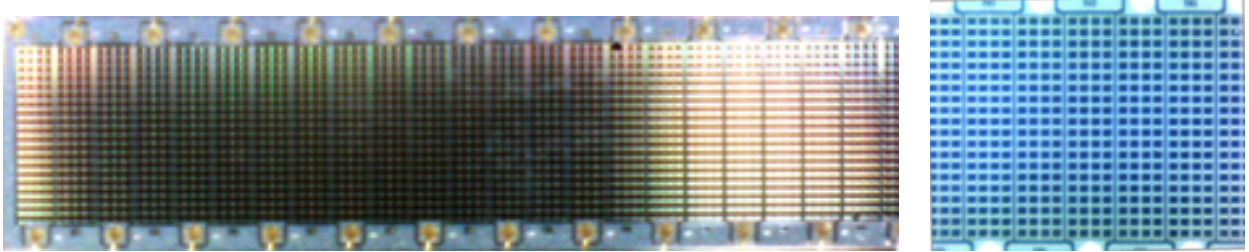


Fig. 4.5: *Left:* Close-up view of a Hamamatsu MPPC 5883 SiPM array, suitable for use in a scintillating fibre tracker. *Right:* Microscope picture of several channels of the Hamamatsu MPPC 5883 SiPM array revealing the individual pixels. Each SiPM on the array has $4 \times 20 = 80$ pixels.

A silicon photomultiplier (SiPM, fig. 4.5) [110, 111, 112, 113] is a novel solid state photodetector. In principle, it consists of a matrix of avalanche photo diodes (APDs) that are operated in the Geiger mode, i.e. above the breakdown voltage. Simply put, an APD is based on a p-n junction between two semiconductors with a reverse bias voltage applied to it so that photo-electrons are accelerated in the resulting electric field creating an avalanche of secondary ionisation. The single matrix elements are called pixels and the output signal is then proportional to the number of pixels that have fired. The mode of operation leads to a high intrinsic gain of the SiPM on the order of 10^5 to 10^6 . In addition, they have the virtues of insensitivity to magnetic fields, high quantum efficiency, as well as compactness and auto-calibration. The latter is due to the fact that the single photo-electron peaks are visible in the spectrum (fig. 4.27 *left*). Dark noise rates of SiPMs typically are on the order of a few hundred kHz.

Silicon photomultipliers will be used for the readout of both the scintillating fibres in the tracker and the scintillator layers of the electromagnetic calorimeter and possibly also for the time-of-flight system. Their modelling is therefore an important part of the digitisation chain in the simulation and their key features, present for both tracker and calorimeter, are summarised in the following. A detailed discussion and measurements of the properties of SiPMs in the context of the PEBS project can be found in [98]. In addition to individual SiPMs suitable for use in the ECAL, SiPM arrays have recently become available that combine a number of SiPMs next to each other on the same wafer. These compact devices are well suited for the tracker readout.

Since the actual avalanches created in the SiPM pixels are not simulated by Geant4, a model for the response of the SiPMs has to be adopted. The ionisation energy loss dE/dx of a particle over a simulated step of length Δx is provided by the simulation. This will be turned into photons by the scintillating fibre material with an efficiency ϵ_{scint} (with units of keV^{-1}). The fibre will trap a fraction ϵ_{trap} of these photons due to total internal reflection, and the mirrored surface at one end of the fibre will lead to an increase by a factor of f_{mirror} . Finally, a fraction ϵ_{opt} of the photons arriving at the SiPM end of the fibre will be optically coupled into the SiPM, which in turn has a limited geometrical

4 Design study for PEBS based on Monte Carlo simulations

efficiency ϵ_{geom} , given by the ratio of active pixel area to the total area subtended by the fibre end. The product $\epsilon_{\text{qe}} \epsilon_{\text{abe}}$ of the quantum efficiency and the avalanche breakdown efficiency of a single SiPM pixel will then determine if an incoming photon will actually trigger a breakdown. The mean number of photons in an SiPM is then given by

$$N_{\text{ph}} = \frac{dE}{dx} \Delta x \epsilon_{\text{scint}} \epsilon_{\text{trap}} f_{\text{mirror}} \epsilon_{\text{opt}} \epsilon_{\text{geom}} \epsilon_{\text{qe}} \epsilon_{\text{abe}} \quad (4.8)$$

At the moment, cross-talk, arising from UV photons created during the avalanche process and subsequently triggering a neighbouring pixel, is not considered. Attenuation in the fibre, i.e. a position-dependent ϵ_{trap} is neglected at the moment as the attenuation length is large compared to the fibre length in our case.

For all simulations presented here, the manufacturer's values of $\epsilon_{\text{scint}} = 8 \text{ keV}^{-1}$ and $\epsilon_{\text{trap}} = 0.056$ for round fibres and $\epsilon_{\text{trap}} = 0.073$ for square fibres were adopted, for the Bicon fibres employed during the testbeam campaign presented in chapter 5 [114]. It is assumed that $f_{\text{mirror}} = 1.6$. The quantity ϵ_{opt} is difficult to determine and it is practical to combine the last four factors in equation (4.8) in a single overall coupling efficiency

$$\epsilon_{\text{coup}} \equiv \epsilon_{\text{opt}} \epsilon_{\text{geom}} \epsilon_{\text{qe}} \epsilon_{\text{abe}} \quad (4.9)$$

This quantity determines the overall light yield measured with the SiPMs. It contains the photo-detection efficiency

$$\epsilon_{\text{pde}} = \epsilon_{\text{geom}} \epsilon_{\text{qe}} \epsilon_{\text{abe}} \quad (4.10)$$

As presented in detail in chapter 5, a typical light yield to be expected from the PEBS tracker modules is 10 photo-electrons per cluster for the standard configuration. The value of $\epsilon_{\text{coup}} = 0.1$ has been chosen to match this result.

In reality, the number of pixels fired is subject to random fluctuations. Therefore, the digitisation for each SiPM proceeds as follows:

- From all steps during the simulated particle propagation in the given fibre, the accumulated energy deposition ΔE is calculated.
- The number N_{gen} of generated photons is drawn from a Poissonian distribution with mean $\Delta E \cdot \epsilon_{\text{scint}}$.
- The number of photons coupled to the available SiPM pixels is drawn according to a binomial distribution with the number of trials N_{gen} and probability $\epsilon_{\text{trap}} \cdot f_{\text{mirror}} \cdot \epsilon_{\text{coup}}$.
- In the case of the tracker, certain fibres deposit their photons on two adjacent SiPMs. This is simulated by drawing the number of photons on the left SiPM from a binomial distribution with the number of photons obtained from the previous step and probability $1/2$. The right SiPM then receives the remaining photons.
- According to the noise level N_{noise} set by the user, and given as a mean number of photons, a number of noise photons is drawn for each SiPM from a Poissonian distribution with mean N_{noise} .

4.2 Design study for PEBS and implementation in the Monte Carlo simulation

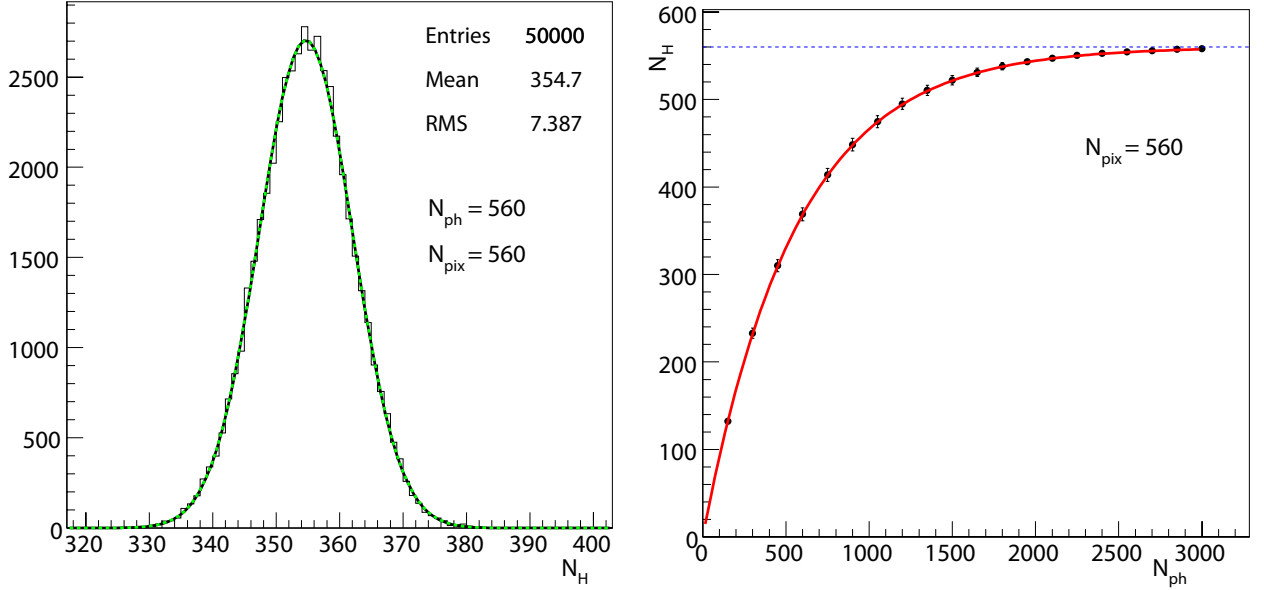


Fig. 4.6: *Left:* Simulated distribution of raw amplitude N_H (fired pixels) for a Geiger-mode array of 560 SiPM pixels, with $N_{ph} = 560$ incoming photons, assuming perfect geometric and quantum efficiency, together with a fit of a Gaussian distribution (black line) and a Gaussian with mean and variance according to (4.12) and (4.13) (green dotted line). *Right:* Raw amplitudes obtained for an array of 560 pixels, as a function of the number of incoming photons. The error bars correspond to the standard deviation obtained from a fit of a Gaussian to the distribution found at each N_{ph} . Also included is the analytic curve according to equation (4.11).

- The photons reaching the sensitive area of an SiPM are distributed on the pixel matrix. For the simulation of the pixel matrix, a random pixel number is drawn for each photon from a uniform distribution and the corresponding pixel is then activated. The total number of activated pixels then yields the raw SiPM amplitude, given in units of pixels.
- The number n of pixels is smeared by a Gaussian with a width of $\sigma_n = \sqrt{n + 1}\sigma$ [115]. The parameter σ determines the width of the photo-electron peaks in the SiPM spectrum. The purpose is to model the electronic noise of the SiPMs and thus to obtain the smeared-out peak structure characteristic of an SiPM (cf. fig. 4.27). For the tracker, a value of $\sigma = 0.1$ is adopted, while the measured value of $\sigma = 0.15$ [116] is taken for the ECAL SiPMs.
- Hit information is stored for each SiPM whose amplitude exceeds a given threshold.

The response of an SiPM to a given number of incident photons is illustrated in figure 4.6. It shows the distribution of the number N_H of fired pixels for a SiPM matrix of $N_{pix} = 560$ pixels hit by 560 incident photons. As some pixels are hit by more than one photon, the mean number of N_H is smaller than N_{pix} .

In order to get a reliable determination of the energy of an ECAL shower, the departure of the SiPM response from linearity, as is evident in the figure, has to be corrected for.

4 Design study for PEBS based on Monte Carlo simulations

To this end, the number of fired pixels has to be translated to the true amplitude, i.e. the number of incident photons. This requires an analytic expression for the mean number of pixels N_H fired by a number of photons N_{ph} incident on an array of N_{pix} pixels. In the case of $N_{\text{pix}} \gg 1$, such an expression can be derived as follows:

A small group dN'_{ph} of photons will increase the number of fired pixels by dN'_H . If N'_H pixels have already fired at that point, one has

$$dN'_H = dN'_{\text{ph}} \cdot \left(1 - \frac{N'_H}{N_{\text{pix}}}\right)$$

After rearrangement, one can take the continuous limit and integrate both sides:

$$\int_0^{N_H} \frac{dN'_H}{1 - \frac{N'_H}{N_{\text{pix}}}} = \int_0^{N_{\text{ph}}} dN'_{\text{ph}}$$

This leads to

$$N_H = N_{\text{pix}} \left(1 - \exp\left(-\frac{N_{\text{ph}}}{N_{\text{pix}}}\right)\right) \quad (4.11)$$

From the inverse of the above, the desired amplitude N_{ph} can be calculated.

From a combinatorial point of view, the problem of the SiPM response can be treated by considering an urn model where N_{ph} balls are distributed into N_{pix} urns and asking for the number of urns with at least one ball. This approach is more difficult but it yields the exact result for the mean of this number, and also its variance [117]:

$$N_H = N_{\text{pix}} \left(1 - \left(1 - \frac{1}{N_{\text{pix}}}\right)^{N_{\text{ph}}}\right) \quad (4.12)$$

$$\sigma^2(N_H) = N_{\text{pix}}(N_{\text{pix}} - 1) \cdot \left(1 - \frac{2}{N_{\text{pix}}}\right)^{N_{\text{ph}}} + N_{\text{pix}} \cdot \left(1 - \frac{1}{N_{\text{pix}}}\right)^{N_{\text{ph}}} - N_{\text{pix}}^2 \cdot \left(1 - \frac{1}{N_{\text{pix}}}\right)^{2N_{\text{ph}}} \quad (4.13)$$

(4.12) becomes (4.11) in the limit $N_{\text{ph}} \rightarrow \infty$.

4.2.4 Time-of-flight system

In the simulation, the time-of-flight system is modelled by two layers of scintillator modules above and below the tracker, each. Each layer consists of modules made of polystyrene with dimensions 100×5 mm.

4.2.5 Electromagnetic calorimeter

Principle of operation

Electromagnetic calorimeters [118, 119] are widely used in high energy physics to measure the energies of electrons and photons. They are based on the physics of the electromagnetic cascade. For electrons with energies larger than ~ 10 MeV, the main energy loss

4.2 Design study for PEBS and implementation in the Monte Carlo simulation

mechanism is bremsstrahlung. On the other hand, photons in this energy range lose their energy predominantly by pair creation. This means that an impinging electron will radiate bremsstrahlung photons, and the ones with sufficient energy will in turn create secondary electrons and positrons. These processes will be repeated, thus giving rise to a cascade of particles with lower and lower energies. Below a critical energy ϵ , the dominant energy loss mechanisms are ionisation and excitation for electrons and Compton scattering and photoelectric effect for photons. Therefore, towards the end of the cascade, energy will be dissipated instead of being used for the creation of additional particles. These processes thus lead to the development of an *electromagnetic shower*.

The main features of a shower can be characterised by a single parameter, the radiation length X_0 that depends on the absorber material. It represents the average distance z that an electron needs to travel in a material to reduce its energy to $1/e$ of its initial energy E_0 . Similarly, the intensity I_0 of a photon beam will be reduced by a factor of $1/e$ after a path length of $9/7 X_0$. For the common absorber materials lead and tungsten, the radiation lengths are $X_0^{\text{Pb}} = 5.612$ mm and $X_0^{\text{W}} = 3.504$ mm, respectively.

The longitudinal shower profile can then be described as a function of $t \equiv z/X_0$, where z is the coordinate along the shower axis, and is parameterised to a good approximation by the formula

$$\frac{dE}{dt} = E_0 b \frac{(bt)^{a-1} e^{-bt}}{\Gamma(a)} \quad (4.14)$$

where E_0 is the total energy and a and b are parameters. b sets the scale of the shower and a in turn gives the position of the shower maximum which is calculated to be

$$t_{\text{max}} = \frac{a-1}{b} \quad (4.15)$$

from (4.14). It depends logarithmically on energy,

$$t_{\text{max}} \approx \log \frac{E_0}{\epsilon} + t_0 \quad (4.16)$$

where $t_0 = -1/2$ for electrons and $t_0 = +1/2$ for photons and ϵ is the critical energy, at which losses by bremsstrahlung and ionisation are equally large. In lead, $\epsilon \approx 7$ MeV.

The transverse size of an electromagnetic shower is determined by multiple scattering and, to a lesser extent, by bremsstrahlung photons emitted away from the shower axis. The typical scale is the Molière radius R_M which is given in terms of the radiation length and the critical energy, and it can be approximated by

$$R_M \approx 21 \text{ MeV} \frac{X_0}{\epsilon} \quad (4.17)$$

It represents the average lateral deflection of electrons at the critical energy after traversing one radiation length. The values of the Molière radii for lead and tungsten are $R_M^{\text{Pb}} = 16$ mm and $R_M^{\text{W}} = 9.3$ mm, respectively.

A calorimeter can be used for an energy measurement because the total energy deposition by all charged particles in a shower is proportional to the energy of the incident particle. The total track length T_0 of the shower, defined as the sum of all ionisation tracks, is

4 Design study for PEBS based on Monte Carlo simulations

$T_0 \propto X_0 E_0 / \epsilon$. The intrinsic energy resolution of an ideal calorimeter will then be due to statistical fluctuations in the track length: $\sigma(E) \propto \sqrt{T_0}$. In reality, imperfections in the calorimeter response will lead to an additional constant term in the relative energy resolution, which becomes

$$\frac{\sigma(E)}{E} = \frac{a}{\sqrt{E}} \oplus c \quad (4.18)$$

where \oplus denotes a quadratic sum. As will be seen, leakage effects due to the finite size of the calorimeter and the limited dynamic range of the SiPMs used for the readout give the most important contribution to c and might even cause it to rise with energy.

In general, calorimeters can be divided into two groups. In the first group, called homogeneous calorimeters, the same material serves as absorber and detection medium. For example, PbWO_4 combines high charge number Z and thus small radiation length with the properties of a scintillator so that the light yield obtained in a crystal of such a material is a measure of the energy of an incident electron. In the other group, called inhomogeneous calorimeters, layers of absorber material, such as lead or tungsten, are followed by active detection layers, for example in the form of a plastic scintillator. The drawback of inhomogeneous calorimeters is their lower energy resolution due to the fact that only a part of the shower is visible in the active material and that part is subject to statistical fluctuations. On the other hand, the sandwich design of an inhomogeneous calorimeter allows one to not only measure the *energy*, but also the *shape* of the shower, i.e. determine the shower profile dE/dt . This means that an inhomogeneous calorimeter can be used for particle identification and it is therefore the design of choice for PEBS, where the calorimeter plays a vital role in the suppression of the proton background. In addition, the degradation of the energy resolution due to the leakage effect can be reduced by fitting the shower profile with (4.14) and thus extrapolating the energy deposition on the missing layers.

The particle identification capability is based on the principle that the shower induced by a proton traversing the calorimeter looks different than that of an electron. First, protons create secondaries by hadronic interactions, for which the hadronic interaction length λ_I sets the scale. For a good absorber, the radiation length is much smaller than the interaction length, $X_0 \ll \lambda_I$. Second, the angles of the trajectories of secondaries with respect to the shower axis are large, compared to the bremsstrahlung case. This can be seen from the distribution of transverse momenta in inelastic hadron-hadron scattering, which has a cross section $d\sigma/dp_T^2 \propto \exp(-bp_T)$ with $b \approx 6 \text{ GeV}^{-1}$ [120]. Hence, the mean transverse momentum is given by $\langle p_T \rangle = 0.33 \text{ GeV}$. To summarise, proton showers start deeper in the calorimeter, are broader than electromagnetic ones, and have less regular shape.

Design

The electromagnetic calorimeter is located at the bottom of the detector. It performs a destructive measurement of the energy of electrons and can be used for proton suppression. From the considerations above, the design parameters of the electromagnetic calorimeter can already be narrowed down considerably. A high- Z absorber material is needed, and lead or tungsten are the prime candidates. Both have an excellent ratio of

4.2 Design study for PEBS and implementation in the Monte Carlo simulation

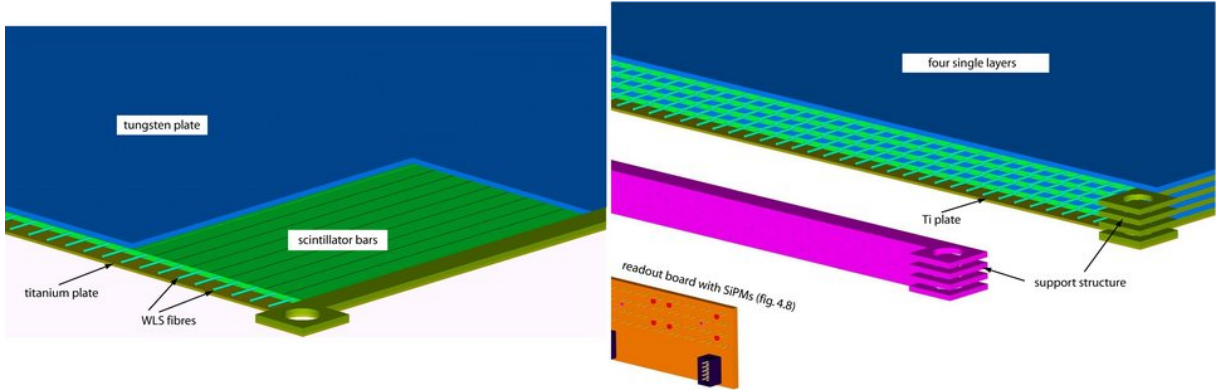


Fig. 4.7: Exploded drawing of a single ECAL layer at the bottom of a superlayer (*left*) and one superlayer (*right*).

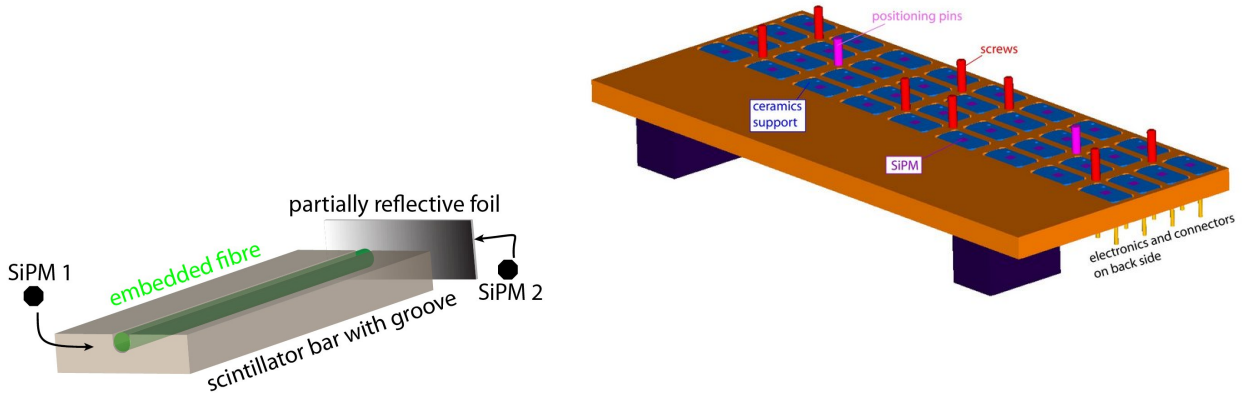


Fig. 4.8: *Left:* ECAL fibre readout sketch. *Right:* Mechanical drawing of the ECAL board foreseen to position the silicon photomultipliers at the sides of the calorimeter sandwich.

the radiation and hadronic interaction lengths $X_0/\lambda_I \approx 0.035$ leading to good proton suppression, as well as short X_0 allowing the construction of a thin calorimeter which in turn means large geometric acceptance. The overall thickness of the calorimeter should allow a measurement that includes at least the shower maximum. According to (4.16) this translates into a minimum thickness of roughly $10X_0$. The longitudinal and transverse readout granularities must be somewhat smaller than X_0 and R_M , respectively.

The design chosen features twenty layers of 2 mm tungsten absorber sheets followed by a layer of scintillator bars of 2 mm thickness and 7.75 mm width each. Embedded in each scintillator bar is a wavelength shifting (WLS) fibre used to transport the scintillation light to the fibre ends where it is detected by SiPMs.

Four layers each will be grouped into a superlayer, supported by a 1 mm plate of titanium (fig. 4.7). Five superlayers are placed with alternating directions to allow a three-

dimensional image of the shower to be taken. The total thickness of the calorimeter will be as small as 8.4 cm and be equivalent to 11.4 radiation lengths.

A challenge in the construction of the calorimeter is introduced by the fact that its dynamic range must be sufficient to cover the range extending from minimally ionising particles to the light produced in the shower maximum of a 200 GeV electron. This problem is overcome by putting a partially reflective foil with a reflectivity of roughly 90 % in front of one of the two SiPMs (fig. 4.8 (*left*)), thereby reducing the light incident on one SiPM and increasing it on the other. The precise positioning of the SiPMs in front of the WLS fibres will be done by embedding them in an aluminium plate like the one sketched in figure 4.8 (*right*) which can be screwed to the side of the absorber-fibre sandwich and will also contain the necessary front-end electronics.

Simulation of fibre and SiPM response

The electromagnetic calorimeter is made out of alternating layers of tungsten absorber and scintillator bars. Layers are grouped into multilayers and these are rotated to alternating orientations so that a three-dimensional picture of the shower development can be taken.

The response of the detection chain in the electromagnetic calorimeter, consisting of the scintillator bars, partially reflective foil and silicon photomultipliers (fig. 4.8), is modelled such that it matches the results of test measurements performed at ITEP Moscow [115]. There, the light yield of a scintillator bar with an embedded wavelength-shifting fibre that was equipped with a mirror on one end and read out by a SiPM on the other end was measured for minimally ionising particles (MIPs) crossing the fibre bar over its entire length. An average yield of $\bar{n}_\gamma = 10$ photons was found. Without the reflective end, a ratio of $A = 1.5$ was found for the light yields at the near and far ends of the fibre bars. The average number $n_{\gamma,\text{mip}}$ of trapped photons *per hemisphere* for a MIP in the ECAL fibre bars will therefore be

$$n_{\gamma,\text{mip}} = \bar{n}_\gamma \cdot \frac{1}{\int_0^1 (A^{-x} + A^{-2+x}) dx} = \bar{n}_\gamma \cdot \frac{\log A}{1 - \frac{1}{A^2}} \quad (4.19)$$

For an actual simulated energy deposition ΔE in the calorimeter, the mean number n_γ of trapped photons per hemisphere is then obtained by using the energy loss $dE/dx = 2.052 \text{ MeV/cm}$ of the scintillator material and the thickness d of a scintillator bar:

$$n_\gamma = \frac{\Delta E}{d \frac{dE}{dx}} \cdot n_{\gamma,\text{mip}} \quad (4.20)$$

Let $x_s \in [0, 1]$ be the relative coordinate along the fibre bar. The light attenuation in the fibre as well as the reflectivity R and transmissivity $T = 1 - R$ of the partially reflective foil at $x_s = 1$ are then taken into account by calculating the average number of photons

4.2 Design study for PEBS and implementation in the Monte Carlo simulation

arriving at SiPM 1 ($x_s = 0$) and SiPM 2 ($x_s = 1$) as

$$n_1 = n_\gamma \cdot \left(e^{-\log A \cdot x_s} + e^{-\log A \cdot (1-x_s)} \cdot R \cdot \frac{1}{A} \right) \quad \text{and} \quad n_2 = n_\gamma \cdot \left(e^{-\log A \cdot (1-x_s)} \cdot T \right) \quad (4.21)$$

The number of fired pixels n_{pix}^1 and n_{pix}^2 on the two SiPMs is generated by drawing two numbers of incident photons from Poisson distributions with mean n_1 and n_2 , respectively, and applying the procedure outlined in section 4.2.3. It was found [116] that a systematic uncertainty from the non-uniformity of the SiPM response has to be taken into account by randomly smearing the number of pixels used in the simulation of the SiPM response by applying a Gaussian smearing with a standard deviation of $\sigma_{\text{pix}}^{\text{sys}} = 10$ pixels.

Finally, the output signals N_1 and N_2 of the two SiPMs are drawn from two Gaussian distributions of mean $n_{\text{pix}}^{1,2}$ and standard deviation $\sqrt{n_{\text{pix}}^{1,2}} \sigma_{\text{peak}}$ to take into account the smearing of the photo peaks as described by the smearing parameter $\sigma_{\text{peak}} = 0.15$.

For a good energy resolution and linearity of the calorimeter, the reconstructed number of incident photons $n_{\gamma, \text{rec}}^{1,2}$ must now be extracted from the number of fired pixels. To this end, formula (4.12) is inverted. Attenuation is corrected for using the same factors as in eq. (4.21).

To finally exploit the beneficial effect of the partially reflective foil, a weighted average of the two SiPM signals is calculated as the last step. Assuming Gaussian likelihoods, the weighted average is calculated as [121]

$$n_{\gamma, \text{rec}} = \frac{\frac{n_{\gamma, \text{rec}}^1}{(\sigma_{\gamma, \text{rec}}^1)^2} + \frac{n_{\gamma, \text{rec}}^2}{(\sigma_{\gamma, \text{rec}}^2)^2}}{\frac{1}{(\sigma_{\gamma, \text{rec}}^1)^2} + \frac{1}{(\sigma_{\gamma, \text{rec}}^2)^2}} \quad (4.22)$$

For the evaluation of (4.22), the errors on the reconstructed numbers of photons are needed. They are obtained from a toy Monte Carlo study incorporating the effects outlined in this paragraph minus attenuation. Figure 4.9 contains the resulting histogram which is used for the interpolation of the errors. In the case that the reconstructed number of photons for SiPM 1 (without the reflective foil in front) exceeds a given threshold, only the SiPM behind the reflective foil is used for the signal reconstruction.

4.2.6 Transition radiation detector

Principle of operation

A moving charged particle crossing the boundary between two media of different refractive index emits transition radiation. Qualitatively, this occurs because the field configuration created by the moving charge must be different deep inside the second medium as compared to the one deep inside the first. The necessary change in configuration leads to some pieces of the field being shaken off as radiation. We will briefly review the physics of transition radiation here to show how this effect can be used for particle identification [122, 123, 124, 125].

A calculation of the spectral and angular dependence of the radiated energy for a charge entering a medium with electric permittivity ϵ begins with the observation that for fre-

4 Design study for PEBS based on Monte Carlo simulations

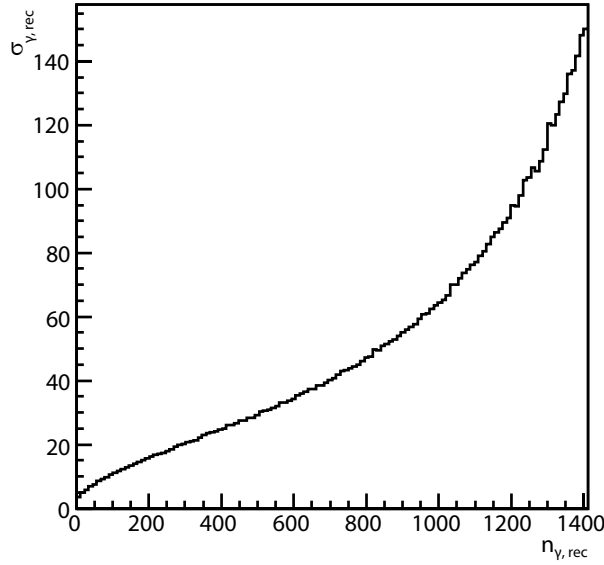


Fig. 4.9: Results of the toy Monte Carlo used for the determination of the error on the number of reconstructed photons in an ECAL fibre bar.

quencies above the optical resonance region, the index of refraction is not far from unity. This means that the Fourier component of the induced polarisation $\mathbf{P}(\mathbf{x}, \omega)$ can be evaluated approximately by

$$\mathbf{P}(\mathbf{x}, \omega) = \left(\frac{\epsilon(\omega)}{\epsilon_0} - 1 \right) \mathbf{E}_i(\mathbf{x}, \omega) \quad (4.23)$$

where \mathbf{E}_i is the Fourier transform of the electric field of the incident particle in vacuum. This can be used to calculate the dipole radiation field caused by the polarisation $\mathbf{P}(\mathbf{x}, \omega)$. For a particle with charge ze crossing the boundary between media with electric permittivities ϵ_1 and ϵ_2 , the resulting angular and spectral dependence of the transition radiation energy is

$$\frac{d^2 I}{d\omega d\theta} = \frac{2z^2 \alpha \hbar \theta^3}{\pi} \left(\frac{1}{\gamma^{-2} + \theta^2 + \omega_1^2/\omega^2} - \frac{1}{\gamma^{-2} + \theta^2 + \omega_2^2/\omega^2} \right)^2 \quad (4.24)$$

Here, $\omega_{1,2}$ are the plasma frequencies of the media which determine the electric permittivity,

$$\epsilon_i(\omega) \simeq 1 - \frac{\omega_i^2}{\omega^2} \quad (4.25)$$

The plasma frequency ω_p depends on the number density n_e of electrons in the medium, $\omega_p^2 = n_e e^2 / \epsilon_0 m_e$. For a typical radiator, polyethylene, $\hbar \omega_p^{\text{CH}_2} = 20.9$ eV, while for air $\hbar \omega_p^{\text{air}} = 0.7$ eV.

Integrating over the emission angle θ gives the differential energy spectrum

$$\frac{dI}{d\omega} = \frac{z^2 \alpha \hbar}{\pi} \left(\left(\frac{\omega_1^2 + \omega_2^2 + 2\omega^2/\gamma^2}{\omega_1^2 - \omega_2^2} \right) \cdot \log \left(\frac{1/\gamma^2 + \omega_1^2/\omega^2}{1/\gamma^2 + \omega_2^2/\omega^2} \right) - 2 \right) \quad (4.26)$$

4.2 Design study for PEBS and implementation in the Monte Carlo simulation

The total energy radiated at a single boundary then becomes

$$I = \frac{z^2 \alpha \hbar}{3} \gamma \frac{(\omega_1 - \omega_2)^2}{\omega_1 + \omega_2} \quad (4.27)$$

The proportionality of the energy I to $\gamma = E/mc^2$ is the key to particle identification. For electrons in the GeV-range, $\gamma \gtrsim 1000$, while $\gamma \sim 1$ for protons of the same energy due to their much higher mass. The angular and spectral distributions can be shown to be such that most of the emission is in the forward direction, in a cone with half-angle $1/\gamma$, and is emitted in the form of x-ray photons for highly relativistic particles, with the energy scale of the photons given by $\gamma\omega_p$. A proportional chamber filled with a gas with a high x-ray absorption coefficient, such as xenon, is commonly used for detection of transition radiation for that reason. As the x-ray photons are emitted almost along the direction of the charged particle, the detected signal will be the sum of the energy deposition due to ionisation and the absorbed x-ray photons.

As the probability of emission of a transition radiation photon at a single boundary is of the order of α according to (4.27), radiators consisting of many interfaces have to be employed in practice. An important quantity is the formation zone of a material, given by

$$Z = \frac{4c}{\omega} \left(\frac{1}{\gamma^2} + \theta^2 + \frac{\omega_p^2}{\omega^2} \right)^{-1} \quad (4.28)$$

If the thickness of a radiator element is smaller than Z , the yield will be strongly suppressed. The calculation of the transition radiation yield behind a stack of radiators then takes additional effects into account. First, transition radiation is now emitted at both sides of a single radiator. Then, if the spacing between the individual radiators is larger than the formation zone in air the total flux of x-ray photons will be the incoherent sum of the individual fluxes. In addition, absorption of x-ray photons inside the radiator stack has to be considered.

The radiator that was chosen for PEBS, based on the experience with the AMS-02-TRD, is of irregular form. It consists of a fleece made of polypropylene-polyethylene fibres of nominal thickness $10 \mu\text{m}$ that are revealed in a picture taken with an electron microscope (fig. 4.10). Here, transition radiation is emitted at the numerous fibre-air interfaces. The calculation of the transition radiation yield of such a radiator is further complicated by the fact that the thicknesses of the fibres and corresponding air gaps are not constant but follow a given random distribution. This is handled by the Geant4 simulation, as outlined in more detail in section 4.2.8.

Design and implementation in the simulation

The transition radiation detector is based on the one constructed for the AMS-02 experiment [126, 127]. It consists of two parts of eight layers each, located between the tracker layers. Each TRD layer contains a mat of irregular radiator fleece of 20 mm thickness and eight modules of sixteen straw tubes each (figure 4.11) of 868 mm length. The straw tubes contain a thin tungsten wire operated at high voltage and an 80/20 mixture of Xe/CO₂ and they are used to detect both ionisation losses of charged particles and the x-ray tran-

4 Design study for PEBS based on Monte Carlo simulations

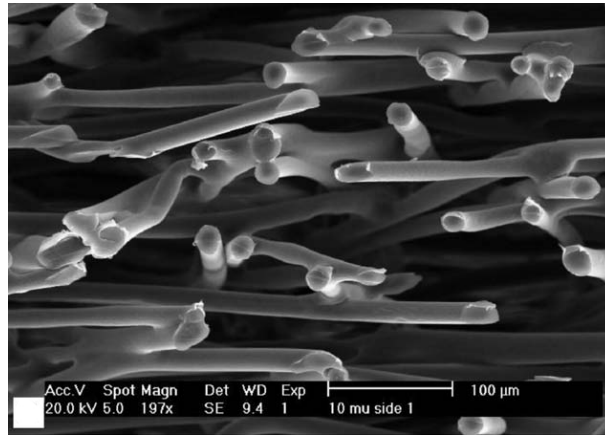


Fig. 4.10: Scanning electron microscope picture of an irregular radiator material: polypropylene fibres (Freudenberg LRP375BK). Reprinted from [132], Copyright 2006, with permission from Elsevier.

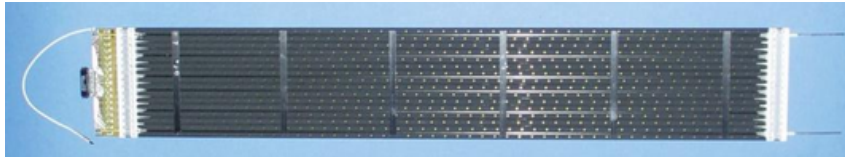


Fig. 4.11: A picture of a TRD straw module used for the AMS-02 experiment.

sition radiation photons created by light particles such as positrons in the fleece radiator. For mechanical stability, longitudinal and lateral carbon-fibre stiffeners are added. The

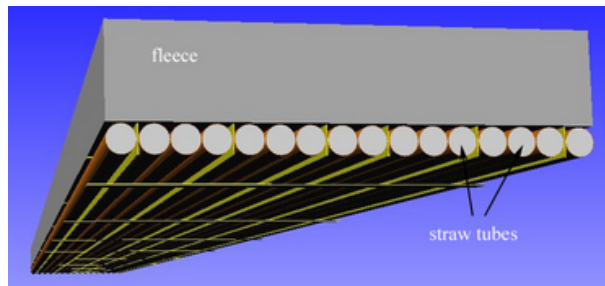


Fig. 4.12: Visualisation of a TRD module in the Geant4 simulation. The radiator fleece, straw tubes, and carbon-fibre stiffeners are visible.

tasks of the TRD are proton suppression and determination of the slope angle λ of tracks. In the simulation (fig. 4.12), the straw tube walls are modelled as tubes of $72 \mu\text{m}$ Kapton, with a tungsten wire of $30 \mu\text{m}$ diameter in the middle. The gas mixture has a density of 4.885 mg/cm^3 . The radiator fleece consists of polypropylene and polyethylene with number ratio 85/15 and has a density of 0.06 g/cm^3 . The performance of the TRD depends on the microscopic properties of the radiator, and section 4.2.8 was devoted to their de-

4.2 Design study for PEBS and implementation in the Monte Carlo simulation

termination and modelling.

The overall material budgets of the tracker and the TRD are calculated to be only 6 % and 5.5 % of a radiation length, respectively.

4.2.7 Physics processes

Geant4 offers a wide variety of physics models for the interactions of the different particle species with the available materials, covering an energy range from 250 eV up to several PeV [107]. In many cases, concurrent or alternative models are available, and it is the user's responsibility to choose the most appropriate set of physics implementations suitable for her application. The choice of models describing hadronic processes is especially large and it ranges from data-driven models to parameterised and theory-driven models, some of them optimised for speed, others for accuracy. In the following, the choice of models for the simulation of the PEBS detector will be outlined briefly and the Geant4 class names employed will be given for reference in those cases where they are not apparent.

For the interactions of γ -rays, the standard photoelectric effect, Compton scattering, and pair conversion are used. Electrons and positrons undergo multiple scattering, ionisation losses, and bremsstrahlung losses. In addition, positrons will annihilate at rest. The standard processes are used throughout, with the important exception of the ionisation losses in the TRD gas mixture. These are described by the photo-absorption ionisation model as implemented in the class `G4PAIModel`. This is important for a proper determination of the TRD proton rejection and is elaborated on in section 4.2.8. The same electromagnetic processes are implemented using the appropriate standard classes for muons, protons, deuterons, tritons, pions, kaons, α -particles, heavier ions, as well as for some more exotic mesons and baryons and their respective antiparticles. A default cut value for the range of secondary particles of 0.5 mm was used throughout the simulation, with the exception addressed in section 4.2.8. For completeness, the more exotic effects of photo-, electro-, and muo-production of hadrons as well as synchrotron radiation are included as implemented in the `G4EmExtraPhysics` class. Particular care has to be taken with the simulation of transition radiation, which remains a challenging task. Section 4.2.8 contains details about the procedure.

The physics of inelastic hadronic interactions is given by the `HadronPhysicsQGSP_BIC` class [128, 129]. It applies a quark-gluon string model for the modelling of interactions of high energy hadrons above 25 GeV. Interactions at intermediate energies are modelled by the low energy parameterised (LEP) model, and below 10 GeV, the Geant4 binary cascade [130] for primary protons and neutrons replaces the LEP model. The binary cascade is used because it promises a better description of the production of secondary particles produced in interactions of protons and neutrons with nuclei. The high energy interaction creates an excited nucleus, which is passed to the Geant4 precompound model modelling the nuclear de-excitation. Nuclear capture of negative particles and neutrons at rest is modelled by the Chiral Invariant Phase Space (CHIPS) model.

Also included are the standard decay physics, hadron elastic scattering, and stopping physics. Ion physics is handled by the `G4IonBinaryCascadePhysics` class.

4.2.8 Adjustment of parameters for the simulation of transition radiation with testbeam data

This section is devoted to a comparison of the transition radiation (TR) and ionisation energy loss distributions obtained from the Monte Carlo simulation based on Geant4 to electron and proton testbeam data [131]. The data were taken with a prototype consisting of 20 layers of fleece radiator and straw tube proportional chambers, filled with Xe/CO₂, during a testbeam conducted in the context of the AMS-02 experiment at CERN in the year 2000. Impressive agreement is found for the simulation of TR for electrons and very good agreement for the ionisation loss distributions for protons over a wide range of incident energies. The implications of slight deviations in the tails of the proton energy loss spectra on calculated proton suppression factors are studied briefly to assess the accuracy of the predictions obtained in this design study. The testbeam data are also used to adjust various parameters of the Geant4 simulation governing the microscopic structure of the radiator fleece. Only few validation studies for Geant4 concerned with transition radiation and ionisation energy losses in thin absorbers have been published so far [133, 134, 135, 136].

Description of the testbeam prototype and simulation

The setup used in the testbeam consisted of prototype modules for the AMS-02-TRD which were grouped in 20 layers (see fig. 4.13). In each module, the TR x-ray photons are generated in a 2 cm thick irregular fleece radiator made of polyethylene and polypropylene, with a density of $\rho = 0.06 \text{ g/cm}^3$. They are subsequently detected in proportional wire chambers in the form of straw tubes made of aluminised kapton foils which have an inner diameter of 6 mm and are filled with an 80 : 20 mixture of Xe/CO₂ at a pressure of $p = 1 \text{ atm}$. The 30 μm gold-plated tungsten wires in the straw tubes were operated at a voltage of 1480 V for a gas-gain of 6000. Temperature and pressure were continuously monitored during the testbeam.

Layers 3, 4, 17 and 18 were rotated by 90° with respect to the others to provide track coordinates in all spatial dimensions. Two towers of modules were put next to each other and staggered by half the thickness of a module.

Protons and electrons were recorded at several energies at the CERN X7 and H6 beamlines in 2000. An extensive description of the testbeam setup is found in [126, 137].

The prototype setup was implemented in a Geant4.8.2 simulation (fig. 4.13). This includes the radiator mats, kapton straw tubes with gas mixture and tungsten wires, and carbon fibre stiffeners, as well as the trigger scintillators and the acryl glass entry window that the beam particles had to traverse. A gas density of $\rho_{\text{Xe/CO}_2} = 4.885 \text{ mg/cm}^3$ was employed. Primary protons and electrons were generated according to the energies chosen and angular distribution measured in the testbeam.

Geant4 offers several physics process classes for the simulated generation of transition radiation photons. They have in common that they are based mainly on the approach of calculating the work done by a relativistic charge crossing the boundary between two media against the electric fields induced by the charge in the vicinity of the boundary [135]. The classes available include models with fixed and gamma-distributed radiator foil and

4.2 Design study for PEBS and implementation in the Monte Carlo simulation

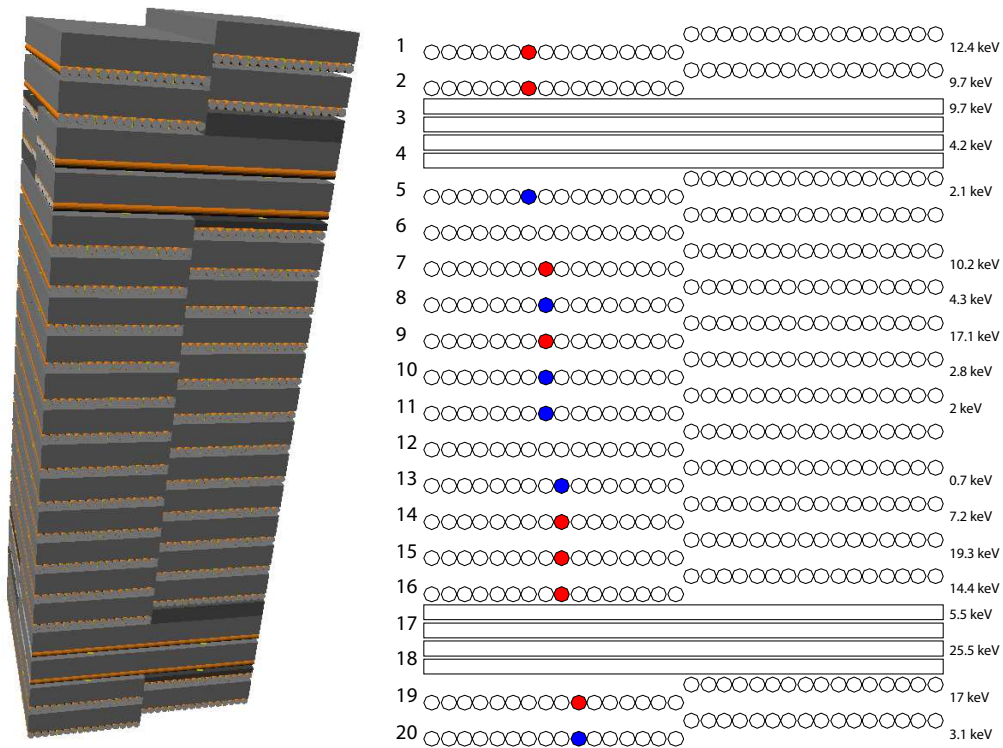


Fig. 4.13: (left) Visualisation of the testbeam prototype in the Geant4 simulation. The staggered modules and rotated layers are visible, complete with radiator fleece stacks, gas-filled straw tubes and carbon stiffeners. (right) Schematic drawing of an electron event in a front view of the prototype. Several high energy depositions (> 6.5 keV) along the track are characteristic of an electron.

4 Design study for PEBS based on Monte Carlo simulations

gas thicknesses, as well as a model for the simulation of additional TR photons generated in straw tube walls. In the first case, both a model with TR photon absorption taken into account and a simplified transparent version are available.

The appropriate model for the irregular fleece radiator employed in the testbeam setup is the `G4GammaXTRadiator` [138]. In this model, the fleece fibre and gas thicknesses z are assumed to vary according to the distribution [136]

$$p_j(z) = \left(\frac{\alpha_j}{\bar{z}_j}\right)^{\alpha_j} \frac{z^{\alpha_j-1}}{\Gamma(\alpha_j)} \exp\left(-\frac{\alpha_j z}{\bar{z}_j}\right) \quad (4.29)$$

where \bar{z}_j is the mean thickness of the j -th medium in the radiator and the α_j parameters describe the relative thickness fluctuations δ_j which are found to be

$$\delta_j = \frac{\sqrt{\langle(z_j - \bar{z}_j)^2\rangle}}{\bar{z}_j} = \alpha_j^{-1/2} \quad (j = 1, 2) \quad (4.30)$$

The signal detected in the straw tubes is the sum of those from absorbed TR x-ray photons and the ionisation losses of the primary particle. The standard electromagnetic processes in Geant4 fail to reproduce the energy loss spectra in thin absorbers, such as the straw tube gas mixture. Instead, the photo absorption ionisation (PAI) model [139] as implemented in Geant4 [133] is used.

It should be stressed that the Geant4 processes were applied as-is, i.e. no modifications (“tuning”) of any kind were made. Only the simulation parameters related to the microscopic structure of the radiator need to be chosen.

A description of the raw data processing procedure is given in [126]. Once energy calibration and gas density dependent gas gain corrections have been performed, a track fit is done to select clean single-track events, and the energy depositions for each layer along the track are stored for further analysis.

Adjustment of parameters for the simulation of transition radiation

The simulation results depend on a number of parameters, some of which are known, e.g. the gas density ρ and number fraction n_{Xe} of xenon, while others have to be determined from a fit to the data. In particular, the structure of the radiator fleece mats is for a given density determined by the mean fibre diameter \bar{z}_1 and the fluctuation parameters $\alpha_{1,2}$ of the fibres and gas in the radiator, respectively.

The parameters are obtained from a χ^2 -minimisation procedure as follows. First of all, MC and data electron spectra are normalised with respect to each other, taking only the energy interval [$E_{\text{min}} = 0.5$ keV; $E_{\text{max}} = 20$ keV] into account. This eliminates the influence of artefacts in the data, namely inefficiencies of the straw tubes (at low energies) and cutoff values introduced by the ADCs employed (at high energies). The χ^2 is then calculated from the error-weighted quadratic sum of the MC-data differences over all layers and all

4.2 Design study for PEBS and implementation in the Monte Carlo simulation

energy bins within the interval quoted above:

$$\chi^2 = \sum_{E_j \in [E_{\min}, E_{\max}]} \frac{(F_{i,j}^{\text{MC}} - F_{i,j}^{\text{data}})^2}{\sigma_{\text{data},i,j}^2 + \sigma_{\text{MC},i,j}^2} \quad (4.31)$$

where i numbers layers, E_j is the j -th energy bin, $F_{i,j} \equiv (dN/dE)_{i,j}$ and the errors are approximated by $\sigma_{i,j} = N_i^{-1} \cdot \sqrt{\Delta N_{i,j}}$ in the usual way. Here, N_i is the normalisation factor for layer i and the $\Delta N_{i,j}$ are the raw counts.

Because the fibre thickness fluctuation parameters $\alpha_{1,2}$ are unknown, first the nominal value of $\bar{z}_1 = 10 \mu\text{m}$ is assumed and χ^2 is calculated for simulation results in the (α_1, α_2) -plane. Figure 4.14 shows the result as a contour plot. Plotted is the value χ^2/n where n is

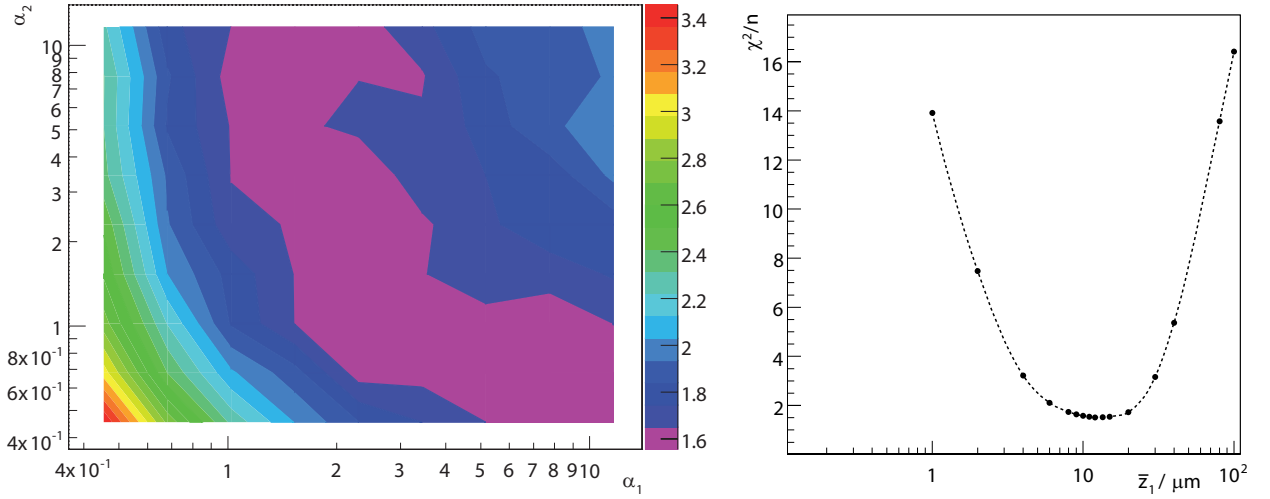


Fig. 4.14: Left: χ^2/n values from variation of α_1 and α_2 . A minimum is found at $(5, \frac{2}{3})$. Right: χ^2/n values from variation of \bar{z}_1 . The nominal value is $\bar{z}_1 = 10 \mu\text{m}$.

the total number of energy bins used. A minimum is found at roughly $\alpha_1 = 5$ and $\alpha_2 = \frac{2}{3}$. As can be seen from the figure, the quality of the match does not depend too sensitively on the chosen values as the region with values close to the minimum is quite large, spanning almost a decade. The quoted values for $\alpha_{1,2}$ are fixed, and \bar{z}_1 is subsequently varied. The resulting χ^2/n -plot is depicted in figure 4.14. A minimum is found at $\bar{z}_1 = 12 \mu\text{m}$ which is in good agreement with the nominal value.

Comparison of TR spectra

With all parameters set to the optimised values derived above, the electron spectra obtained from data and simulation can be compared. Figures 4.15, 4.16 and 4.17 show data and simulation spectra for layers 1, 3 and 5, respectively. These layers were chosen because an incoming particle had to traverse different amounts of radiator fleece material before entering each of these (cf. fig. 4.13). Only half a layer of fleece was present in front of layer 3 for the events considered here, while the fleece in front of layer 5 had 1.5

4 Design study for PEBS based on Monte Carlo simulations

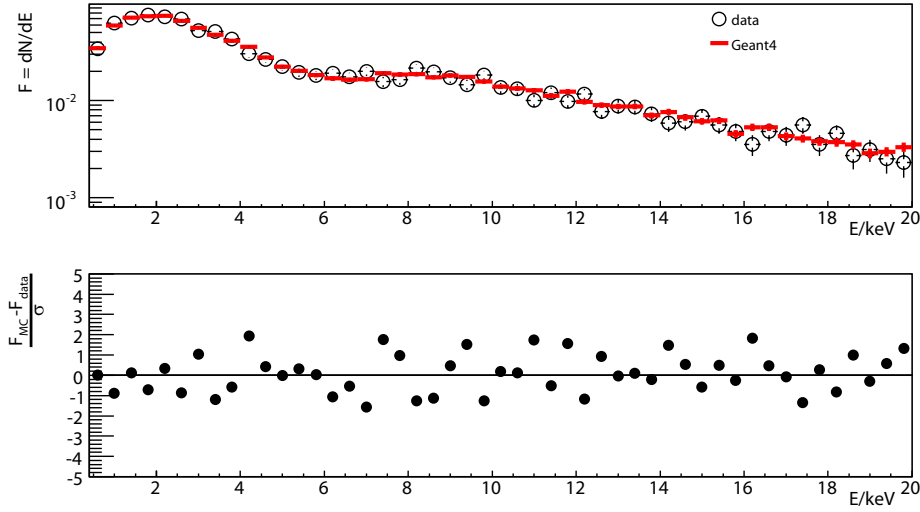


Fig. 4.15: Ionisation loss and transition radiation spectra from data and Geant4 simulation, for 20 GeV electrons, in layer 1 of the prototype (*top*) and corresponding residual plot (*bottom*).

Here, $\sigma = \sqrt{\sigma_{\text{data}}^2 + \sigma_{\text{MC}}^2}$.

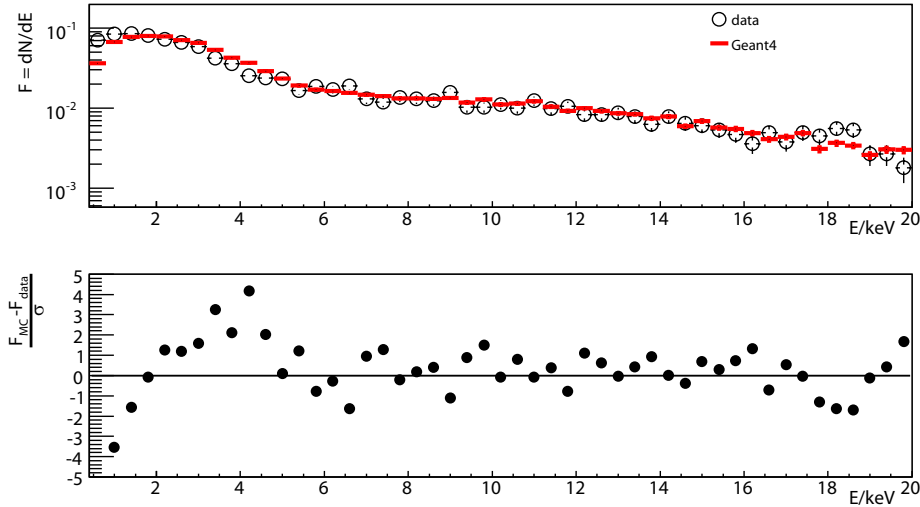


Fig. 4.16: Ionisation loss and transition radiation spectra from data and Geant4 simulation, for 20 GeV electrons, in layer 3 of the prototype (*top*) and corresponding residual plot (*bottom*).

times the usual thickness. The agreement between data and simulation spectra is very good. This can also be seen from the residual plot in figure 4.18 showing a histogram of all values of $\frac{F_{i,j}^{\text{MC}} - F_{i,j}^{\text{data}}}{\sigma_{i,j}}$, where $\sigma_{i,j} = \sqrt{\sigma_{\text{data},i,j}^2 + \sigma_{\text{MC},i,j}^2}$, from all layers and bins within the threshold interval. They follow a Gaussian distribution with mean and RMS values of 0.02 and 1.1. Figure 4.19 shows the mean energy deposition for data and simulated electrons of 20 GeV. The good description of the TR yield in each layer is illustrated here. The deviation of the simulation from the data is below the layer-to-layer variation in the

4.2 Design study for PEBS and implementation in the Monte Carlo simulation

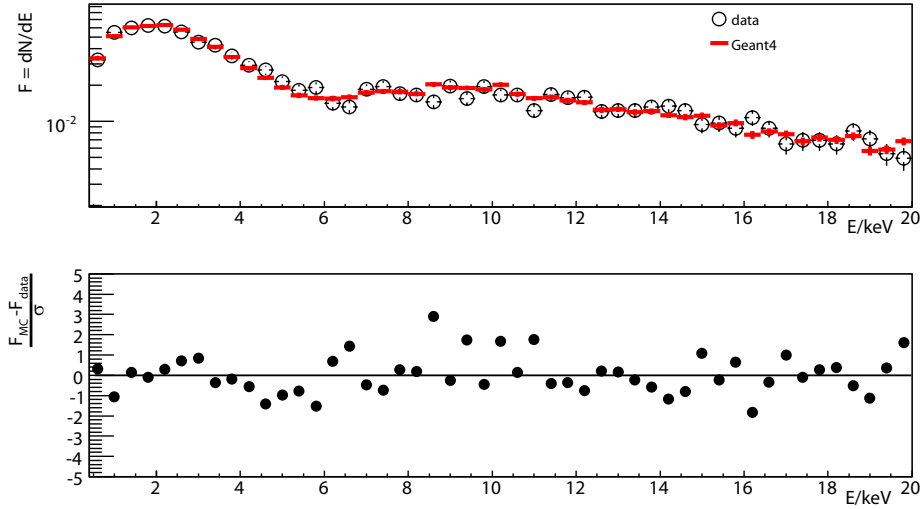


Fig. 4.17: Ionisation loss and transition radiation spectra from data and Geant4 simulation, for 20 GeV electrons, in layer 5 of the prototype (*top*) and corresponding residual plot (*bottom*).

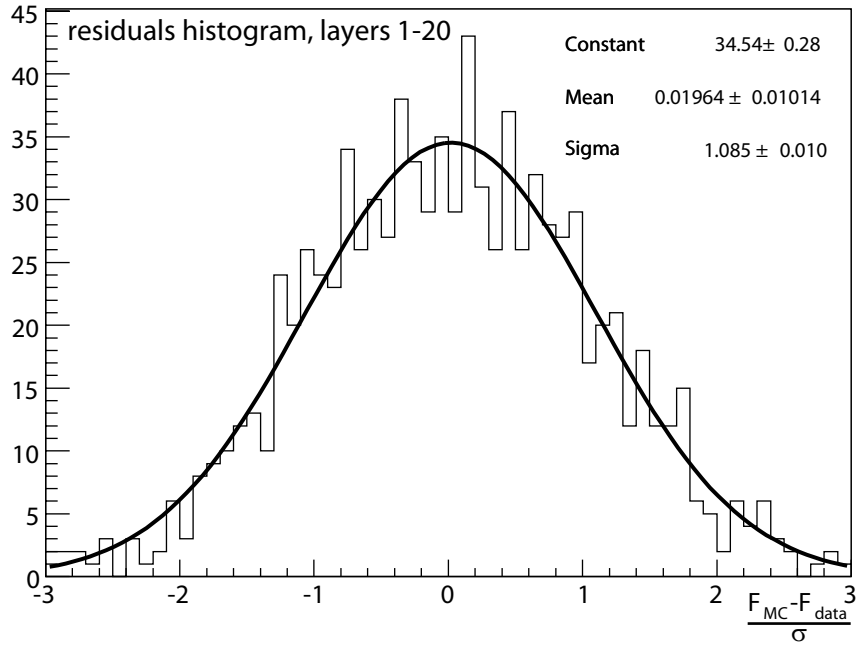


Fig. 4.18: Histogram of residuals for electron spectra, containing energy bins from all layers.

data. Both the effect of the slope towards saturation in the first layers as the effect of varying radiator thickness around the rotated layers 3, 4, 17, 18 are well reproduced.

Comparison of proton energy loss spectra

For studies of the proton rejection power of a TRD, the ionisation energy loss spectra for protons must be reproduced accurately by the simulation. Figures 4.20 and 4.21 show the

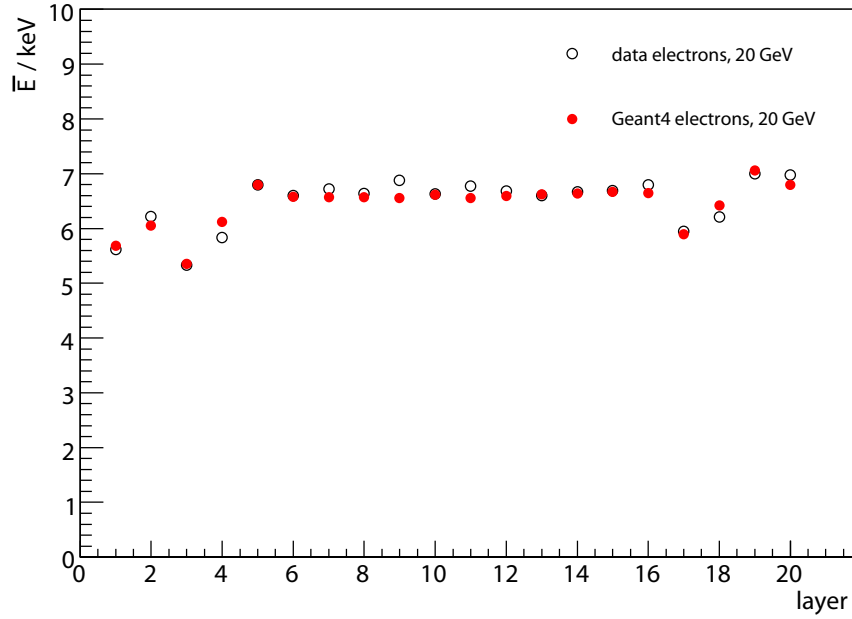


Fig. 4.19: Mean electron energy deposition as a function of layer number, for data and simulation.

spectra for data and for simulated protons of 20, 60 and 200 GeV, respectively. All layers have been included because the energy deposition is independent of the layer number for protons. The range cut, employed in Geant4 to determine the production of secondary particles, was set to 10 mm, larger than the diameter of the straw tubes. Reducing this value unexpectedly worsens the agreement of simulation and data. This might point to a problem in the handling of knock-on electrons in the PAI model employed. While the overall agreement for lower tube energies is good, the figures show an underestimation of energy depositions above roughly 12 keV in the Geant4 simulation, on the order of 25%.

Proton rejection study

An important figure of merit of a transition radiation detector is its proton rejection R_p for a certain electron efficiency ϵ_e . Here, $R_p \equiv 1/P(e|p)$ where $P(e|p)$ is the probability for a proton to be misidentified as an electron, when satisfying the selection criteria that a fraction ϵ_e of the single-track electrons survive.

The likelihood method is a simple way to determine the proton rejection. From the single-layer energy depositions $(E_k)_{k=1}^{20}$, the likelihoods for an event to be proton- or electron-like are calculated as the geometric means $\bar{P}_{p,e} = \sqrt[20]{\prod_{k=1}^{20} P_{p,e}(E_k)}$, where the single-layer probabilities $P_{p,e}$ are taken from the normalised mean respective spectra. The event is then classified as an electron if $-\log(L) \equiv -\log(\bar{P}_e/(\bar{P}_e + \bar{P}_p))$ is below a certain cut. Protons that are misidentified as electrons by this method can be divided into two categories. This is illustrated in figure 4.22 showing as an example the $-\log(L)$ -distributions obtained for testbeam data of 200 GeV protons and 20 GeV electrons. The first and most important category of misidentified protons comprises protons with several

4.2 Design study for PEBS and implementation in the Monte Carlo simulation

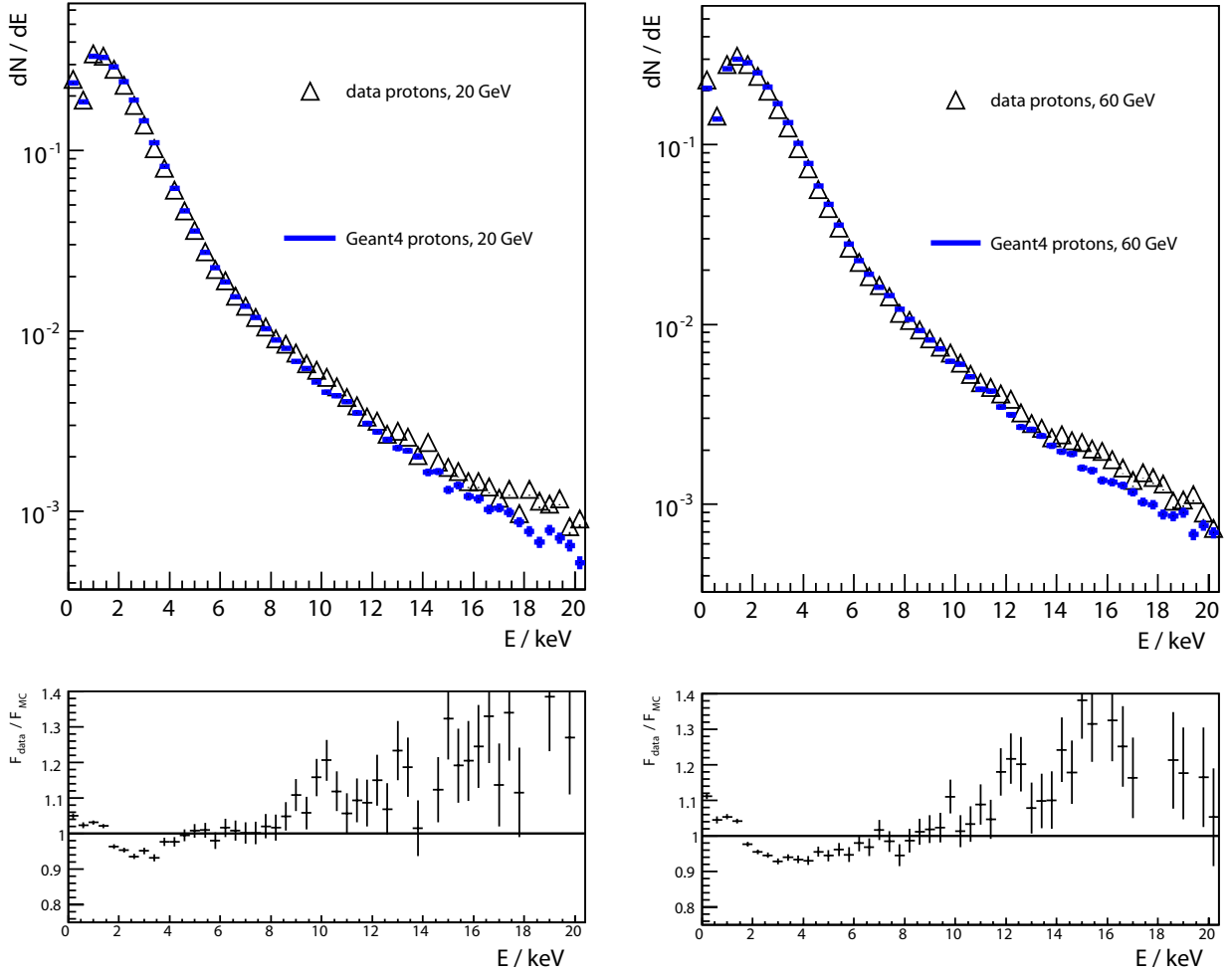


Fig. 4.20: Top: Ionisation energy loss spectrum from all layers for 20 GeV (left) and 60 GeV (right). Bottom: Corresponding ratio of spectrum from testbeam data to Geant4 spectrum.

high energy depositions on their track which are due to the statistical fluctuations in the energy loss. This effect can be evaluated by a simple toy Monte Carlo (“toy MC”) study as follows: Energy depositions $(E_k)_{k=1}^{20}$ are generated randomly according to the mean normalised spectra obtained from testbeam data, as shown in the preceding sections. This procedure is repeated N times. The $-\log(L)$ -values obtained in this way are also drawn in figure 4.22. Comparing their distribution to the data reveals the second category of misidentified protons: events with a small $-\log(L)$ -value ($-\log(L) \lesssim 0.55$) that is clearly in the electron-like region. Such events are extremely unlikely to arise from statistical fluctuations. Instead, they indicate the presence of particles other than protons, e.g. secondaries arising from interactions in the material traversed or from beam contamination. For example, an incident proton can transfer a high amount of energy to an atomic electron which in turn flies almost parallel to the path of the primary. This leads to an event with high energy depositions in almost every layer and subsequently an electron-like value of $-\log(L)$. The electron contamination of the proton beam de-

4 Design study for PEBS based on Monte Carlo simulations

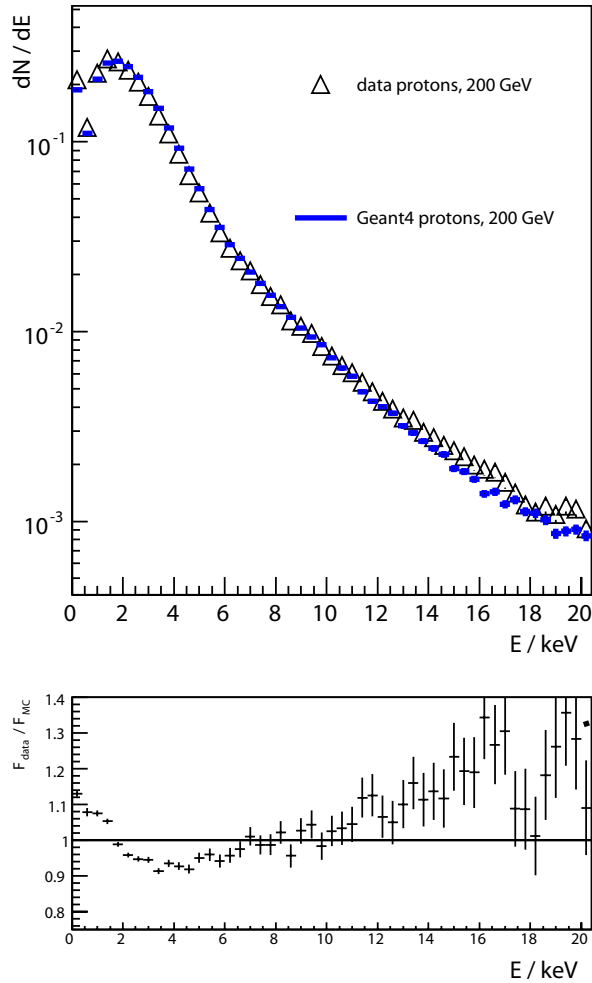


Fig. 4.21: *Top:* Ionisation energy loss spectrum from all layers for 200 GeV protons. *Bottom:* Corresponding ratio of spectrum from testbeam data to Geant4 spectrum.

depends strongly on energy but remains below the order of 10% [140]. This number was further reduced by using Cherenkov counters to veto on fast particles like electrons in the testbeam. Their inefficiency has been estimated to be 1.15‰ [137]. Therefore, the contamination of the proton sample will only play a minor role.

On the other hand, there is a number of electron events in the $-\log(L)$ -region characteristic of protons ($-\log(L) \gtrsim 0.9$) that is not accounted for by statistical fluctuations in the energy deposition. As the corresponding energy depositions along the track are *lower* than expected in this case, it is clear that this component cannot be due to additional particles. Instead, it must be caused by contamination with relativistic particles with low TR yield, such as protons, muons, pions or kaons. From fig. 4.22 this contamination is estimated to be of the order of a few‰.

In the context of this thesis, it is interesting to quantify the effect of the observed slight deviations in the tails of the Geant4 proton energy loss distributions on calculated proton rejections. To that end, two toy MC studies have been conducted as described above,

4.2 Design study for PEBS and implementation in the Monte Carlo simulation

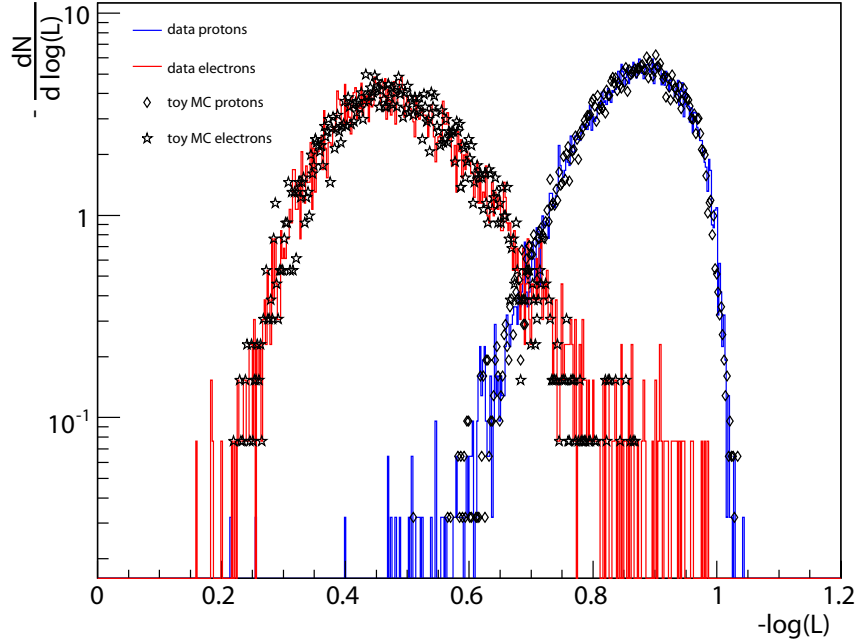


Fig. 4.22: Log-Likelihood distributions for 200 GeV protons and 20 GeV electrons. The results of the toy MC study described in the text are added to estimate the distributions expected for purely statistical fluctuations of the energy loss.

one using the spectra obtained in the testbeam, the other using the Geant4 spectra. This was repeated for various incident proton energies. Spectra for 20 GeV electrons, where the TR yield is in saturation, were used as reference. The resulting proton rejections are depicted in the left-hand side of figure 4.23, each for an electron efficiency of 90%. The rejections obtained in the two cases differ by roughly a factor of two. However, the right-hand side of the figure demonstrates the very steep dependence of the proton rejection on the corresponding electron efficiency. The observed difference in rejection translates into a difference in electron efficiency of $\sim 2.5\%$ at $\epsilon_e \sim 0.9$. These curves offer a more complete picture of the discrepancy between testbeam data and Geant4 proton spectra than the rejection value at a fixed electron efficiency.

Figure 4.23 also shows the proton rejections obtained when taking the actual E_k values from testbeam data or simulated events. They are lower than the rejections calculated for the respective toy MCs. This is due to a contribution from events belonging to the second category introduced above. The difference is larger in the case of the data than the Geant4 simulation. While this might be due to inaccurate cross sections in the simulation, the beam contaminations mentioned above prevent us from drawing such a conclusion. To summarise, while slight deviations in the tails towards higher energy depositions in the proton spectra prevent us from accurately predicting the behaviour of the TRD with respect to proton suppression, a good picture of the overall performance can be obtained. The parameters describing the microscopic structure of the fleece radiator that were found to give the best description of the electron spectra in this section are used throughout this design study.

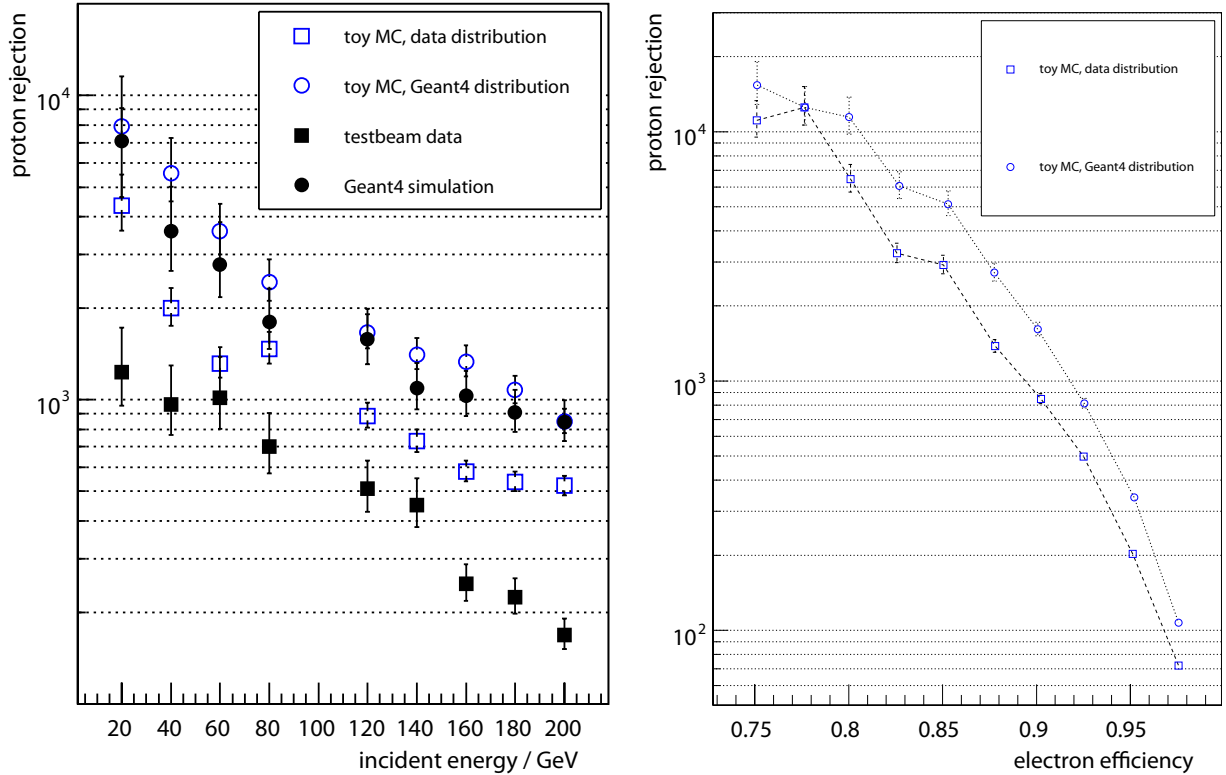


Fig. 4.23: *Left:* Proton rejection for various energies of the incident protons, at a corresponding electron efficiency of 90 %. The results of the toy MC study are used to evaluate the effect of the observed slight deviations in the tails of the Geant4 proton energy loss distributions with respect to the testbeam data, reducing the sensitivity to beam contaminations and other systematic effects as far as possible. The proton rejections obtained when taking the actual E_k values from testbeam data or simulated events are shown, too. *Right:* Proton rejection as a function of electron efficiency, for incident protons of 120 GeV, in the context of the toy MC study described in the text, for the distributions obtained from testbeam data and Geant4 simulation.

4.3 Event reconstruction

The events produced by the simulation only contain raw information, such as amplitude and position, for the hit channels in the various subdetectors. In addition, information about the primary and secondary tracks exceeding a momentum of 100 MeV and created above the ECAL, is included. Before one can use these events to study the behaviour of the detector, higher-level objects have to be created that represent pictures of the particles as seen by the subdetectors. For the tracker and the TRD, tracks have to be found and their curvature and orientation have to be determined to yield the particle's momentum. In the calorimeter, a shower has to be identified and the shower orientation and parameters can then be retrieved. In general, one is interested in clean single-track events, which offer the best prospects for unambiguous particle identification.

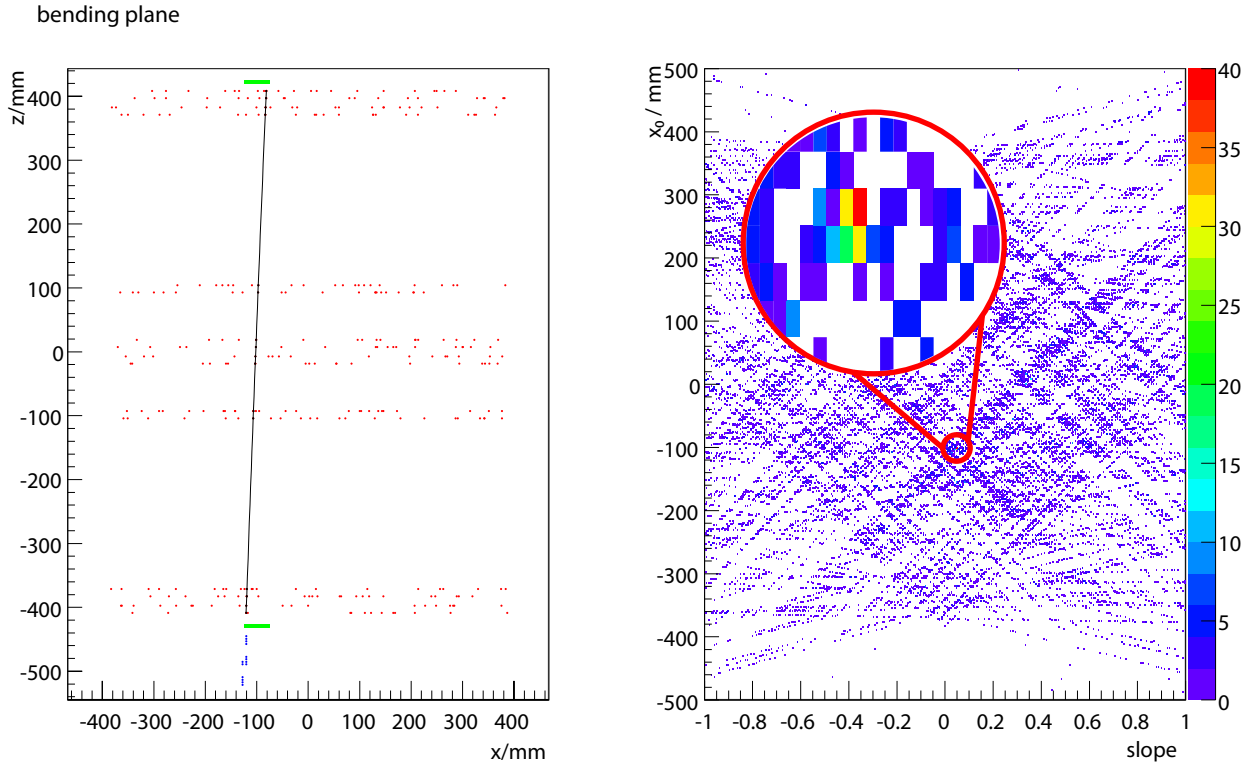


Fig. 4.24: *Left:* Example of a 20 GeV proton track, for an average noise level of 0.24 photons in the tracker. Tracker hits are marked in red, ECAL hits in blue, and TOF hits in green. *Right:* Histogram used for track finding. The clearly discernible maximum in the x_0 -slope-plane corresponds to the track corridor.

In a first step, a track in the TRD is identified as follows. First, a seed track is created from the digis on those layers with exactly one digi. This seed track is then interpolated and additional digis within one tube diameter from the seed track are added. This simple algorithm works because the noise level in the TRD is expected to be low.

In the second step, clusters of neighbouring SiPM channels are identified in the tracker and for the subsequent track finding and fitting, the position is calculated from a weighted mean of the amplitudes A_i :

$$\vec{x} = \frac{\sum_i A_i \vec{x}_i}{\sum_i A_i} \quad (4.32)$$

The SiPMs to be employed in the tracker are noisy to a certain extent. Therefore, a track finding algorithm had to be developed to reliably find tracks even in the presence of noise hits. The idea for the approach adopted here is inspired by the Hough transform [141], and the algorithm proceeds as follows:

- For each *pair* of tracker clusters, calculate the intercept and slope for the straight line defined unambiguously by the two clusters, and fill the resulting values into a two-dimensional histogram. The idea here is that a track can be approximated

4 Design study for PEBS based on Monte Carlo simulations

by a straight line to first order. This means that all pairs of clusters lying on the track will give the same slope and intercept. On the other hand, a pair of clusters containing a noise cluster will only rarely lead to a given value of slope and intercept.

- Find the maximum bin in the histogram obtained in this way and calculate the corresponding straight line. Loop the tracker layers adding the cluster nearest to the straight line, provided the distance does not exceed a maximum value. An example of the histogram in the intercept-slope-plane obtained for an event simulated with a mean noise level of 0.24 photons is shown in figure 4.24.
- Find outliers in the candidate track. This is done both by using a robust circle fit provided by Blobel [142] to identify outliers, and by looking for clusters whose removal from the candidate track leads to a significantly reduced χ^2 in a circle fit.
- Because a χ^2 fit prefers a low number of clusters on the track, a single noise cluster will sometimes be chosen instead of a segment of the real track on the outer tracker superlayers. This situation is remedied by looking for a segment of clusters on the uppermost and lowermost layers, respectively, with similar slope as the candidate track's. The single cluster is replaced by the clusters of the segment so obtained if the inclination of each pair that can be formed from its clusters matches the one of the candidate track.
- A final track fit is then performed. A circle fit is done for the tracker clusters in the bending plane to obtain the curvature, while a line fit is performed for the TRD hits to get the inclination angle λ . The rigidity is then calculated according to eq. (4.3).

It turns out that a good determination of the charge sign of a particle (sec. 4.4.1) can only be achieved if care is taken to identify events in which an incoming electron or positron radiates a hard bremsstrahlung photon which subsequently undergoes pair creation inside or above the tracker volume. Typically, additional track segments close to the primary track will be present in the lower quarter of the tracker in this case. If the track finding algorithm chooses clusters from a segment belonging to one of the secondaries, the ensuing determination of the momentum will be incorrect (fig. 4.25). The algorithm for finding additional track segments is similar to the one used for track finding. After the clusters belonging to the primary track have been removed from the sample, line segments on the lowest four tracker layers are searched in the vicinity of the track, by looking for peaks in a slope-intercept-histogram calculated from each pair of clusters.

In the third step, a possible shower in the electromagnetic calorimeter is identified. First, the shower axis is reconstructed. To this end, the total amplitude in each ECAL layer is calculated. Then, two robust straight line fits with equal weights are performed separately for the xz - and yz -projections of the shower to determine the shower axis. The vertical shower profile dE/dz is then calculated to determine the shower shape and energy variables as follows.

Starting from (4.14) and for perpendicular incidence, the energy deposition $\Delta E(z)$ in a

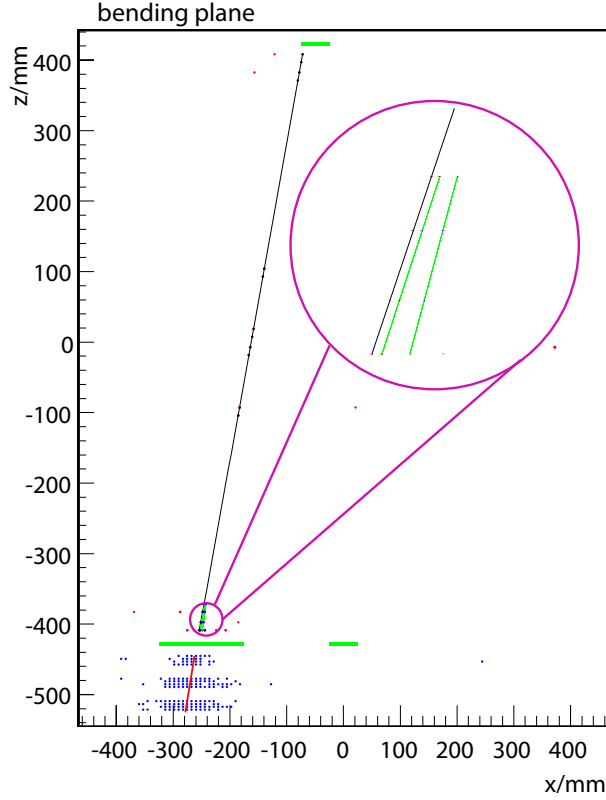


Fig. 4.25: Example of an event with additional track segments caused by secondaries created by a hard bremsstrahlung photon. The event information is drawn in the same way as in fig. 4.24. Here, a 100 GeV positron radiates a photon of 19.9 GeV inside the upper TOF system and the photon in turn converts to an e^+e^- -pair inside the lower TRD. The resulting three-prong signature on the lowest tracker layers is magnified. Additional track segments identified by the algorithm described in the text are shown in green. The primary positron was misreconstructed as having a momentum of -45.9 GeV in this event.

layer at position z is given by

$$\Delta E(z) = E_0 \frac{(bz)^{a-1} e^{-bz}}{\Gamma(a)} b \Delta z \quad (4.33)$$

The goal of the following is to extract the shower energy E_0 and the shower shape parameters a and b . The scale of the shower development is given by b , and a then determines the position of the shower maximum (eq. (4.15)).

For an ideal calorimeter of infinite length, E_0 is given by

$$\int_0^{\infty} \frac{\Delta E}{\Delta z}(z) dz = E_0$$

4 Design study for PEBS based on Monte Carlo simulations

For the PEBS calorimeter with its limited depth z_m , leakage effects have to be taken into account. In fact,

$$\frac{1}{E_0} \int_0^{z_m} \frac{\Delta E}{\Delta z}(z) dz = \int_0^{bz_m} \frac{x^{a-1} e^{-x}}{\Gamma(a)} dx = \gamma_p(a, bz_m) \quad (4.34)$$

Here, γ_p denotes the incomplete Gamma function. It can be calculated numerically and is included in standard computer libraries such as the GNU scientific library [143]. From (4.34), E_0 can be calculated if a and b are known. For their determination, the first two moments $m_{1,2}$ of the vertical shower distribution are calculated,

$$m_i = \frac{\int_0^{z_m} z^i \frac{\Delta E}{\Delta z}(z) dz}{\int_0^{z_m} \frac{\Delta E}{\Delta z}(z) dz} \quad (4.35)$$

The calculation gives

$$m_1 = \frac{a}{b} \frac{\gamma_p(a+1, bz_m)}{\gamma_p(a, bz_m)} \quad \text{and} \quad m_2 = \frac{a(a+1)}{b^2} \frac{\gamma_p(a+2, bz_m)}{\gamma_p(a, bz_m)} \quad (4.36)$$

For each event, the moments $m_{1,2}$ are calculated using the definition (4.35) and a and b can then be extracted using an iterative solution of (4.36), starting from the zeroth-order equations

$$m_1 = \frac{a}{b} \wedge m_2 = \frac{(a+1)a}{b^2} \quad \Rightarrow \quad b = \frac{m_1}{m_2 - m_1^2} \wedge a = bm_1 \quad (4.37)$$

Using these starting values for a and b , the incomplete Gamma functions in (4.36) can be calculated and better values of a and b can be obtained. The iteration is continued until convergence is reached.

In order to compare showers of different angles of inclination, the shower development is better described using the radiation length as the scale. From inspection of eq. (4.14), this can simply be achieved by introducing a new scale parameter \hat{b} and requiring scale invariance

$$\hat{b}t = bz \quad (4.38)$$

Introducing the effective radiation length per absorber layer $w \equiv \Delta t/\Delta z = (d/X_0)/\cos \lambda$, where d is the thickness of an absorber layer, one gets

$$\hat{b} = \frac{b}{w} = \frac{b}{d/X_0} \cos \lambda \quad (4.39)$$

a and \hat{b} are stored for further analysis. It turns out that the determination of the shower parameters using this method of moments is more stable and reliable than a fit of the longitudinal shower profile (fig. 4.26). To give an example, the energy resolution for 200 GeV positrons is found to be 6.5 % for the method of moments, but only 8.3 % for the shower fit. The method of moments has the additional advantage that no statistical errors of the individual energy depositions are required as for a fit based on χ^2 minimisation.

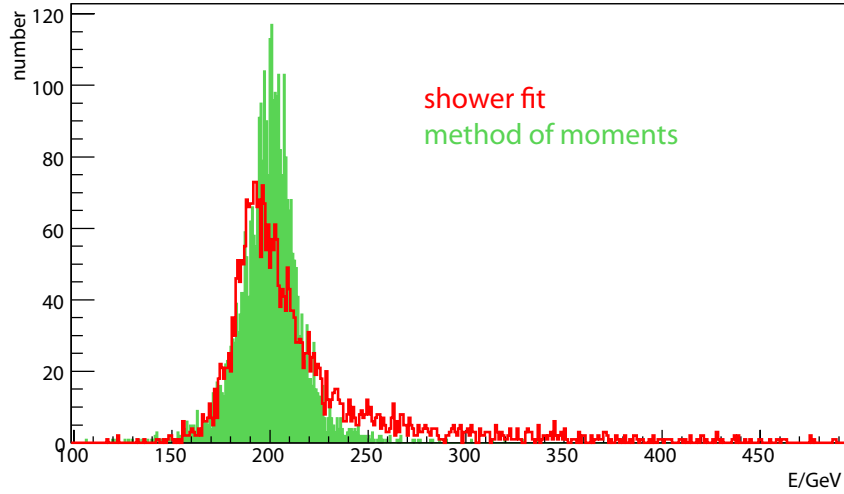


Fig. 4.26: Comparison of reconstructed ECAL energies for 200 GeV positrons, calculated by the method of moments and obtained from a fit of the shower profile (4.14).

4.4 Projected performance

This section deals with the performance of the tracker, electromagnetic calorimeter, and transition radiation detector, as predicted by the Geant4 Monte Carlo simulation described above. The results presented here were obtained using a dedicated analysis suite which works with the reconstructed objects that were found as outlined in section 4.3.

4.4.1 Momentum resolution

The key figure of merit for the tracker is its momentum resolution. The momentum resolution is directly related to the error in the curvature measurement by equations (4.3) and (4.4). The results in this section were obtained using a noise level of zero for the tracker. The effective coupling efficiency (eq. (4.9)) was adjusted such that the mean cluster amplitude is close to 10 photons, in accordance with the preliminary testbeam results found in section 5.2. This is illustrated in figure 4.27 showing both the amplitude distribution of the SiPM array channels individually and the summed cluster amplitudes in the tracker. In the former, the auto-calibrating capability of SiPMs is apparent from the individually resolved first photo-peaks. The Gaussian smearing of the photo-peaks mentioned in section 4.2.3 is visible, too. In the latter, the mean cluster amplitude of roughly 10 photons is demonstrated.

A number of track quality cuts was applied before considering an event for the analysis of the momentum resolution. A minimum number of eleven clusters (figure 4.28) and a minimum track length of 750 mm were required for the track to ensure a sufficient lever arm for the momentum measurement. Events containing additional track segments in the lower quarter of the tracker, possibly caused by secondaries, were discarded. Furthermore, tracks with $\chi^2 > 150$ for the track fit were discarded. The χ^2 distribution is shown in figure 4.28 before the cut was applied. A high value of the χ^2 hints at the inclusion of a

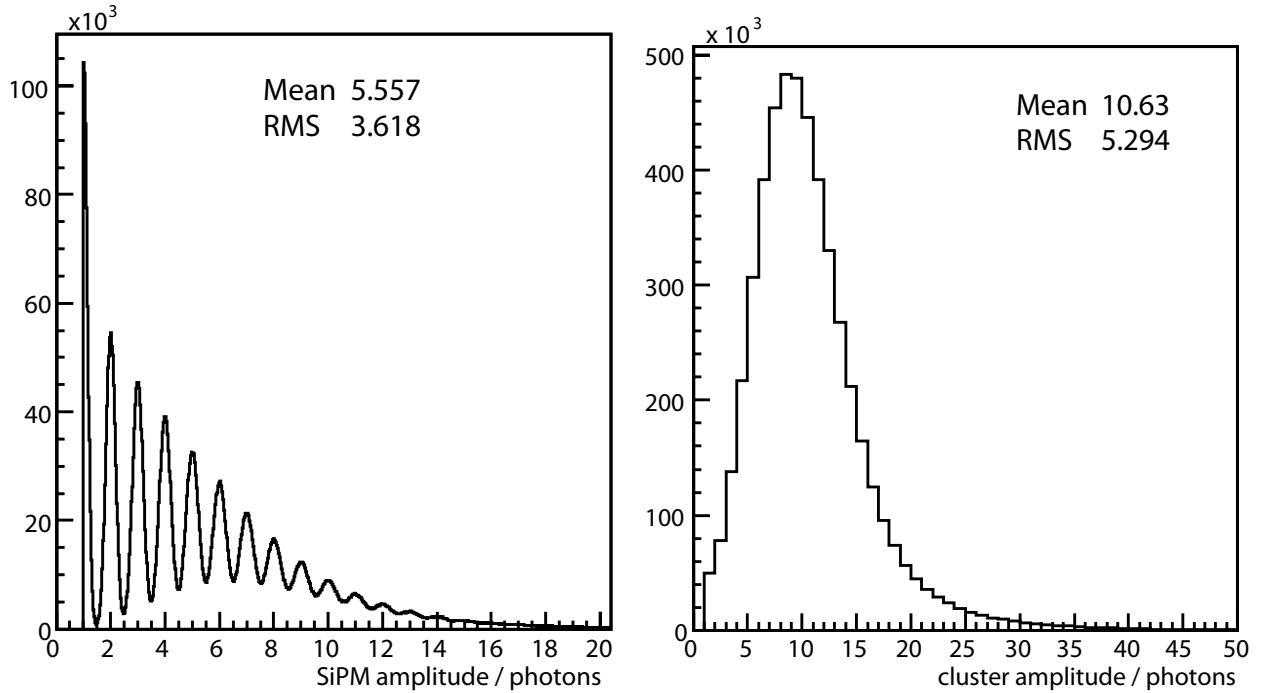


Fig. 4.27: *Left:* Distribution of amplitudes (in photons) on all SiPM channels belonging to reconstructed proton tracks. *Right:* Distribution of cluster amplitudes (in photons) for reconstructed proton tracks.

spurious hit in the track which usually leads to a wrong momentum determination. For the determination of the momentum resolution, the quantity p_{MC}/p_{rec} was then histogrammed versus p_{MC} for simulated events. Here, p_{MC} is the generated momentum of a particle and p_{rec} is its reconstructed momentum. p_{MC}/p_{rec} is the appropriate quantity because the distribution of the curvature is approximately Gaussian. For each bin in p_{MC} , the resulting distribution is then fit by a Gaussian to obtain the mean and standard deviation. These two values are shown in figure 4.29 as a function of p_{MC} and separately for three particle species, positrons, protons, and muons. The mean $\langle p_{MC}/p_{rec} \rangle$ is close to one for muons and protons while it deviates from one by a few percent in the case of positrons showing that p_{rec} serves as a good, unbiased estimator for the true momentum. The momentum resolution $\sigma(p_{MC}/p_{rec})$ is slightly different for the three species. Muons have the cleanest signature and for all practical purposes do not interact inside the tracker. In general, protons also produce clean signatures but occasional interactions lead to a small deterioration of the momentum resolution. For positrons, both $\langle p_{MC}/p_{rec} \rangle$ and $\sigma(p_{MC}/p_{rec})$ suffer from bremsstrahlung losses inside the tracker volume. This effect is illustrated in figure 4.30. There, the quantity

$$y \equiv \frac{\sum_{\text{tracker}} p_{\gamma}}{p_{MC}}$$

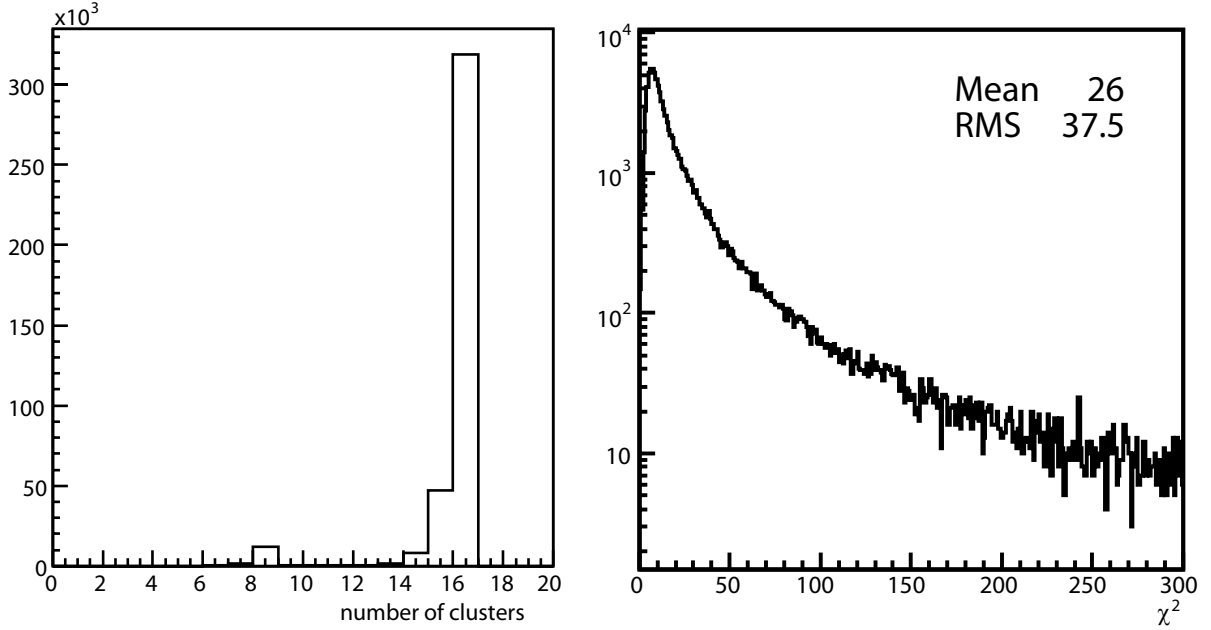


Fig. 4.28: *Left:* Distribution of number of cluster in tracker track. The number of layers is 16. Occasionally, tracks with clusters located only on the eight central tracker layers are found for low-energetic events ($\lesssim 3$ GeV) because the track-finding algorithm is optimised for high-momentum tracks. *Right:* Distribution of χ^2 -values for track fits, for positrons of all energies. A quality cut is done at $\chi_{\text{cut}}^2 = 150$.

i.e. the fraction of momentum radiated away as bremsstrahlung, is plotted as a function of $x \equiv p_{\text{MC}}/p_{\text{rec}}$. For the extreme case that the error in reconstructed momentum is given by the bremsstrahlung losses, one obtains

$$x = \frac{p_{\text{MC}}}{p_{\text{rec}}} = \frac{p_{\text{MC}}}{p_{\text{MC}} - \sum p_{\gamma}} = \frac{p_{\text{MC}}}{p_{\text{MC}} - y p_{\text{MC}}} \Rightarrow y = 1 - \frac{1}{x} \quad (4.40)$$

The concentration of events between the line $p_{\text{MC}}/p_{\text{rec}} = 1$ and this curve in figure 4.30 demonstrates the importance of the bremsstrahlung losses.

Bremsstrahlung losses also cause non-Gaussian tails in the distribution of the reconstructed momenta. These are not taken into account by the Gaussian fits which is justifiable by the fact that the energy measurement in the calorimeter will be used to filter events with large bremsstrahlung losses.

According to equations (4.3) and (4.4), the momentum resolution can be parameterised as

$$\sigma \left(\frac{p_{\text{MC}}}{p_{\text{rec}}} \right) = a_{\text{msc}} \oplus b_{\text{res}} \cdot p_{\text{MC}} \quad (4.41)$$

where $a \oplus b \equiv \sqrt{a^2 + b^2}$. The parameter a_{msc} reflects the contribution from multiple scattering and dominates at low energies. The parameter b_{res} describes the uncertainty arising from the limited position resolution and is the dominating term at high energies. The momentum resolution shown in figure 4.29 is fitted to eq. (4.41), separately for the

4 Design study for PEBS based on Monte Carlo simulations

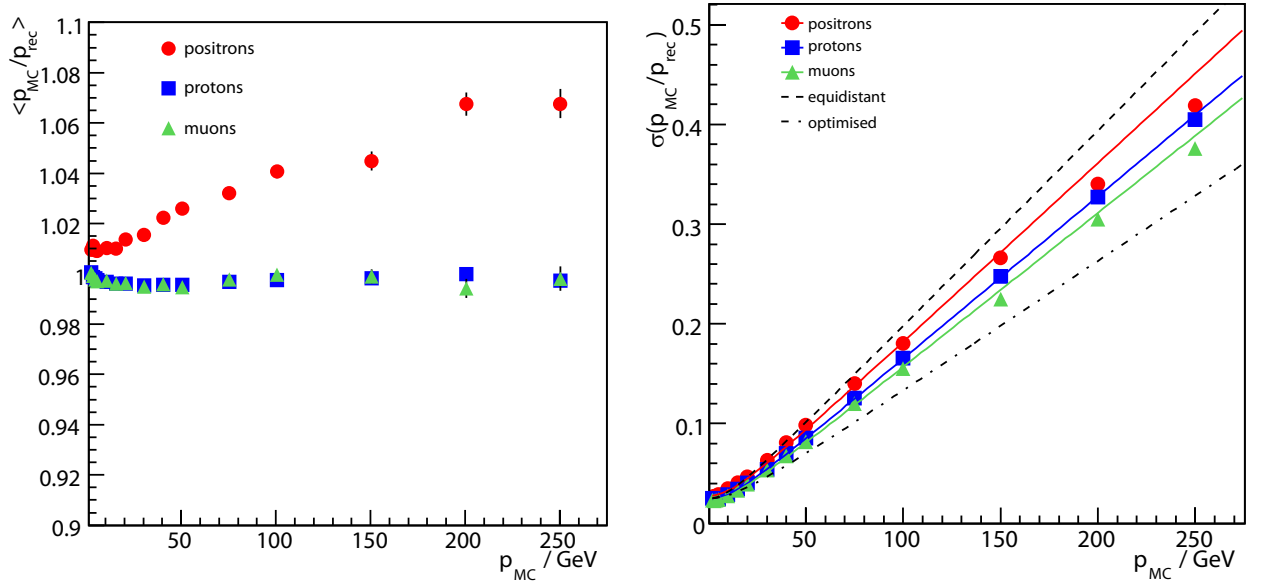


Fig. 4.29: Tracker momentum resolution as a function of incident momentum for positrons, protons, and muons. Mean value of p_{MC}/p_{rec} (left) and $\sigma(p_{MC}/p_{rec})$ of an individual measurement (right), together with fits according to equation (4.41) and the expectations for the case of the equidistant and optimised geometry according to equations (4.6) and (4.7), respectively.

three species. Values of $a_{msc}^{\mu} = 2.3\%$ and $b_{res}^{\mu} = 0.16\%/GeV$ for muons, $a_{msc}^p = 2.4\%$ and $b_{res}^p = 0.16\%/GeV$ for protons, and $a_{msc}^e = 2.7\%$ and $b_{res}^e = 0.18\%/GeV$ for positrons were obtained. As expected, these values lie between the theoretical expectations for the equidistant (eq. (4.6)) and optimised (eq. (4.7)) geometries, calculated for 16 tracker layers with a mean $BL^2 = 0.57\text{ Tm}^2$ and a spatial resolution of $56\ \mu\text{m}$ that was extracted from the simulation for isotropically incident muons. As the testbeam results presented in section 5.2 will show, this number is on the optimistic side as compared to what is achieved at the current level of design. An intrinsic resolution of $70\ \mu\text{m}$ has been achieved for perpendicularly incident particles whereas the simulation predicts $43\ \mu\text{m}$ for this case.

For a clean measurement of positrons on top of a background of electrons, a good efficiency for the determination of the charge sign is mandatory. The fraction of positron events reconstructed with wrong charge sign by the tracker as a function of the incident momentum is given in figure 4.30. It is negligible below 100 GeV and gradually rises due to the deteriorating momentum resolution towards higher energies. If the rigidity resolution follows a Gaussian distribution with standard deviation $\sigma_p(p)$, the expected fraction f of events with misreconstructed charge sign can be calculated to be

$$f = \frac{1}{2} \left(1 - \text{erf} \left(\frac{1}{2} \frac{\sqrt{2}}{\sigma_p(p)} \right) \right) \quad (4.42)$$

This is the trend followed by the simulation results in figure 4.30.

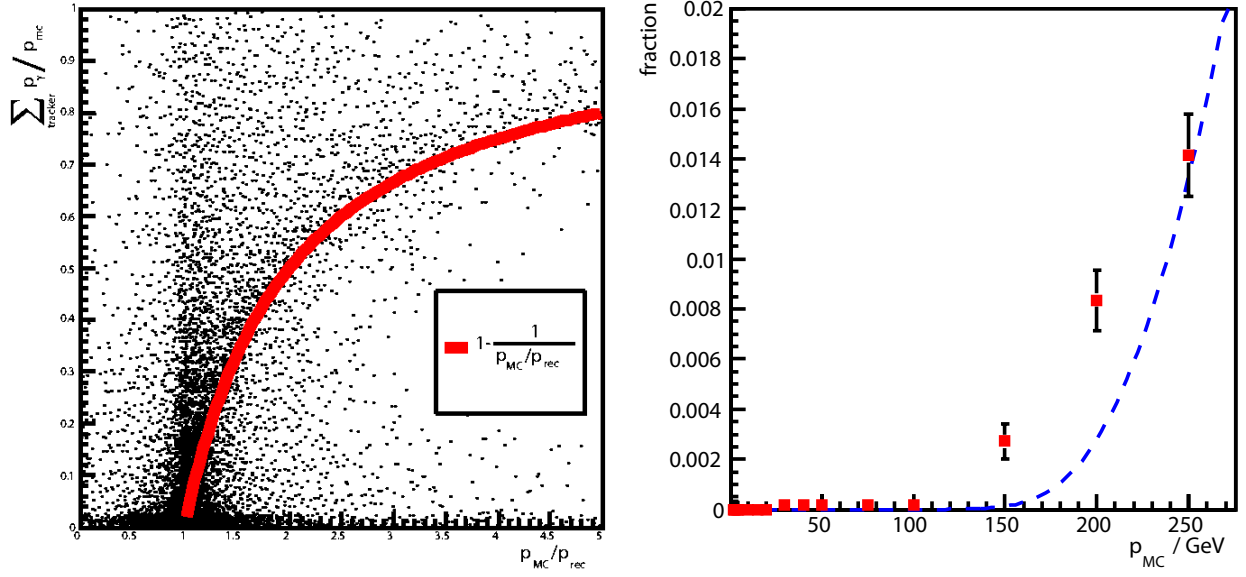


Fig. 4.30: *Left:* Relative amount of bremsstrahlung losses of incident positrons in the tracker as a function of $p_{\text{MC}}/p_{\text{rec}}$. The expected curve (eq. (4.40)) for the extreme case, where the error in the reconstructed momentum equals the bremsstrahlung loss, is included, too. *Right:* Fraction of positron events reconstructed with wrong charge sign by the tracker as a function of the incident momentum, together with the expectation according to eq. (4.42).

The track positions that enter the momentum determination are calculated as weighted means of the individual SiPM channel amplitudes according to eq. (4.32). The higher the light yield of the scintillating fibre and SiPM chain per particle the more accurate this weighted mean can be calculated. Figure 4.31 contains the momentum resolution of 100 GeV protons, again according to a fit to eq. (4.41), as a function of the light yield. The curve is shown both as a function of the overall coupling efficiency ϵ_{coup} , as defined in (4.9), which is actually used as an input to the simulation, and the resulting mean total cluster amplitude of the tracker clusters so obtained. A rather strong dependence of the momentum resolution on the light yield is observed.

4.4.2 Angular resolution

The combined angular resolution of the tracker and the TRD is important. For example, the reconstructed track direction is used together with the reconstructed shower axis in the calorimeter to separate positrons from protons. The angular resolution obtained for positrons in the simulation is shown in figure 4.32. The difference of the reconstructed and generated angles is $\Delta\theta$. It is measured by the tracker in the bending plane and by the TRD in the non-bending plane. For the former, a resolution on the order of 0.1 mrad is found at high energies, and 1 mrad for the latter.

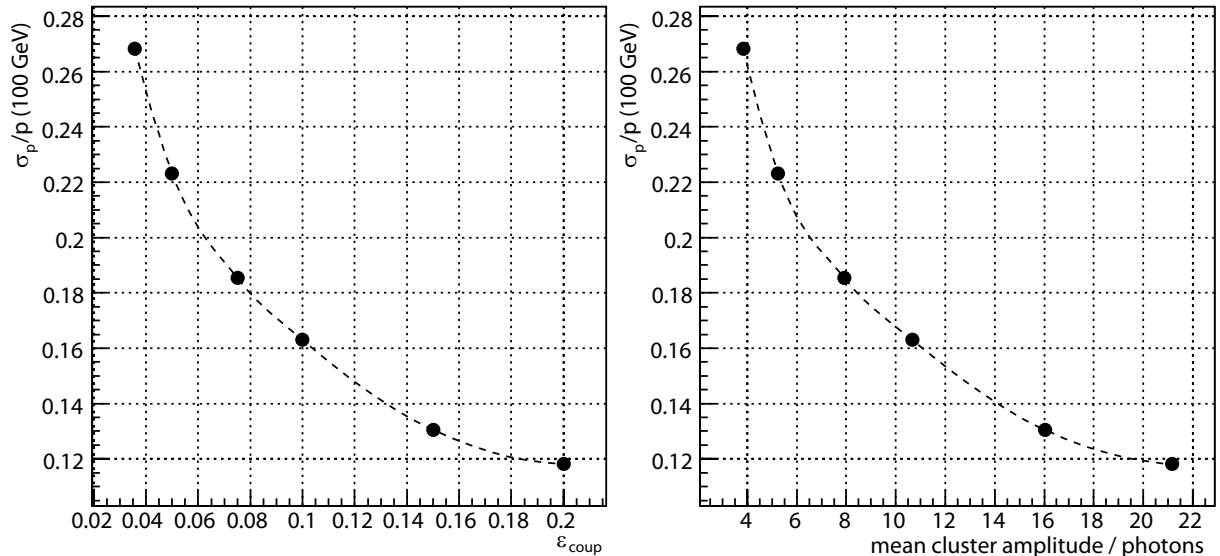


Fig. 4.31: Momentum resolution for 100 GeV protons according to a fit of (4.41), as a function of the overall coupling efficiency ϵ_{coup} (left) or the corresponding mean cluster amplitude in photons (right).

4.4.3 Impact of SiPM noise

In reality, fake hits will be present in the tracker that are caused by the unavoidable noise of the SiPM arrays. The track finding algorithm presented in section 4.3 was designed to overcome the difficulties caused by SiPM noise as far as possible. To study the effectiveness of the algorithm and thus the tracker performance for different noise levels, the mean noise level of the SiPM channels, given in photo-electrons, was varied. Using a threshold of 2 photo-electrons per SiPM channel, the track finding efficiency was extracted for each setting of the noise level. Protons of 2 GeV and 20 GeV momentum were examined. The result is shown in figure 4.33. The curves labelled “efficiency” include all events including a track passing the tracker quality cuts described in section 4.4.1. In addition, a “good track” is defined as having $|p_{\text{rec}} - p_{\text{MC}}|/\sigma_p < 4$ and a reconstructed direction within 2° of the true direction. For high-momentum tracks, the tracker performance begins to deteriorate at a noise level of around 0.1. For low-momentum tracks, the track finding algorithm is not that appropriate as it is optimised for tracks with small curvature, and the track finding efficiency is therefore lower.

Although the mean noise level of an SiPM depends strongly on the type of SiPM and the conditions under which it is operated, especially the temperature, the testbeam results presented in section 5.2 show that the noise level will be around 0.06. This number is valid for the Hamamatsu SiPM arrays studied in the testbeam at a temperature of $T \sim 16^\circ\text{C}$. Typically, the noise level is reduced in half when the temperature of the device is lowered by $\sim 8^\circ\text{C}$ [99].

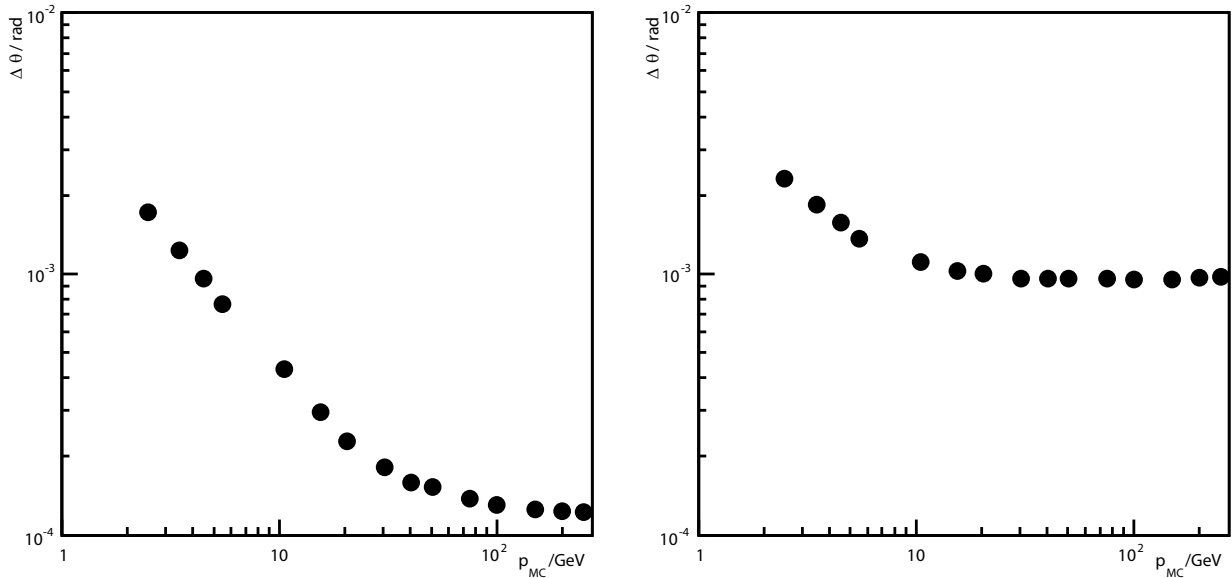


Fig. 4.32: Median difference of reconstructed and generated angles, separately for the projection to the bending plane as measured by the tracker (*left*) and to the non-bending plane as measured by the TRD (*right*), as a function of the momentum of the incident positrons.

4.4.4 Impact of module thickness

An obvious way to increase the light output of the scintillating fibre stacks used in the tracker is to increase their thickness in terms of the number of fibre layers per module. Figure 4.33 shows the momentum resolution obtained for 100 GeV protons as a function of the number of fibre layers per SiPM. The height of the SiPM channels was scaled accordingly but the number of pixels was kept fixed. The momentum resolution reaches a flat minimum at seven layers of fibres. It slowly rises again beyond this point which can be understood from the increasing uncertainty in the z coordinate for a thick fibre stack. In practice, the increasing difficulty of producing a homogeneous fibre stack with many layers has to be taken into account, as small deviations from the nominal positions of fibres in the lower layers tend to cause larger displacements in the upper layers [99]. If this difficulty can be overcome in the production of the fibre stacks, a configuration using seven fibre layers can be expected to give the best spatial resolution.

4.4.5 ECAL energy resolution

The key figures of merit for the electromagnetic calorimeter are its energy resolution and its rejection power against protons (sec. 4.4.6). Figure 4.34 illustrates the calorimetric energy measurements of electrons and positrons. It shows the mean longitudinal shower shapes obtained from the simulation. The response to positrons of different energies is depicted in the figure. Both the increase in integrated amplitude according to (4.14) and the logarithmic dependence of the location of the shower maximum on the incident energy according to (4.16) are visible. The figure also demonstrates that the shower maximum

4 Design study for PEBS based on Monte Carlo simulations

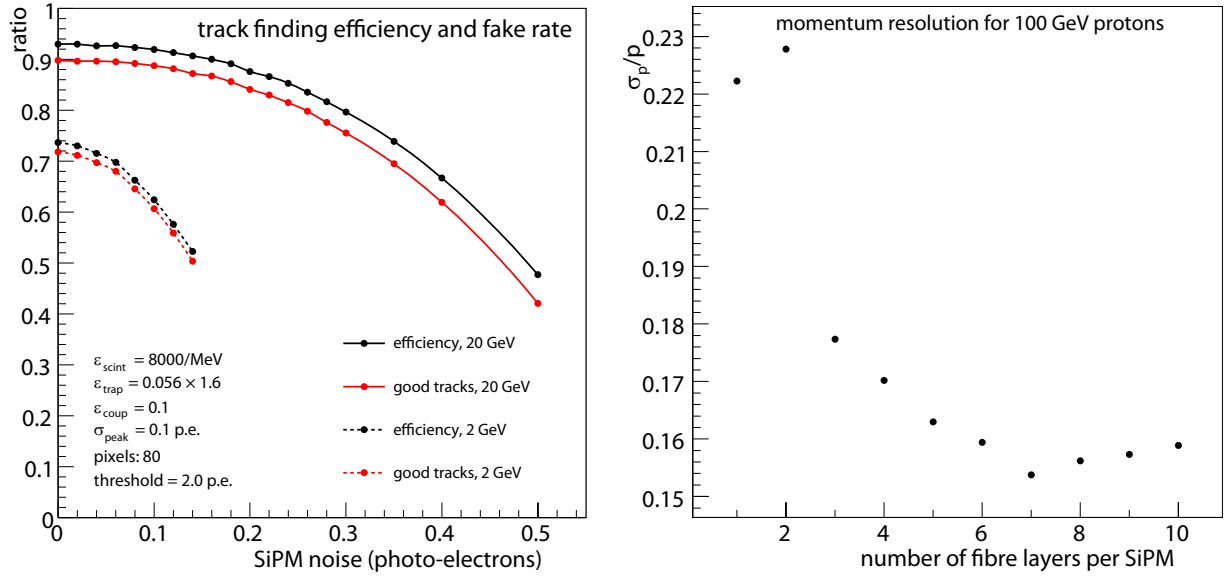


Fig. 4.33: *Left:* Track finding efficiency as a function of the mean noise level in the tracker SiPMs. The plot shows the fraction of proton events for which a track surviving the quality cuts described in the text is found. An event is further labelled as containing a good track if both momentum and track direction are reconstructed correctly. Protons of 2 GeV and 20 GeV momentum are examined, respectively. *Right:* Momentum resolution for 100 GeV protons as a function of the number of fibre layers in front of each SiPM array channel in the tracker.

is well contained in the ECAL at all energies of interest here.

The energy resolution of the ECAL is derived from distributions of the reconstructed shower energy E_0 (in photons), separately for various incident energies. As a first step, the calibration curve of the ECAL is obtained (fig. 4.35). It shows the mean value of E_0 found from Gaussian fits to the E_0 -distributions of the individual measurements as a function of the incident momentum. The response shows a slight deviation from linearity that can be attributed to the imperfect correction of the SiPM response function. A parabolic fit has been applied to the ECAL response curve. This fit was then used to calculate the reconstructed energy (in GeV) on an event-by-event basis. The resulting distributions were fit by Gaussians to yield the mean and standard deviation and thus the relative energy resolution $\sigma(E)/E$. Only showers completely contained within the ECAL acceptance were used for this study. Figure 4.36 shows the projected energy resolution obtained in this way. The energy resolution for the standard configuration with 20 layers and SiPMs with 560 pixels was fitted to the parameterisation of (4.18) up to an energy of 30 GeV to obtain $a = 15.5\% \cdot \sqrt{\text{GeV}}$ and $c = 5.3\%$. Above this energy, two effects worsen the energy resolution.

First of all, the limited depth of the calorimeter cannot completely be corrected for. This is demonstrated by the additional curves in the figure showing the resolution for calorimeters with different numbers of layers. A significant effect is seen already for a variation of 10% of the depth. However, each ECAL layer will contribute around 30 kg to the weight budget.

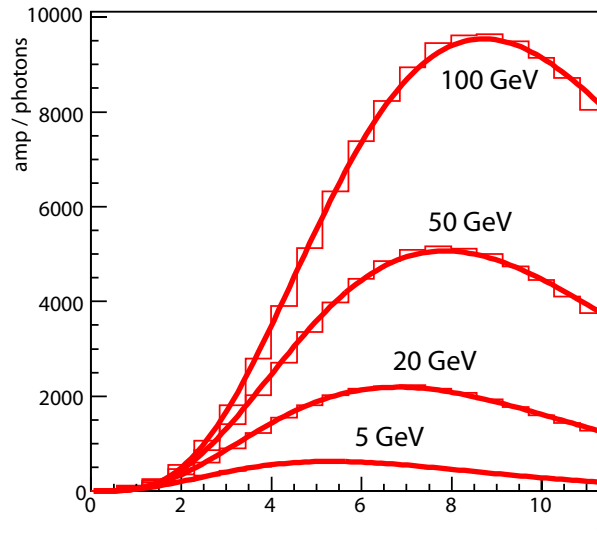


Fig. 4.34: Average longitudinal ECAL shower shapes for various energies of the incident positrons. The mean amplitude (in reconstructed photons) is plotted as a function of the depth $t = x/X_0$ in the calorimeter. One bin corresponds to one layer of absorber. A fit of the parameterisation according to (4.14) is included, too.

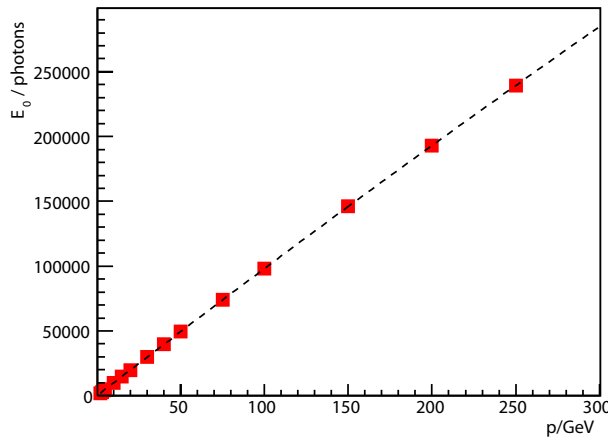


Fig. 4.35: Linearity of ECAL response: Mean reconstructed shower energy E_0 (in photons), as a function of the incident momentum. The response function has been fitted by a parabola.

The second effect is the limited dynamic range of the SiPMs. As the figure shows, the energy resolution remains somewhat lower for the ideal case of an unlimited number of pixels. For this case, the partially reflective foil is not needed and was replaced by an ideal mirror in the simulation. This effect is small compared to the first one as the limited dynamic range is compensated by the ECAL design featuring the partially reflective foil. To be more quantitative, both the overall thickness of the ECAL and the number of SiPM pixels used for its readout have been varied around the values of the standard design to study the corresponding change in energy resolution (fig. 4.37). While there is a drastic

4 Design study for PEBS based on Monte Carlo simulations

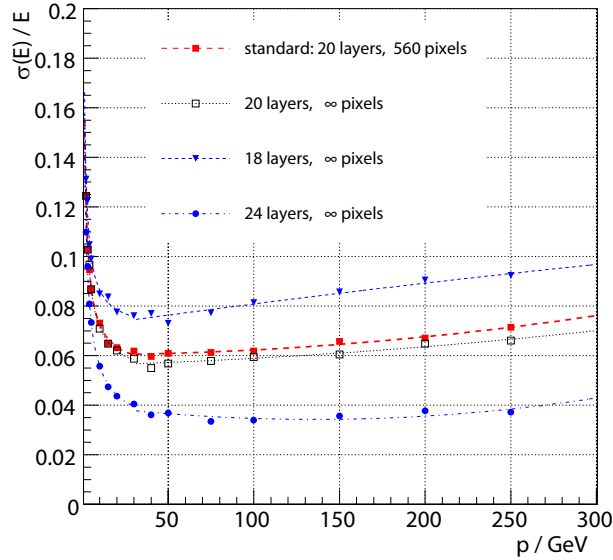


Fig. 4.36: ECAL energy resolution as a function of incident momentum, for the standard configuration with 20 layers and SiPMs with 560 pixels, for the ideal case of a single SiPM with unlimited number of pixels, and for varying number of layers. The parameterisations are described in the text.

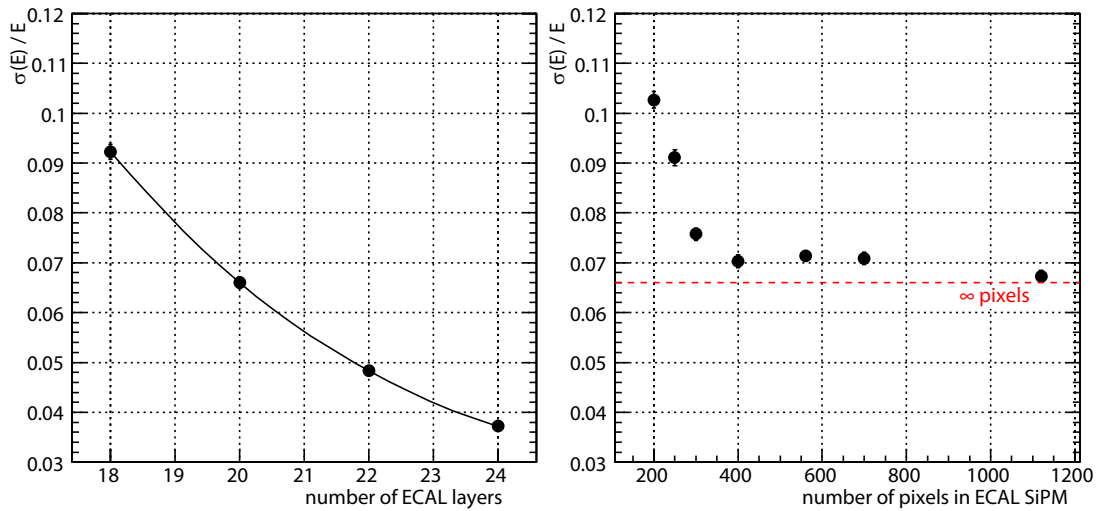


Fig. 4.37: ECAL energy resolution at 250 GeV, as a function of the number of ECAL layers, i.e. the total thickness, for a fixed number of 560 pixels (*left*), and for varying numbers of SiPM pixels, at a fixed number of 20 layers (*right*). The solid line is a spline interpolation, used to guide the eye only.

dependence of the energy resolution on the ECAL thickness, the resolution cannot be significantly improved by increasing the number of SiPM pixels above a certain threshold, located around 400 for the present design.

For the reasons described above, a parabolic fit had to be used to describe the energy

resolution above 30 GeV. For the standard configuration, it reaches a value of 0.07 at 250 GeV. Comparing this to the tracker resolution in figure 4.29 shows that the overall performance of the detector, especially the E/p matching used for proton discrimination, will be limited by the tracker because of its considerably worse resolution.

4.4.6 ECAL rejection and efficiency analysis

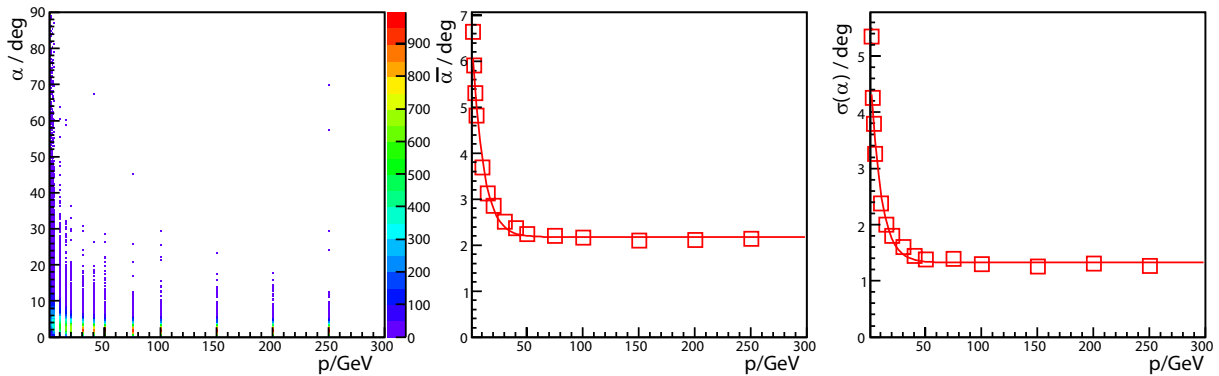


Fig. 4.38: Example of procedure for automatic cut determination: Distribution of reconstructed angle α between ECAL shower and track found in tracker and TRD for positrons, as a function of momentum (*left*). For each bin in p , the projection along the α -axis is calculated, a Gaussian fit is performed, and the mean values (*middle*) and standard deviations σ (*right*) are extracted. Suitable fits to the mean and σ values are performed. The momentum-dependent cut can then be calculated according to the results of these fits.

The most important task for the electromagnetic calorimeter is the reliable suppression of the proton background. In order to study the projected ECAL rejection, a cut-based shower shape analysis was performed. Momentum-dependent cuts were applied to five variables on an event-by-event basis:

- the shower energy E_0 as determined from the longitudinal shower shape as described in section 4.3,
- the sum over the amplitudes in each layer,
- the location t_{\max} of the shower maximum,
- the ratio f_M of energy within one Molière radius around the shower axis, and
- the angle α between the shower axis and the reconstructed track in the tracker

A procedure for the automatic determination of the momentum-dependent cut was developed and the idea is shown for the example of the track angle α (fig. 4.38). The values obtained for the positron sample are first histogrammed versus the generated momentum p . Then, Gaussian fits are applied to the distributions in each momentum bin to obtain the mean $\bar{\alpha}$ and standard deviation $\sigma(\alpha)$ as a function of momentum. Suitable

4 Design study for PEBS based on Monte Carlo simulations

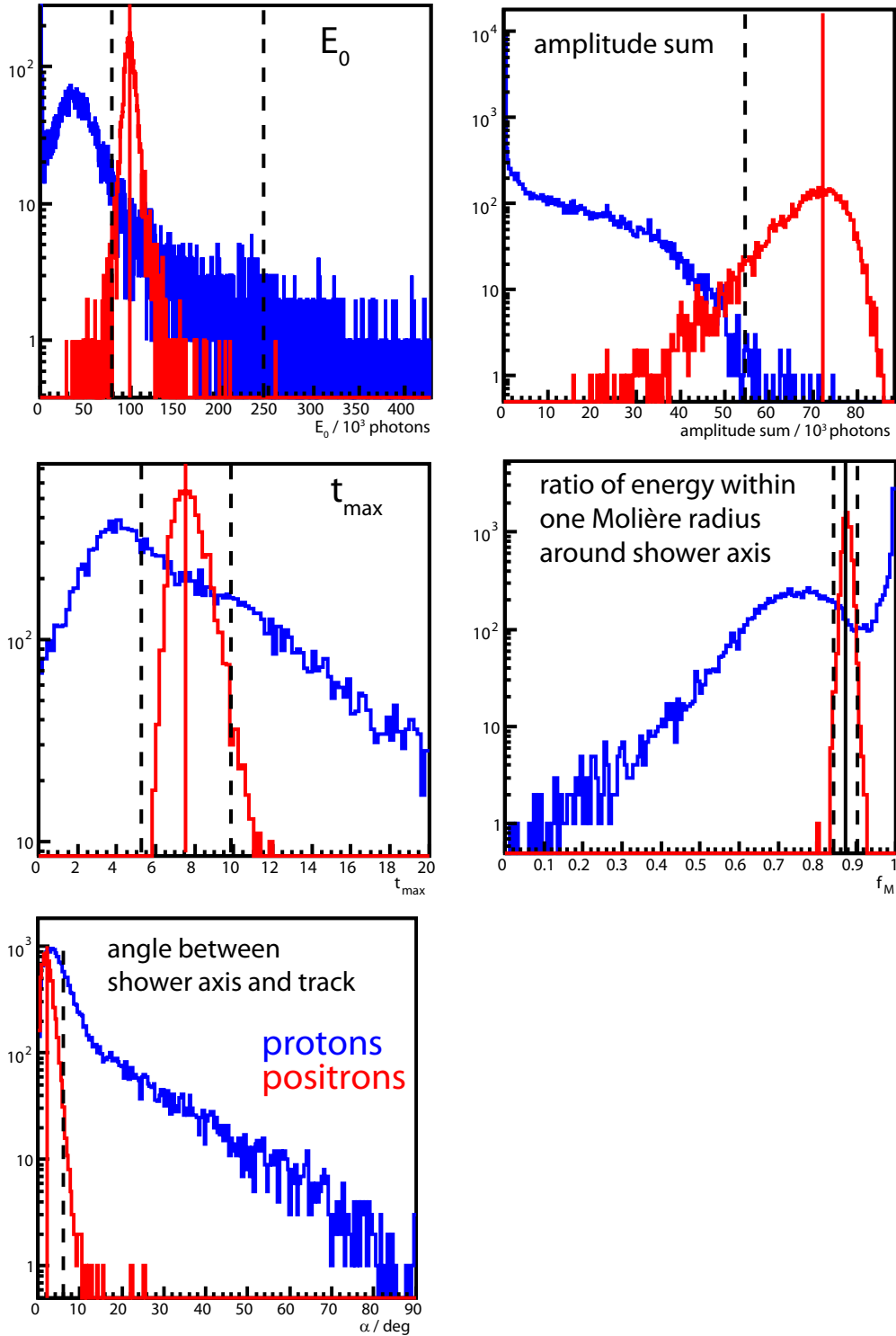


Fig. 4.39: ECAL cuts: Distributions of the shower variables used for proton discrimination: shower energy E_0 as determined from the shower fit, sum over layer amplitudes, shower maximum t_{\max} , ratio f_M of energy within one Molière radius around the shower axis, and angle α between shower axis and reconstructed track. Distributions are shown for positrons (red) and protons (blue) for a momentum of 100 GeV. The mean values for positrons (continuous lines) as well as the cuts (dashed lines) automatically determined by the analysis procedure are shown, too.

4.4 Projected performance

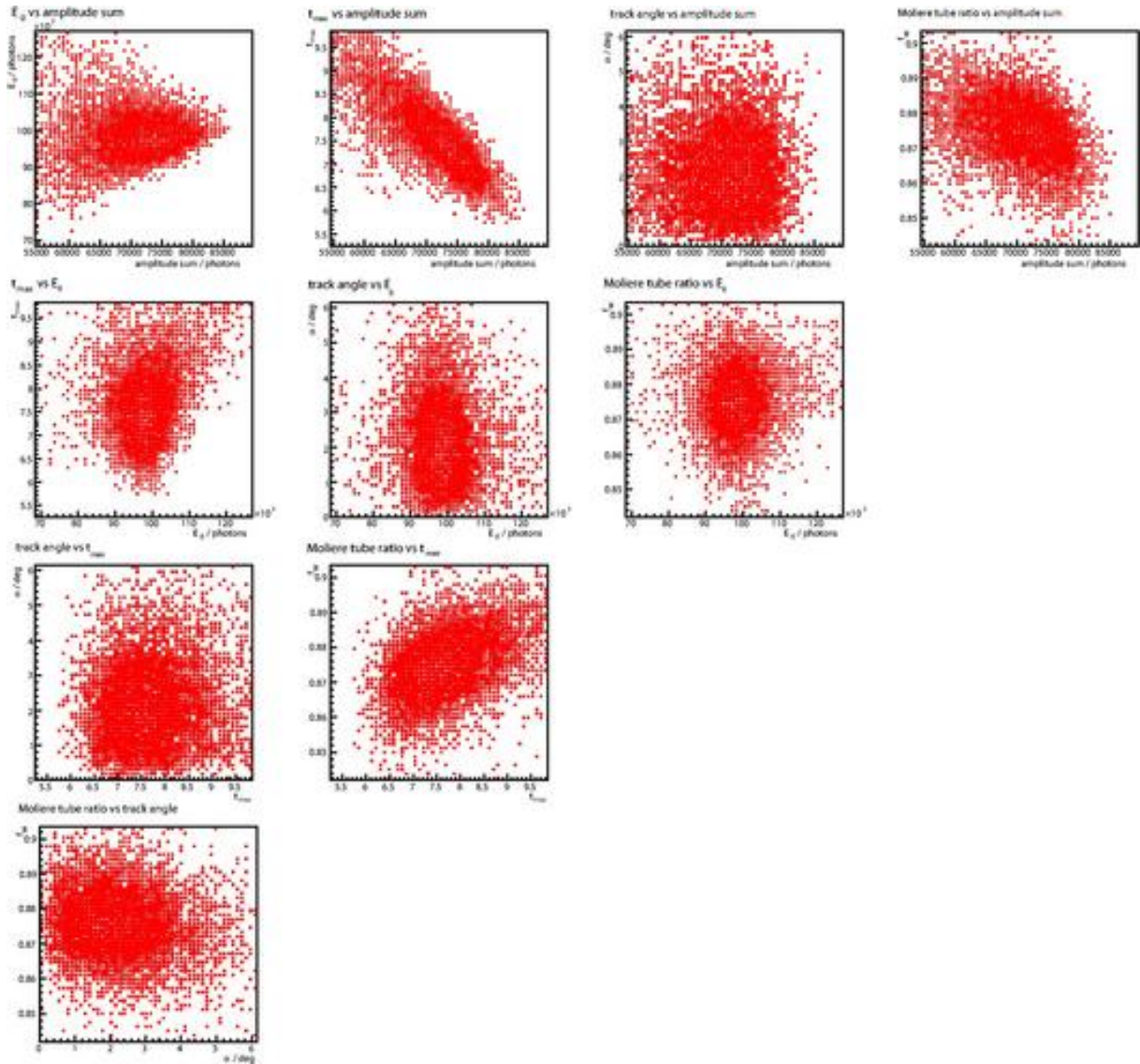


Fig. 4.40: Correlations between the five shower variables used for proton discrimination. Distributions for 100 GeV positrons are shown.

4 Design study for PEBS based on Monte Carlo simulations

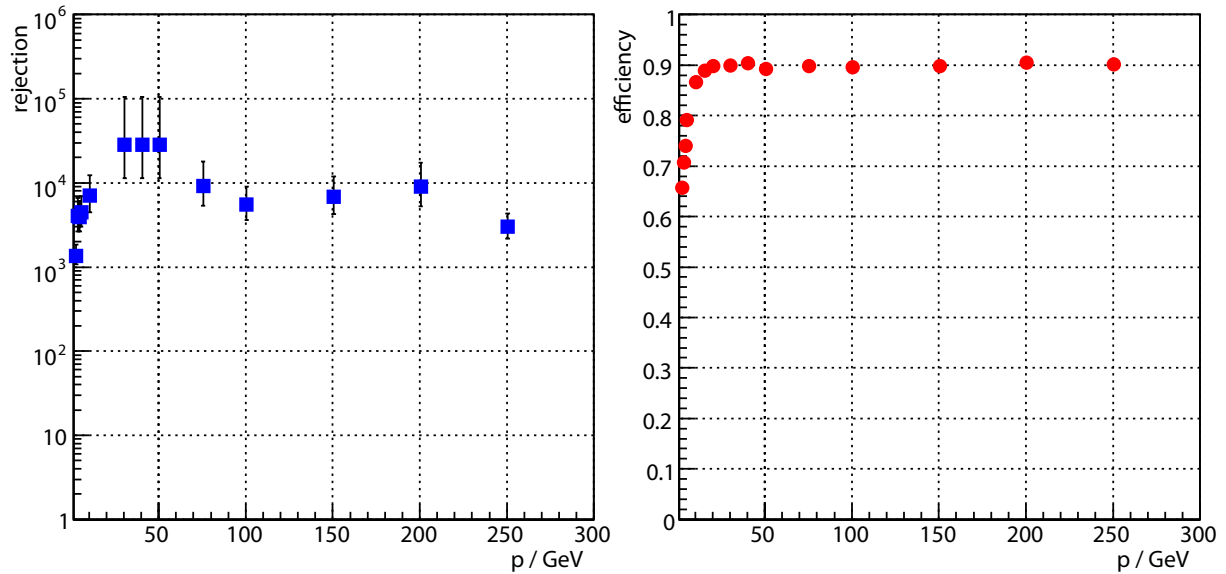


Fig. 4.41: Projected ECAL rejection against protons (*left*) and corresponding positron efficiency (*right*), as a function of momentum of the incident particle. The generated momenta provided by the simulation have been used for all cuts.

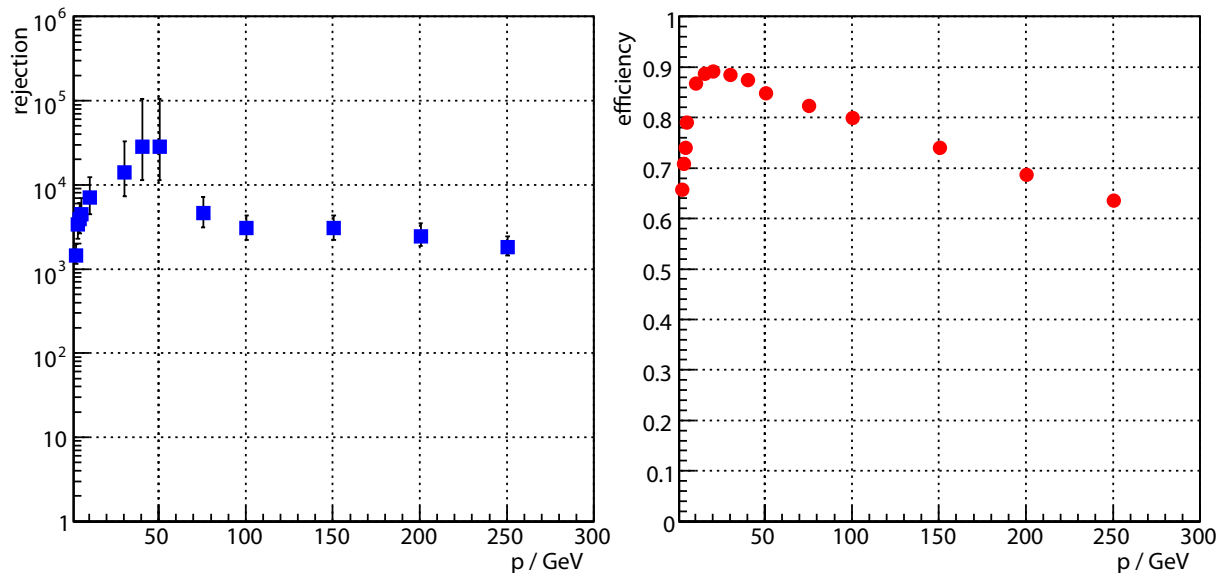


Fig. 4.42: Projected ECAL rejection against protons (*left*) and corresponding positron efficiency (*right*), as a function of momentum of the incident particle. The momenta reconstructed by the tracker and the TRD have been used for all cuts.

parameterisations are then fitted to both curves, and the momentum-dependent cuts are finally defined at $\bar{\alpha}(p) \pm n_{\alpha,\pm} \cdot \sigma(p)$. The cut parameters $n_{i,\pm}$ are chosen appropriately for the various cuts. As an example, figure 4.39 shows the distributions of the five shower parameters for positrons and protons of 100 GeV momentum, together with the cuts determined for this momentum. The E_0 distribution peaks at lower values for protons than for positrons. $n_{E_0,-} = 2$ is chosen while the small tails towards large E_0 -values allow an upper cut of $n_{E_0,+} = 15$, needed to allow for errors in the momentum reconstruction. In the case of the amplitude sum, only a lower cut of $n_{\text{sum},-} = 3$ is used. The distributions of t_{max} , f_M , and α show clean peaks in the positron case while the corresponding proton distributions are smeared out across the parameter ranges. Cuts at $n_{\pm} = 3$ are used for these variables.

For an assessment of the ECAL performance alone, the cuts are calculated on an event-by-event basis using $p = p_{\text{MC}}$, while for a realistic assessment of the overall detector performance, $p = p_{\text{rec}}$ has to be used. In this case, the limited momentum resolution of the tracker worsens the overall performance. An event surviving all five cuts is classified as a positron or electron, respectively. Correlation plots of the five shower variables are shown in figure 4.40 for the case of 100 GeV positrons. Except for the correlation of the amplitude sum and t_{max} which reaches a value of -0.8 , the cut variables are largely uncorrelated.

The proton rejection and corresponding positron efficiency are plotted in figures 4.41 and 4.42 as a function of momentum and using the generated and reconstructed momenta, respectively. In both cases, the proton rejection reaches a maximum of roughly $3 \cdot 10^4$ at around 50 GeV. It drops to $3 \cdot 10^3$ and $2 \cdot 10^3$ at high energies for generated and reconstructed momenta, respectively. The electron efficiency is at 90 % using the generated momenta, but it becomes considerably worse using the reconstructed momenta, dropping to 65 % at 250 GeV. This is mainly due to the deteriorating momentum resolution of the tracker at high energies which causes many positron events to lie outside the corridors for the cuts on E_0 and the amplitude sum.

A beneficial effect of using a calorimeter for proton suppression is illustrated in the distribution of reconstructed momenta for 100 GeV proton events which were misidentified as positrons or electrons by the ECAL (fig. 4.43). Because the ECAL sets an upper boundary on the energy of a particle, the reconstructed momenta of particles passing the ECAL cuts will be lower than the actual momenta. This means that they will contribute to energy bins with a much higher relative positron flux (fig. 2.3). In contrast to this, the corresponding distribution for protons misidentified by the TRD (sec. 4.4.7) simply is determined by the momentum resolution of the tracker.

Distributions like the one in fig. 4.43 give a better picture of the behaviour of the complete detector than rejections alone. Unfortunately, the amounts of Monte Carlo statistics needed to obtain them turn out to be prohibitive.

4.4.7 TRD rejection

The determination of the projected TRD performance was performed analogously to section 4.2.8. The accumulated distributions of energy depositions in the TRD tubes, for positrons and protons of 20 GeV momentum, respectively, are shown in figure 4.44. The

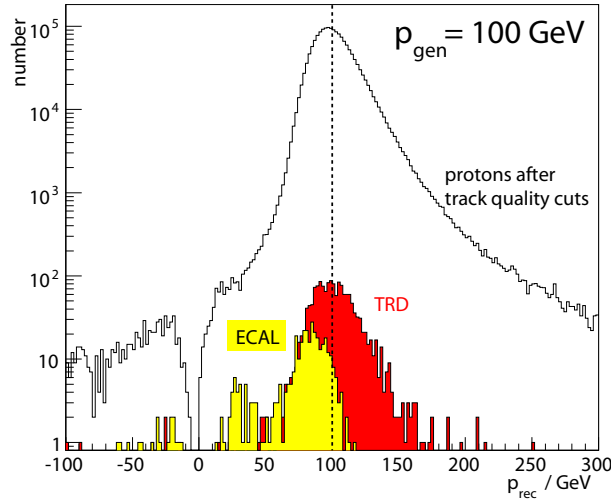


Fig. 4.43: Distributions of reconstructed momenta for 100 GeV proton events misidentified as positrons or electrons by the ECAL and the TRD, respectively. The hollow curve gives the distribution of all tracks passing the simple quality cuts outlined in section 4.4.1.

ionisation peaks for both species as well as the characteristic shoulder caused by the transition radiation of positrons are visible. The figure also contains a plot of the mean energy depositions for each layer. Here, the two-part structure of the TRD is evident in the positron curve, where the mean energy deposition reaches its saturation value after a couple of layers. Between layers 7 and 8, the central tracker layers absorb the x-ray transition radiation photons generated in the first half of the TRD. The proton and electron log-likelihoods $-\log(L)$, defined analogous to section 4.2.8, are then calculated on an event-by-event basis according to the incident energy from the tube energy distributions, like the ones shown in fig. 4.44. Finally, the proton rejection and corresponding positron efficiency are determined by setting a cut in the $-\log(L)$ -distributions (fig. 4.45). As an example, the result for 20 GeV protons and positrons is shown in figure 4.46. At a positron efficiency of 80 %, the rejection begins to deteriorate and therefore, the proton rejection is shown for this efficiency as a function of momentum in the right-hand side of figure 4.46. At 100 GeV, the projected proton rejection is at the level of 700 for 80 % positron efficiency.

4.4.8 Acceptance calculation

The geometric acceptance A determines the gathering power of a cosmic-ray detector and hence, the size of the statistical errors attributed to a flux measurement performed by the detector. It is defined as the factor of proportionality between the counting rate C of a detector and an isotropic flux Φ :

$$C = A\Phi \quad (4.43)$$

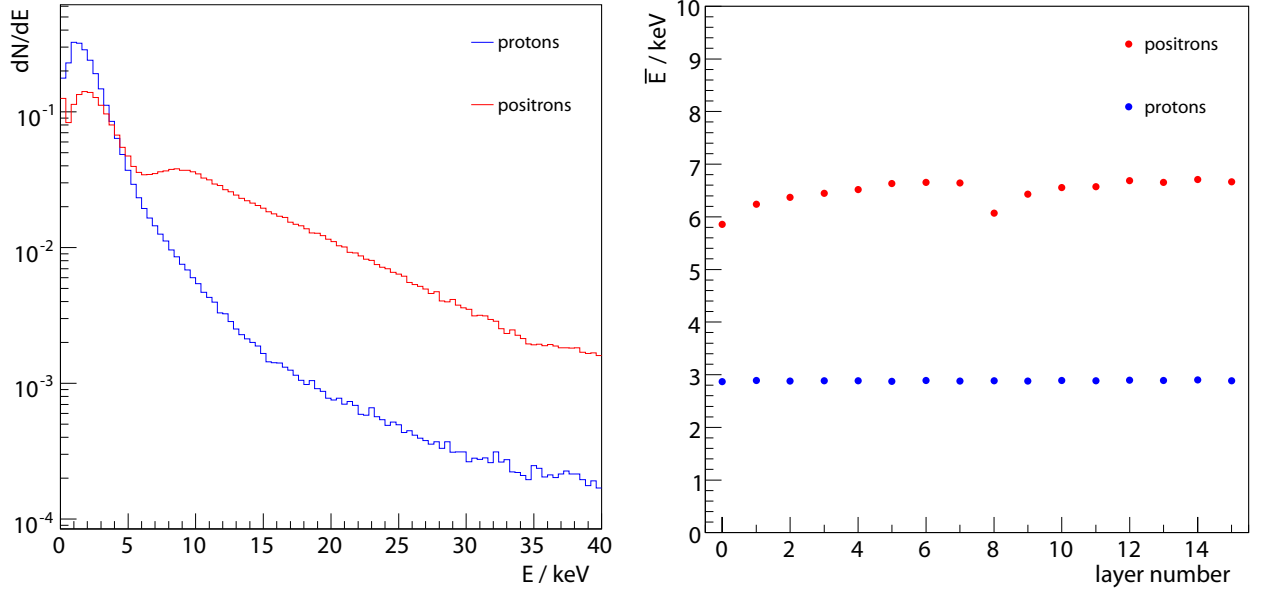


Fig. 4.44: *Left:* Distribution of simulated energy depositions in the TRD tubes, for positrons and protons of 20 GeV momentum, respectively. Data from all layers are included in this plot. *Right:* Mean energy depositions in the TRD tubes, as a function of layer number, for positrons and protons of 20 GeV momentum, respectively. The central tracker layers are located between layers 7 and 8, reducing the mean value for positrons by absorbing the TR x-ray photons.

For an idealised detector, consisting of a given number of detection planes, the geometric acceptance is given by [144]

$$A = \int_{\Omega} d\omega F(\omega) \int_S d\sigma \cdot \hat{\mathbf{r}} \quad (4.44)$$

where $d\sigma$ is the element of surface area of the last telescope sensor to be penetrated, S is the total area of the last telescope sensor, $d\omega = d\phi d(\cos\theta)$ is an element of solid angle, Ω is the domain of ω , limited by the other telescope sensors, and $\hat{\mathbf{r}}$ is a unit vector in the direction of ω . $F(\omega)$ is the angular dependence of the incident flux, with $F(\omega) = 1$ for isotropic incidence.

For an ideal telescope consisting of a single planar detector that is hit by particles from one of its two sides, the geometrical acceptance is easily calculated from (4.44) to be

$$A = \pi a \quad (4.45)$$

where a is the surface area of the detector.

For a detector such as PEBS, with many detector planes, an analytical calculation of (4.44) becomes impossible. An elegant approach in this case is a Monte Carlo integration which proceeds as follows: In the first step, a random point is chosen at the opening aperture of the detector. A random direction is chosen from the appropriate angular distribution: The directions of incidence on a given surface element on the planar aperture will be

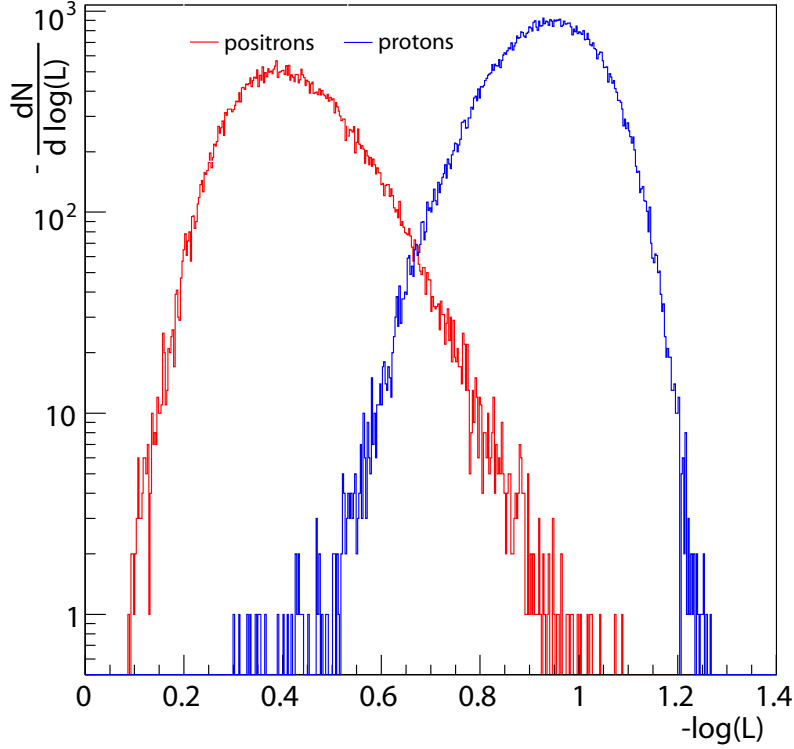


Fig. 4.45: Distributions of log-likelihood $-\log(L)$ used for proton discrimination in the TRD, for positrons and protons of 20 GeV momentum.

weighted by $F(\omega)$ and a factor $\cos \theta$ from $d\sigma \cdot \hat{\mathbf{r}}$. The weighted solid angle then becomes

$$\cos \theta F(\omega) d \cos \theta d\phi = \frac{1}{2} F(\omega) d \cos^2 \theta d\phi$$

For isotropic incidence, one therefore chooses $\cos^2 \theta$ and ϕ randomly from uniform distributions with the appropriate bounds. In the second step, a trajectory with the starting point and direction obtained in the first step is followed through the detector to see if it intersects all sensitive planes. These two steps are then repeated many times and the acceptance can finally be calculated as

$$A = \frac{\text{number of trajectories hitting all planes}}{\text{number of trajectories started}} \cdot A_{\text{ap}} \quad (4.46)$$

where A_{ap} is the acceptance of the aperture, calculated from (4.45).

In order to obtain the acceptance for the PEBS detector, the Monte Carlo approach was followed, using the dimensions of fig. 3.4. Figure 4.48 shows the intersection points of those straight line trajectories that are found to traverse the entire detector on some of the idealised detector planes, ranging from the upper TOF layer, which constitutes the aperture of PEBS, to the lowest ECAL layer. Figure 4.47 shows the zenith and azimuth angle distributions for the same trajectories. The mean zenith angle is found to be 21° . The maxima in the azimuth angle distribution are spaced by 90° and are due to the square

4.4 Projected performance

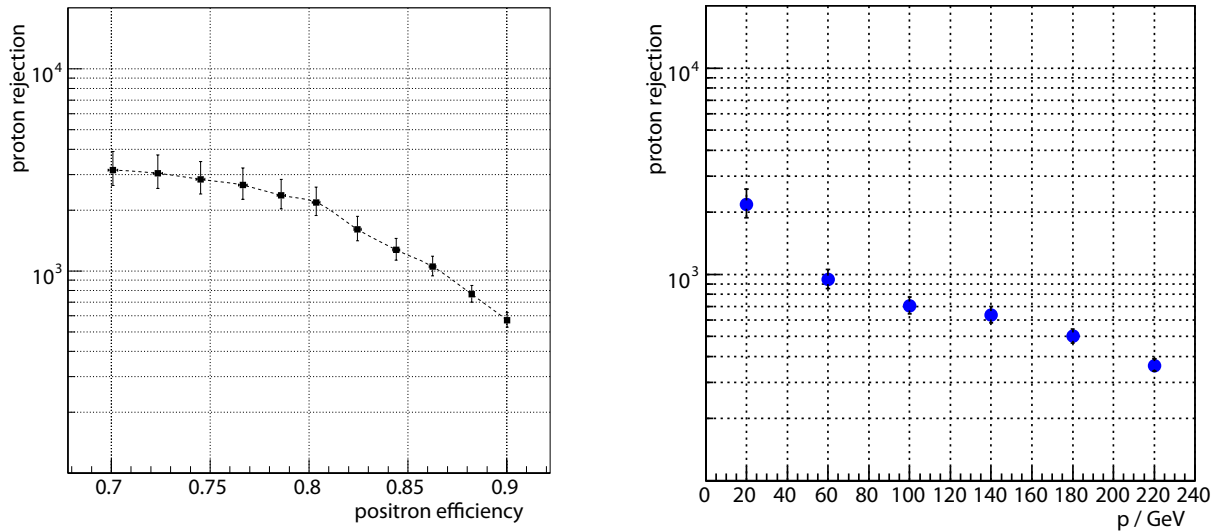


Fig. 4.46: *Left:* Rejection achieved by the TRD against 20 GeV protons, as a function of the corresponding positron efficiency, according to the simulation. *Right:* Rejection achieved by the TRD against protons, as a function of incident momentum, at 80% positron efficiency.

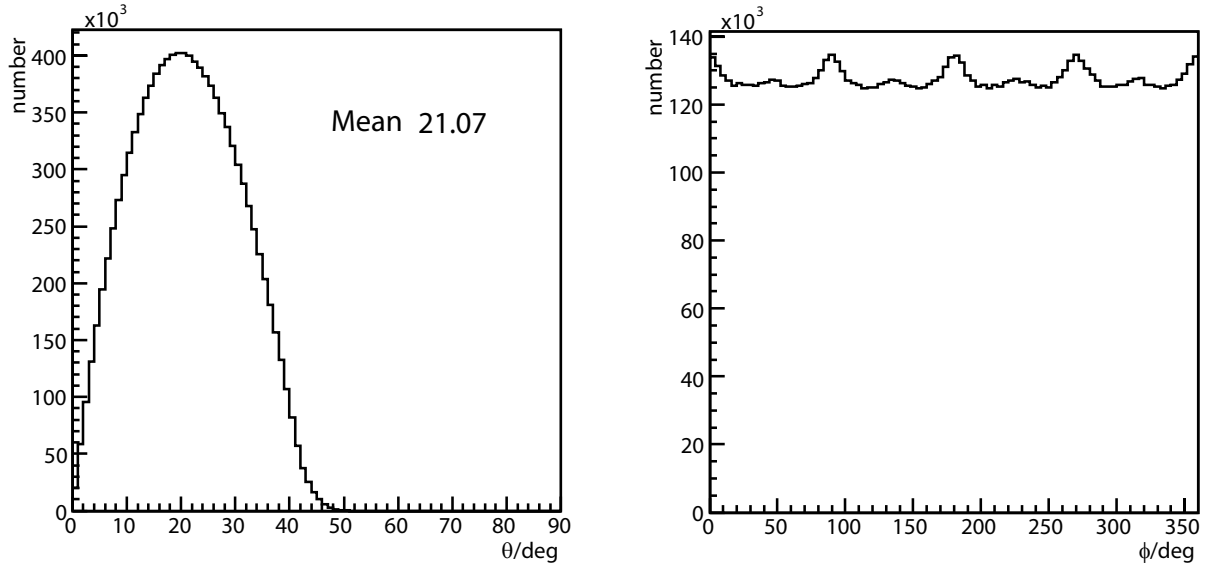


Fig. 4.47: Distribution of zenith angles (*left*) and azimuth angles (*right*) for straight lines within the geometrical acceptance of the PEBS detector.

shape of the detector.

The acceptance of PEBS found from a Monte Carlo integration using 100 million trajectories was found to be $3850 \text{ cm}^2\text{sr}$. The trigger rate that the readout electronics and data acquisition chain needs to handle can then be estimated from the proton flux. Taking

4 Design study for PEBS based on Monte Carlo simulations

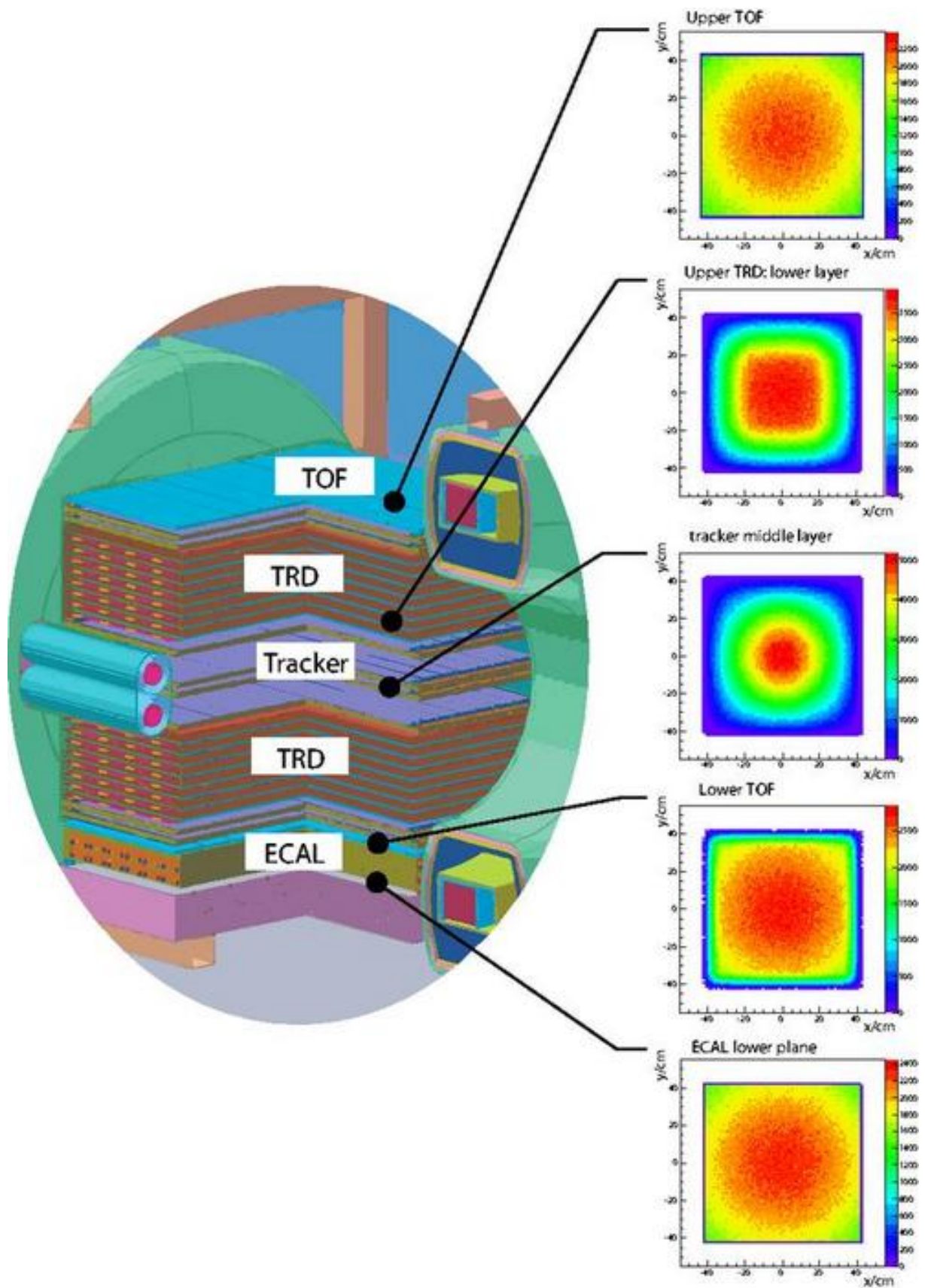


Fig. 4.48: Acceptance calculation: Distributions of intersection points of trajectories found to be within the detector acceptance on the individual detector planes.

4.4 Projected performance

	$\langle n_H \rangle$	channel number	amplitude	volume per event for subdetector
Tracker	64	16 bit	16 bit	2048 bit
ECAL	85	16 bit	16 bit	2720 bit
TRD	22	12 bit	16 bit	616 bit
TOF	8	8 bit	16 bit	32 bit
total				5416 bit ≈ 700 byte

Tab. 4.1: Calculation of the expected event size, based on 20 GeV protons, with a mean noise level of 0.06 pixels in the tracker. The column labeled $\langle n_H \rangle$ gives the mean number of hits to be stored, extracted from the Monte Carlo simulation.

the BESS 1997 data, taken at solar minimum, allowing for 10% Helium admixture, extrapolating the data to zero energy and neglecting all other particle species, an expected trigger rate of roughly 1.5 kHz is calculated. Low-energetic particles, whose fluxes are poorly known and highly variable, and that might saturate the trigger, are expected to be efficiently absorbed in the remaining atmosphere at flight altitude. For example, a residual grammage of 3.7 g/cm² corresponds to 30 mm of polycarbonate.

Given these numbers, the expected data volume can be calculated (tab. 4.1). For a flight duration of 40 days, roughly five billion events will have to be recorded, requiring a disk capacity of roughly 4 TB.

4 Design study for PEBS based on Monte Carlo simulations

5 PEBS tracker prototype testbeam campaign

The design of a novel detector technology, such as the scintillating fibre tracker for PEBS, requires constant experimental checks. In order to study the response of the key tracker components – scintillating fibres read out by silicon photomultipliers – to minimally ionising particles with high statistics, several prototype modules were subjected to a 10 GeV proton beam at the T9 beamline at the European Organisation for Nuclear Research, CERN, near Geneva, over the years 2006-2008. Key questions to be answered by these tests were the photo-electron yield and the corresponding spatial resolution of the prototypes.

The testbeam results can be compared to the predictions of dedicated Monte Carlo simulations to see if all relevant effects affecting the behaviour of the detector have been modelled appropriately. In turn, these simulations can be incorporated into the full simulation of PEBS.

5.1 First testbeam 2006

For a first proof of principle, two bundles of square fibres of $300\ \mu\text{m}$ width were used during the first testbeam which took place in October 2006.

5.1.1 Setup description

A photograph of the testbeam setup is shown in figure 5.1 and figure 5.2 contains a schematic drawing of the setup and a close-up view of the fibre bundles. The fibre bundles were constructed from square, $300\ \mu\text{m} \times 300\ \mu\text{m}$ multi-clad fibres of type Bicon BCF-20 [114]. Each fibre was covered by a thin layer of white extra-mural absorber (EMA) coating which is used to suppress optical crosstalk between adjacent fibres. Each of the two fibre bundles was 10 fibres wide and 3 fibres high and was stabilised by glue. Each stack of three consecutive fibres was read out by an individual SiPM, located inside the copper block visible in fig. 5.2. This readout scheme is illustrated in figure 5.3. The first fibre bundle was read out by Photonique SiPMs of type SSPM-050701GR while Photonique SSPM-0606EXP SiPMs were used for the second one. The copper block containing the SiPMs was cooled to approximately -15°C using a combination of a Peltier element and liquid cooling agent flowing through the copper block. The far side of the fibre bundles, not read out by SiPMs, was connected to a conventional photomultiplier tube (PMT) which was replaced during the testbeam by a highly reflective aluminium foil in order to study the enhancement of the photo-electron yield.

Several auxiliary elements completed the testbeam setup. In addition to the fibre bundles, located at the centre of the setup, five scintillator panels were used for triggering purposes, located at the outermost ends of the setup. Two scintillator panels (T1 and T4 in fig. 5.2)

5 PEBS tracker prototype testbeam campaign

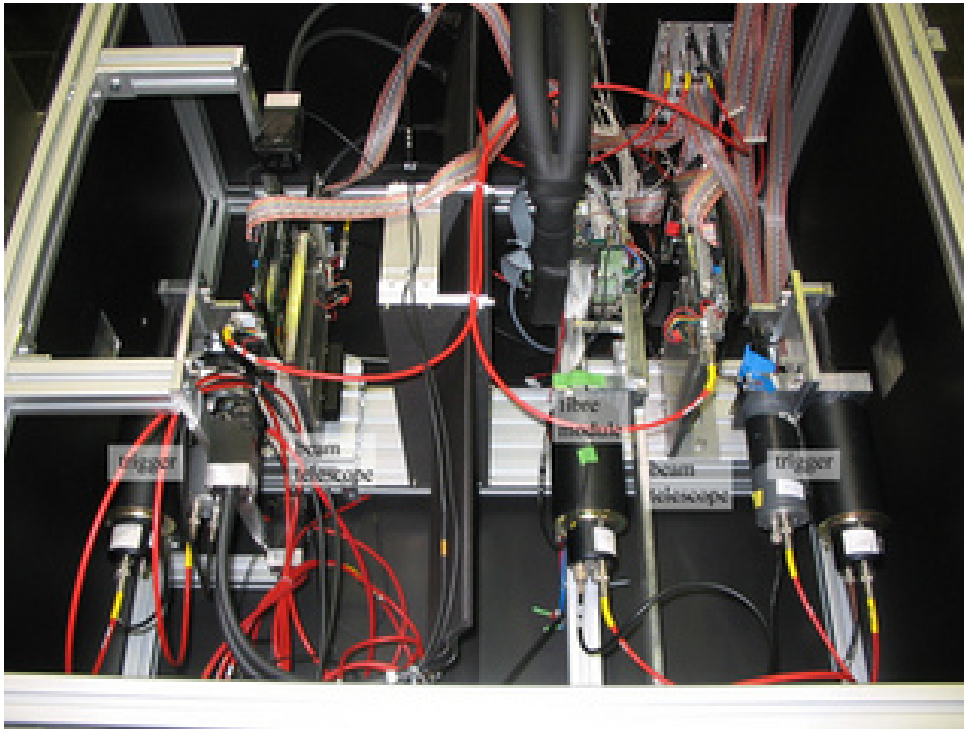


Fig. 5.1: A photograph of the setup used in the 2006 testbeam. The fibre bundles are sitting in front of the central PMT, right of the AMS-02 anticounter panels. Further out, the beam telescope modules and then the trigger counters are visible.

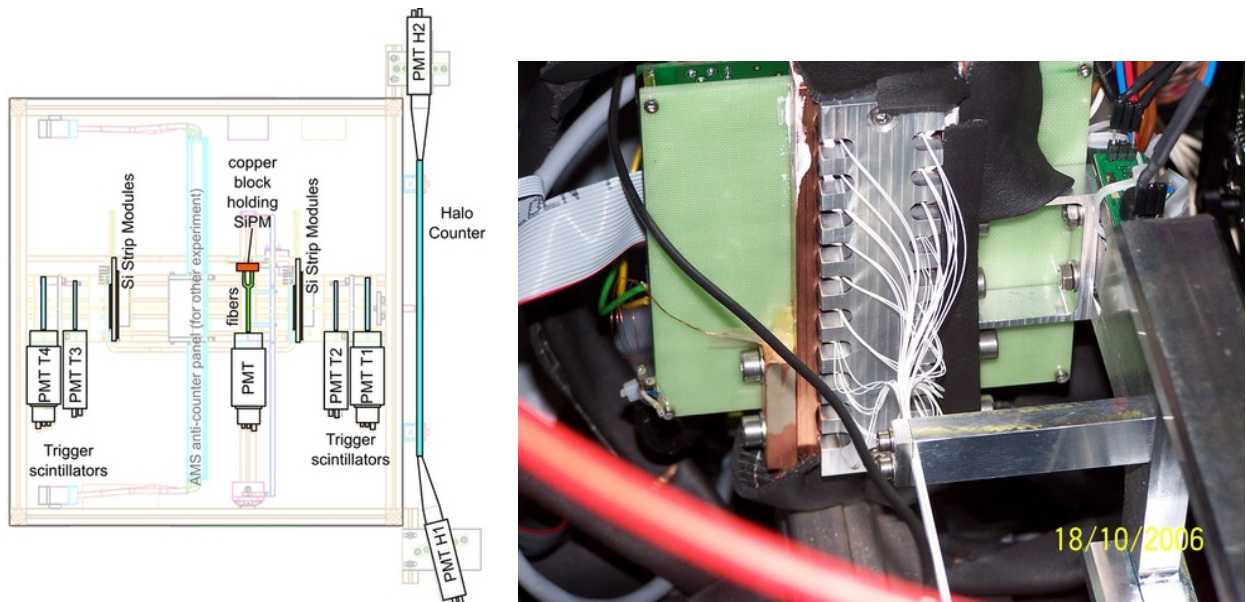


Fig. 5.2: *Left:* Schematic drawing of the testbeam setup. Reprinted, with permission, from [98]. The beam would traverse the setup from right to left. *Right:* The two 3×10 fibre bundles up close. Three consecutive fibres each were read out by an SiPM sitting in the copper block visible behind the aluminium frame.

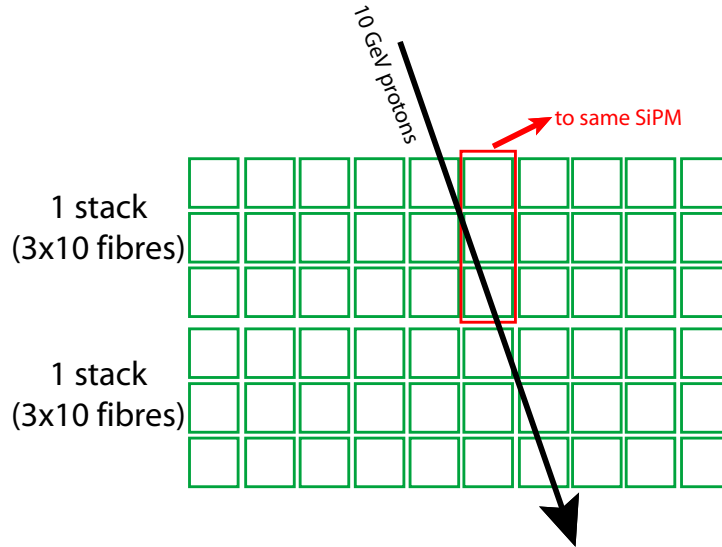


Fig. 5.3: Readout scheme used in the 2006 testbeam.

had dimensions $100\text{ mm} \times 50\text{ mm}$, and two others (T2 and T3) had dimensions $100\text{ mm} \times 5\text{ mm}$, adapted to the width of the fibre bundles. A veto counter, consisting of scintillator material with a hole of $60\text{ mm} \times 60\text{ mm}$, was used to select clean single-track events. All trigger scintillators were connected to ordinary PMTs.

For the determination of the spatial resolution, a reference measurement is mandatory, preferably with a detector whose resolution is small compared to the expected result. For that purpose, four silicon strip detectors identical to those used in the tracker endcap of the CMS experiment at the Large Hadron Collider at CERN were employed [145, 146]. The modules were of type W4 and their shape was trapezoidal because they were intended for use in an $r\phi$ -detector. The active area of each module was 115.16 mm long and its width changed from 58.06 mm to 71.272 mm over the length of the module. With 512 readout strips, the readout pitch p varied from $113\text{ }\mu\text{m}$ to $139\text{ }\mu\text{m}$. Two modules each were used to determine the trajectory coordinates parallel and perpendicular to the fibre direction, respectively. The spatial resolution achieved by one silicon strip sensor is therefore around $p/\sqrt{12} \approx 36\text{ }\mu\text{m}$, but this value becomes considerably smaller once charge sharing between adjacent strips is taken into account.

In addition to the fibre modules for PEBS, two anticounter scintillator panels for the AMS-02 experiment were tested at the same time [45].

The trigger logic was implemented using NIM electronics. The output signals of T1 and T4 were discriminated and used as input to an AND-coincidence unit. The same was done for T2 and T3. A final AND-coincidence was formed from these two AND-coincidences and provided the main trigger. This final coincidence could be blocked by the veto counter whose two PMTs were connected to a discriminator and hence to an OR-coincidence. The output signal of this OR-coincidence was connected to the common inhibit of the final AND-coincidence. A dead time of $1\text{ }\mu\text{s}$ was started after an AND-coincidence of T1 and T4 using a re-triggerable gate generator to ensure a clean event. In addition, a

5 PEBS tracker prototype testbeam campaign

dead time of 10 ms was started in parallel to the main trigger signal to make sure that event processing could be safely completed before the next trigger.

The readout chain was started by the main trigger signal. The SiPM signals were amplified and inverted and then digitised by LeCroy 2249A CAMAC ADCs whose gates were opened for 100 ns by the main trigger signal. The bias voltages for the SiPMs were adjusted separately.

The four APV25 chips [147] located on each CMS silicon sensor modules sample their signal each 25 ns and store it in 192-cell circular pipelines. An ARC system [148], normally used to test the CMS silicon modules, was employed to control the APV25 chip and connected to the same readout PC as the CAMAC controller used to steer the ADCs digitising the SiPMs. Upon reception of the main trigger signal, the ARC system would stop the signal sampling in the APV25 chips and transmit the values in the pipeline slots corresponding to a predefined offset in time. The data from the ARC system and the CAMAC ADCs were then assembled into a combined event on the readout PC and written to disk. The timing of the trigger and readout system was adjusted such that the SiPM signals arrived during the gate in the CAMAC ADCs while the offset in the ARC system was matched to the delay between the passage of the beam particle and the arrival of the main trigger signal. Coherent events were assured by linking the entire readout software into one executable. Many more details on the trigger logic and readout system are found in [98]. The overall readout rate was limited by the ARC system to about 60 Hz. Taking the allocated beam and its bunch structure into account, an effective trigger rate of roughly 2 Hz was achieved over the course of the testbeam.

Figure 5.4 shows a screen shot of the dedicated online software developed for the testbeam that offered a graphical user interface to remotely control the data taking, monitor the incoming raw data, and read the temperature and humidity sensors located inside the testbeam setup.

5.1.2 Analysis procedure

The first step in the analysis chain is the identification of clean single-track events in the beam telescope. The information available for each event consists of the raw ADC counts for all 2048 channels in the four beam telescope modules. First, the pedestal and noise values for each channel are calculated using dedicated pedestal runs that were taken with random triggers every few hours throughout the testbeam. Here, the pedestal and noise are defined as the empiric mean and standard deviation of the ADC counts distribution in each channel. For a given event, the significance s_i of a channel i belonging to APV25 j is then calculated as

$$s_i = \frac{S_i - p_i - c_j}{\sigma_i} \quad (5.1)$$

from the signal S_i , pedestal p_i and noise σ_i of channel i , all given in ADC counts. c_j is the common-mode noise of the 128 channels belonging to the given APV25, defined as the median of the pedestal-subtracted signals. The common-mode noise is a uniform shift in the pedestals of all channels of a chip that varies from event to event, usually caused by an external source of noise. As an example, figure 5.5 shows the noise values found for the four modules in several pedestal runs scattered over the duration of the testbeam. The

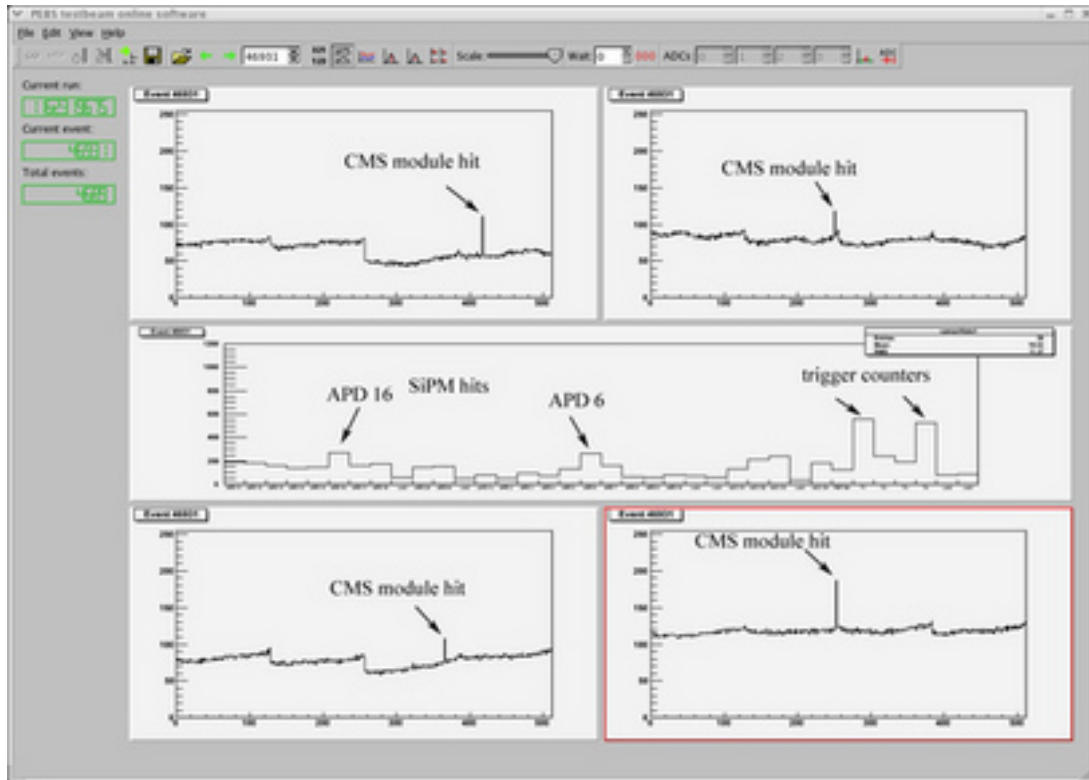


Fig. 5.4: Graphical user interface of the online software used for data acquisition during the testbeam. A golden event is shown here: all four CMS modules have exactly one cluster and there are hits in two SiPMs reading out two consecutive fibre slots (numbers 6 and 16 in this case). In addition, the energy deposition in the trigger counters is visible.

variation in time is small and a good strip has a noise level of around 1.4 ADC counts. There are, however, a number of noisy or dead strips, and one of the modules had one dead APV25 chip.

Next, a cluster finding algorithm is applied to each module. A seed strip having at least $s_i \geq 4$ is searched and neighbouring clusters with $s_{i \pm k} \geq 2$ are added to the cluster. A single-track event is then defined as having exactly one such cluster on each module in the beam telescope. Figure 5.6 depicts the reconstructed cluster positions for each of the four beam telescope modules. The strips of modules 1 and 3 were oriented parallel to the fibres, while those of modules 0 and 2 were oriented perpendicular to the fibres. The distributions are governed by the vertical and horizontal beam profiles, respectively, as well as by the noisy and dead strips mentioned above. Here, the cluster position was calculated as the weighted mean of the participating strip numbers, using the amplitudes corrected for pedestal and common-mode noise as weights.

The next task is to calculate the intersection point of the particle track with the fibre module. The trapezoidal shape of the beam telescope modules complicates this matter. A track fit is performed, with the goal of finding the trajectory $\vec{x}(z)$ which is taken to be a straight line. z is the coordinate perpendicular to the planes of the beam telescope modules. For a given z , let u and v be the coordinates of a point measured in the frame

5 PEBS tracker prototype testbeam campaign

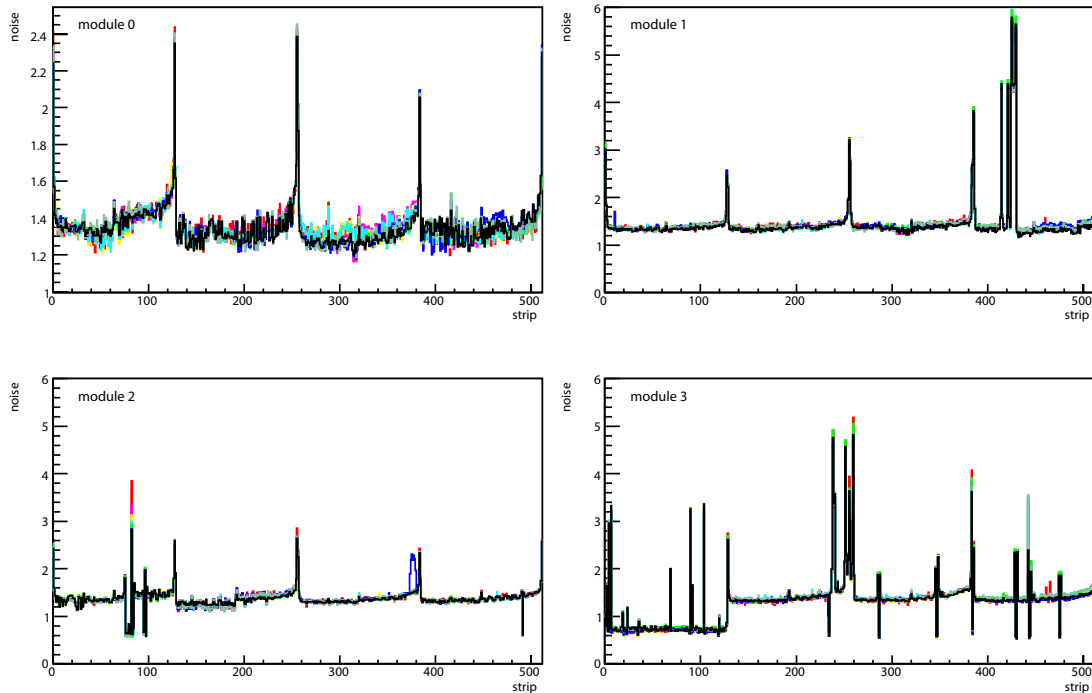


Fig. 5.5: Noise values (in ADC counts) for the four CMS beam telescope modules, as a function of the strip number. Noise obtained during different pedestal runs over the course of the testbeam is shown in different colours. The scale for module 0 was magnified to illustrate the changes over time. High noise values at strips 0, 128, 256, 384, and 512 mark the boundaries between two APV25 readout chips. Strips with anomalously high or low noise indicate noisy or dead channels. The first APV25 on module 3 was inoperative.

of a beam telescope module. The coordinates x and y of this point as measured in the frame of the testbeam setup box can be obtained by using the rotation matrix

$$R = \begin{pmatrix} \cos \alpha & -\sin \alpha \\ \sin \alpha & \cos \alpha \end{pmatrix}$$

where α is the angle of rotation for the strip at the centre of a given cluster which can be calculated from the strip number, the orientation of the module inside the setup, and the module geometry. The covariance matrix of a point measured on the module is taken to be

$$V = \begin{pmatrix} \sigma_u^2 & 0 \\ 0 & \sigma_v^2 \end{pmatrix}$$

σ_u and σ_v are determined by the strip length l and pitch d at the centre: $\sigma_u = l/\sqrt{12}$ and $\sigma_v = d/\sqrt{12}$. The covariance matrix U in the x, y -frame needed for the calculation of the χ^2 of the track fit can then be obtained using standard error propagation [79] as

$$U = AVA^T \tag{5.2}$$

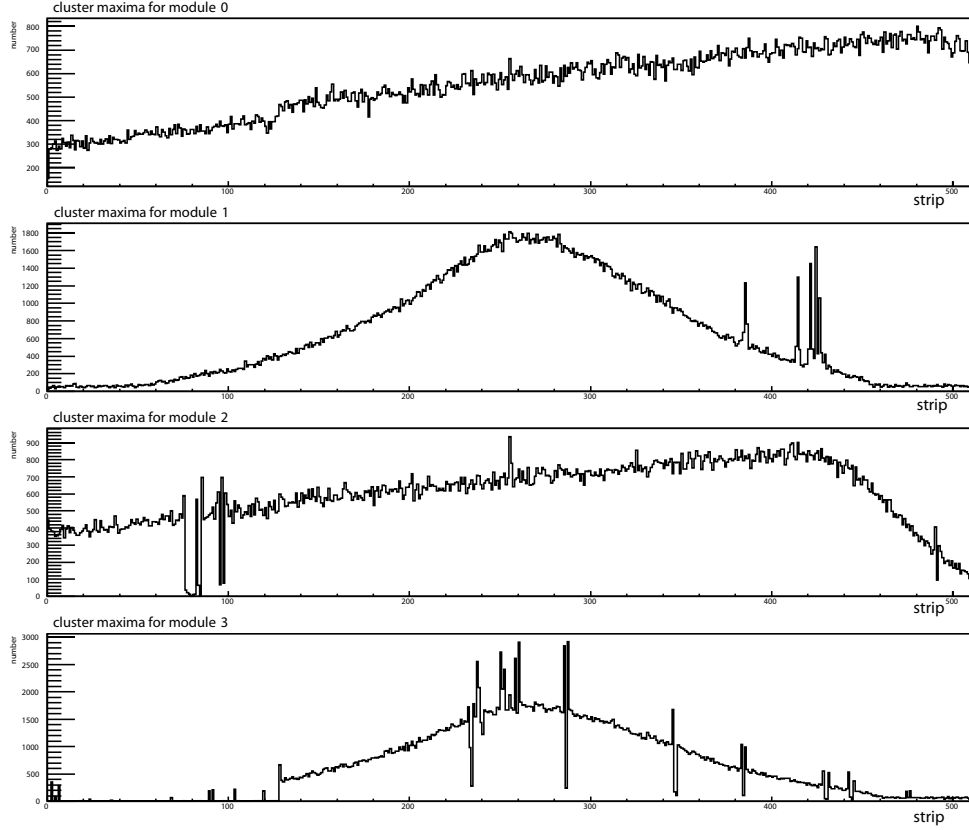


Fig. 5.6: Reconstructed cluster positions on the beam telescope modules. The beam profile determines the shape of the distributions. In additions, some noisy and some dead strips are visible, especially on modules 1 and 2, and the first APV25 readout chip for module 3 is seen to be not operational here. The strips of modules 1 and 3 were oriented parallel to the fibres, while those of modules 0 and 2 were oriented perpendicular to the fibres.

where A is the matrix of derivatives

$$A = \begin{pmatrix} \frac{\partial x}{\partial u} & \frac{\partial x}{\partial v} \\ \frac{\partial y}{\partial u} & \frac{\partial y}{\partial v} \end{pmatrix}$$

Introducing an index $m \in [1, 4]$ to label the four clusters on the track, and letting Δx_m and Δy_m be the track residuals on the m -th module, the χ^2 that has to be minimised during the track fit is given by

$$\begin{aligned} \chi^2 &= \sum_{m=1}^4 \Delta \vec{x}_m^T U_m^{-1} \Delta \vec{x}_m \\ &= \sum_{m=1}^4 \frac{\Delta x_m^2 c_m^2 \sigma_v^2 + \Delta x_m^2 s_m^2 \sigma_u^2 + \Delta y_m^2 c_m^2 \sigma_u^2 + \Delta y_m^2 s_m^2 \sigma_v^2 + 2\Delta x_m \Delta y_m c_m s_m (\sigma_y^2 - \sigma_x^2)}{\sigma_u^2 \sigma_v^2} \end{aligned} \quad (5.3)$$

5 PEBS tracker prototype testbeam campaign

where $\Delta\vec{x}_m \equiv (\Delta x_m, \Delta y_m)$, and $c_m \equiv \cos \alpha_m$ and $s_m \equiv \sin \alpha_m$.

In order to obtain the mean photo-electron yield and spatial resolution of the fibre modules, the individual SiPMs have to be calibrated to yield the pedestal p , i.e. the loca-

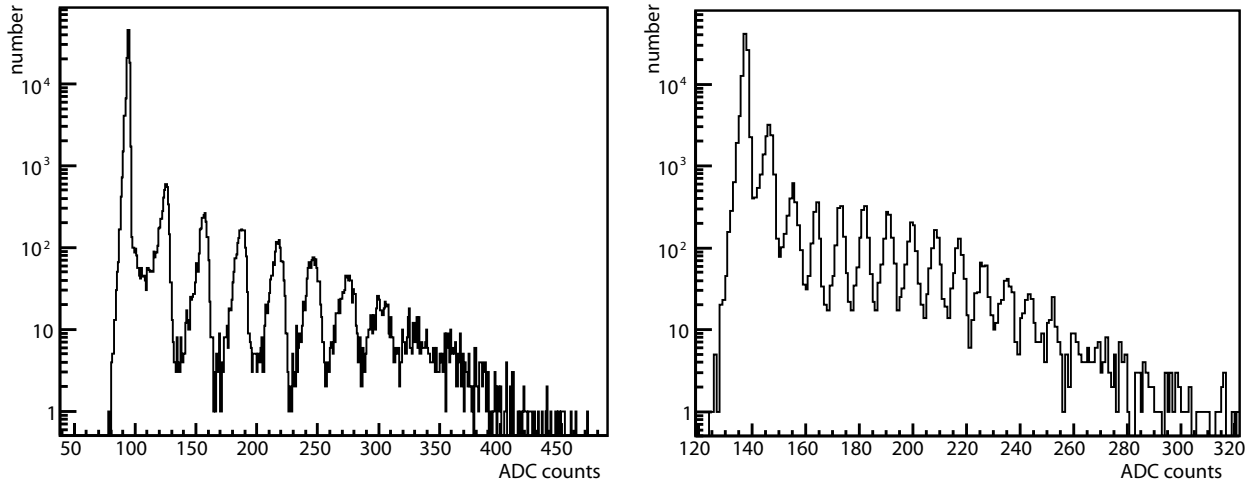


Fig. 5.7: Two examples (fibre channels 1 and 12) of raw ADC spectra observed with SiPMs of type SSPM-050701GR (*left*) and SSPM-0606EXP (*right*), for runs with perpendicular incidence and reflective foil at one end of the fibre bunches, as used for the pedestal and gain calibration.

tion of the 0-photo-electron-peak, and the gain g , i.e. the mean distance between two photo-electron peaks, measured in ADC counts. The signal s (in photo-electrons) is then calculated from the amplitude a (in ADC counts) simply by

$$s = \frac{a - p}{g} \quad (5.4)$$

Two examples of the raw ADC spectra observed for runs with perpendicular incidence and reflective foil at one end of the fibre bunches are shown in figure 5.7. The individual photo-electron-peaks are easily identified, and a semi-automatic peak finding procedure was used for the determination of their locations. Pedestal and gain were then calculated individually for each SiPM.

For the analysis of the prototype performance, the beam telescope can now be used to interpolate the intersection point (x, y) of the particle trajectory with the fibre module. With the number of photo-electrons determined for all SiPM channels in a given event, all fibres whose amplitude exceeded a cut of 2 photo-electrons were identified and the intersection point was histogrammed for those fibres. The results for one of the fibre bunches are shown in figure 5.8. Each fibre is shown in a different colour and the figure can be interpreted as showing a picture of the fibre module taken by the beam telescope. The determination of the spatial resolution requires the knowledge of the fibre positions with respect to the beam telescope. These are measured by projecting the histograms shown in the figure to the y -axis and fitting a Gaussian to each of them. The mean of the Gaussian is then taken as the position of the respective fibre, as illustrated in figure 5.9.

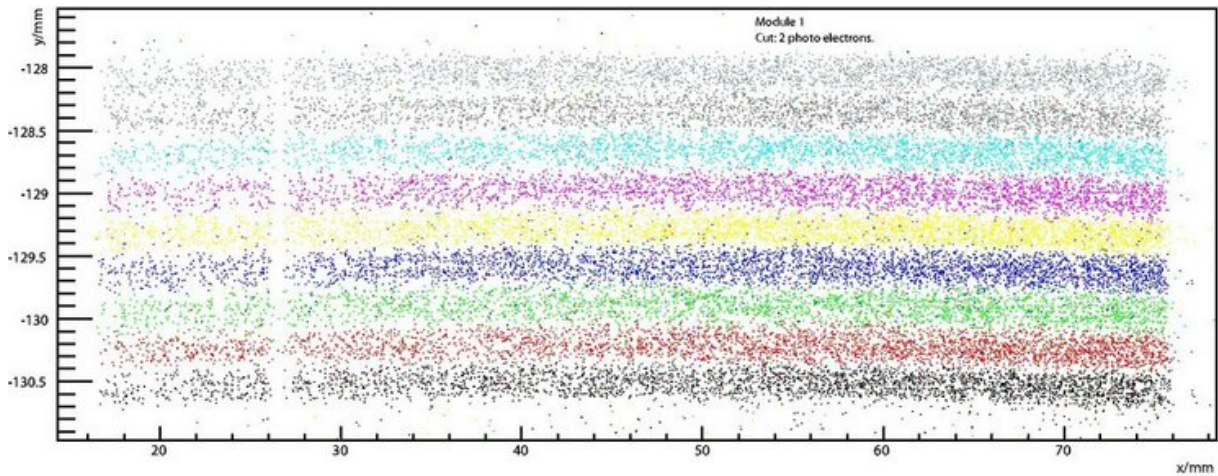


Fig. 5.8: Coordinates interpolated from beam telescope tracks for hits in the fibres of fibre module 1. A cut of 2 photo-electrons was employed in this case. Each colour corresponds to a single fibre. The figure may be interpreted as a picture of the fibre bunch, taken by the beam telescope. The gap at $x \sim 26$ mm is due to dead strips in module 2 of the beam telescope, as shown in figure 5.6.

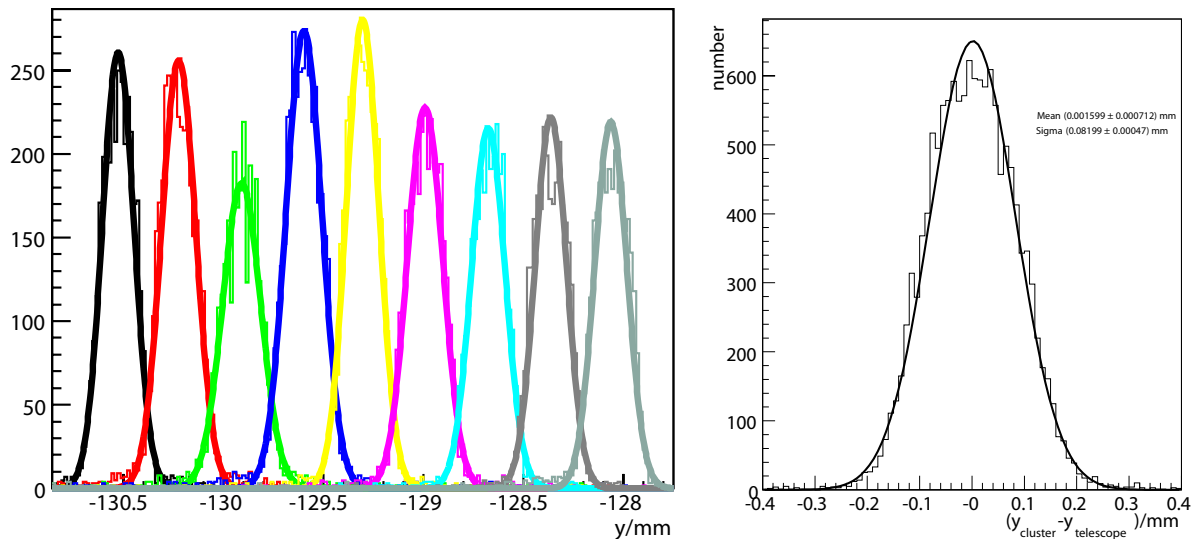


Fig. 5.9: *Left:* Determination of the fibre positions from projections onto the y -axis. *Right:* Determination of the spatial resolution from the distribution of track residuals. Distributions for fibre module 1 are shown as an example.

Figure 5.10 contains a plot of the fibre positions so obtained as a function of the fibre number. The slope determined from a straight-line fit is then the mean distance between two fibres. The value of $308.4 \mu\text{m}$ found for both modules is in excellent agreement with the nominal fibre thickness of $300 \mu\text{m}$ considering that a small amount of glue may be present between the fibres. The figure also shows histograms of the residuals of the fibre positions with respect to a straight line, and root mean square values for the deviation

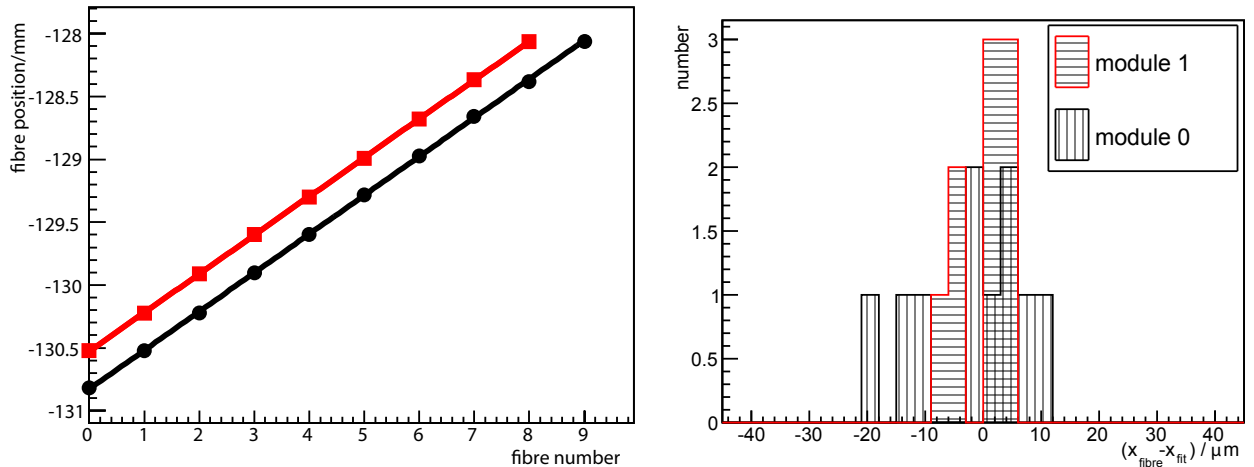


Fig. 5.10: Determination of mean fibre pitch from a straight-line fit to the positions obtained as shown in figure 5.9 (*left*) and residual plots for the fits (*right*). The mean fibre pitch is $308.4 \mu\text{m}$ for both modules, and the root mean square values for the deviation of the fibre positions from the ideal ones are $9.2 \mu\text{m}$ for module 0 and $4.1 \mu\text{m}$ for module 1.

of the fibre positions from the ideal ones are found to be $9.2 \mu\text{m}$ and $4.1 \mu\text{m}$ for the two modules.

The determination of the spatial resolution proceeds as follows. Using an algorithm analogous to the one used for cluster finding on the beam telescope modules, clusters of neighbouring fibre channels are identified. Here, a cut of 3 photo-electrons is used for the seed channel, and 2 photo-electrons for the neighbouring channels. The y coordinate is then calculated as the weighted mean of all N channels belonging to the cluster,

$$y = \frac{\sum_{i=1}^N s_i y_i}{\sum_{i=1}^N s_i} \quad (5.5)$$

where the signals s_i are given in photo-electrons and the fibre positions were determined as in figure 5.9. The difference of the track intersection point as measured by the beam telescope and the cluster position according to (5.5), $y_{\text{cluster}} - y_{\text{telescope}}$, was then histogrammed and the standard deviation of a Gaussian distribution fitted to the histogram is called the spatial resolution. This is illustrated in figure 5.9, too. For perpendicular incidence, spatial resolutions of $82 \mu\text{m}$ and $88 \mu\text{m}$ are found for the two modules, read out by SiPMs of types SSPM-050701GR and SSPM-0606EXP with lower and higher noise rate, respectively. This has to be compared to the expectation of $b/\sqrt{12} \approx 87 \mu\text{m}$ where $b = 300 \mu\text{m}$ is the fibre width. However, the region of the fibre that will actually produce scintillation light is reduced somewhat by the extension of the protective cladding of around $12 \mu\text{m}$ to both sides.

Using the information provided by the beam telescope, the signal spectra and noise spec-

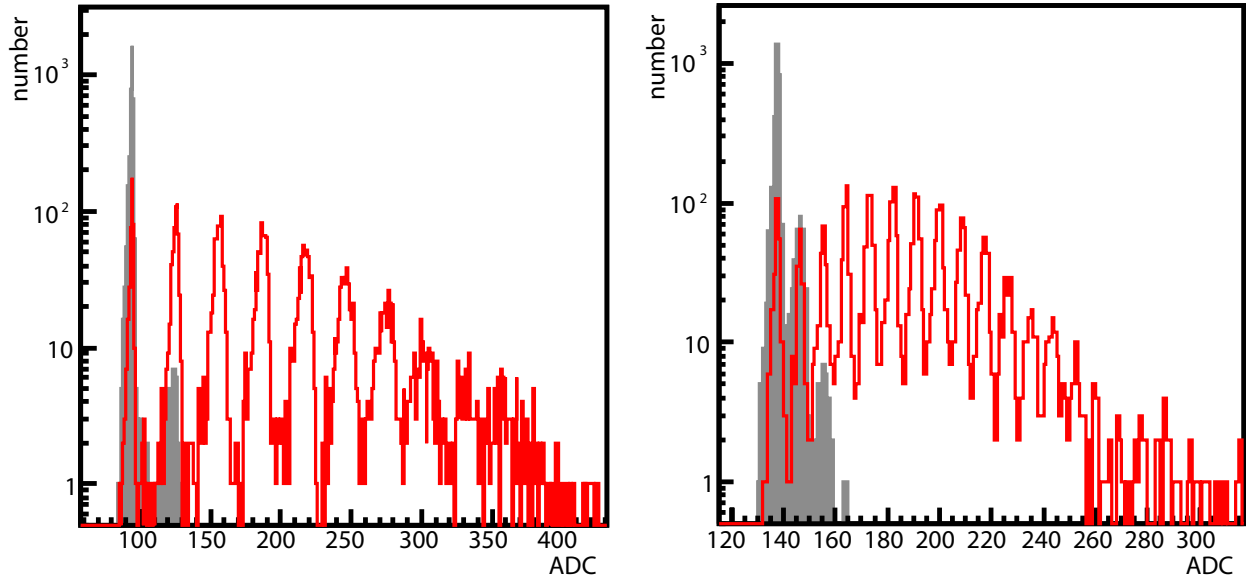


Fig. 5.11: Two examples (fibre channels 1 and 12) of raw ADC spectra observed with SiPMs of type SSPM-050701GR (*left*) and SSPM-0606EXP (*right*), for runs with perpendicular incidence and reflective foil at one end of the fibre bunches. Events for which the beam telescope indicated a hit in the corresponding fibres are histogrammed in red, while the grey histograms show the dark count. The histograms have been scaled to equal integral. The individual photo-peaks are clearly visible.

tra can be extracted from the raw ADC spectra. Two examples, for the same channels as in fig. 5.7, are shown in figure 5.11. An event is counted for the signal spectrum if the beam telescope indicated a hit within $100\ \mu\text{m}$ of the fibre centre and for the noise spectrum if the hit was at least $500\ \mu\text{m}$ away from the fibre centre. For a correct determination of the photo-electron yield, the effect of optical pixel crosstalk must be taken into account. Occasionally, photons created during an avalanche in one of the SiPM pixels will trigger a discharge in one of the neighbouring pixels, with a probability $p_{\text{crosstalk}}$. In the analysis of [98], 1.94 ± 0.27 and 3.12 ± 0.19 photo-electrons were found for the SiPMs of type 050701GR without and with reflective foil, respectively. For the SSPM-0606EXP, the numbers are 3.59 ± 0.24 and 5.43 ± 0.31 . $p_{\text{crosstalk}}$ is found to be on the 5-10 % level.

The mounting containing the fibre modules could be rotated in steps of $\alpha_{\text{slot}} = 10^\circ$ around an axis parallel to the fibres to study the dependency of the spatial resolution on the angle of incidence. Data at nominal values of -10° , 0° , 10° , 20° , 30° , and 40° were taken, but without the reflective foil. The analysis procedure outline so far was repeated for each orientation. As a cross-check, the fibre distance was obtained like in fig. 5.10 and is shown in figure 5.12 as a function of the nominal angle of rotation. As the measured distance d is the one projected into the plane of the beam telescope, it can be expected to follow

$$d = d_0 \cos(n\alpha_{\text{slot}}) \quad (5.6)$$

5 PEBS tracker prototype testbeam campaign

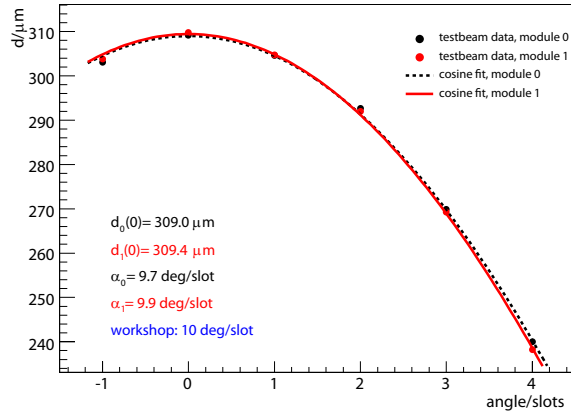


Fig. 5.12: Mean distance of adjacent fibre slots, projected into the beam telescope plane, as a function of rotation angle. The angle is given as the number of slots moved forward on the rotator arm, with a nominal value of $10^\circ/\text{slot}$. Allowing for roughly $10\ \mu\text{m}$ of glue between the fibres, the nominal values both of the fibre thickness and the angular distance between two slots are recovered.

where n is the number of slots on the fibre mounting that the modules were rotated by. Indeed, a fit of a cosine function gives excellent agreement with the nominal values, as shown in the figure.

For the determination of the spatial resolution as a function of the angle of incidence, treated in the next section, an additional effect has to be taken into account. As a particle traversing the fibre modules with a certain angle will deposit energy across more than one

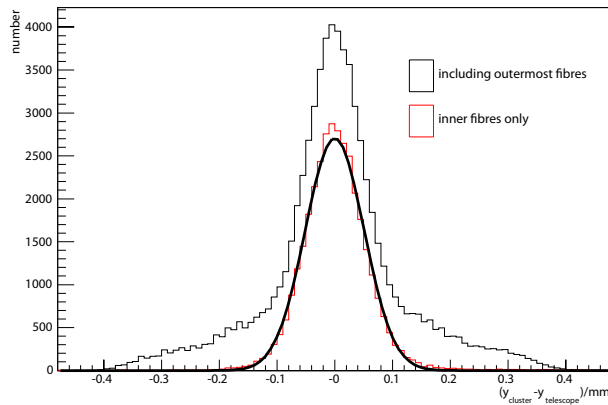


Fig. 5.13: The effect of ignoring the outer two fibre slots on each side on the calculated spatial resolution is shown here. For the inner fibres, the distribution of the track residuals becomes Gaussian. Monte Carlo data at 40° rotation of the fibre bunch were used here.

SiPM channel, the information for tracks grazing the outermost fibres will be incomplete and the intersection points determined according to (5.5) will be of limited accuracy. This is illustrated in figure 5.13 showing that the intersection points of trajectories can only be

measured reliably at high angles if the outermost two fibres are ignored. Naturally, this can only happen at the expense of tracking efficiency.

5.1.3 Prototype performance and comparison to Monte Carlo study

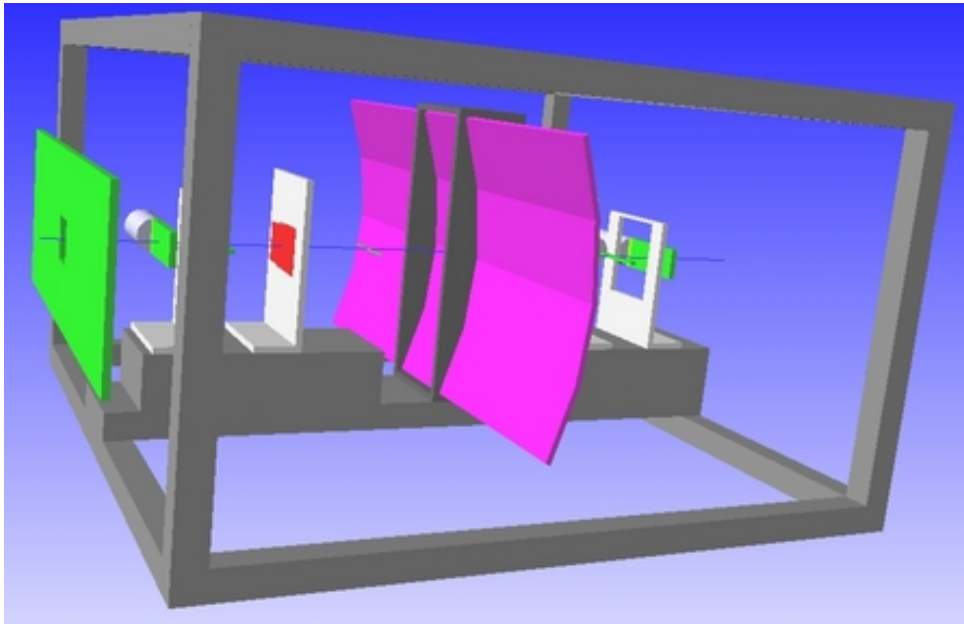


Fig. 5.14: Visualisation of the detector setup used in the Geant4 simulation of the testbeam. The veto and trigger scintillators are shown in green, CMS beam telescope models are painted in red, and the AMS-ACC panels are pink. The fibre bunch is barely visible on this scale and is located in front of the ACC panels. Structural elements and PMTs are shown in grey.

For the generalisation of the testbeam results, a Geant4 Monte Carlo simulation of the testbeam setup was created (fig. 5.14). All components in or close to the beam were included, namely the veto and trigger scintillators with PMTs, beam telescope modules and ACC panels with mounting frames, and the scintillating fibres, as well as the aluminium carrier frame. The simulation and digitisation of the scintillating fibres and the SiPMs used for their readout closely follows the prescriptions used for the full PEBS simulation as outlined in section 4.2.3. For an energy deposition in one of the CMS modules, two hits were generated in the channels adjacent to the intersection point, with their amplitudes calculated from a simple linear interpolation based on the position of the energy deposition. The results were then stored in the same format as the actual testbeam data so that the same analysis as described in the previous section can be applied to the simulated data.

From a Gaussian fit to the distribution of track residuals $y_{\text{track}} - y_{\text{cluster}}$, the spatial resolution can now be calculated for both data and simulation (fig. 5.15). This has been done for all angles of incidence at which data were taken during the testbeam. It must be noted however, that the spatial resolution determined from the track residuals is measured in the coordinate frame fixed by the beam telescope. The spatial resolution $\sigma_{y'}$ measured

5 PEBS tracker prototype testbeam campaign

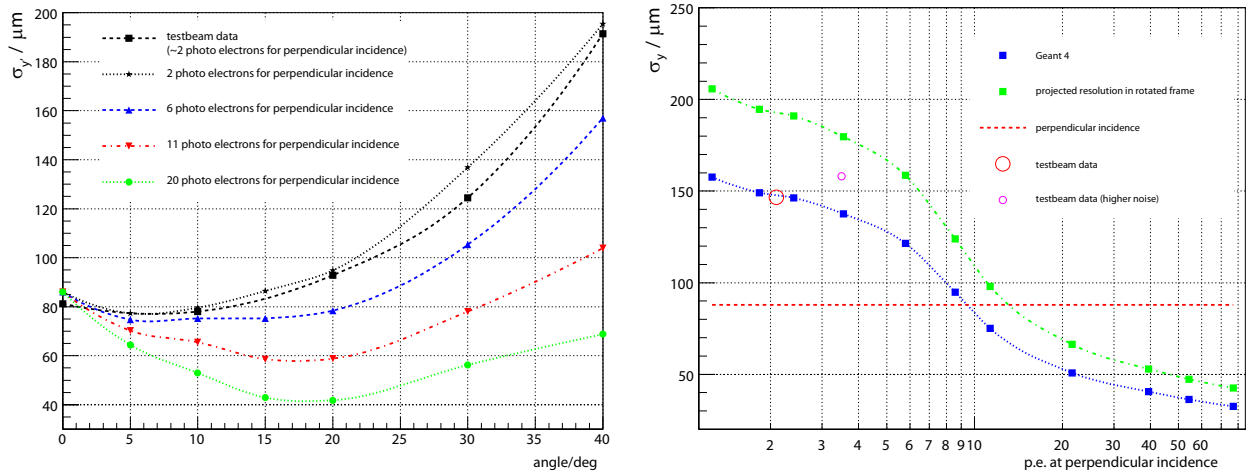


Fig. 5.15: *Left:* Spatial resolution as a function of angle of incidence. Simulation results for various overall light yields, given by the number of mean photo-electrons at perpendicular incidence, are shown, together with testbeam results. *Right:* Spatial resolution of the fibre module as obtained from the Geant4 simulation. The spatial resolution is shown for an angle of incidence of 40° as a function of the photo-electron yield for perpendicular incidence. The blue curve shows the resolution obtained in the plane parallel to the beam telescope modules, while the green curve shows the resolution in the plane parallel to the fibre module, as calculated from (5.7). The value at perpendicular incidence is indicated by the horizontal line. For comparison, the values found in the testbeam are shown, for the fibre bunch read out by the SSPM-050701GR (big circle) and the SSPM-0606EXP (small circle). In the latter case, the deviation from the Monte Carlo curve is explained by the higher noise of this SiPM type.

in the coordinate frame fixed to the fibre bunches can be calculated by correcting for the projection effect as follows:

$$\sigma_{y'} = \frac{\sigma_y}{\cos \alpha} \quad (5.7)$$

where α is the angle of rotation of the fibre bunches as above.

Overall, there is good agreement between the simulation and the testbeam data over the entire range of the angle of incidence. This indicates a good modelling of the detector physics. The simulation can therefore be used to extrapolate the spatial resolution for higher photo-electron yields. The results indicate that there is no dependence of the spatial resolution on the photo-electron yield for small angles of incidence. This is expected because a particle will only deposit energy in a single fibre in this case, leading to a resolution of $b/\sqrt{12}$. For higher angles however, the cluster position is calculated as a weighted mean of the fibre positions which promises an improvement in the spatial resolution as the discretisation imposed by the fibre width is somewhat removed. On the other hand, the individual weights are subject to statistical fluctuations that tend to deteriorate the spatial resolution. The fluctuations become smaller for higher light yields. Also, the fact that the energy deposition is distributed across several fibres at higher angles of incidence means that each individual fibre will receive less photo-electrons. The interplay of these effects produces a steep decline in the spatial resolution for low

photo-electron yields at high angles of incidence. For higher photo-electron yields, the dependence on the angle of incidence becomes much less severe, and a minimum is reached at intermediate angles. For very high photo-electron yields, the distribution of the signal across fibres becomes very effective in improving the spatial resolution beyond the value of $b/\sqrt{12}$.

5.2 Second testbeam 2008

After the first testbeam had been completed, the technology for production of ribbons of round fibres of $250\ \mu\text{m}$ diameter was developed allowing the construction of a tracker module prototype according to the design outlined in section 4.2.2. The second testbeam took place at CERN in June 2008 and lasted two weeks. Right in time for the testbeam, arrays of SiPMs made by Hamamatsu became available and were used to create one tracker prototype module. The response of this module consisting of scintillating fibres of $250\ \mu\text{m}$ diameter and a Hamamatsu SiPM array to 10 GeV protons at perpendicular incidence will be studied in the remainder of this section in order to justify the assumptions made in section 4.2.3. In addition, a readout board for the SiPMs based on the VA32 amplifier/shaper chip was developed. The CMS beam telescope modules were replaced by two silicon ladders built for the AMS-02 tracker. This meant that the same DAQ system could now be used for both the beam telescope and the SiPMs, allowing a readout rate that was an order of magnitude higher than in the first testbeam.

5.2.1 Setup description

The testbeam setup (fig. 5.16) is based on the one used for the first testbeam. Two trigger scintillators, a veto scintillator, two silicon ladders serving as a beam telescope, and four fibre module prototypes were mounted to an aluminium frame. The setup was hermetically closed on all sides to remove any ambient light and equipped with desiccant bags to reduce humidity to a minimum. The fibre modules could be rotated around their longitudinal axis to study their behaviour with respect to different angles of incidence. Again a 10 GeV proton beam provided by the T9 beamline at CERN was used.

Five prototype modules were tested:

- A module made of square Bicron BCF-20 fibres of $300\ \mu\text{m}$ width with the same geometry as in the first testbeam for comparison, but this time read out by individual Hamamatsu S10362-11-100C SiPMs.
- A module made out of five layers of round Bicron BCF-20 fibres of $250\ \mu\text{m}$ diameter, the inner 16 fibre columns of which were read out by individual Hamamatsu S10362-11-100C SiPMs.
- A module made of five layers of round Kuraray SCSF-81M fibres [149] of $250\ \mu\text{m}$ diameter, the inner 16 fibre columns of which were read out by individual Hamamatsu S10362-11-100C SiPMs.

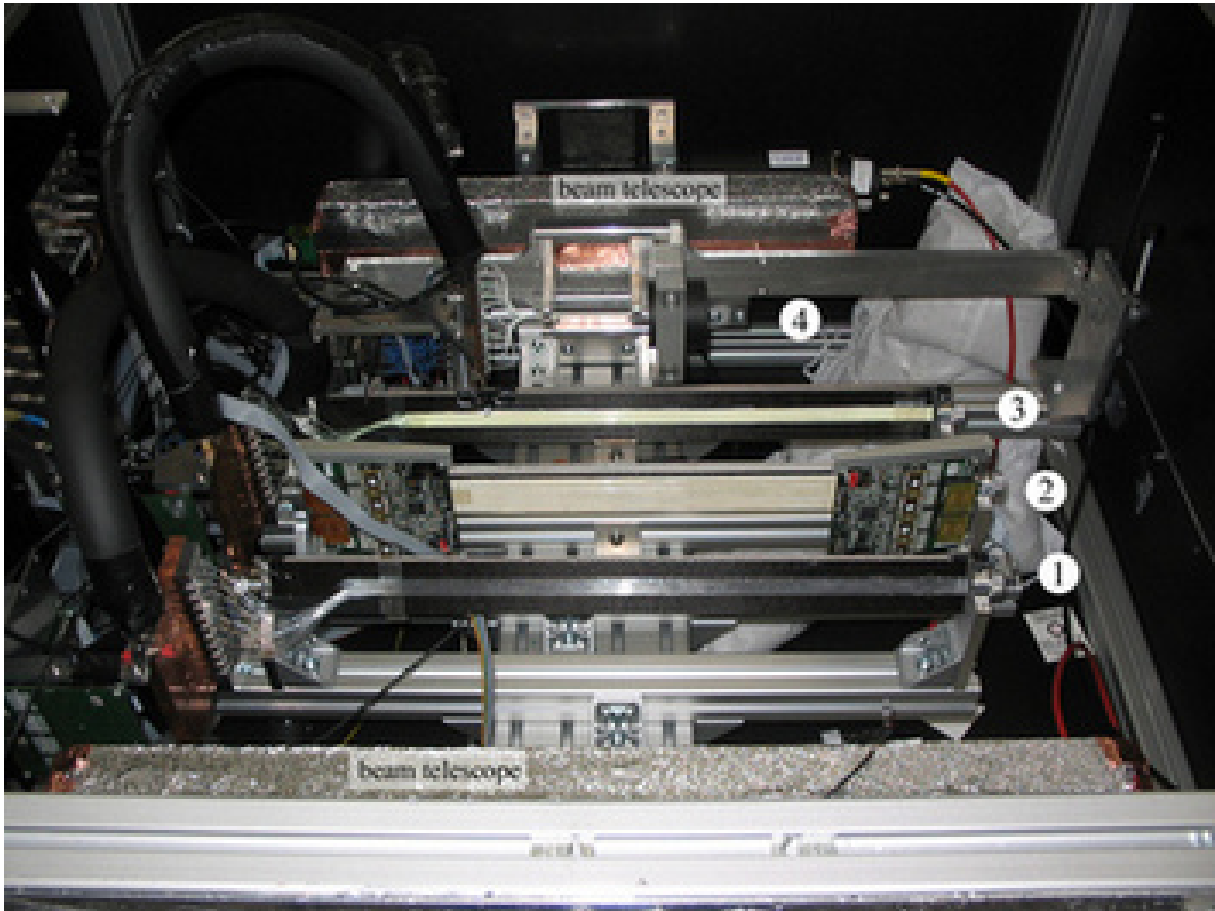


Fig. 5.16: A photograph of the 2008 testbeam setup after installation of the module containing the Hamamatsu SiPM arrays. Four fibre modules are visible at the centre of the picture: from front to rear, round Kuraray fibres with individual readout (1), the module read out by Hamamatsu SiPM arrays, with round Kuraray fibres (front) and round Bicron fibres (rear) ((2), fig. 5.17), round Bicron fibres with individual readout (3), and square Bicron fibres with individual readout (4). The beam telescope ladders are located inside the boxes wrapped with aluminium foil. The PMT reading out the rear trigger counter is visible, too.

- A module with a fibre ribbon consisting of 5×128 fibres on each side, one ribbon made of Bicron fibres, the other one made of Kuraray fibres, with readout by IRST-itc SiPM arrays located on a hybrid as sketched in fig. 4.3. This module was replaced halfway through the testbeam by
- a module with a fibre ribbon consisting of 5×128 fibres on each side, one ribbon made of Bicron fibres, the other one made of Kuraray fibres, with readout by IRST-itc arrays on one side and Hamamatsu MPPC 5883 arrays (fig. 4.5) on the other side (fig. 5.17). Only one Hamamatsu array was operative due to difficulties in the hybrid production. This one was located in front of the Kuraray fibres. The data taken by this array will be studied in the following.

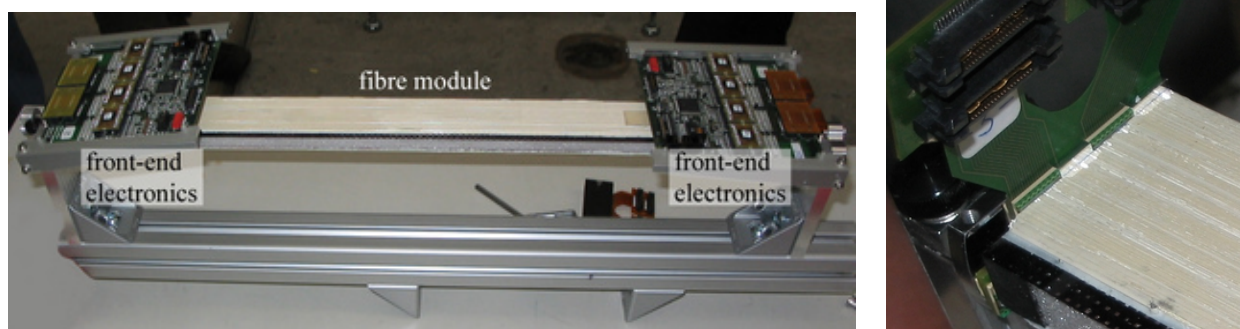


Fig. 5.17: *Left:* The fibre module with readout by Hamamatsu SiPM arrays before installation. The front-end electronics boards used in the testbeam are visible at the sides. *Right:* Close-up view of one end of the module before connection to the front-end electronics board. The SiPM arrays themselves are sitting in front of the fibres, but their connector pads as well as part of the reflective foils are visible.

While the individual SiPMs were located inside copper blocks that were cooled to around -12°C , the SiPM arrays were operated at a temperature that varied between 16°C and 18°C along with the day-night cycle. All SiPMs were connected to VA.32/75 chips. The VA [150] is a high dynamic range charge-sensitive preamplifier-shaper circuit, with simultaneous sample and hold. It has a multiplexed analog readout and is available in versions with different numbers of input channels and gains. It was used for the readout of both the beam telescope and the SiPMs here.

The AMS-02 ladders [151] used as a beam telescope are made up of double-sided silicon micro-strip detectors. Each ladder is composed of several silicon sensors of dimensions $72.045 \times 41.360 \text{ mm}^2$ and $300 \mu\text{m}$ thickness. The sensors have metallisations on both sides, parallel to the length of the ladder on the front (S-)side and perpendicular on the rear (K-)side, with readout pitches of $110 \mu\text{m}$ and $208 \mu\text{m}$, respectively. The readout strips of the individual sensors are daisy-chained. In total, a ladder provides 1024 readout channels, 640 for the S-side and 384 for the K-side. As the readout strips on the K-side are transverse, a single readout channel there corresponds to a series of spatial positions due to the daisy-chaining. The spatial resolution of an AMS-02 ladder has been demonstrated to be $10 \mu\text{m}$ on the S-side and $30 \mu\text{m}$ on the K-side [152]. The signals induced on the readout strips are preamplified and shaped by VA64 chips located on the front-end electronics boards adjacent to the ladders.

The DAQ system used in the testbeam is based on components used for the AMS-02 experiment [153]. Two TDR2 boards gather the signals stored on reception of a trigger signal by the VAs of both the ladders and the SiPMs. A TBS board provides the bias voltage for the silicon ladders while a TPSFE board creates the low voltages needed by the system. A JINF board serves as event builder, assembling the information provided by the TDR2s to form a coherent event. This event is then stored until the JINF is queried by the readout software. The readout software runs on an ordinary PC connected

5 PEBS tracker prototype testbeam campaign

to the JINF from its parallel port operated in EPP mode. All boards are powered and communicate with each other via a common backplane.

The TDR2s can be operated in either raw or compressed mode. For the SiPM readout, the raw mode is used meaning that the raw data from all 1024 channels, only a fraction of which are actually connected to an SiPM, are transferred, at the expense of readout rate. Contrary to this, the silicon ladders are read out in compressed mode. Using pedestal and noise values calculated for each channel from data taken in a dedicated calibration run, performed before each physics run, clusters are identified by a digital signal processor (DSP) located on the TDR2. A correction for common-mode noise is performed automatically, too. Only the clusters are then included in the event, resulting in a significant reduction in event size and corresponding increase in readout rate. Overall, a readout rate of roughly 200 Hz was achieved in the testbeam.

The two trigger scintillators had dimensions of $14 \times 4 \times 1 \text{ cm}^3$ and were read out by ordinary PMTs. The veto scintillator was the same as used in the first testbeam. The trigger scheme was again based on NIM electronics and had to be optimised for speed as the hold signal for the VA_32/75 chips reading out the SiPMs had to arrive around 65 ns after the particle crossing as the SiPM signal pulse reaches its maximum at that time. This was achieved by using only a single coincidence of the two PMTs reading out the trigger scintillators. The two PMTs at each side of the veto panel and the busy signal of the JINF were used as a veto on the coincidence. A post-event dead-time of $150 \mu\text{s}$ was started along with the hold signal, and a pre-event dead-time of $5 \mu\text{s}$ was started by a signal from any of the trigger PMTs.

5.2.2 Data analysis

The analysis presented here deals with the data taken with one Hamamatsu SiPM array in front of a ribbon of Kuraray fibres, with 10 GeV protons at perpendicular incidence. The fibre ribbon consisted of five layers of fibres of $250 \mu\text{m}$ diameter, at a nominal pitch of $275 \mu\text{m}$. The spacing of the readout channels on the SiPM array was $250 \mu\text{m}$. In total, 672 003 events were taken in this configuration over a time interval of 51.5 hours.

The coordinate system employed here is defined such that the z -axis is parallel to the beam while the x -axis is parallel to the S-side strips of the beam telescope ladders and therefore roughly parallel to the fibres. Therefore, the fibres are used to measure the y -coordinate.

The analysis procedure begins with the analysis of the beam telescope data with the aim of identifying clean single-track events which will then be used to unambiguously study the behaviour of the fibre module. The amplitude distributions (fig. 5.18) for the two ladders show two distinct components, a contribution from noise clusters at low amplitudes and a Landau-shaped contribution from signal clusters. Quality cuts at 17 and 80 ADC counts are applied to remove noise clusters and clusters with unusually high energies, and only clusters inside this interval are considered in the following.

The effect of this cut is visible in the distributions of the hit positions for the two ladders (fig. 5.19). Here, the locations of clusters are shown, separately for all clusters and for clusters allowed by the amplitude cuts. Readout channels 0 to 639 correspond to the

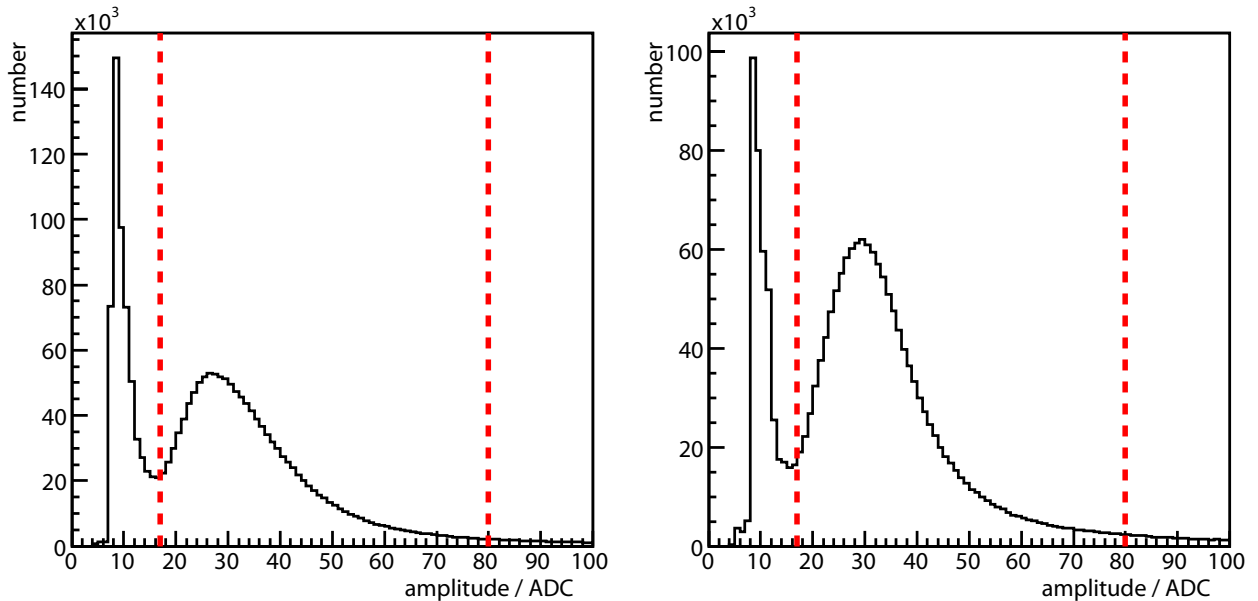


Fig. 5.18: Distributions of cluster amplitudes on the first (*left*) and second (*right*) beam telescope ladders. Only clusters with amplitudes between the cut values indicated by the dashed lines are considered in the analysis.

front (S-)side while channels 640 to 1023 belong to the rear (K-)side. For the S-side, the area where one expects to find signal clusters is limited by the fact that the width of the trigger counters is smaller than the width of a beam telescope ladder. Indeed, a number of noisy strips are apparent on both ladders as well as a substantial number of noise hits outside the acceptance of the beam telescope. Those can already be removed by a fair amount using the amplitude cut.

In all this, the position c of a cluster of n strips is calculated as a simple weighted mean

$$c = \frac{\sum_{i=1}^{n-1} c_i A_i}{\sum_{i=1}^{n-1} A_i} \quad (5.8)$$

At this point, c is still given as a channel number. The A_i are the strip amplitudes as provided by the TDR2, i.e. pedestal subtracted and corrected for common-mode noise, and the c_i are the corresponding channel numbers. The TDR2 adds the two neighbouring strips to an identified cluster for safety reasons. But they do not contain information about the location of the track. The sum is therefore taken excluding the outermost two strips.

The next requirement imposed on an event is that it have exactly one signal cluster on each side of each of the two ladders. In order to further remove spurious tracks from the data sample, the fact that the proton beam was collimated and of limited angular aperture can be taken into account (fig. 5.20 *left*). For particles passing the setup under a given angle whose variation is limited, a correlation between the cluster positions p_1 and p_2 on the first and second ladders is expected. This is exactly what is seen in the beam

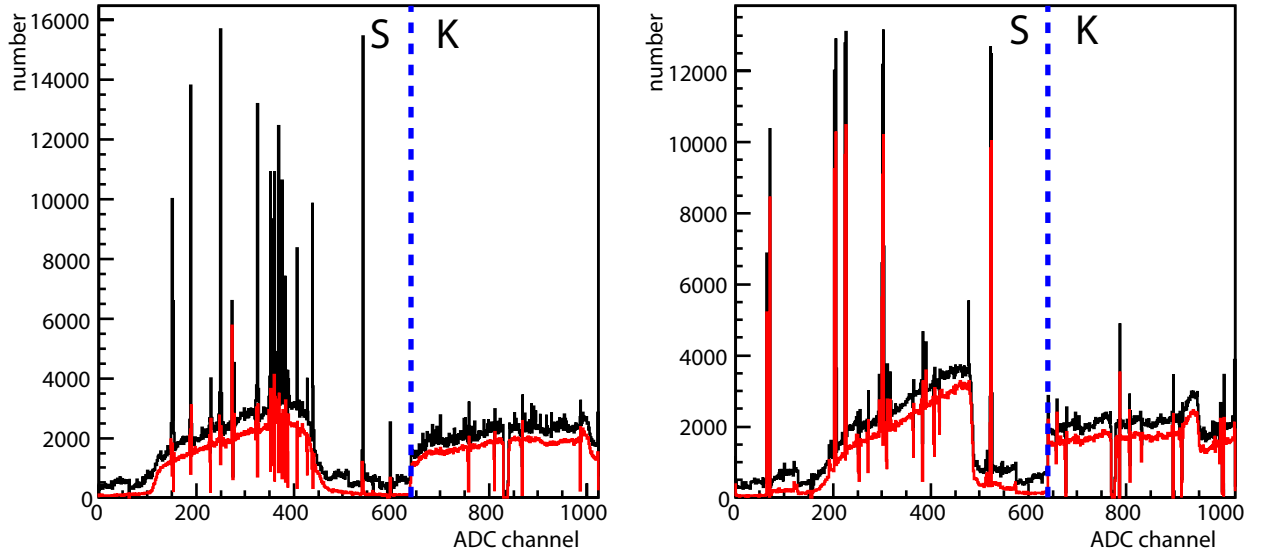


Fig. 5.19: Distributions of cluster positions for the first (*left*) and second (*right*) beam telescope ladders. The dashed lines separate the front (S-) and back (K-) sides of the ladders with 640 and 384 readout channels, respectively. Distributions before cuts are shown in black, distributions after the cut on the cluster amplitude (fig. 5.18) are shown in red.

telescope data, and a set of cuts in the (p_1, p_2) -area are defined. Events falling within the cut on the S-side and one of the cuts of the K-side at the same time are considered clean single-track events in the following.

On the K-side, the effect of the daisy-chaining of readout channels is apparent and the x coordinate of a passing track a priori cannot be reconstructed unambiguously. Three distinct branches in the (p_1, p_2) -area can be identified (fig. 5.20 *left*). However, the assumption of a smooth beam profile and the limited length of the trigger counters employed can be used to remove the ambiguities. Plotting the K-side cluster position K_1 on the first ladder against $K_1 - K_2$ where K_2 is the K-side cluster position on the second ladder removes the first ambiguity and reveals a new problem (fig. 5.20 *right*). The small gap between the individual silicon sensors in the ladder causes a shift, exactly located at channel $832 = 640 + 384/2$, in the beam profile that has to be corrected for. An empirical shift of 4 readout channels is introduced for the appropriate clusters. At the same time, the tracks located in the upper right corner in the figure are shifted to the leftmost end. Using these shifts and corrections for the K-side, and knowing the readout pitch of $110 \mu\text{m}$ and $208 \mu\text{m}$ for the S- and K-sides, respectively, the y and x coordinates can be calculated for each cluster. A track object is then created for those events with exactly one signal cluster on each side of each of the ladders so that the track position at a given depth z in the setup can be interpolated unambiguously. The beam profile so reconstructed (fig. 5.21) turns out to be smooth and regular. As an example, the figure also shows a picture of one of the trigger counters taken by the beam telescope. The exposure is determined by the beam profile and by the location of a number of dead or noisy strips on either of the beam telescope ladders.

As a further cross-check, the beam telescope occupancy for clean single-track events iden-

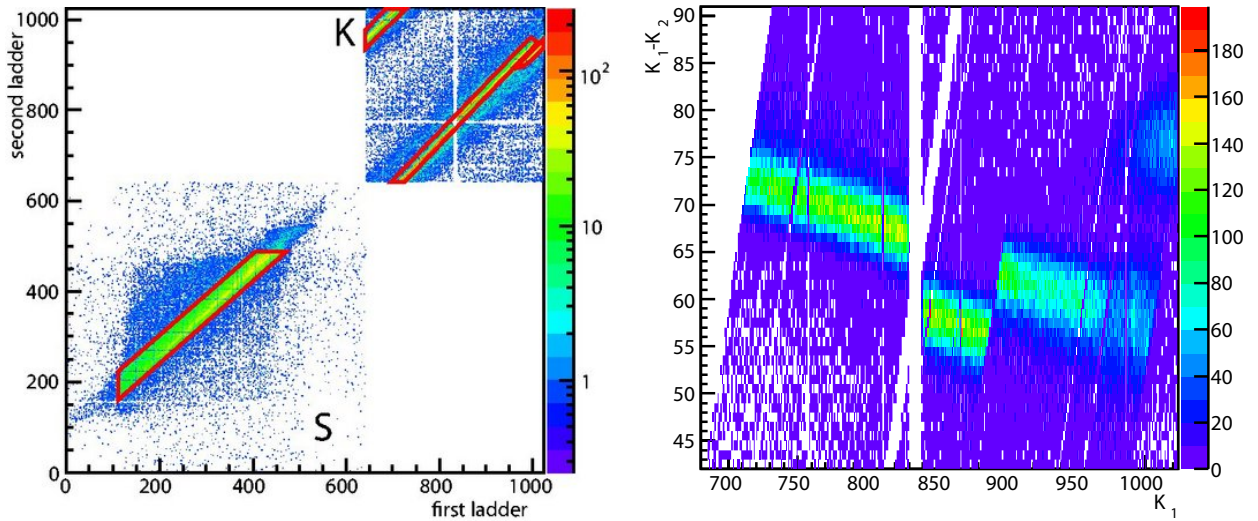


Fig. 5.20: *Left:* Positions of clusters on the two beam telescope ladders. Only events with exactly one cluster remaining after the cuts on cluster amplitude (fig. 5.18) on each side of each ladder are included. The collimation of the beam allows the rejection of spurious hits and only the events within the red cut areas are used for the analysis of the performance of the fibre modules. The peculiar structure for the K side (strip number ≥ 640) is due to the daisy-chaining of the readout strips. *Right:* Difference $K_1 - K_2$ in back-side cluster positions, measured in strip numbers, vs. K_1 . The offset caused by the gap between individual silicon wafers is visible at $K_1 = 850 \sim 900$ and the ambiguity in cluster position due to the daisy-chaining is seen at $K \gtrsim 1000$.

tified as above is examined (fig. 5.22). The distributions are now regular except for some gaps caused by dead or noisy strips that no longer contribute to the event sample. In addition, the width of the S-side distribution is governed by the dimension of the trigger scintillators.

Having established the beam telescope as a reference for the fibre modules and restricting ourselves to clean single-track events in the following, one can now turn to the analysis of the SiPM data. It starts from the raw ADC data of the SiPM array. A plot of the raw ADC spectra for all 32 channels contained in the SiPM array considered (fig. 5.23) shows that all of them were functional during the data taking. As the width of an individual channel is very small compared to the width of the beam profile and the trigger scintillators, the raw spectra are by far dominated by the pedestal peaks. The first step in the analysis of the fibre data is the determination of the positions of the fibres in the coordinate frame defined by the beam telescope. To this end, a simple amplitude cut well above the pedestal and occasional noise hits, taken here at 1000 ADC counts, is applied and the interpolated track position for the z of the fibre module is plotted using separate colours for the readout channels (fig. 5.25 *left*). The individual channels are not as well separated as in fig. 5.8 for the simple reason that, due to the positioning of the round fibres in the tightest arrangement, a track crossing the fibre module will usually generate scintillation light that is then accumulated on at least two adjacent SiPM array channels.

5 PEBS tracker prototype testbeam campaign

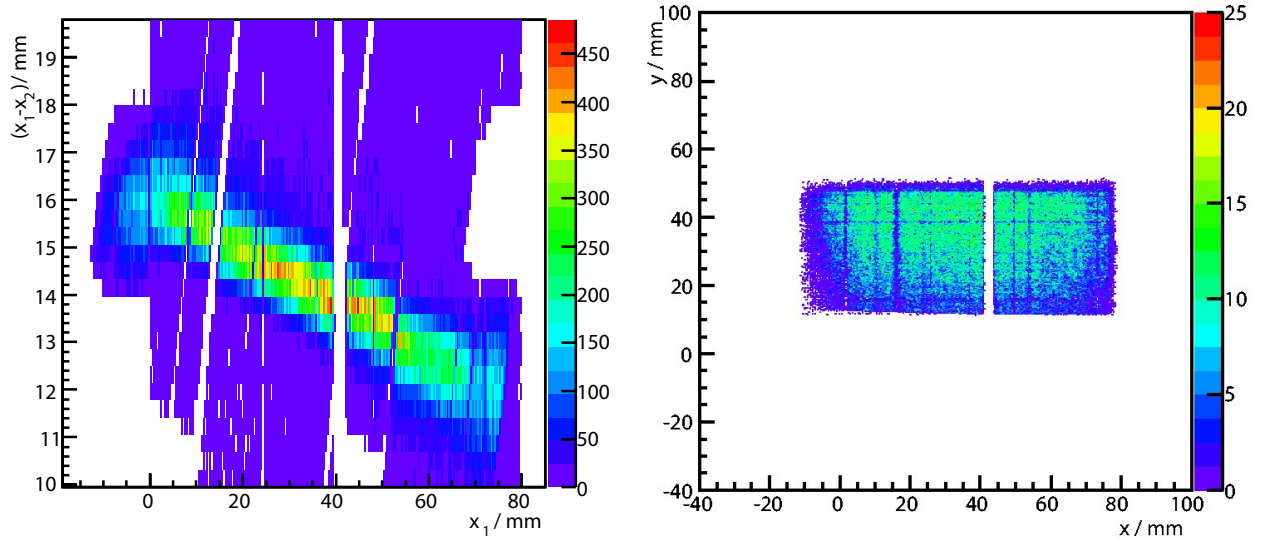


Fig. 5.21: *Left:* Correlation of the x coordinates measured by the two beam telescope ladders after corrections for ambiguity and offset. *Right:* x and y coordinates interpolated at the z -position of the first trigger counter from tracks passing all quality selection cuts. The exposure is governed by the beam profile and some gaps are due to noisy or dead strips on the beam telescope.

For a first estimate of the fibre positions, the scatter plot for each fibre is projected to the y -axis and the mean obtained from a Gaussian fit is taken as the fibre position. As a cross-check, this position is plotted as a function of the channel number (fig. 5.25 *right*). The slope of a straight-line fit to the resulting curve matches the nominal pitch of the readout channels very well.

Using the fibre positions so obtained, the signal and background spectra for all the SiPM channels can be found (fig. 5.26). To this end, events in which the track passed within $\Delta y \leq 100 \mu\text{m}$ of the fibre position were used to fill the signal spectrum of the respective fibre, while the background spectra were filled from events with a track passing well outside the area subtended by the SiPM array under study. Two observations are in order. First, the noise level of the Hamamatsu SiPMs turns out to be very low, with anything besides the pedestal peak barely visible on a linear scale. Second, the photo-electron-peak structure is not as clearly discernible as expected from figs. 4.27 and 5.7. This can be attributed to the sensitivity of the gain of the SiPMs to small variations in the bias voltage over the course of the testbeam. However, a calibration of the SiPMs is still possible. The pedestal position for a given SiPM channel is easily found from the location of the peak in the dark spectrum. The gain can be determined from the positions of the first few peaks in the signal spectra with an accuracy of roughly 10%. It turns out to be nearly uniform across the SiPM array and is taken to be 120 ADC counts in the following. The number of photo-electrons for a given channel is then calculated according to (5.4).

For a determination of the spatial resolution of the module, a possible tilt angle between the longitudinal axis of the fibres and the S-side strips of the beam telescope ladders has

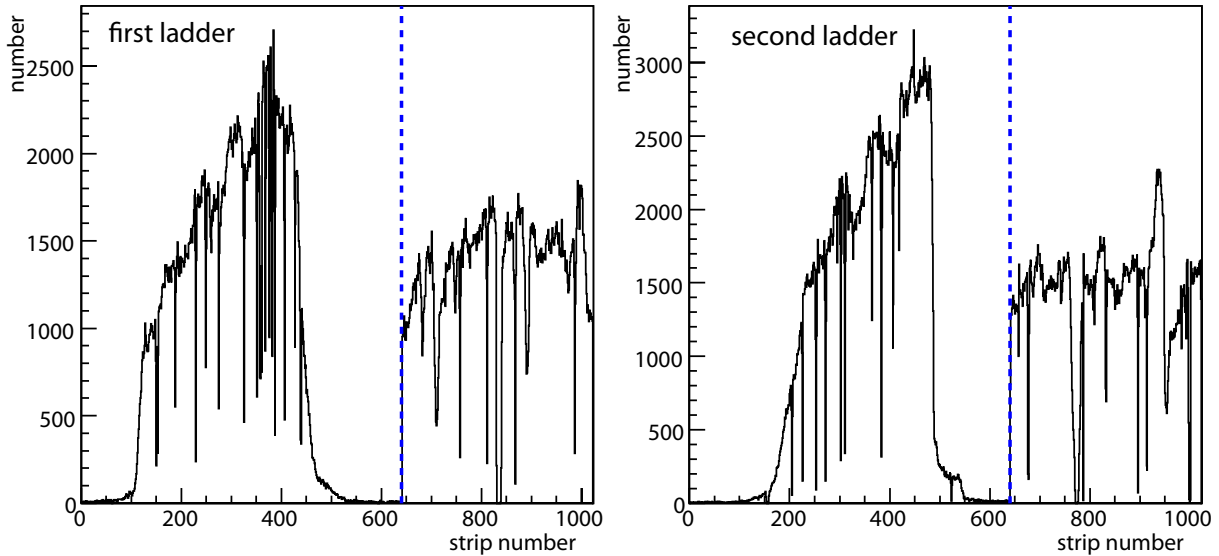


Fig. 5.22: Occupancy plots for the two beam telescope ladders after all quality selection cuts. The boundary between the S (front) and K (back) sides is marked by a dashed line. Apart from the gaps caused by noisy or dead strips, the distribution of events is uniform on the K side and is shaped by the trigger acceptance and beam profile for the S side. The spikes and background seen in the initial distributions (fig. 5.19) are gone.

to be corrected for. For this purpose, the projections of the fibre scatter plots in fig. 5.25 are calculated for slices along x (fig. 5.27). The mean values found in Gaussian fits to these projections give the mean fibre location y in a given interval in x . The fibres are then parameterised as straight lines and a fit is done for each of them to determine the fibre parameterisation $y_i(x)$ for fibre i . A typical tilt angle of 1.5 mrad was found in this way. Knowing the locations of the fibres, a fiducial area can be defined excluding the outermost two fibres covered by the SiPM array, to make sure that clusters on the edge of the active area are not included in the distributions. Only tracks crossing the module within the fiducial area are considered.

In the next step in the analysis, fibre clusters are identified. Starting from a channel with at least 1.5 photo-electrons, neighbouring channels are added to the cluster as long as their amplitude exceeds 0.5 photo-electrons. The position of the fibre cluster is then calculated as

$$y_{cl}(x) = \frac{\sum_i s_i y_i(x)}{\sum_i s_i} \quad (5.9)$$

where the sum is taken only over the channel with the highest amplitude and its immediate neighbours at most. For the determination of the spatial resolution, only the cluster with the highest total amplitude is considered. The distribution of the cluster size (fig. 5.28 *left*) shows that clusters are typically rather broad. This might be due to the rather large gap, on the order of 250 μm , between the fibre end and the silicon photomultiplier because of a protective layer of epoxy coating on the SiPM [99]. As a consequence, light exiting

5 PEBS tracker prototype testbeam campaign

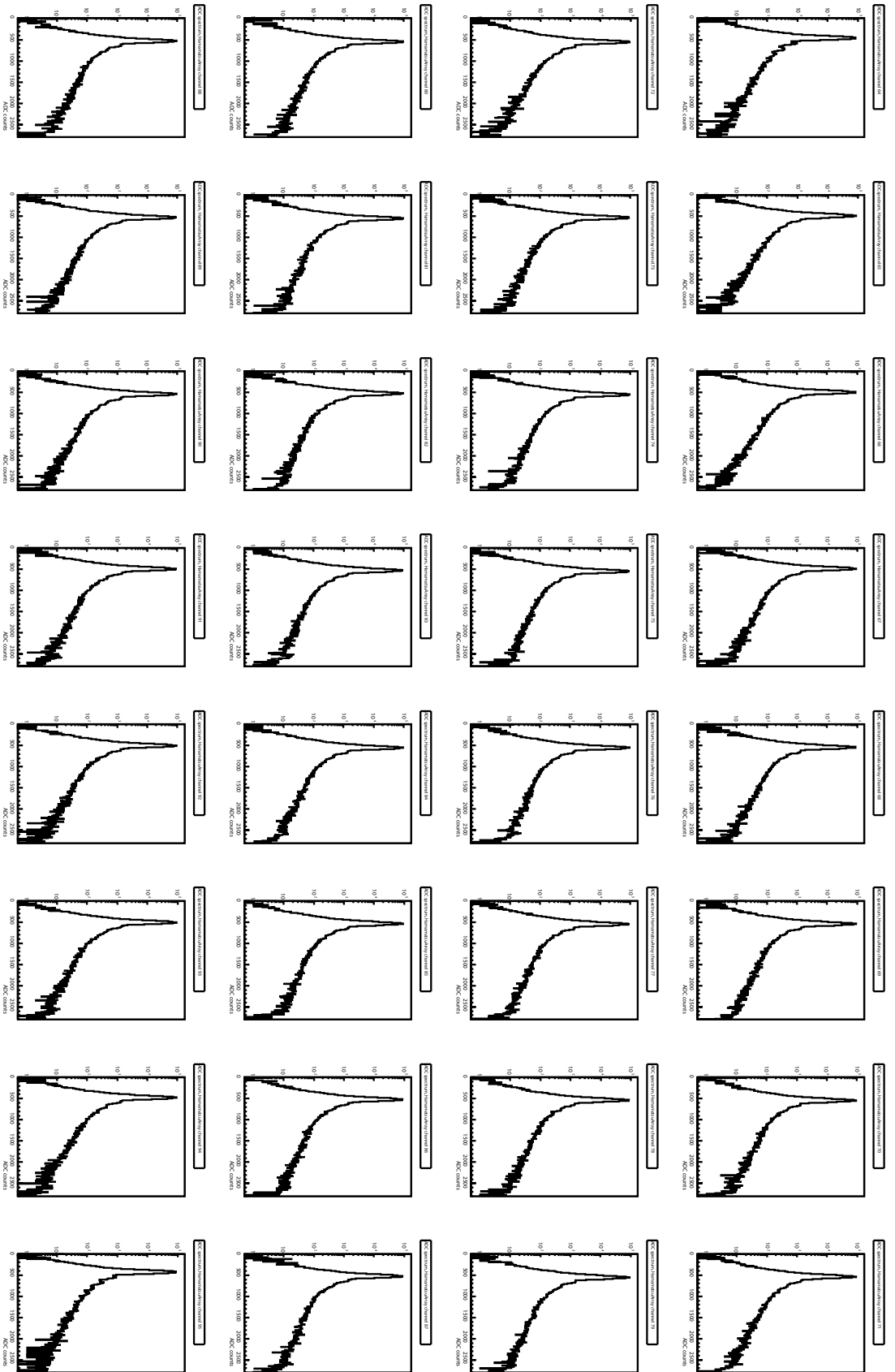


Fig. 5.23: Raw ADC spectra of all 32 SiPMs contained in the Hamamatsu array considered here. All channels were alive. Figure 5.24 contains a magnified version of two example spectra.

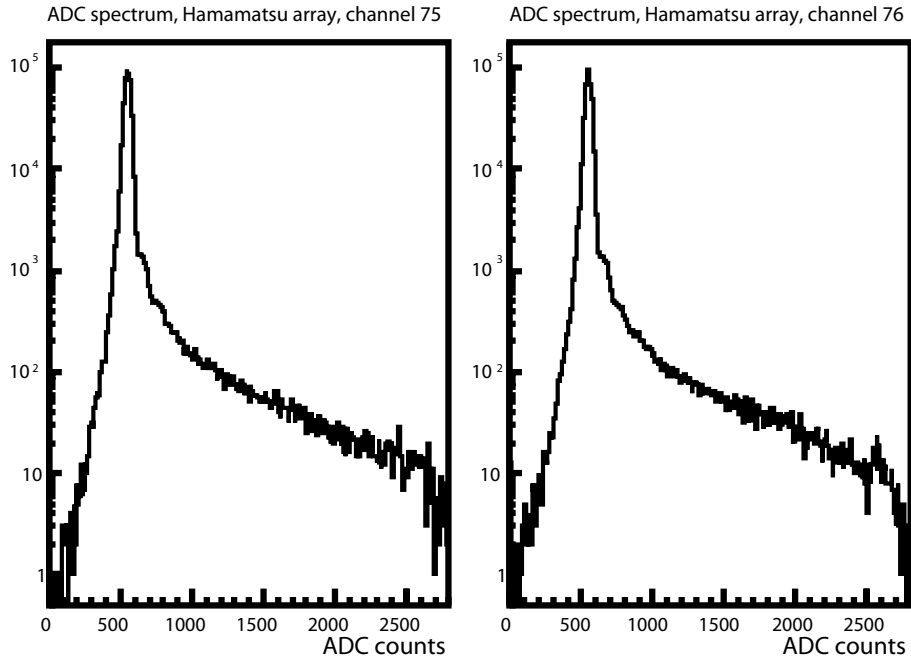


Fig. 5.24: Magnified version of two spectra from fig. 5.23.

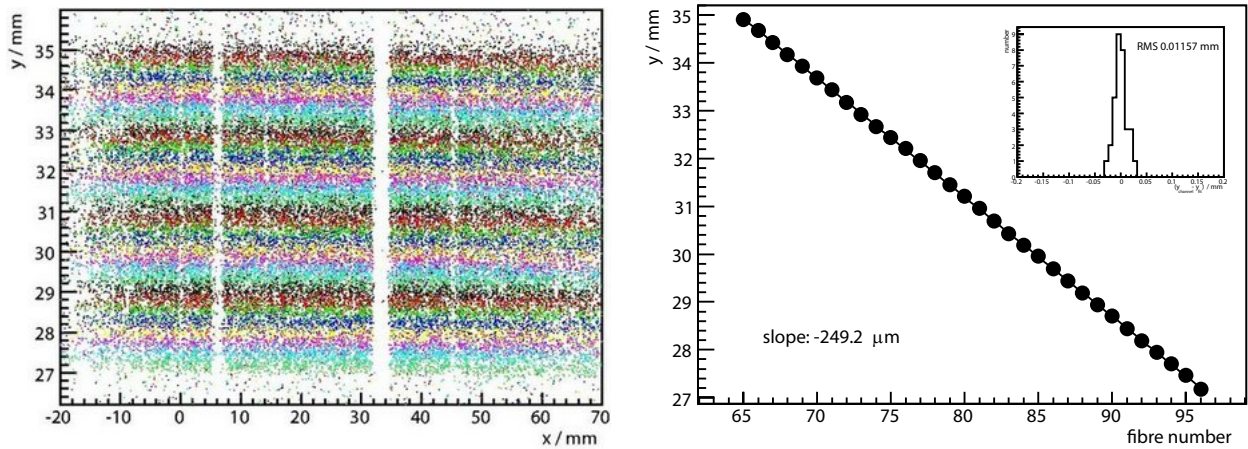


Fig. 5.25: *Left*: Intersection points of tracks interpolated to the z position of the fibre module, for fibre hits exceeding an amplitude of 1000 ADC counts. Fibres are marked by different colours. *Right*: Measured y positions from Gaussian fits to the projections of the above, as a function of the fibre number. A line fit gives the measured pitch of the readout channels, in excellent agreement with the nominal value of $250\ \mu\text{m}$. The inset contains the distribution of the fit residuals.

a given fibre might reach a neighbouring SiPM channel. This effect is the reason for the prescription of taking the sum in (5.9). The low threshold used in the cluster finding means that there are occasional noise clusters present, too (fig. 5.28 *right*), but it ensures an overall tracking efficiency of 99%.

5 PEBS tracker prototype testbeam campaign

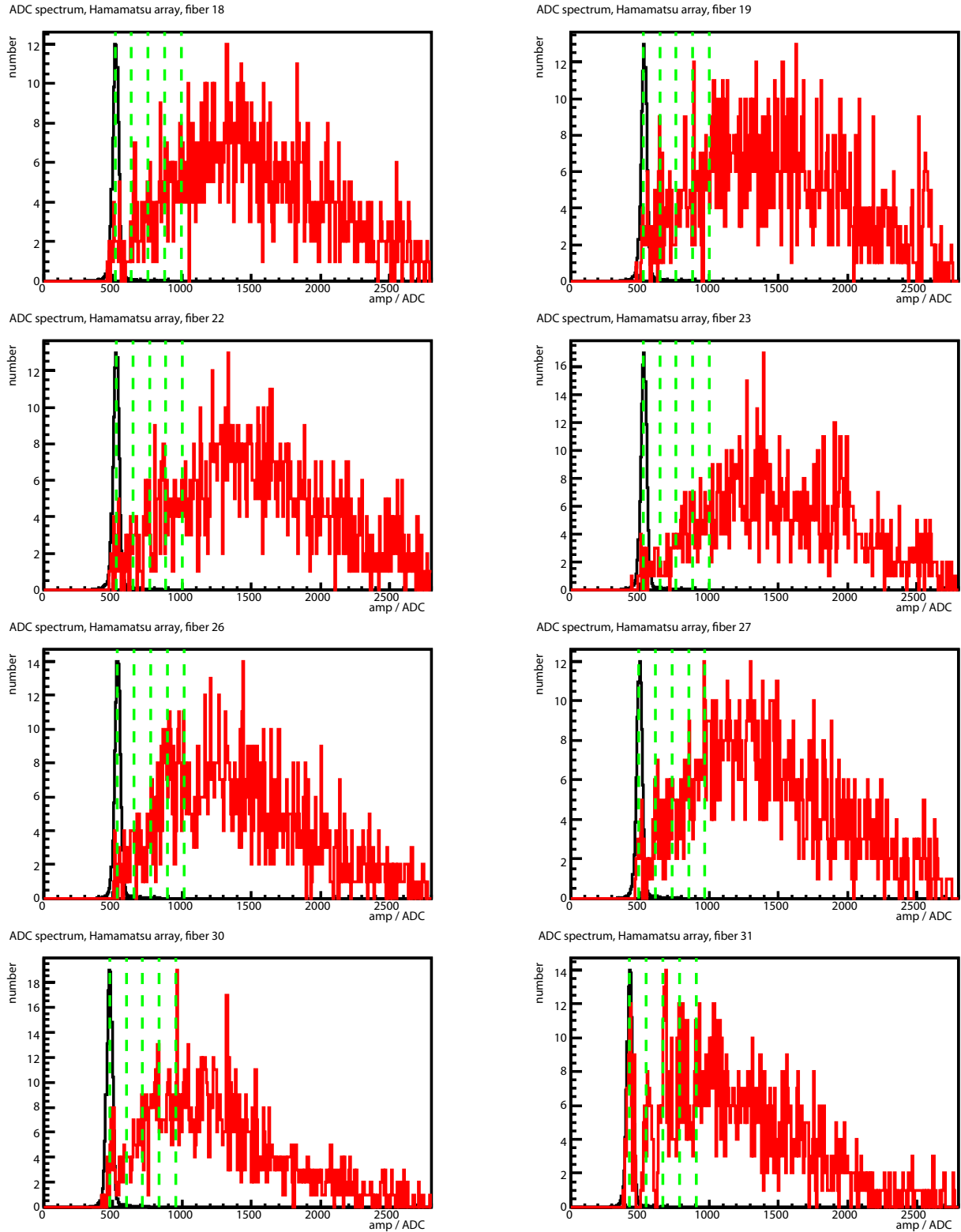


Fig. 5.26: Dark and signal spectra for eight of the 32 SiPM channels. The signal spectra (red) are filled for hits within $100 \mu\text{m}$ of the mean y position (fig. 5.25) of a given fibre, the dark spectra (black) are obtained from events in which the beam does not pass through the area subtended by the SiPM array. The dashed lines indicate the expected peak positions for a gain of 120 ADC counts. The dark spectra have been scaled to have the same maximum as the signal spectra.

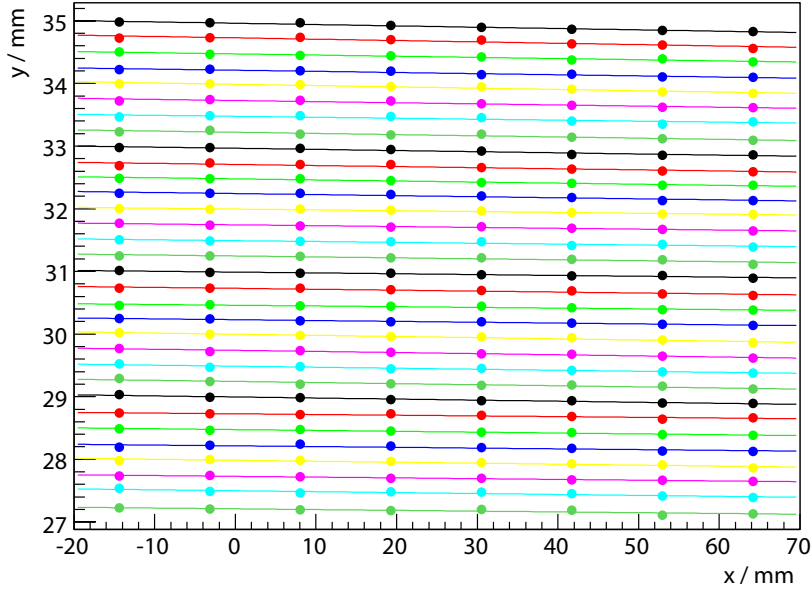


Fig. 5.27: Fibre positions along x , the coordinate along the fibres, taken from Gaussian fits to slices of the (x, y) -distributions (fig. 5.25 left). A straight line is fitted to each fibre.

From the interpolated track position and the measured cluster position, the track residual $y_{\text{cl}} - y_{\text{tr}}$ can be calculated. The resulting distribution (fig. 5.29) is well described by a sum of two Gaussians. Each Gaussian is determined by its amplitude A_i , mean μ_i and standard deviation σ_i . For a robust estimation of the parameters, μ_1 and σ_1 are first calculated from a fit taking only an inner window of width d around the mean of the track residuals histogram into account. In a second step, σ_1 and $\mu_1 = \mu_2$ are kept fixed and only σ_2 and the amplitudes $A_{1,2}$ are varied. The function

$$N(y) = A_1 \exp\left(-\frac{1}{2} \left(\frac{y - \mu_1}{\sigma_1}\right)^2\right) + A_2 \exp\left(-\frac{1}{2} \left(\frac{y - \mu_2}{\sigma_2}\right)^2\right) \quad \text{with } y = y_{\text{cl}} - y_{\text{tr}} \quad (5.10)$$

is fitted to the entire histogram. The average spatial resolution is then defined as

$$\sigma = \sqrt{\frac{A_1 \sigma_1^2 + A_2 \sigma_2^2}{A_1 + A_2}} \quad (5.11)$$

d is chosen such that the χ^2 of this final fit is minimized, however the result for the spatial resolution is rather insensitive to the exact value of d .

A fit according to this procedure yields widths of $78 \mu\text{m}$ and $184 \mu\text{m}$ with relative amplitudes of 93% and 7%, respectively. Taking the weighted mean according to (5.11) results in an overall spatial resolution of $89 \mu\text{m}$. Plotting the track residuals as a function of the time t and the coordinate x along the fibres (fig. 5.30) reveals systematic effects.

5 PEBS tracker prototype testbeam campaign

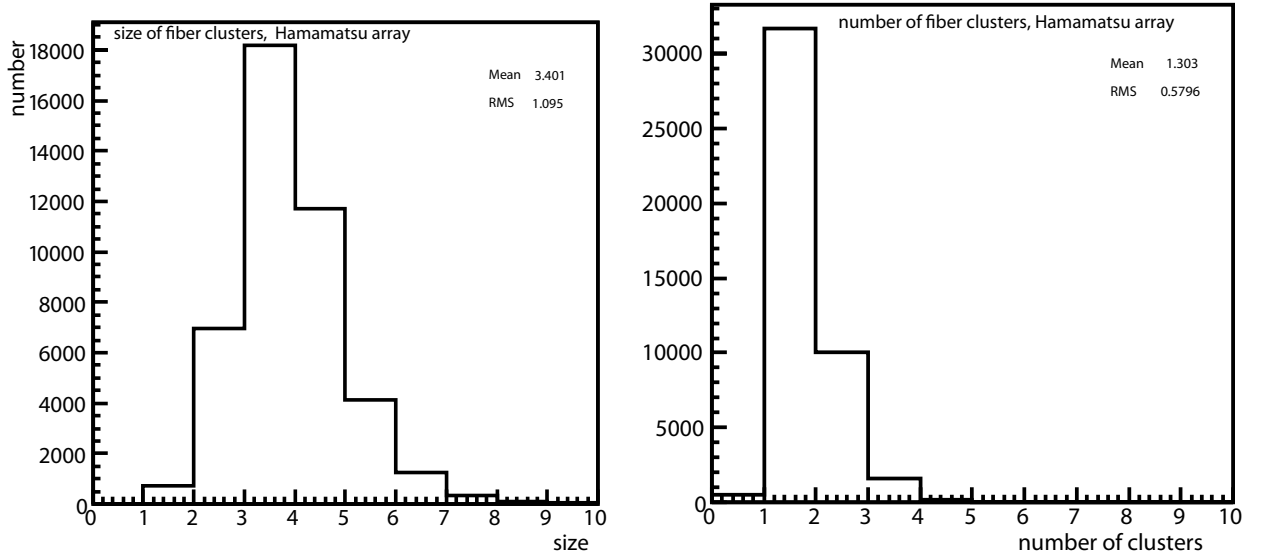


Fig. 5.28: *Left:* Distribution of the size of fibre clusters, for tracks inside the fiducial area, and taking only the cluster with the highest amplitude into account. *Right:* Distribution of the number of fibre clusters found for the Hamamatsu array considered here, for tracks inside the fiducial volume.

The mean track residual moves with time inside a range of roughly $20 \mu\text{m}$ and follows a periodic trend with a period of 1 day, as described by

$$\Delta y(t) = \Delta y_0 + A t \sin\left(\frac{2\pi}{1 \text{ d}} \cdot t + \phi_0\right) \quad (5.12)$$

which indicates a temperature effect. A dependence on x is seen with the same order of magnitude and the shift of the mean track residual is well described by a parabola. In fact, restricting the fiducial area to a small range in x and the first twelve hours of data taking, a spatial resolution of $76 \mu\text{m}$ and a distribution with very small non-Gaussian tails are obtained (black curve and inlet in fig. 5.29).

This value reflects the result found for the inner Gaussian when looking at the complete event sample. Apparently, this intrinsic resolution is deteriorated by effects causing non-Gaussian tails. While the exact nature of these effects is still under investigation [99], the results of this study point to two possible sources: First, as the behaviour of the silicon photomultipliers depends sensitively on the bias voltage, variations in this value, possibly correlated with temperature fluctuations, over the course of the measurement might cause the SiPMs to work in a non-ideal way. The bias voltage should therefore be monitored carefully during future testbeam measurements. A second effect may be a slight departure of the fibre geometry from the straight line shape assumed in this analysis.

To obtain the spatial resolution of the fibre module alone, the limited resolution of the beam telescope needs to be corrected for. For the testbeam setup, a Geant4-based Monte Carlo simulation assuming a resolution of $10 \mu\text{m}$ [152] for the two silicon ladders shows that the estimated resolution with which the track can be reconstructed at the position

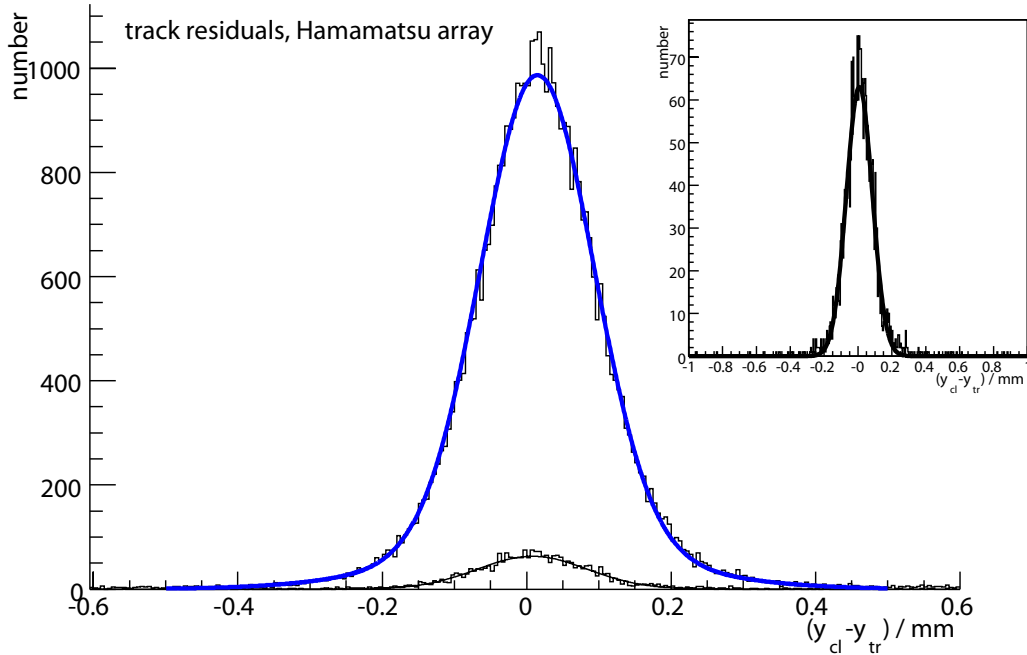


Fig. 5.29: Residuals of fibre cluster positions, using only the innermost three channels for the calculation of the fibre cluster position, with respect to the interpolated track position. For the full dataset and a fiducial area excluding the outermost two fibre channels on each side of the array, a spatial resolution of $89\ \mu\text{m}$ is obtained from a fit of a sum of two Gaussians (blue curve). The corresponding tracking efficiency is 99%. For a dataset comprising only the first twelve hours of data-taking and restricted to a fiducial area given by $x \in [10, 30]\ \text{mm}$, a resolution of $76\ \mu\text{m}$ is obtained with almost no non-Gaussian tails (black curve and inset).

of the fibre module is on the order of $30\ \mu\text{m}$ for 10 GeV protons with perpendicular incidence [99]. Quadratically subtracting this value yields intrinsic and total resolutions of $70\ \mu\text{m}$ and $84\ \mu\text{m}$, respectively.

The simulation presented in section 4.2 gives a spatial resolution of $43\ \mu\text{m}$ for perpendicularly incident muons under ideal circumstances. The improvement to be gained from the ongoing study [99, 154] of the detector design, construction and operation is therefore substantial.

Before the mean number of photo-electrons can be calculated, it is necessary to determine the probability ϵ for inter-pixel crosstalk which turns out to be larger than in the 2006 testbeam. The basic idea is to look for the broadening of the dark spectra of the SiPM channels compared to the expectation for Poissonian noise. A toy Monte Carlo study was created in [99] to reproduce the measured dark spectra. It implements the pulse shape of an SiPM as sampled by a VA chip at random times, with the number of samples drawn from a Poisson distribution whose mean is determined by the noise rate. For each fired pixel, an additional pixel is fired with the probability ϵ , taking the limited number of pixels into account. The output spectrum is calculated using a given gain. It turns out (fig. 5.31) that reasonable agreement between the measured dark spectra and

5 PEBS tracker prototype testbeam campaign

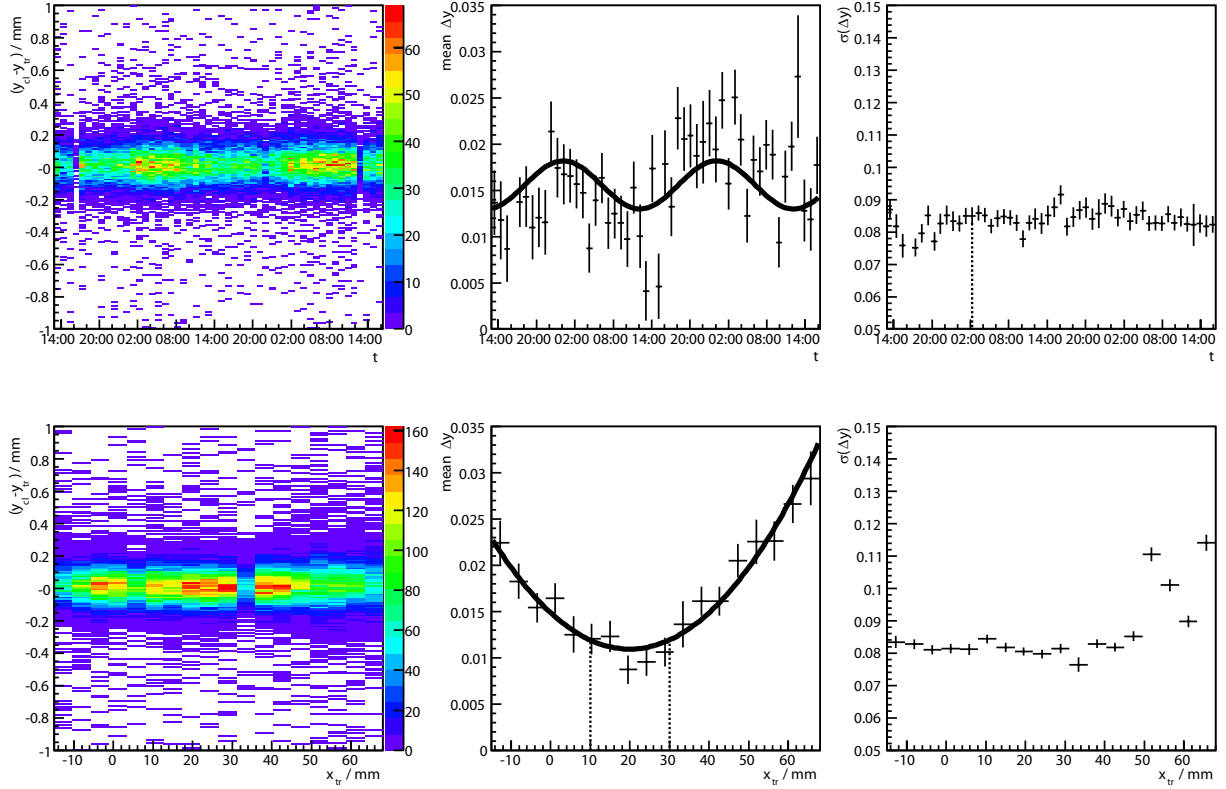


Fig. 5.30: Track position residuals as a function of time (*top*) and position along the fibre (*bottom*). Both mean (*middle*) and standard deviation (*right*) obtained from Gaussian fits to slices of the respective distributions are plotted. The variations of the mean values are fitted with eq. (5.12) and a parabola, respectively. The dashed lines bound the intervals for which the black curve in fig. 5.29 is obtained.

the toy Monte Carlo simulation is achieved for a crosstalk probability of $\epsilon = 0.4$, a noise rate of 160 kHz, and a gain of 120 ADC counts.

As shown in section 4.4.1, the mean number of photo-electrons per cluster is an important input value to the full detector simulation. As a function of the position across the module, the average cluster amplitudes (in fired pixels) are calculated (fig. 5.32). Using (4.12) to correct for the limited number $N_{\text{pix}} = 80$ of pixels and the result that crosstalk increases the number of fired pixels on average by a factor of $1/(1 - \epsilon)$ [115], the corrected number N_{pe} of photo-electrons is calculated from the number N_H of fired pixels as

$$N_{\text{pe}} = \frac{\log\left(1 - \frac{N_H}{N_{\text{pix}}}\right)}{\log\left(1 - \frac{1}{N_{\text{pix}}}\right)} \cdot (1 - \epsilon) \quad (5.13)$$

Within the range subtended by the Hamamatsu SiPM array, a mean of 10.7 photo-electrons is found. This number was used in the simulation results presented in chapter 4.

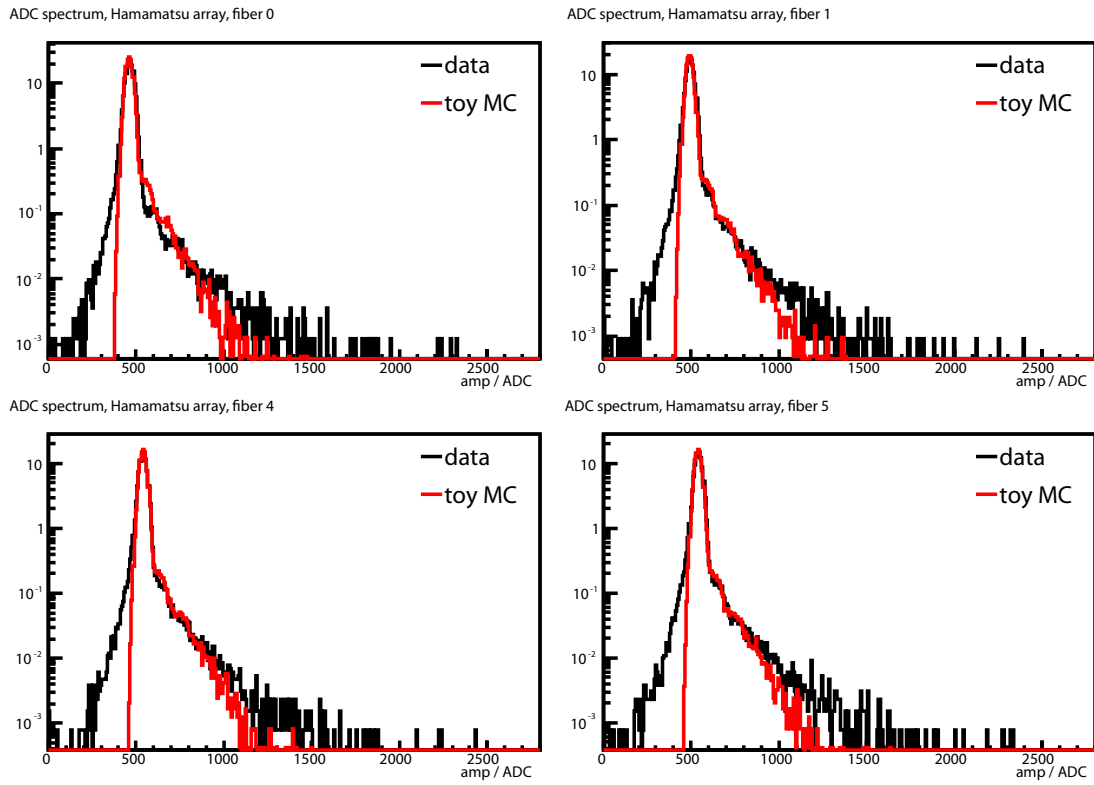


Fig. 5.31: Dark spectra for four of the 32 SiPM array channels, compared to predictions of the toy Monte Carlo study described in the text, for a crosstalk probability of 0.4, a noise rate of 160 kHz, and a gain of 120.

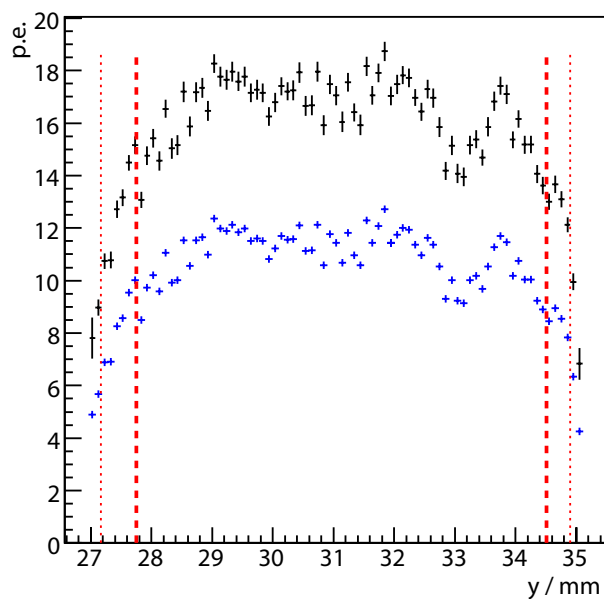


Fig. 5.32: Mean cluster amplitudes as a function of the interpolated track position across the fibre module (black). After correction for inter-pixel crosstalk and the limited number of pixels, the blue curve is obtained, shown here without error bars for clarity. The positions of the outermost fibres are indicated by the thin dashed lines, while the thick dashed lines mark the approximate boundaries of the fiducial area. A mean corrected number of 10.7 photo-electrons is found within the outer boundary.

6 Constraining supersymmetry with cosmic-ray data

The indirect search for dark matter is the most important task for the PEBS and AMS-02 detectors. In this chapter, the improvement to be expected from PEBS or AMS-02 data over the currently available data will be evaluated. In order to quantify this improvement, a certain model for dark matter has to be chosen. The signal fluxes of positrons, antiprotons and others, as well as the dark matter relic density and other observables, can then be calculated in the framework of the model. Of the many candidates for dark matter, the supersymmetric neutralino is by far the most popular [155, 156, 157, 158, 160, 161, 162]. Therefore, this case was chosen as an example for this study, and in addition, it was restricted to the mSUGRA model whose limited number of free parameters makes it a convenient playground for the study of SUSY phenomenology. Assuming that mSUGRA is realised in nature and that at least some part of the dark matter is made up of neutralinos, the study proceeds as follows: First, some more details about the model are outlined and the connection to cosmic-ray and other observables is described. A large fraction of the mSUGRA parameter space has been systematically scanned. After compiling a good part of the presently available data with implications for the models included in these scans, the situation once PEBS or AMS-02 data are available will be studied, focusing on two benchmark parameter points.

Very recently, the positron fraction data of the PAMELA experiment have become available. In the final section 6.5 of this chapter, it will be discussed how the conclusions drawn from the study presented here may be altered in light of these new data.

6.1 Model description

6.1.1 mSUGRA and observables

As stated in section 2.4, a single point in the mSUGRA parameter space is characterised by the soft SUSY breaking scalar and fermionic mass parameters m_0 and $m_{1/2}$ at the GUT scale, the ratio of the Higgs vacuum expectation values, $\tan\beta$, the trilinear scalar coupling A_0 at the GUT scale, and the sign of the Higgs mass parameter μ . The ISAJET 7.75 software package [163] is used to solve the renormalisation group equations and calculate the mass spectrum of supersymmetric particles and their couplings at the electroweak scale. Various observables, described in detail below, are then calculated with the help of the DarkSUSY 4.1 [164], micrOMEGAs 2.0.6 [165], and ISATOOLS [163] codes. In particular, the DarkSUSY software predicts electron, antiproton and γ -ray fluxes from neutralino annihilations in the Galactic halo.

6 Constraining supersymmetry with cosmic-ray data

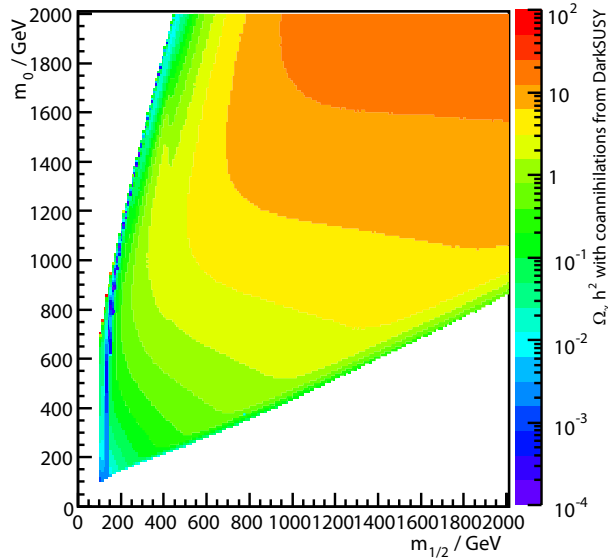


Fig. 6.1: Neutralino relic density $\Omega_\chi h^2$ in the $m_{1/2}$ - m_0 -plane, for $\tan\beta = 40$ and $m_t = 170.9$ GeV. The parameter space is bounded by the regions where no electroweak symmetry breaking occurs (at large values of m_0) or where the LSP would be a charged particle (at large values of $m_{1/2}$).

Several observables can be used to exclude regions of the mSUGRA parameter space. The most important ones are the neutralino relic abundance, the anomalous magnetic moment of the muon, and the $b \rightarrow s\gamma$ branching ratio.

The data on temperature anisotropies in the cosmic microwave background gathered by the WMAP experiment [166], in combination with other cosmological observations such as the spatial distribution of galaxies, give a density of the cold, non-baryonic matter of [5]

$$\Omega_{\text{nbm}} h^2 = 0.106 \pm 0.008 \quad (6.1)$$

where h is the Hubble constant in units of $100 \text{ km s}^{-1} \text{ Mpc}^{-1}$ and Ω denotes a density in units of the critical density.

The calculation of the present-day relic density of neutralinos is an involved task. The procedure followed by DarkSUSY is outlined in [167] and starts with the Boltzmann equation

$$\frac{dn}{dt} + 3Hn = -\langle\sigma_{\text{eff}}v\rangle(n^2 - n_{\text{eq}}^2) \quad (6.2)$$

for the summed number density $n = \sum_{i=1}^N n_i$ of the neutralino (n_1) and the $N - 1$ supersymmetric particles that will eventually decay to the neutralino if R-parity is conserved. The second term on the left-hand side comes from the dilution due to the expansion of the Universe, and

$$\langle\sigma_{\text{eff}}v\rangle = \sum_{ij} \langle\sigma_{ij}v_{ij}\rangle \frac{n_i^{\text{eq}}}{n^{\text{eq}}} \frac{n_j^{\text{eq}}}{n^{\text{eq}}} \quad (6.3)$$

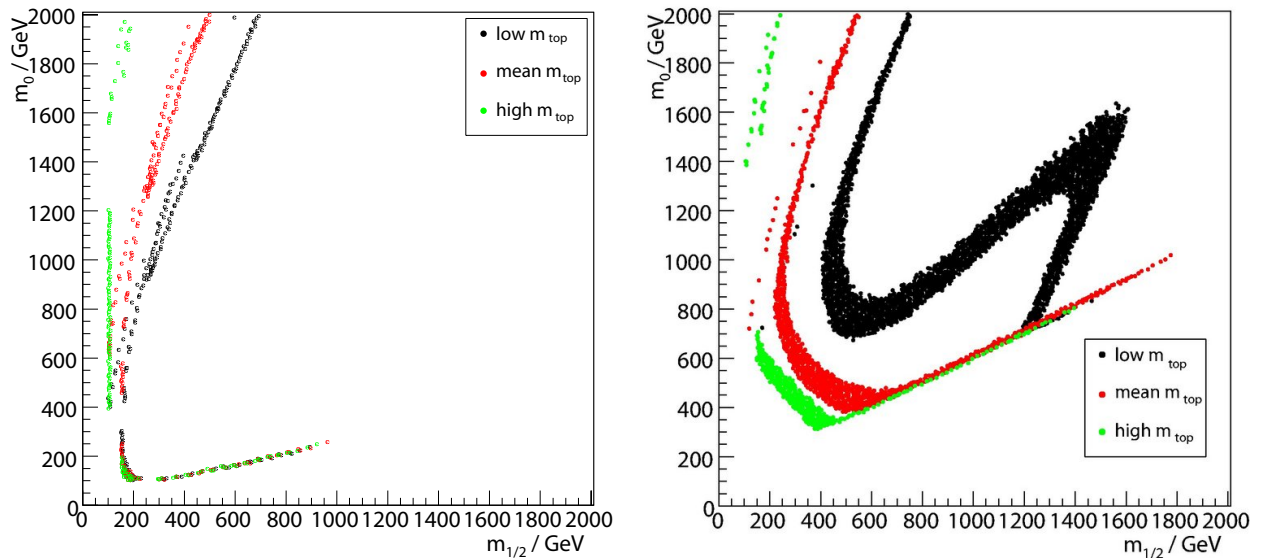


Fig. 6.2: mSUGRA parameter points fulfilling the relic density constraint to within 3σ , for $\tan\beta = 20$ (left) and $\tan\beta = 50$ (right), depending on the mass of the top quark. Points for top quark masses of 167.18 GeV, 170.9 GeV and 174.62 GeV are shown.

and brackets denote thermal averaging and $v_{ij} = \sqrt{(p_i \cdot p_j)^2 - m_i^2 m_j^2} / E_i E_j$. n^{eq} denotes number densities at thermal equilibrium. The annihilation cross sections entering (6.3) not only include $\chi_i^0 \chi_j^0$ -annihilations ($i, j = 1..4$) to all possible final states, but also coannihilations between the neutralinos, charginos and sfermions.

Figure 6.1 shows the predicted relic neutralino density for a scan of the $m_{1/2}$ - m_0 -plane, for $\tan\beta = 40$ and $m_t = 170.9$ GeV. It varies over many orders of magnitude and the cosmological constraint (6.1) allows only a tiny portion of that space. It turns out however that the allowed region changes with $\tan\beta$. Also, the relic density predicted for a certain mSUGRA parameter point depends strongly on the mass m_t of the top quark. This is illustrated in figure 6.2 where parameter points in the $m_{1/2}$ - m_0 -plane yielding a value of the relic density within 3σ of the value quoted above are plotted for two values of $\tan\beta$. For high values of $\tan\beta$, the appearance of the rapid annihilation funnel, where the $\chi\chi \rightarrow A \rightarrow f\bar{f}$ cross section is large, depends on the value adopted for m_t . The latest result from the Tevatron Electroweak Working Group is used [168]:

$$m_t = (172.6 \pm 0.8 \pm 1.1) \text{ GeV} \quad (6.4)$$

Adding the statistical and systematic errors in quadrature yields $\sigma_{m_t} = 1.36$ GeV. m_t is varied in our scans, but in order to keep the number of parameters limited, $A_0 = 0$ is set in the following.

The magnetic moment of the muon is related to its intrinsic spin by the gyromagnetic ratio g_μ :

$$\vec{m} = g_\mu \frac{e}{2m_\mu} \vec{S} \quad (6.5)$$

6 Constraining supersymmetry with cosmic-ray data

While the Dirac equation predicts $g = 2$ for a structureless spin- $\frac{1}{2}$ particle, quantum loop effects lead to a small deviation, parameterised by the anomalous magnetic moment $a_\mu \equiv (g_\mu - 2)/2$ [5]. a_μ has been measured to enormous precision by the E821 experiment at the Brookhaven National Lab that finds for the charge average [169]

$$a_\mu^{\text{exp}} = (11659208.0 \pm 5.4 \pm 3.3) \cdot 10^{-10} \quad (6.6)$$

The standard model prediction for a_μ can be calculated from diagrams like those shown

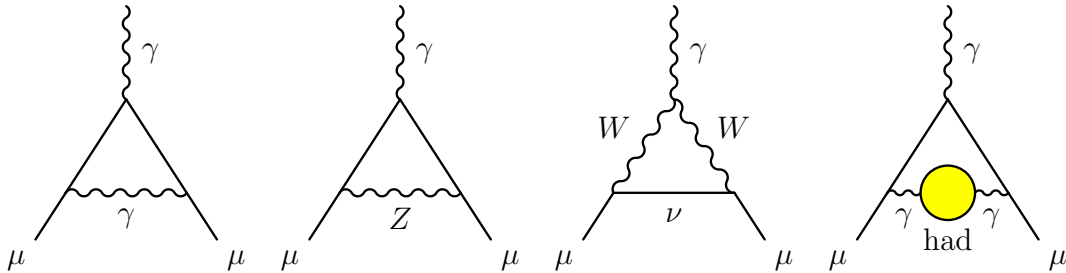


Fig. 6.3: Representative diagrams contributing to a_μ^{SM} : first-order QED (*left*), lowest-order weak (*middle*) and lowest-order hadronic (*right*). Figure taken from [5].

in figure 6.3 and is the sum $a_\mu^{\text{SM}} = a_\mu^{\text{QED}} + a_\mu^{\text{EW}} + a_\mu^{\text{had}}$ of the contributions from QED, loop diagrams involving W^\pm , Z and Higgs particles, and hadronic loops. The latter is determined from $\sigma(e^+e^- \rightarrow \text{hadrons})$ data and dominates the theoretical error. Overall, the standard model prediction is [5]

$$a_\mu^{\text{SM}} = (11659178.8 \pm 5.8) \cdot 10^{-10} \quad (6.7)$$

This means that there is a 3.4σ deviation of

$$\Delta a_\mu = a_\mu^{\text{exp}} - a_\mu^{\text{SM}} = (29.2 \pm 8.56) \cdot 10^{-10} \quad (6.8)$$

of the measured and theoretical values. The theoretical value gets amended in a supersymmetric theory leading to regions in the mSUGRA parameter space where the discrepancy is cancelled and that can therefore be considered to be preferred by the experimental results (fig. 6.4). The sign of the supersymmetric contribution to a_μ is identical to the sign of μ , so that only the case $\mu > 0$ is considered in the following.

The branching ratio BR of the penguin decay $b \rightarrow s\gamma$ is sensitive to supersymmetric contributions caused by additional loop diagrams containing the superpartners. From [5], one calculates for the mean experimental value:

$$BR(b \rightarrow s\gamma) = (3.63 \pm 0.50) \cdot 10^{-4} \quad (6.9)$$

The results given by mircOMEGAs for this observable turn out to be negative for some regions in the parameter space. Therefore, only the calculation of DarkSUSY was used.

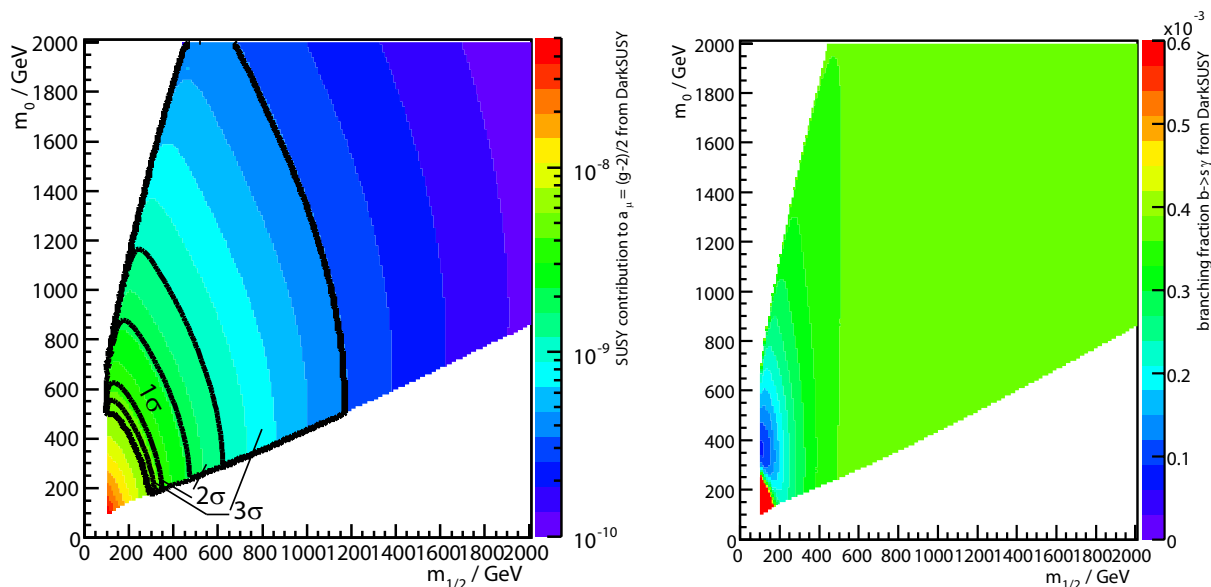


Fig. 6.4: *Left:* SUSY contribution to a_μ in the $m_{1/2}$ - m_0 -plane, for $\tan\beta = 40$ and $m_t = 170.9\text{ GeV}$. The preferred region is indicated at the 1σ , 2σ and 3σ -levels. *Right:* Branching fraction for $b \rightarrow s\gamma$ decays in the $m_{1/2}$ - m_0 -plane, for $\tan\beta = 40$ and $m_t = 170.9\text{ GeV}$, as calculated by DarkSUSY.

Direct searches by the experiments at the LEP collider set lower bounds on sparticle masses, thereby already providing some constraints on the mSUGRA parameter space. For example, the data indicate a neutralino mass $m_{\chi^0} > 46\text{ GeV}$ and a chargino mass $m_{\chi^\pm} > 94\text{ GeV}$ at the 95% confidence level [5]. Limits for other sparticle species also exist but do not play an important role in the context of this study. Figure 6.5 illustrates

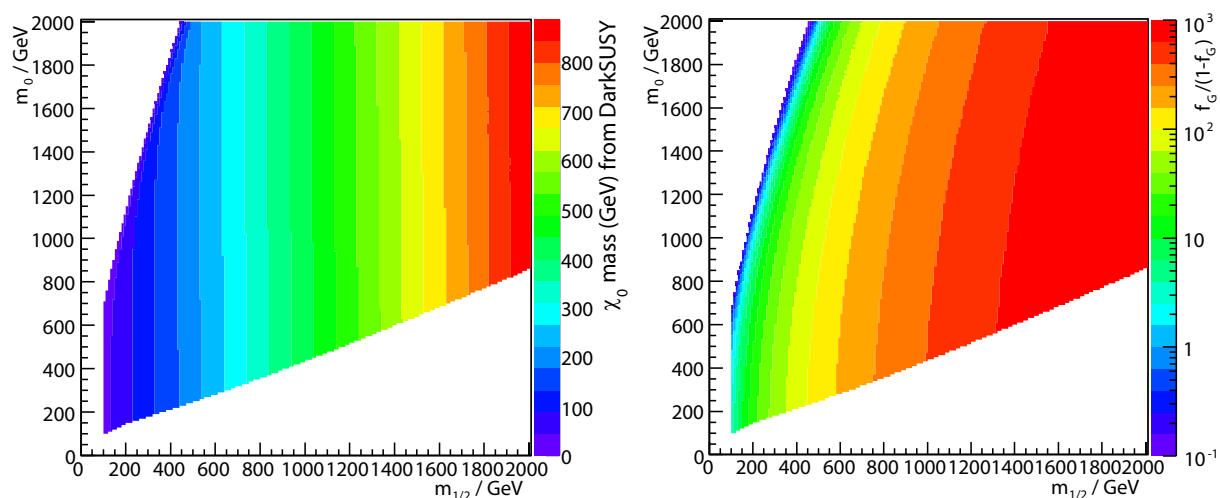


Fig. 6.5: Neutralino mass (*left*) and content $f_G/(1-f_G)$ as defined by (2.16) (*right*) in the $m_{1/2}$ - m_0 -plane, for $\tan\beta = 40$ and $m_t = 170.9\text{ GeV}$.

6 Constraining supersymmetry with cosmic-ray data

the fact that m_χ is roughly proportional to $m_{1/2}$. The figure also shows the ratio of the gaugino and higgsino fractions of the neutralino for a given scan in the $m_{1/2}$ - m_0 -plane, which determines the preferred annihilation channels.

A number of experiments are searching for WIMPs directly, looking for elastic collisions of WIMPs with nuclei in terrestrial targets [170]. The differential rate for WIMP elastic scattering off nuclei can be expressed as

$$\frac{dR}{dE_R} = N_T \frac{\rho_0}{m_W} \int_{v_{\min}}^{v_{\max}} d\mathbf{v} f(\mathbf{v}) \frac{d\sigma}{dE_R} \quad (6.10)$$

where N_T denotes the number of target nuclei, m_W is the WIMP mass, $f(\mathbf{v})$ is the WIMP velocity distribution in the Earth frame and $d\sigma/dE_R$ is the WIMP-nucleus differential cross section. $\rho_0 = 0.3 \frac{\text{GeV}}{\text{cm}^3}$ is the local density. v_{\min} is determined by the WIMP and nuclear masses and the energy threshold of the detector, and v_{\max} is the escape velocity of the WIMP.

Two separate components contribute to the differential WIMP-nucleus cross section, an effective scalar coupling between the WIMP and the nucleus and an effective coupling between the spin of the WIMP and the total spin of the nucleus. Therefore,

$$\frac{d\sigma}{dE_R} \propto \sigma_{SI}^0 F_{SI}^2(E_R) + \sigma_{SD}^0 F_{SD}^2(E_R) \quad (6.11)$$

where $\sigma_{SI,SD}^0$ are the spin-independent and spin-dependent WIMP-nucleus cross sections in the limit of zero momentum transfer and $F_{SI,SD}^2(E_R)$ denote the nuclear form factors. As a WIMP in the GeV-TeV mass range will deposit a recoil energy of around 50 keV and the predicted event rates for neutralinos can be as low as 10^{-6} per kg and day, a WIMP detector must have low energy threshold, low background and high target mass. In the detector, the recoil energy is transformed into a measurable signal, such as charge, light or phonons, and powerful background discrimination can be achieved by observing two signals simultaneously. Classes of WIMP detectors currently deployed include cryogenic detectors at mK temperatures, such as CDMS [171], liquid noble element detectors, e.g. XENON10 [172], and superheated liquid detectors, such as COUPP [173]. While a convincing WIMP signal has not been observed yet, the limits imposed by some of these detectors are already quite stringent (fig. 6.8).

6.1.2 Cosmic rays

As has been shown, neutralino annihilation in the Galactic halo leads to the production of positrons (and electrons), antiprotons and γ -rays in the GeV-range. This assumed primary source of cosmic rays has to be distinguished from the so-called secondary component. Cosmic-ray particles, mostly protons, react with the interstellar matter creating stable secondary particles and γ -rays via π^0 -production in the process. γ -rays are also produced by bremsstrahlung processes, synchrotron radiation of electrons in the Galactic magnetic field and inverse Compton-scattering of electrons on background photons from starlight and the cosmic microwave background. Because of their small mass, electrons

quickly lose energy due to synchrotron and bremsstrahlung radiation.

For the evaluation of the secondary cosmic-ray component, the Galprop package as described in section 2.6 is used. The conventional model was chosen to calculate the background positron, antiproton and γ -ray fluxes. At the same time as investigating a possible primary signal, the PEBS or AMS-02 positron data will be used to refine the propagation model itself. It will therefore be assumed that the secondary component is known with good precision and the study will be restricted to this one model.

The calculation of the expected primary flux of positrons from neutralino annihilation for a given model is done by DarkSUSY and proceeds as follows: In a first step, the local annihilation rate is calculated as $1/2(\rho_\chi(\vec{x})/m_\chi)^2\sigma_{\text{ann}}v$. For this purpose, the standard modified isothermal profile for the halo density ρ_χ is used, given by

$$\rho_\chi(r) = \rho_0 \cdot \frac{1 + \left(\frac{r_0}{a_h}\right)^2}{1 + \left(\frac{r}{a_h}\right)^2} \quad (6.12)$$

with the local density $\rho_0 = 0.3 \frac{\text{GeV}}{\text{cm}^3}$, the galactocentric distance of the sun $r_0 = 8.5$ kpc and the length scale $a_h = 3.5$ kpc. Other halo profiles are frequently used in the literature and they can differ greatly in their behaviour near the galactic centre. Nevertheless, as one is primarily interested in the positrons, which quickly lose energy and therefore originate in the solar neighbourhood, the influence of the choice of halo model on the expected fluxes can be expected to be small.

In a second step, the production rate of positrons is estimated by folding together the branching ratio into a given two-body final state with the Monte Carlo simulation of the hadronisation and/or decay of that state as implemented in DarkSUSY. The relevant final states for positrons are $\ell^+\ell^-$, $q\bar{q}$, W^+W^- , Z^0Z^0 , $W^\pm H^\mp$, ZH_1^0 , ZH_2^0 , $H_1^0H_3^0$ and $H_2^0H_3^0$ at tree-level, and $Z\gamma$ and gg at one-loop level. For the hadronisations and decays, the results from a Pythia 6.154 [175] simulation are tabulated and interpolated.

The third step is the propagation of the signal flux through the interstellar medium to obtain the local interstellar flux. The default implementation is used, an analytical solution of a diffusion equation with energy losses and cylindrical symmetry as outlined in [157], that is implemented in DarkSUSY. In a more sophisticated approach, an additional interface from DarkSUSY to Galprop will be necessary to treat both background and signal fluxes by the same propagation model.

Lastly, the local interstellar signal fluxes obtained from Galprop and DarkSUSY ($\Phi_i^{\text{sig}}(e^+) = \Phi_i^{\text{sig}}(e^-)$) are subjected to solar and geomagnetic modulation. Solar modulation is modelled by the force-field approximation introduced in section 2.5.4 and equation (2.31) is used for cutting off the fluxes due to the geomagnetic effect. From a fit to the AMS-01 electron spectrum (fig. 2.4), the solar modulation parameter ϕ as well as the cutoff rigidity R_c and steepness γ_c are extracted for the background flux. Using the same ϕ for electrons and positrons, a different set of cutoff parameters is then fitted for the positrons to the AMS-01 positron flux. The goal of this procedure is to provide a good description of the positron fraction data at lower energies, where the SUSY signal does not contribute significantly, so that the χ^2 used below to compare different models to the positron data is governed by the signal region at higher energies.

6.2 Constraints on mSUGRA parameter space from currently available data

In this section, it will be investigated which regions of the mSUGRA parameter space are compatible with measurements of the various observables discussed in the previous section. Especially interesting is the question how much information the presently available positron data can contribute to this problem. The results of this section will guide us in our choice of example scenarios for the discussion of the physics potential of PEBS and AMS-02 in the following sections. The new positron fraction data from PAMELA will be left aside for the moment. They will briefly be considered in section 6.5.

In order to evaluate the constraining power of the positron fraction data, the (mSUGRA, m_t)-parameter space was scanned as described below and the χ^2 was calculated, defined as follows:

$$\chi_{e^+/(e^++e^-)}^2 = \sum_i \left(\frac{\Delta f_i}{\sigma_i} \right)^2 \quad \text{with} \quad \Delta f_i \equiv f_i^{\text{model}} - f_i^{\text{data}} \quad \text{and} \quad (6.13)$$

$$f_i^{\text{data/model}} \equiv \frac{\Phi_i^{\text{data/model}}(e^+)}{\Phi_i^{\text{data/model}}(e^+) + \Phi_i^{\text{data/model}}(e^-)} \quad (6.14)$$

where Φ denotes fluxes and i denotes energy bins. The positron fraction from data $f_i^{\text{data}}(e^+)$ is the weighted mean of most of the existing data, as presented in figure 2.5. The model fluxes are calculated as the sum of the modulated background flux and the boosted modulated signal flux:

$$\Phi_i^{\text{model}}(e^\pm) = \Phi_i^{\text{bg,mod}}(e^\pm) + f_b \cdot \Phi_i^{\text{sig,mod}}(e^\pm) \quad (6.15)$$

The boost factor f_b in equation (6.15) is used as the only free parameter in a minimisation of $\chi_{e^+/(e^++e^-)}^2$ for a given point in the mSUGRA parameter space. The asymmetric errors σ^+ and σ^- of the cosmic-ray data are treated according to the recommendation of [5]:

$$\sigma_i = \begin{cases} \sigma_i^+ & \Delta f_i > \sigma_i^+ \\ \frac{\sigma_i^+ - \sigma_i^-}{\sigma_i^+ + \sigma_i^-} \Delta f_i + \frac{2\sigma_i^+ \sigma_i^-}{\sigma_i^+ + \sigma_i^-} & \sigma_i^- < \Delta f_i < \sigma_i^+ \\ \sigma_i^- & \Delta f_i < -\sigma_i^- \end{cases} \quad (6.16)$$

For the positron fraction and all results quoted here, the following grid¹ was scanned:

- m_0 and $m_{1/2}$ from 100 GeV to 2000 GeV in steps of 10 GeV,
- $\tan \beta$ from 10 to 60 in steps of 10, and
- m_t from 167.18 GeV to 174.62 GeV in steps of 0.465 GeV.

¹The range adopted for m_t was motivated by the confidence interval current at the time the analysis was performed [176].

6.2 Constraints on mSUGRA parameter space from currently available data

In addition, a small part of the coannihilation region was scanned using a finer sampling of $\tan\beta$ in order to obtain smoother χ^2 -contours. Roughly four million parameter sets are included in the scans.

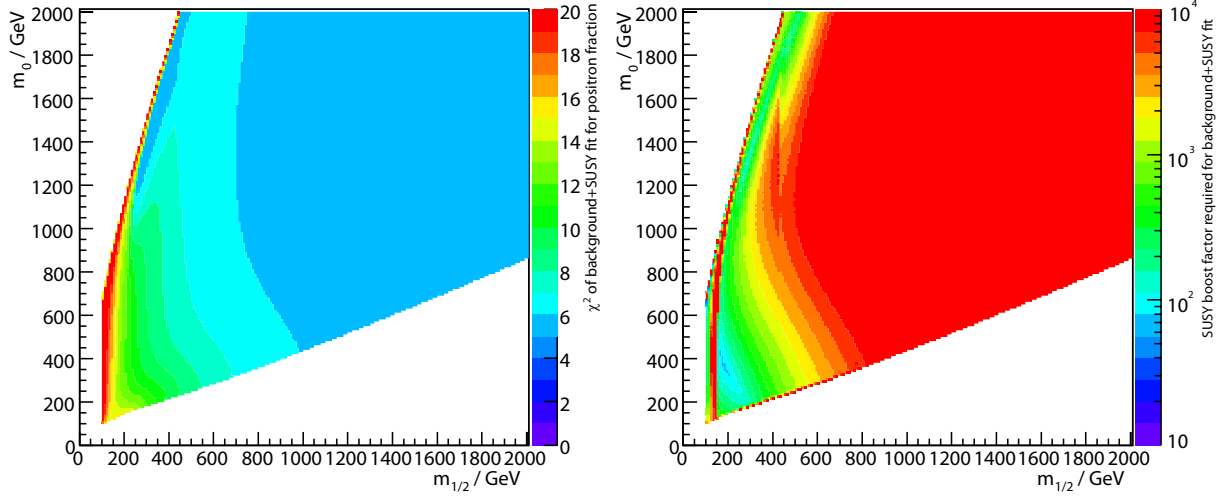


Fig. 6.6: $\chi_{e^+/(e^++e^-)}^2$ and corresponding boost factor for the positron fraction, for $\tan\beta = 40$ and $m_t = 170.9$ GeV.

Figure 6.6 illustrates the behaviour of $\chi_{e^+/(e^++e^-)}^2$ for given values of $\tan\beta$ and m_t : Except for very low values of $m_{1/2}$, the χ^2 -contour is essentially flat and therefore lacks predictive power. The figure also shows the corresponding boost factor obtained in the minimisation of (6.13). It varies over many orders of magnitude along with the calculated value of $\langle\sigma_{\text{ann}}v\rangle$ (fig. 6.7 *left*) because the overall signal amplitude is fixed by the positron fraction data.

The boost factor f_b included in (6.15) can be interpreted as a measure of the clumpiness of the dark matter. Under the influence of their own gravitational attraction, dark matter particles will form clumps thus enhancing the local WIMP density over that found for a smooth distribution. Since the annihilation rate scales as the square of the number density, the *local* boost factor for a given clump is:

$$f_b = \frac{\langle\rho^2\rangle_{\text{cl}}}{\langle\rho\rangle_{\text{cl}}^2} \quad (6.17)$$

The overall factor that the positron flux is boosted by compared to a smooth distribution is strongly affected by the propagation process as the influence of clumps decreases with increasing distance.

It was shown recently that it is difficult to accommodate boost factors differing much from unity in the light of Λ CDM N-body simulation results [159]. For models that already seem unlikely, boost factors no larger than 20 can be obtained. Such a configuration requires either a dark matter clump very close to the solar system or extremely peaked density profiles for the clumps. Other scenarios, such as dark matter density spikes around intermediate mass black holes [177] can yield boost factors of up to a few thousand.

6 Constraining supersymmetry with cosmic-ray data

Naively, one will expect models with lower neutralino relic density $\Omega_\chi h^2$ to have higher signal fluxes because of the higher annihilation cross sections, as implied by equation (2.5). In turn, this means lower boost factors. Figure 6.7 shows the best-fit boost factors to the positron and electron signal flux obtained in the mSUGRA models considered in this

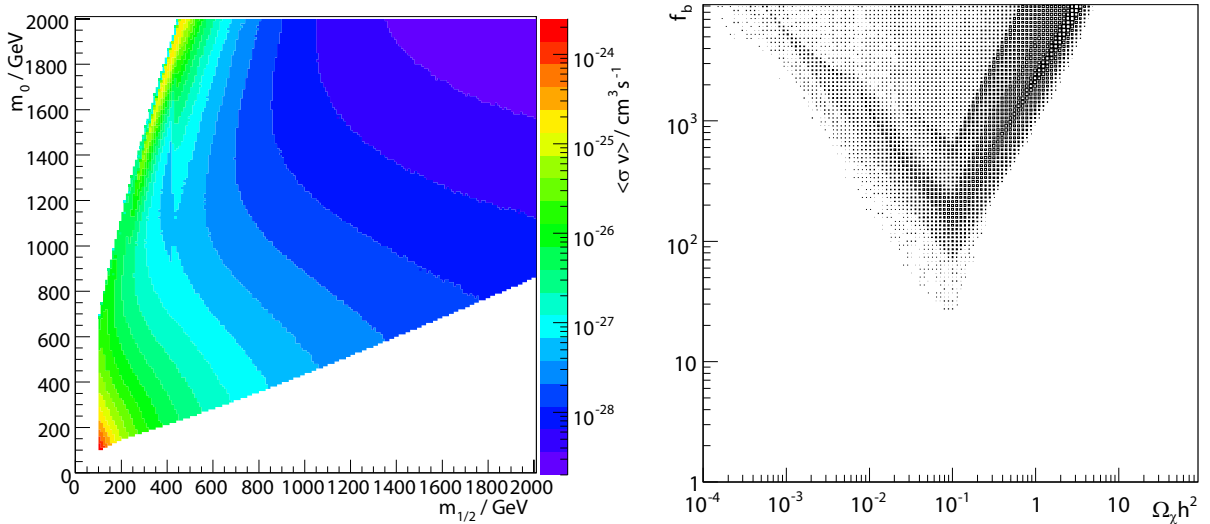


Fig. 6.7: *Left:* $\langle \sigma_{\text{ann}} v \rangle$ calculated by DarkSUSY, in the $m_{1/2}$ - m_0 -plane, for $\tan \beta = 40$ and $m_t = 170.9$ GeV. *Right:* Best-fit positron fraction boost factor f_b plotted against the corresponding neutralino relic density $\Omega_\chi h^2$ for mSUGRA models considered here. The boost factor rises towards low relic densities due to the rescaling according to eq. (6.19).

study, plotted against the corresponding $\Omega_\chi h^2$. Assuming that the Galactic dark halo density equals the neutralino relic density, the neutralino density in models featuring a neutralino relic density that cannot account for the entire density of non-baryonic matter must be rescaled as follows [158]:

$$\rho_\chi(r) = \left(\frac{\Omega_\chi h^2}{\Omega_{\text{nbm}} h^2} \right) \rho(r) \quad (6.18)$$

It was chosen to apply this rescaling for all models with $\Omega_\chi h^2 \leq 0.1$. This affects the boost factor as

$$f_b \rightarrow f_b \left(\frac{\Omega_\chi h^2}{0.1} \right)^{-2} \quad (6.19)$$

As is obvious from the figure, this means that the lowest boost factors are found in models that have neutralino relic densities small enough as to just require no rescaling. The figure also implies that it is difficult to accommodate a scenario that explains the positron fraction excess as being due to neutralino annihilations without needing boost factors larger than 100 or so in the mSUGRA model. The Sommerfeld enhancement effect [178] that has been discussed in the literature to boost the annihilation cross section at non-relativistic speeds is not important in the context of this study. Typically, it becomes sizeable for

6.2 Constraints on mSUGRA parameter space from currently available data

dark matter masses above ~ 1 TeV, but this range is not considered here.

Figure 6.8 shows the latest results of some direct detection experiments. The limits

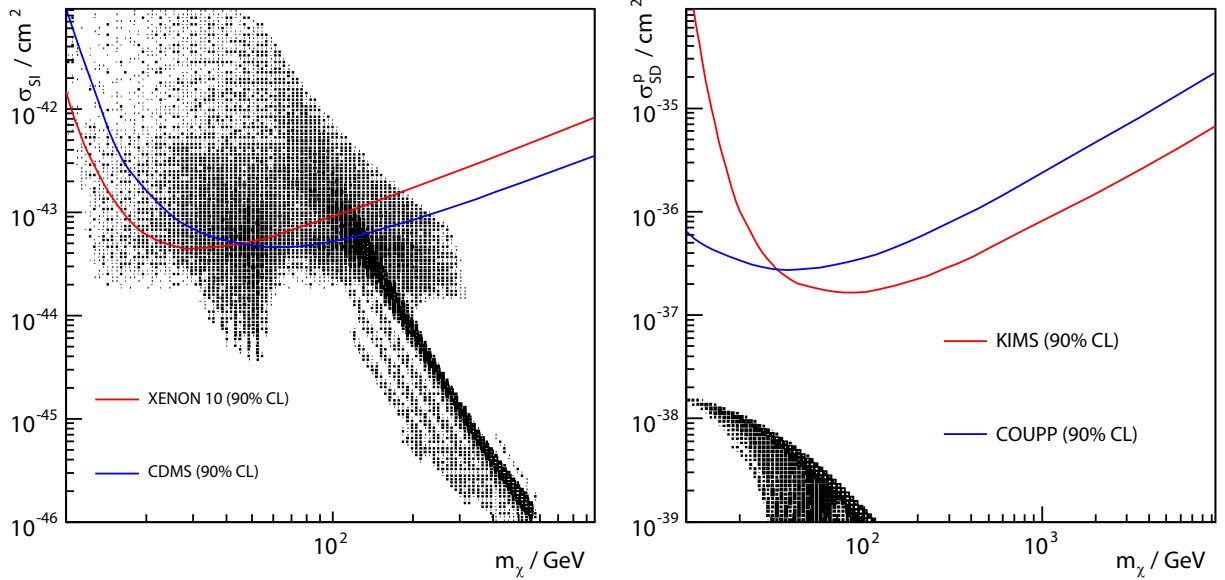


Fig. 6.8: mSUGRA prediction for WIMP-nucleon cross sections, for effective scalar (spin-independent) couplings (*left*) and pure proton spin-dependent couplings (*right*). Models allowed by the constraints on $\Omega_\chi h^2$, Δa_μ and $BR(b \rightarrow s\gamma)$ at the 3σ -level each are included. Also shown are the currently best limits, provided by the XENON10 [172], CDMS [171], COUPP [173] and KIMS [174] experiments, respectively.

obtained on the spin-independent cross section and the cross section for pure proton spin-dependent couplings are drawn as a function of m_χ . mSUGRA models allowed by the constraints on $\Omega_\chi h^2$, Δa_μ and $BR(b \rightarrow s\gamma)$ at the 3σ -level each are included. The measurements by the CDMS and XENON10 experiments already exclude significant amounts of the mSUGRA parameter space. Especially points belonging to the focus point region or the bulk annihilation region at low values of m_0 and $m_{1/2}$ are excluded in this way. On the other hand, measurements of the spin-dependent couplings still need at least an order of magnitude more sensitivity.

All the information gathered so far can now be assembled in a condensed way. For this purpose, a total χ^2 for all mSUGRA parameter points included in the scans is calculated:

$$\begin{aligned}
 \chi_{\text{tot}}^2 = & \chi_{e^+/(e^++e^-)}^2 + \left(\frac{m_t^{\text{scan}} - m_t}{\sigma_{m_t}} \right)^2 + \\
 & \Theta(\Omega_\chi^{\text{scan}} h^2 - \Omega_{\text{nbm}} h^2) \cdot \left(\frac{\Omega_\chi^{\text{scan}} h^2 - \Omega_{\text{nbm}} h^2}{\sigma_{\Omega_{\text{nbm}} h^2}} \right)^2 + \\
 & \left(\frac{\Delta a_\mu^{\text{scan}} - \Delta a_\mu}{\sigma_{\Delta a_\mu}} \right)^2 + \left(\frac{BR_{b \rightarrow s\gamma}^{\text{scan}} - BR_{b \rightarrow s\gamma}}{\sigma_{BR(b \rightarrow s\gamma)}} \right)^2
 \end{aligned} \tag{6.20}$$

6 Constraining supersymmetry with cosmic-ray data

where the superscript ^{scan} denotes a value at a given mSUGRA parameter point and the Heaviside function in front of the relic density term makes sure that only neutralino relic densities in excess of the constraint contribute to the χ^2 .

One proceeds by calculating χ_{tot}^2 for all mSUGRA parameter points in the scans and looking at χ_{tot}^2 in the two-dimensional projections of the (mSUGRA, m_t)-parameter space. The most interesting one, the $m_{1/2}$ - m_0 -plane, is shown in figure 6.9. For a given point in that plane, the minimum value of χ_{tot}^2 obtainable for any pair of $(\tan \beta, m_t)$ is plotted, but only parameter points allowed by the direct detection experiments and LEP mass limits

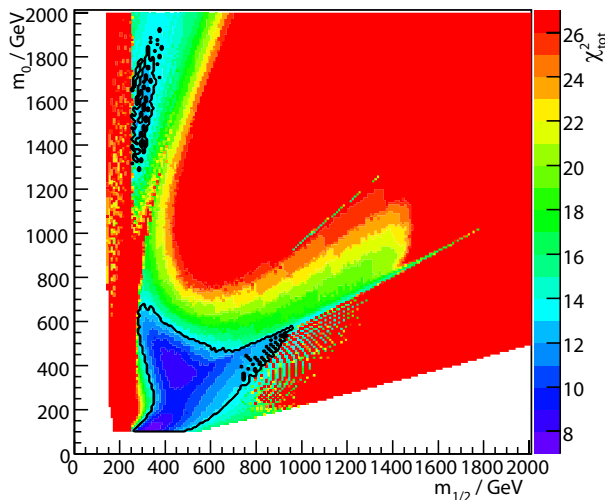


Fig. 6.9: χ_{tot}^2 -contour in the $m_{1/2}$ - m_0 -plane. The minimum obtainable for any value of $(\tan \beta, m_t)$ in the scans is plotted in each point. Also included is the contour for the parameters within the intervals of 90 % confidence level around the minimum. Only parameter points allowed by the direct detection experiments and LEP mass limits are included.

are included. The contour for the parameters within an interval of 90 % confidence level around the minimum, where the number of free parameters considered is three (m_0 , $m_{1/2}$, and $\tan \beta$), is drawn, too [79]. It is stressed that the figure does not provide any evidence for the existence of neutralino dark matter, but rather may indicate some hints on where to look assuming that mSUGRA is realised in nature.

In this sense, low values of χ_{tot}^2 are found for several regions in the mSUGRA parameter space [179]: The lowest values can be found for the $\tilde{\tau}$ -coannihilation regions at low values of m_0 , where $\chi\tilde{\tau}$ -coannihilations contributed significantly to the neutralino annihilation rate in the early Universe. Acceptable values of χ_{tot}^2 are also found in the focus point region at large m_0 , near the boundary of the region forbidden by the absence of electroweak symmetry breaking, and in the A -annihilation funnel occurring for large $\tan \beta$. Unfortunately, only weak conclusions regarding the neutralino mass can be drawn from these results (fig. 6.17).

For illustration purposes, two reference points were chosen, both with acceptable values of χ_{tot}^2 , called PP1 and PP2 in the following, giving a typical example of mSUGRA

6.2 Constraints on mSUGRA parameter space from currently available data

phenomenology in the preferred region:

$$\text{PP1 : } m_0 = 1560 \text{ GeV} \quad m_{1/2} = 260 \text{ GeV} \quad \tan \beta = 40 \quad m_t = 172.76 \text{ GeV} \quad (6.21)$$

$$\text{PP2 : } m_0 = 100 \text{ GeV} \quad m_{1/2} = 310 \text{ GeV} \quad \tan \beta = 20 \quad m_t = 172.76 \text{ GeV} \quad (6.22)$$

PP2 is very close to the lowest value of χ_{tot}^2 in the scans and lies in the $\tilde{\tau}$ -coannihilation region, while PP1 is in the focus point region offering better prospects for discovery with PEBS and AMS-02 as will be seen. Neutralino annihilation is dominated by the $\chi\chi \rightarrow W^+W^-$ channel in this case. Explaining the observed excess in the positron fraction requires large boost factors, as seen above, and best-fit values of 152 and 1492 are obtained for PP1 and PP2, respectively.

Before turning to the detection prospects for PEBS and AMS-02 for these benchmark models, a discussion of the situation for other promising dark matter probes, namely γ -rays, antiprotons and antideuterons follows.

The γ -ray component in the cosmic rays is unique in that it always points directly back to its origin. π^0 s created in the decay chain of WIMP annihilations will constitute an additional source of γ -rays. The best data available so far in the GeV-range was taken by the EGRET detector [52] on board the Compton Gamma Ray Observatory (fig. 6.11).

Again, the χ^2 of a background+model hypothesis was calculated, as

$$\chi_\gamma^2 = \sum_i \left(\frac{\Phi_i^{\text{model}} - \Phi_i^{\text{data}}}{\sigma_i} \right)^2 \quad (6.23)$$

where $\Phi_i^{\text{model}} = \Phi_i^{\text{bg}} + f_b^\gamma \cdot \Phi_i^{\text{sig}}$. The boost factor for the γ -rays is allowed to differ from the one for positrons and electrons. This is due to the fact that the latter originate from regions of space in our vicinity because of their large energy losses whereas the former sample the entire Galaxy. The boost factor is chosen as a free parameter minimising χ_γ^2 for a given mSUGRA parameter point. Figure 6.10 shows the χ_γ^2 obtained and the corresponding boost factors for the same parameters as in fig. 6.6. While the boost factors tend to be even higher than in the positron case, the χ^2 shows a preference for areas with relatively low values of $m_{1/2}$.

A brief discussion of the diffuse γ -ray data in the context of the spectrum of antiprotons follows. The latter has been measured in continuously repeated flights of the BESS experiment [180]. Figure 6.11 shows the EGRET γ -ray data from the inner Galaxy and the best fit of the SUSY signal in the benchmark PP1 model to the data. A rather high boost factor of roughly 500 is needed. The figure also compares the BESS antiproton data to the secondary prediction and the expected SUSY signal. For better comparison, the antiproton data for the years 1995-1999, when solar activity was low, were demodulated according to the force-field approximation and a binned weighted mean was calculated for them using the procedure outlined in [181]. These can then be compared to the unmodulated background and signal fluxes. As the figure shows, the conventional Galprop model slightly underproduces antiprotons, while the plain diffusion model predicts somewhat higher fluxes than are observed. However, no need for an additional signal component is apparent. In fact, as energy losses during propagation are negligible for antiprotons and

6 Constraining supersymmetry with cosmic-ray data

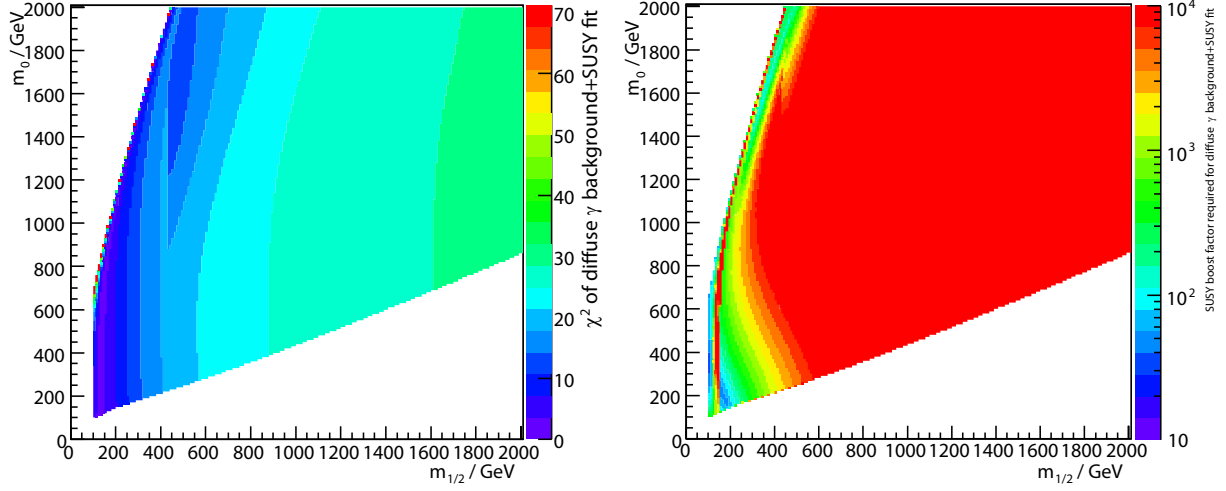


Fig. 6.10: χ^2_γ and corresponding boost factor for γ -ray data, for $\tan\beta = 40$ and $m_t = 170.9$ GeV.

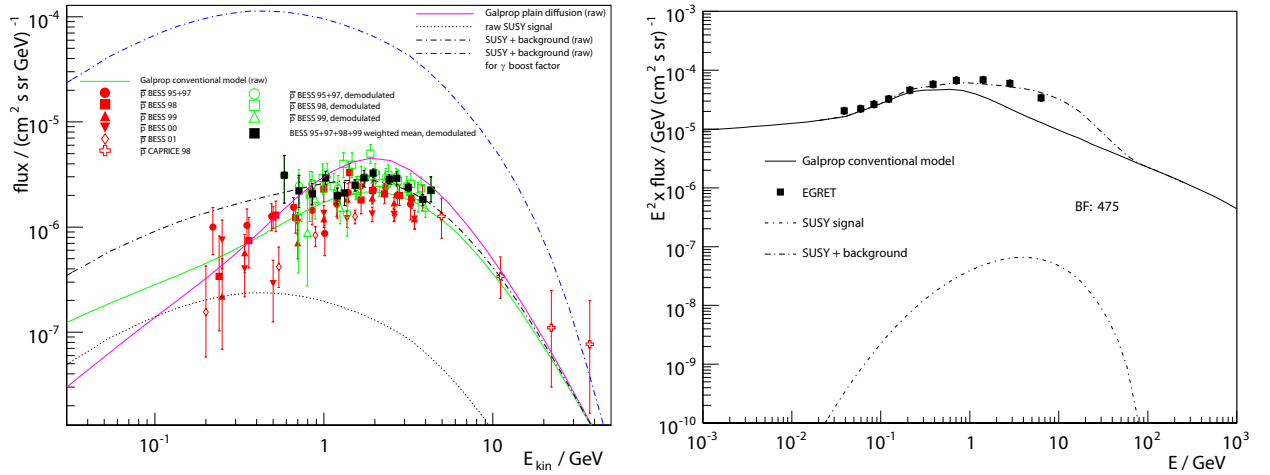


Fig. 6.11: Antiproton data (*left*) and data for diffuse γ -rays from the inner Galaxy ($330^\circ < l < 30^\circ$, $|b| < 5^\circ$) (*right*). Antiproton data are from BESS [50, 87, 187, 188] and CAPRICE [51]. For better comparison, the weighted mean of the demodulated BESS data for the years 1995–99 is also shown. The raw spectra predicted by Galprop’s conventional and plain diffusion models are shown, together with the signal from neutralino annihilation. The predicted spectrum obtained with the boost factor for the best fit to the γ -ray data is included. γ -ray data are from EGRET [52]. The best-fit spectra obtained in the PP1 benchmark model are also shown.

they therefore originate from the entire Galaxy, the boost factors for γ -rays and antiprotons should be comparable. This assumption leads to an antiproton flux that is higher than the measured one by orders of magnitude (fig. 6.11). This problem has been pointed out before [183] and shows that interpreting the EGRET excess in terms of SUSY dark matter is problematic. In fact, simpler explanations for the excess have been put forward. It has been suggested to be due to a systematic effect in the sensitivity determination of

6.2 Constraints on mSUGRA parameter space from currently available data

the EGRET detector [184] and it was demonstrated that an optimised model of cosmic-ray propagation can be found that fits the EGRET data at all energies but requires an upward normalisation of the propagated fluxes by a factor of a few over the locally observed ones [185]. Therefore, it was chosen not to include the γ -ray data in the χ^2_{tot} -scan. A principle comment on the approach taken here is in order. If, as in the case of the antiprotons, the spectral shapes of the background and signal components are similar, tuning the background model alone to fit the data will only lead to valid results if the signal component is small. While this cannot be assumed a priori, the γ -ray spectrum, which is dominated by the π^0 contribution in the inner region of the Galaxy, clearly suggests that it is justified in this case as antiprotons are created in the same reactions as the π^0 s.

Antideuterons constitute an interesting probe for neutralino dark matter because they are not plagued by the problems seen for the antiprotons in fig. 6.11, namely the high flux and similar spectral shape of the secondary component with respect to the annihilation signal [186]. This is because spallation reactions taking place when cosmic-ray protons

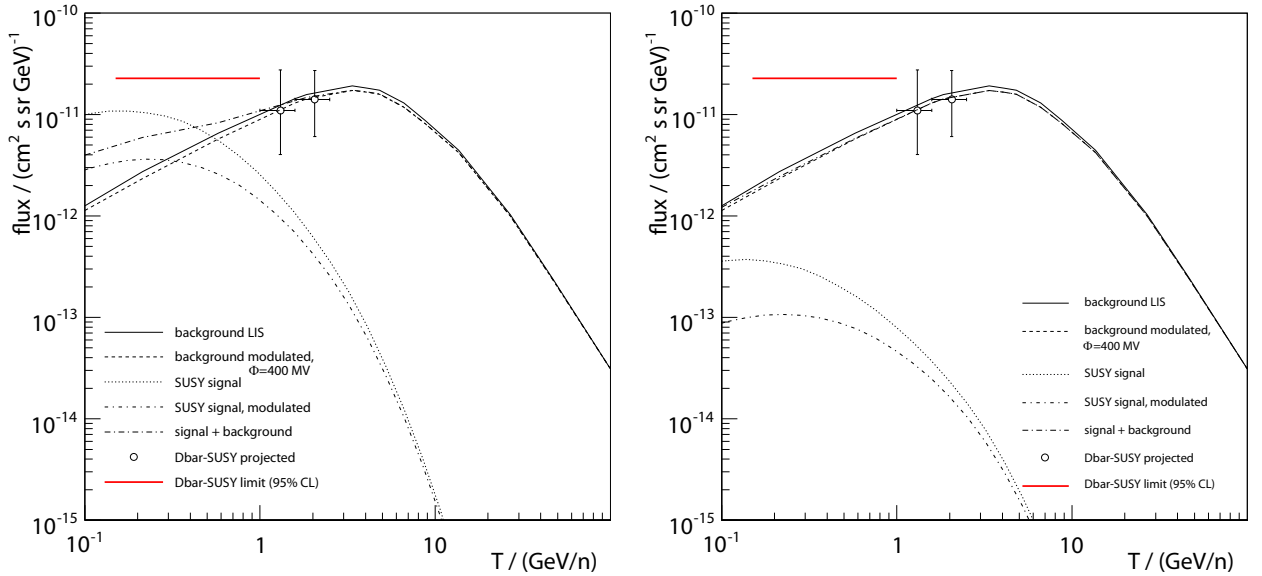


Fig. 6.12: Antideuteron signal from neutralino annihilation for the PP1 (*left*) and PP2 (*right*) benchmark models, together with the background prediction of [186]. Both local interstellar and solar modulated ($\phi = 400$ MV) fluxes are shown. The statistical errors that an experiment with a geometric acceptance of $1.8\text{m}^2\text{sr}$ and a measurement time of 100 d, like the proposed Dbar-SUSY mission [182], will be able to achieve are shown. At low energies, the flux drops below the detection threshold, and the expected 95% CL limits are included, too.

interact with the interstellar matter create very few low-energy particles, and low-energy secondary antideuterons are even further suppressed. On the other hand, the fusion of an antiproton and an antineutron will only be successful if their relative velocity is low. This is the case for neutralino annihilations. Figure 6.12 shows the predicted \bar{D} fluxes from $\chi\chi$ -annihilation as calculated by DarkSUSY for the benchmark models PP1 and PP2,

together with a prediction for the secondary background. While the detection of low-energy antideuterons would constitute a very strong hint at the existence of neutralino dark matter, the expected flux is prohibitively low.

6.3 Projected improvements with PEBS

Having established the most likely regions of the mSUGRA parameter space and having chosen two representative parameter points, one can now turn to examining the prospects for dark matter detection with PEBS.

The positron fraction and its statistical errors to be expected in the PP1 and PP2 models for a detector with a geometric acceptance of $3850 \text{ cm}^2 \text{ sr}$ and an exposure of 40 days, as projected for PEBS, are depicted in figures 6.13 and 6.14, respectively. The improvement

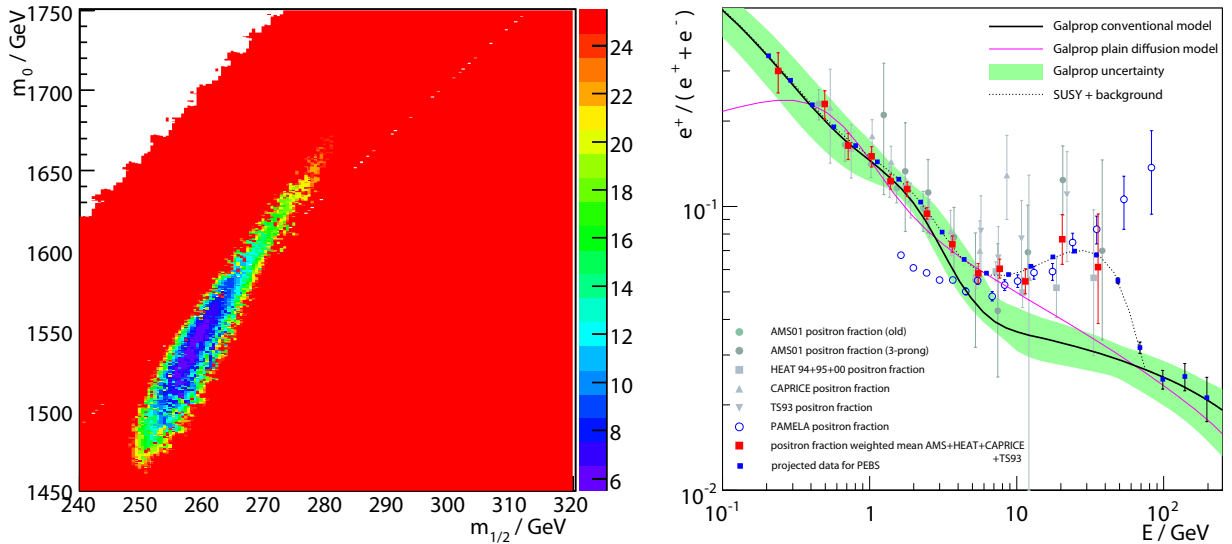


Fig. 6.13: $\chi^2_{e^+/(e^++e^-)}$ -contour for a fit to the projected PEBS data for the parameter point PP1 in a small part of the $m_{1/2}$ - m_0 -plane, for $\tan\beta = 40$ and $m_t = 172.76 \text{ GeV}$ (left) and projected positron fraction for a measurement of 40 days assuming an acceptance of $3850 \text{ cm}^2 \text{ sr}$ (right). Only the signal region above 5 GeV was considered for the calculation of the $\chi^2_{e^+/(e^++e^-)}$.

to be expected over the existing measurements, also shown in the figures, is twofold. First, the statistical uncertainties in the region below 100 GeV will be completely negligible. Second, and probably even more important, the improved energy and charge sign resolution, combined with the larger acceptance, of the next generation of detectors will extend the energy range of the measurements into the currently unexplored regime above this level. This will allow to check for the distinctive return to the background curve which essentially constitutes a smoking gun for some sort of particle dark matter. In our model, the location of the edge - though smeared out during the propagation - is a measure for the neutralino mass, while its steepness and overall form indicate the preferred decay channel. In the case of PP1, the dominant reaction $\chi\chi \rightarrow WW$ leads to the rather prominent slope.

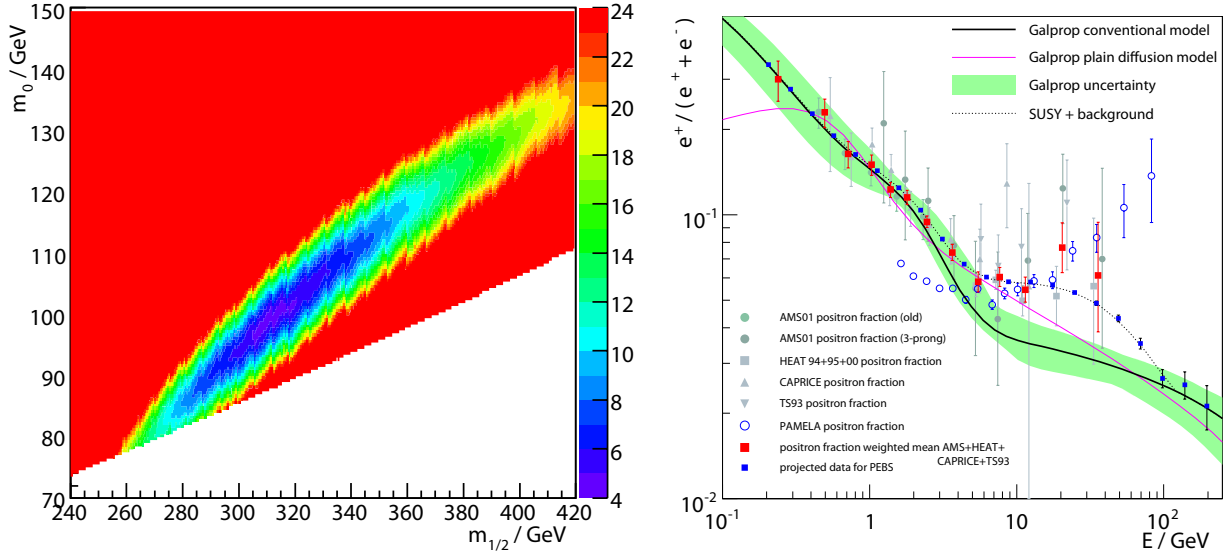


Fig. 6.14: $\chi_{e^+/(e^++e^-)}^2$ -contour for a fit to the projected PEBS data for the parameter point PP2 in the $m_{1/2}$ - m_0 -plane, for $\tan\beta = 20$ and $m_t = 172.76$ GeV (*left*) and projected positron fraction for a measurement of 40 days assuming an acceptance of $3850 \text{ cm}^2\text{sr}$ (*right*). Only the signal region above 5 GeV was considered for the calculation of the $\chi_{e^+/(e^++e^-)}^2$.

Figures 6.13 and 6.14 also contain the $\chi_{e^+/(e^++e^-)}^2$ -contour for projected PEBS data in a finer sampling of the GUT mass scales around PP1 and PP2, respectively. For a given $(\tan\beta, m_t)$ pair, these values can – in principle – be very well constrained using the positron fraction alone. This is in stark contrast to the present-day situation (fig. 6.6).

Looking at the entire parameter space included in the scans, figures 6.15 and 6.16 show those points yielding a projected $\chi_{e^+/(e^++e^-)}^2$ within the 90% confidence level interval around the minimum, for PP1 and PP2, respectively. The problem of displaying the four-dimensional parameter space has been solved here by showing the six possible two-dimensional projections, one for each pair of parameters. While neither $\tan\beta$ nor m_t will be constrained at either point, the quantity that can be determined with great accuracy from the upcoming positron detectors is the neutralino mass. This is illustrated in figure 6.17 showing m_χ for all points included in figs. 6.9, 6.15 and 6.16. The resolution obtainable in principle is on the order of 5 GeV for PP1 while it is 25 GeV for PP2, due to the flatter shape of the signal flux at this point. These results indicate that the mass resolution obtainable in practice will be limited both by the energy resolution of the detector, which was not taken into account here, and the systematic uncertainties in the propagation model. Interestingly, the corresponding boost factors vary over several orders of magnitude.

If supersymmetry is realised in nature, the LHC collider at CERN will have a good chance of creating supersymmetric particles, among them the neutralino. A coherent picture of the dark matter will ideally include the establishing of candidate particles by a collider, proof of its existence in Earth’s vicinity by direct detection experiments and evidence for

6 Constraining supersymmetry with cosmic-ray data

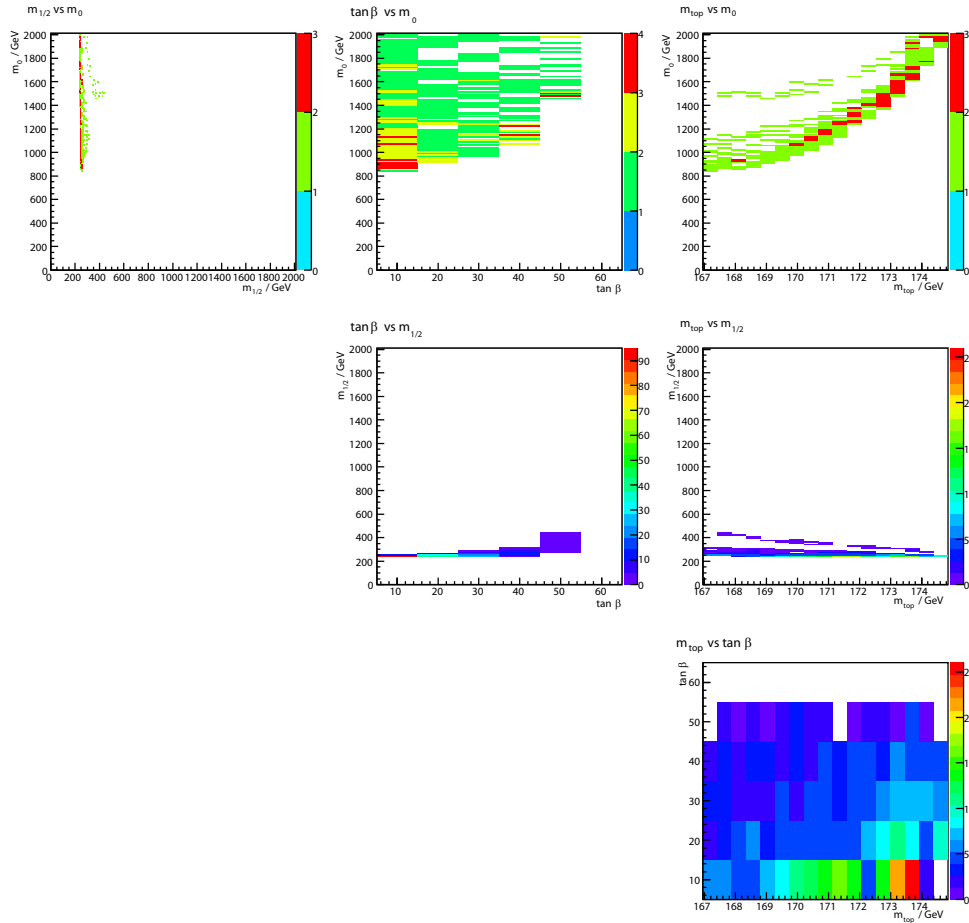


Fig. 6.15: Remaining mSUGRA parameter space from projected PEBS positron fraction alone, for the PP1 parameter point. The z -axis here counts number of models. Only models yielding a $\chi_{e^+/(e^++e^-)}^2$ in the 90% confidence level interval around the minimum are included.

its presence throughout the Galaxy by indirect searches. Independent verification of as many properties of the dark matter as possible by the different approaches will play a key role in this picture. An example for such an interplay would be the prediction of sparticle masses expected from cosmic-ray observations which in turn could be verified by the LHC. For the benchmark parameter point PP1, the predicted mass spectrum of sparticles is depicted in figure 6.18. Again, all points yielding a projected $\chi_{e^+/(e^++e^-)}^2$ within the 90% confidence level interval around the minimum have been included. Unfortunately, while the neutralino and chargino masses can be predicted to the order of 10 to 100 GeV, the other sparticle masses still vary over a range of 1000 GeV.

As a cross-check regarding the sensibility towards the choice of the propagation model, it was tried to fit the projected PEBS data at PP1 (generated with the conventional Gal-prop model) with any mSUGRA model on top of the alternative plain-diffusion model. No parameter set giving a χ^2 below a few thousand was found in this way. One may thus hope that ambiguities arising from the choice of propagation model will not play a major role. Instead, it may be possible to draw conclusions about cosmic-ray propagation

6.4 Comparison to AMS-02

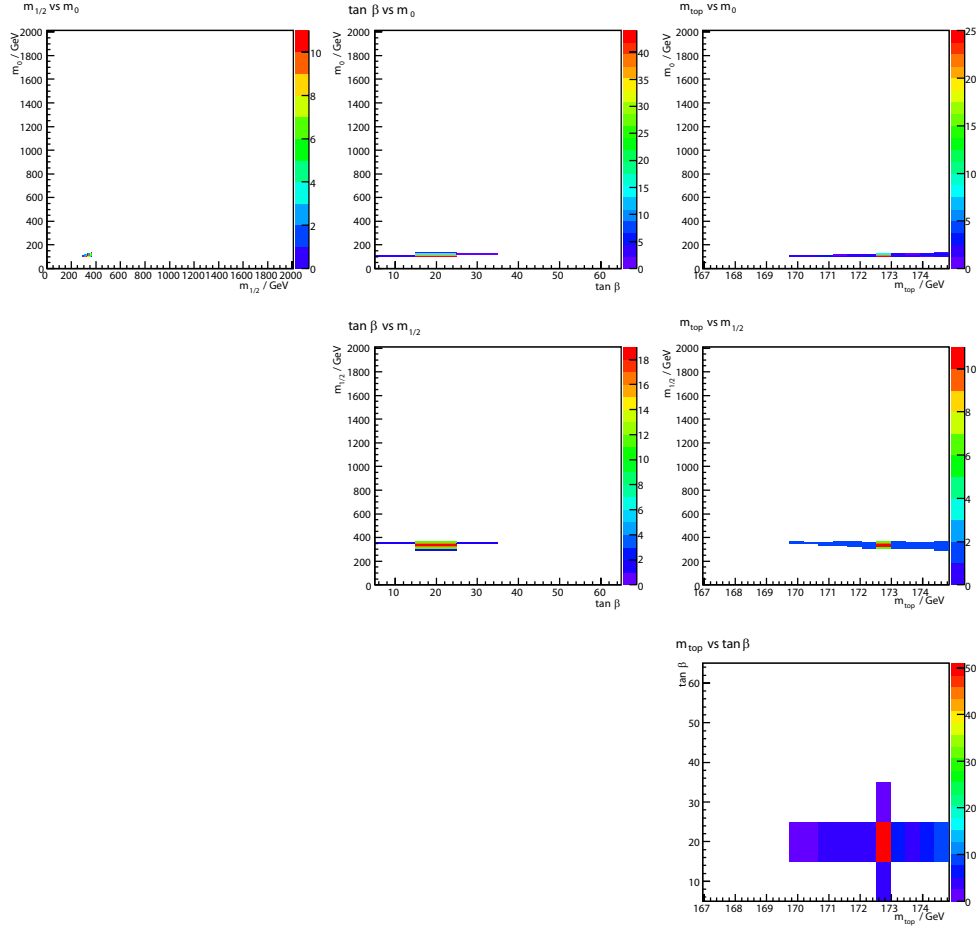


Fig. 6.16: Remaining mSUGRA parameter space from projected PEBS positron fraction alone, for the PP2 parameter point. The z -axis here counts number of models. Only models yielding a $\chi^2_{e^+/(e^++e^-)}$ in the 90% confidence level interval around the minimum are included.

(sec. 2.6) and the presence of a primary signal at the same time.

Figures 6.13 and 6.14 also contain the new positron fraction data measured by the PAMELA experiment. A comparison to the signal spectrum expected for the mSUGRA model at PP1 shows that it matches the data quite well at intermediate energies, but fails to meet the data points at the highest two energies which indicate an even steeper increase with energy. The PP2 model is clearly disfavoured by the PAMELA data because the positron fraction it predicts is much too shallow to follow the rise apparent in the PAMELA data towards high energies.

6.4 Comparison to AMS-02

To put the projected performance of PEBS into perspective, a study of the performance of AMS-02, with a measurement time of three years and an acceptance of $875 \text{ cm}^2 \text{ sr}$,

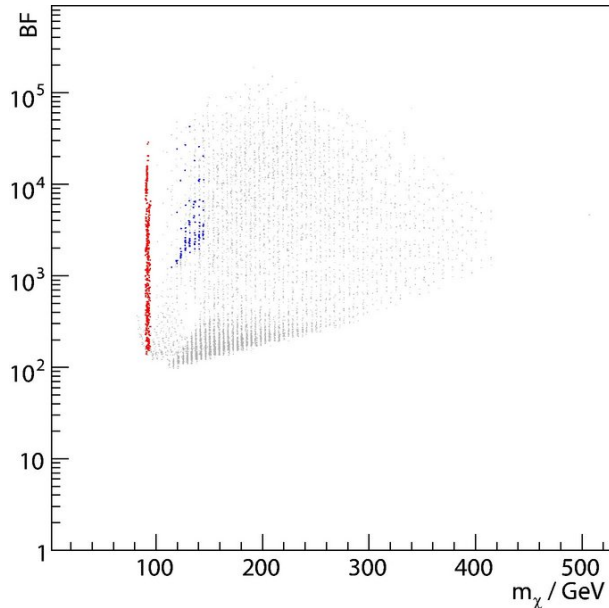


Fig. 6.17: Neutralino mass and positron fraction boost factor for points included in figure 6.15 (large red dots) and for points included in figure 6.16 (large blue dots) and for points corresponding to the 90 % CL interval in figure 6.9 (small grey dots).

was done for the two benchmark parameter points PP1 and PP2 (figs. 6.19 and 6.20). AMS-02 will be able to gather more statistical power than PEBS and the χ^2 -contours are correspondingly smaller. On the other hand, taking the systematic uncertainties, e.g. the limited energy resolution of the calorimeters employed and the limited knowledge of the expected secondary background, into account, it becomes clear that the interpretation of the measurements will be ultimately limited by the systematics at this level of statistical accuracy. Neglecting these effects, a comparison of the projected constraining power of PAMELA, PEBS, and AMS-02 (fig. 6.21) for the PP1 benchmark case shows that PEBS and AMS-02 perform almost equally well, while the smaller acceptance of PAMELA leads to significantly larger confidence level contours in mSUGRA parameter space.

6.5 mSUGRA dark matter in the light of PAMELA data

As found in section 6.3, the mSUGRA models considered so far have difficulties in describing the PAMELA data that have very recently become available. These results have confirmed the excess of positrons with respect to models of purely secondary production at high energies. They have subsequently created a surge of publication activity. The most popular mechanisms invoked to explain the data are the annihilation or decay of particle dark matter and an origin in nearby young pulsars. There, electrons are accelerated in the quasi-static electric fields of the pulsar's magnetosphere to ultra-relativistic energies. They will in turn radiate energetic synchrotron photons which give rise to e^\pm -pairs by pair production in the dense magnetic fields. Ref. [189] contains an extensive list of recent work on these subjects.

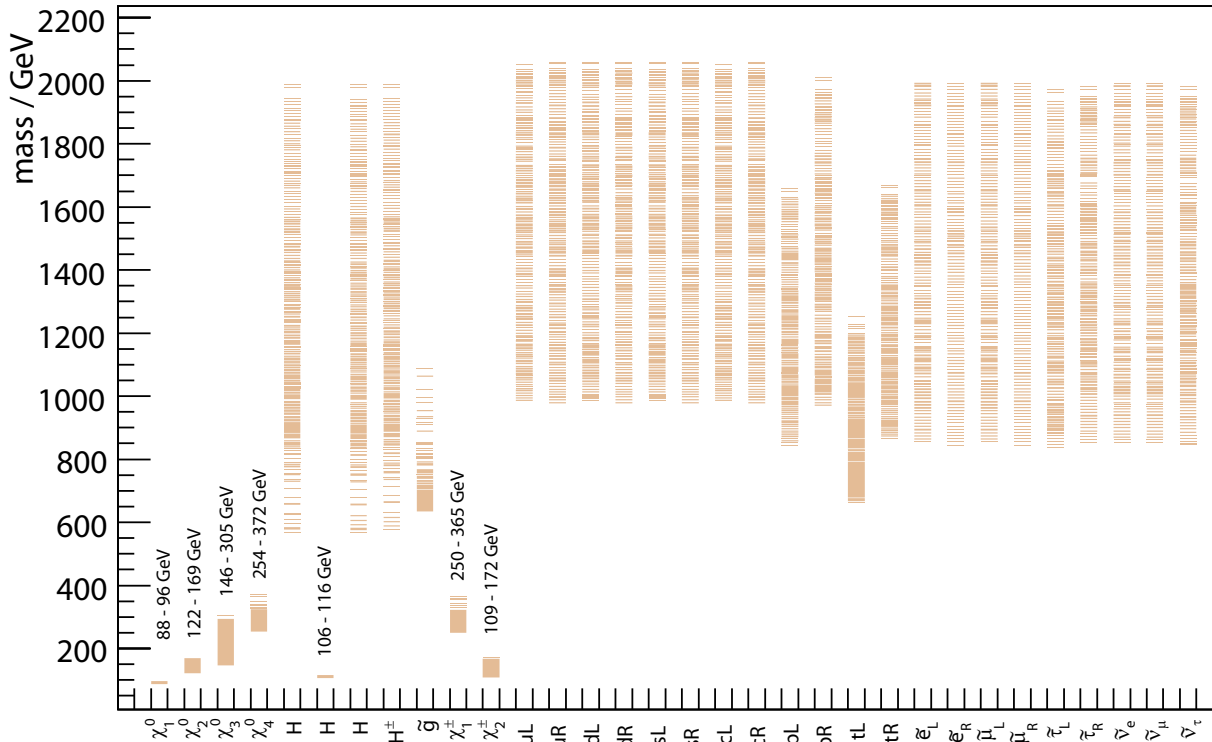


Fig. 6.18: Sparticle mass spectrum for points included in fig. 6.15.

To put the PAMELA results into perspective, the scans of mSUGRA parameter space were extended to cover also the range of higher m_0 , specifically $2000 \text{ GeV} \leq m_0 \leq 4000 \text{ GeV}$, but in the limited ranges of $10 \leq \tan \beta \leq 50$ and $170.435 \text{ GeV} \leq m_t \leq 174.62 \text{ GeV}$, in order to keep the necessary computing time acceptable.

The result is a χ^2 -scan of the extended mSUGRA parameter space (6.22 left), with the χ^2 defined as

$$\chi^2 \equiv \chi_{\text{positron fraction}}^2 + \left(\frac{m_t^{\text{scan}} - m_t}{\sigma_{m_t}} \right)^2 \quad (6.24)$$

The first term refers to the deviation of a given model from the positron fraction data of AMS-01, HEAT, CAPRICE, TS93, and PAMELA, analogous to (6.13). The local interstellar spectra obtained by applying the correction for solar modulation effects described in section 2.7 were used. The statistical uncertainty of the Galprop conventional model was evaluated as in section 2.6, by looking at the B/C-data and the low-energy positron fraction data. The σ_i^2 values used in the calculation of the χ^2 were then calculated as

$$\sigma_i^2 = \sigma_{i,\text{data}}^2 + \sigma_{i,\text{bg}}^2 \quad (6.25)$$

taking the statistical uncertainties both of the data and of the background calculation into account. This is important as the PAMELA data at intermediate energies now have statistical uncertainties that are small compared to the background ones. The boost factor was chosen as to give the best χ^2 . The second term in (6.24) punishes models with a

6 Constraining supersymmetry with cosmic-ray data

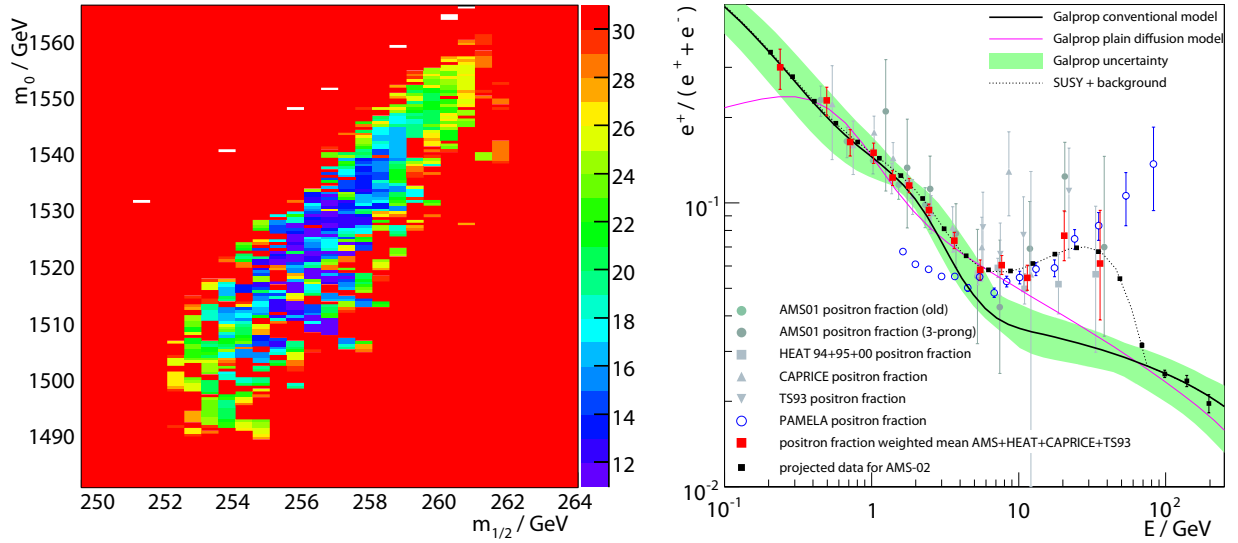


Fig. 6.19: $\chi^2_{e^+/(e^++e^-)}$ -contour for a fit to the projected AMS-02 data for the parameter point PP1 in a small part of the $m_{1/2}$ - m_0 -plane, for $\tan\beta = 40$ and $m_t = 172.76$ GeV (left) and projected positron fraction for a measurement of 3 years assuming an acceptance of $875 \text{ cm}^2\text{sr}$ (right). Only the signal region above 5 GeV was considered for the calculation of the $\chi^2_{e^+/(e^++e^-)}$. Note the reduced scale as compared to fig. 6.13.

top-quark mass differing from the measured value. Only models fulfilling the constraints on relic density and $BR(b \rightarrow s\gamma)$ at the 3σ -level, as well as existing mass limits and direct detection limits, and having a best-fit boost factor of less than 10^4 are considered. The PAMELA data favour either a focus-point scenario, at large values of m_0 , or a coannihilation scenario, at large values of $m_{1/2}$. The remaining parameter space with χ^2 -values close to the minimum is large and extends beyond the range covered in the scans. However, when it is additionally required that supersymmetry cancel the discrepancy in the magnetic moment of the muon at the 3σ -level, two portions of parameter space remain, located between the values $1300 \text{ GeV} \leq m_0 \leq 2500 \text{ GeV}$ and $250 \text{ GeV} \leq m_{1/2} \leq 700 \text{ GeV}$, or between the values $600 \text{ GeV} \leq m_0 \leq 1300 \text{ GeV}$ and $900 \text{ GeV} \leq m_{1/2} \leq 1350 \text{ GeV}$.

As an example, the minimum within the former region is found at the parameter point

$$\text{PP3 : } m_0 = 2040 \text{ GeV} \quad m_{1/2} = 390 \text{ GeV} \quad \tan\beta = 40 \quad m_t = 172.295 \text{ GeV} \quad (6.26)$$

The best-fit positron fraction at PP3 (fig. 6.22 right) has a boost factor of 1510. The lightest neutralino has a mass of $m_\chi = 93$ GeV and annihilates predominantly through the channels $\chi\chi \rightarrow WW$ and $\chi\chi \rightarrow ZZ$ with branching ratios of 83 % and 10 %, respectively. The quality-of-fit achieved in this model is typical for the mSUGRA models within the regions quoted above. While a good description of the PAMELA positron fraction data is possible at intermediate energies, the data points at the two highest energies show deviations of 2.5σ and 2.6σ , respectively. The PAMELA data therefore arguably still indicate a steeper increase than is possible from dark matter annihilations in the mSUGRA

6.5 mSUGRA dark matter in the light of PAMELA data

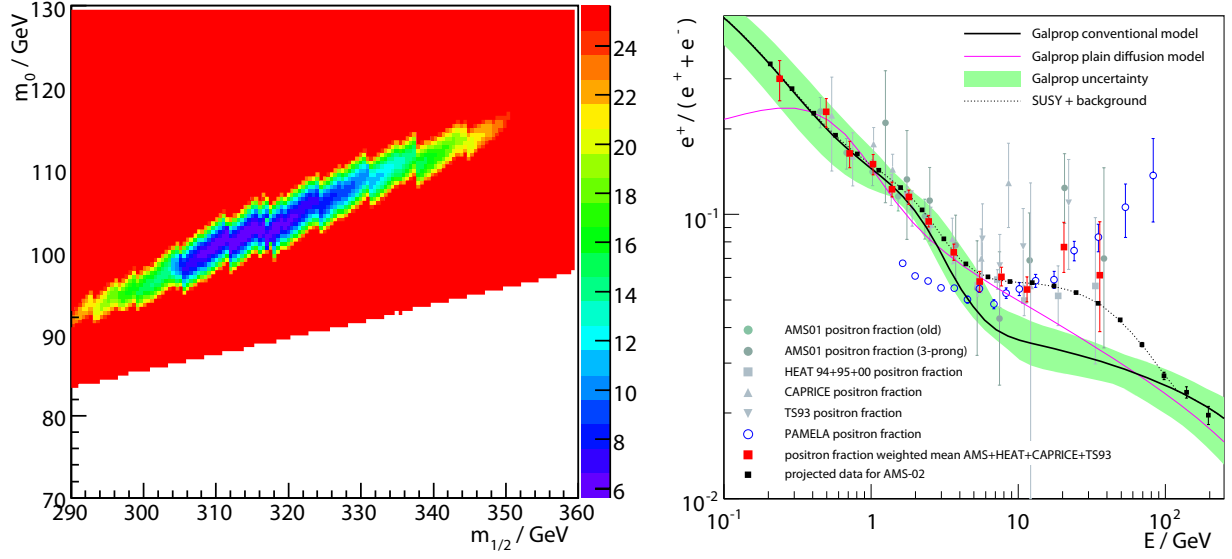


Fig. 6.20: $\chi^2_{e^+/(e^++e^-)}$ -contour for a fit to the projected AMS-02 data for the parameter point PP2 in a small part of the $m_{1/2}$ - m_0 -plane, for $\tan\beta = 20$ and $m_t = 172.76$ GeV (*left*) and projected positron fraction for a measurement of 3 years assuming an acceptance of 875 cm²sr (*right*). Only the signal region above 5 GeV was considered for the calculation of the $\chi^2_{e^+/(e^++e^-)}$.

model. This scenario could also be tested with the statistics and energy range accessible to both PEBS and AMS-02.

It should be stressed that this scenario requires a drastically lower boost factor (on the order of a few) for antiprotons than for electrons lest the antiproton flux from neutralino annihilations exceeds the measured one. This is a rather universal conclusion concerning any kind of dark matter which decays or annihilates into standard model gauge bosons or quarks. As a consequence, the dark matter candidates studied in the recent literature, e.g. in [191, 192, 193] to name only a few, are constructed such that they preferably or exclusively yield leptons.

6 Constraining supersymmetry with cosmic-ray data

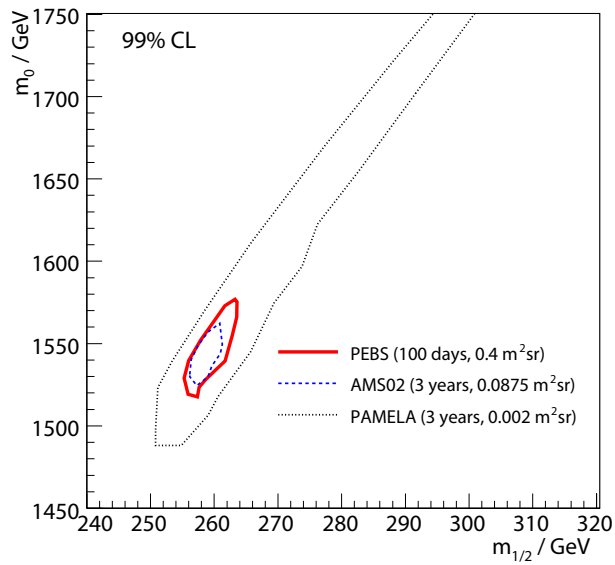


Fig. 6.21: 99% confidence level areas derived from the $\chi^2_{e^+/(e^++e^-)}$ -contours for fits to the projected data from PAMELA, PEBS, and AMS-02, for the parameter point PP1 in a small part of the $m_{1/2}$ - m_0 -plane, for $\tan\beta = 40$ and $m_t = 172.76$ GeV. The statistics that PEBS could accumulate in a series of flights for a total measurement time of 100 days was used. The PAMELA contour refers to the projected data based on acceptance and mission duration, for comparison to the other projects, not to the actual data.

6.5 mSUGRA dark matter in the light of PAMELA data

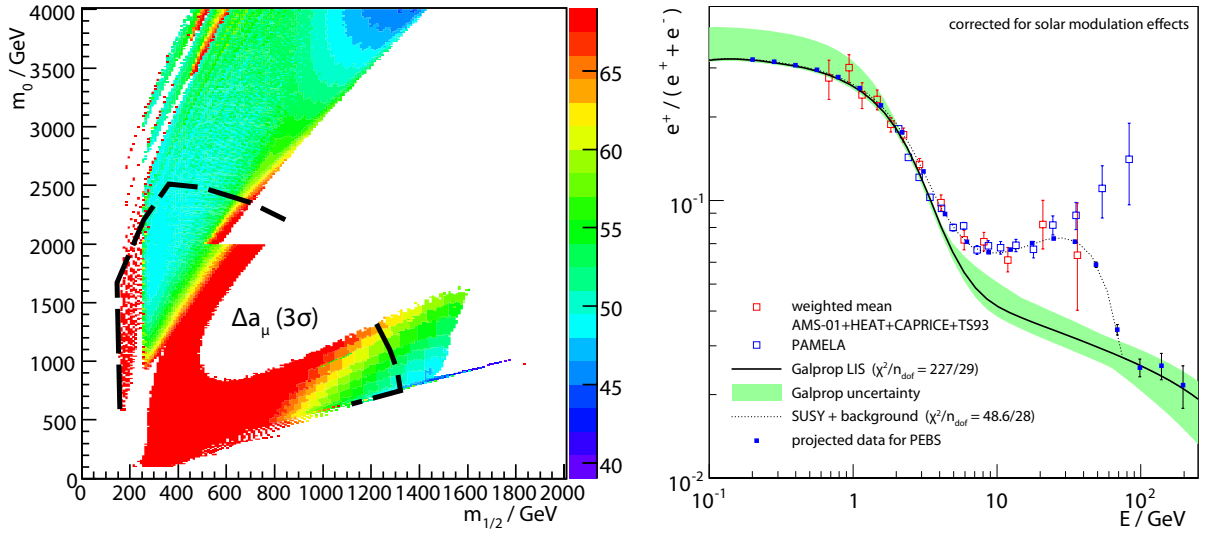


Fig. 6.22: *Left:* χ^2 with respect to the positron fraction data including PAMELA and the top-quark mass, as defined in the text, in the $m_{1/2}$ - m_0 -plane. The correction for solar modulation according to section 2.7 was applied to the data and the local interstellar spectra of the Galprop conventional model were used. The remaining statistical uncertainty of the background model was taken into account in the calculation of the χ^2 . Only models fulfilling the constraints on relic density and $BR(b \rightarrow s\gamma)$ at the 3σ -level, as well as existing mass limits and direct detection limits, and having a best-fit boost factor of less than 10^4 are included. Models additionally giving a value of Δa_μ falling within the preferred region at the 3σ -level lie within the region bounded from above by the dashed line. *Right:* Best-fit positron fraction with respect to the data of AMS-01, HEAT, CAPRICE, TS93, and PAMELA, for the PP3 mSUGRA model.

6 *Constraining supersymmetry with cosmic-ray data*

7 Conclusions and outlook

The longstanding problem concerning the nature of dark matter might finally be solved within the next years. The Large Hadron Collider will commence operations in summer 2009, several direct detection experiments are underway and are pushing their limits to lower and lower cross sections, and the PAMELA detector is in orbit and the first publications on the positron fraction have proven to be intriguing. At the same time, AMS-02 is nearing completion and offers outstanding potential for precision spectroscopy of cosmic rays. And the Fermi Gamma-ray Space Telescope has been launched in June 2008 and might observe the γ -ray signals of dark matter annihilations [190].

It is important to remember that the dark matter conundrum cannot be solved by any of these different approaches alone. If neutralinos are produced by the accelerator, who will be able to tell whether they really constitute the dark matter? A signal in the direct detection experiments is necessary to confirm the presence of dark matter in the solar neighbourhood. On the one hand, a signature in the cosmic-ray spectra, and quite possibly in γ -ray telescopes and neutrino observatories, would go a long way towards establishing the nature of dark matter in the Milky Way and possibly its neighbours. On the other hand, it seems unlikely that the underlying model and its properties can be pinpointed from these measurements alone, without the studies possible at accelerators.

The main focus of this thesis has been a design study for a potential new player in the field, named Positron Electron Balloon Spectrometer (PEBS). The design process has relied to a large extent on the flexible and expandable Monte Carlo simulation of the PEBS detector presented here. It allows the variation of the design parameters and a prediction of the overall detector performance. A reconstruction program was created, too, to study the simulated events as one would do with those from the real detector. It includes algorithms for track finding and fitting and the determination of shower parameters in the calorimeter. An analysis suite was written to study event properties on a statistical basis and extract the key figures of merit for a given detector design.

Intended for a measurement of the cosmic-ray positron fraction on one or more flights at high altitude using a long-duration balloon, PEBS has an unprecedentedly high acceptance of almost $0.4 \text{ m}^2 \text{ sr}$. A first launch could take place in 2012. Using a superconducting magnet to create a mean magnetic field of 0.8 T and a scintillating fibre tracker with silicon photomultiplier readout, it will allow reliable charge-sign and momentum measurements up to at least 100 GeV. The novel silicon photomultiplier has received great attention in the literature in recent years because of its many advantages compared to ordinary photomultiplier tubes. The combination with ultra-thin scintillating fibres of $250 \mu\text{m}$ diameter results in the concept of a novel device for tracking of charged particles, with applications beyond PEBS. Such a tracker could be robust, cover large areas and come at a moderate

7 Conclusions and outlook

price while offering spatial resolution on the order of $70\ \mu\text{m}$ or better. First prototype modules have been subjected to proton testbeams at CERN and the proof of principle for the fibre tracker has been established. The analysis of the data gathered has provided crucial input for the PEBS simulation.

The enormous challenge of reliably identifying positrons in front of the vast proton background is tackled by a combination of two independent subdetectors for particle identification. The electromagnetic calorimeter will consist of layers of tungsten absorber interleaved with scintillator bars, read out by silicon photomultipliers. An analysis of the shower shape and a comparison of the energy measured by the calorimeter to the momentum obtained from the tracker allows for protons to be rejected at the level of 1000 at efficiencies around 70 %. A similar factor is provided by the transition radiation detector whose design is based on the one used for the AMS-02 detector. Using testbeam data acquired with a prototype for the AMS-02-TRD, the accuracy of the simulation of transition radiation and ionisation losses provided by the commonly used Geant4 package has been studied. Excellent agreement was found between the transition radiation spectra in data and simulation. Small discrepancies at the 25 %-level are present in the tails of the proton energy loss spectra but this makes the predicted proton rejections uncertain by a factor of two.

For the case that dark matter is made up of neutralinos as predicted by the popular mSUGRA model, the projected performance of PEBS and AMS-02 has been studied. Looking first at the presently available data on the positron fraction, it was shown that the data show an excess in the positron fraction at energies above roughly 10 GeV which seems impossible to explain with common models for cosmic-ray propagation in the Galaxy. The data could be fit with an mSUGRA model but both the limited statistics and energy range of the available data do not allow for discrimination of different models. While the PAMELA data are already starting to make inroads into the mSUGRA parameter space, this situation might change dramatically with precision data from AMS-02 or PEBS with their big exposure and energy range. A scan of mSUGRA models was performed and models allowed by observational constraints, most notably the neutralino relic abundance, were identified. From a fit to the data, the most likely signal normalisation, related to the amount of clumpiness in the distribution of dark matter and expressed in terms of the boost factor, was determined. It turns out that the required boost factors are quite large and that they must differ significantly from those applicable to antiprotons. Nevertheless, a χ^2 -value can then be calculated for a fit of a given signal hypothesis to the projected data for PEBS and AMS-02, determined by the acceptance and measurement time, and the range of models within a reasonable distance from the χ^2 -minimum can be identified. The volume of parameter space of the given model that will remain after such a procedure was shown to be very small. In fact, the interpretation of the positron fraction measurements will be ultimately limited by the systematic uncertainties at the level of statistical accuracy provided by PEBS or AMS-02.

This thesis is merely a snapshot of ongoing work. On the software side, laboratory and testbeam measurements of prototypes for the various subdetectors will be used to make

the simulation more and more accurate. More layers of detail have to be added. For example, a realistic map of the magnetic field has to be included and more sophisticated track reconstruction routines have to be implemented as a consequence. The physics programme for PEBS has to be developed systematically. On the hardware side, the research and development programme is actively pursued in several laboratories across Europe. If it continues to be successful, the construction of PEBS will be a challenging endeavour requiring many skilled individuals. With luck, a significant scientific result may be achieved that will resonate with both experts and the general public.

7 *Conclusions and outlook*

Bibliography

- [1] E.W. Kolb and M.S. Turner, *The Early Universe*, Addison-Wesley, 1990
- [2] L. Bergström and A. Goobar, *Cosmology and Particle Astrophysics*, Springer, 2006
- [3] D. Samtleben et al., *Annu. Rev. Nucl. Part. Sci.* **57** (2007) 245-283
- [4] A.A. Penzias and R.W. Wilson, *ApJ* **142** (1965) 419-421
- [5] W.-M. Yao et al. (Particle Data Group), *J. Phys. G* **33**, 1 (2006) and 2007 partial update for edition 2008
- [6] C.L. Bennett et al., *ApJ* **583** (2003) 1-23
- [7] B. Leibundgut, *Annu. Rev. Astron. Astrophys.* **39** (2001) 67-98
- [8] W.J. Percival et al., *Mon. Not. R. Astron. Soc.* **381** (2007) 1053-1066
- [9] G. Hinshaw et al., [arXiv:0803.0732v2](https://arxiv.org/abs/0803.0732v2), accepted for publication in *ApJS*
- [10] E. Komatsu et al., [arXiv:0803.0547v2](https://arxiv.org/abs/0803.0547v2), accepted for publication in *ApJS*
- [11] G. Bertone et al., *Phys. Rep.* **405** (2005) 279-390
- [12] U. Seljak et al., *JCAP* 0610 (2006) 014
- [13] E.W. Kolb and R. Slansky, *Phys. Lett. B* **135** (1984) 378-382
- [14] G. Servant and T.M.P. Tait, *Nucl. Phys. B* **650** (2003) 391-419
- [15] S.J. Asztalos et al., *Annu. Rev. Nucl. Part. Sci.* **56** (2006) 293-326
- [16] G.L. Kane et al., *Phys. Rev. D* **49** (1994) 6173
- [17] I.J.R. Aitchison, *Supersymmetry and the MSSM: An Elementary Introduction*, [arXiv:hep-ph/0505105v1](https://arxiv.org/abs/hep-ph/0505105v1)
- [18] X. Tata, University of Hawaii report UH-511-872-97, [arXiv:hep-ph/9706307v1](https://arxiv.org/abs/hep-ph/9706307v1)
- [19] A.H. Chamseddine et al., *Phys. Rev. Lett.* **49** (1982) 970-974
- [20] L. Hall et al., *Phys. Rev. D* **27** (1983) 2359-2378
- [21] R. Barbieri et al., *Phys. Lett. B* **119** (1982) 343-347
- [22] P. Nath et al., *Nucl. Phys. B* **227** (1983) 121-133
- [23] J. Edsjö, *Aspects of Neutrino Detection of Neutralino Dark Matter*, PhD thesis, Uppsala University 1997, [arXiv:hep-ph/9704384](https://arxiv.org/abs/hep-ph/9704384)
- [24] V.L. Ginzburg and S.I. Syrovatskii, *The Origin of Cosmic Rays*, Pergamon Press, 1964
- [25] T.K. Gaisser, *Cosmic Rays and Particle Physics*, Cambridge University Press, 1990
- [26] M.S. Longair, *High Energy Astrophysics*, Cambridge University Press, 1992, reprinted with corrections 2004
- [27] T. Stanev, *High Energy Cosmic Rays*, Springer, 2004
- [28] V.F. Hess, *Physik. Zeitschr.* **13** (1912) 1084-1091

Bibliography

- [29] C.D. Anderson, Phys. Rev. **43** (1933) 491
- [30] S.H. Neddermeyer and C.D. Anderson, Phys. Rev. **51** (1937) 884
- [31] J.C. Street and E.C. Stevenson, Phys. Rev. **52** (1937) 1003
- [32] D.H. Perkins, Nature **159** (1947) 126
- [33] G.D. Rochester and C.C. Butler, Nature **160** (1947) 855
- [34] The Pierre Auger collaboration, Science **318** (2007) 938
- [35] F. Aharonian et al., Astron. Astrophys. **464** (2007) 235-243, [arXiv:astro-ph/0611813v1](#)
- [36] D. Maurin et al., ApJ **555** (2001) 585-596
- [37] I.V. Moskalenko and A.W. Strong, ApJ **493** (1998) 694-707
- [38] A.W. Strong and I.V. Moskalenko, ApJ **509** (1998) 212-228
- [39] I.V. Moskalenko et al., ApJ **565** (2002) 280-296
- [40] V.S. Ptuskin et al., ApJ **642** (2006) 902-916
- [41] A.W. Strong et al., Annu. Rev. Nucl. Part. Sci. **57** (2007) 285-327
- [42] L.J. Gleeson and W.I. Axford, ApJ **154** (1968) 1011-1026
- [43] T. Mizuno et al., Nucl. Sci. Symp. Conf. Rec. (2001) IEEE Vol. 1, 442-446
- [44] J. Abraham et al., Nucl. Instr. Meth. A **523** (2004) 50-95
- [45] P. von Doetinchem, PhD thesis in preparation, RWTH Aachen
- [46] J. Alcaraz et al., Phys. Lett. B **490** (2000) 27-35
- [47] J. Alcaraz et al., Phys. Lett. B **494** (2000) 193-202
- [48] M.A. DuVernois et al., ApJ **559** (2001) 296-303
- [49] J. Alcaraz et al., Phys. Lett. B **484** (2000) 10-22
- [50] T. Maeno et al., Astropart. Phys. **16** (2001) 121-128
- [51] M. Boezio et al., ApJ **561** (2001) 787
- [52] S.D. Hunter et al., ApJ **481** (1997) 205-240
- [53] J.Z. Wang et al., ApJ **564** (2002) 244-259
- [54] Y. Shikaze et al., Astropart. Phys. **28** (2007) 145-167
- [55] M. Casolino et al., [arXiv:astro-ph/0810.4980v1](#)
- [56] J. Nishimura et al., Adv. Space Res. **26** (No 11) (2000) 1827-1830
- [57] S. Torii et al., ApJ **559** (2001) 973-984
- [58] M. Aguilar et al., Phys. Lett. B **646** (2007) 145-154
- [59] J.J. Beatty et al., Phys. Rev. Lett. **93** (2004) 241102
- [60] M. Boezio et al., ApJ **532** (2000) 653-669
- [61] R.L. Golden et al., ApJ **457** (1996) L103-L106
- [62] J. Olzem, Signatures of SUSY Dark Matter at the LHC and in the Spectra of Cosmic Rays, PhD thesis, RWTH Aachen, 2007
- [63] O. Adriani et al., [arXiv:astro-ph/0810.4995v1](#)
- [64] A.J. Davis et al., Proc. ACE 2000 Symposium, AIP, 421
- [65] J.H. Caldwell and P. Meyer, Proc. 15th ICRC (1977),1,243
- [66] J.H. Chapell and W.R. Webber, Proc. 17th ICRC (1981) 2,59

- [67] R. Dwyer and P. Meyer, *ApJ* **322** (1987) 981-991
- [68] M. Garcia-Munoz et al., *ApJ* **280** (1984) L13-L17
- [69] M. Gupta and W.R. Webber, *ApJ* **340** (1989) 1124-1134
- [70] J.J. Engelmann et al., *Astron. Astrophys.* **233** (1990) 96-111
- [71] K.E. Krombel and M.E. Wiedenbeck, *ApJ* **328** (1988) 940-953
- [72] E. Júlíusson, *ApJ* **191** (1974) 331-348
- [73] J.A. Lezniak and W.R. Webber, *ApJ* **223** (1978) 676-696
- [74] R.C. Maehl et al., *Astrophysics and Space Science* **47** (1977) 163-184
- [75] C.D. Orth et al., *ApJ* **226** (1978) 1147-1161
- [76] M. Simon et al., *ApJ* **239** (1980) 712-724
- [77] M.A. DuVernois et al., *Astron. Astrophys.* **316** (1996) 555-563
- [78] A. Lukasiak et al., *Proc. 26th ICRC* (1999) OG1.1.12
- [79] G. Cowan, *Statistical Data Analysis*, Oxford University Press, 1998
- [80] J.M. Clem et al., *ApJ* **464** (1996) 507-515
- [81] H.D. Babcock, *ApJ* **130** (1959) 364
- [82] Solar Influences Data Analysis Center, <http://sidc.oma.be/sunspot-data/>
- [83] H.B. Snodgrass et al., *Solar Physics* **191** (2000) 1-19
- [84] C.J. Durrant and P.R. Wilson, *Solar Physics* **214** (2003) 23-29
- [85] O. Adriani et al., *Phys. Rev. Lett.* **102** (2009) 051101
- [86] K. Abe et al., *Phys. Lett. B* **670** (2008) 103-108
- [87] Y. Asaoka et al., *Phys. Rev. Lett.* **88(5)** (2002) 051101
- [88] P. von Doetinchem, H. Gast, T. Kirn, G. Roper Yearwood, and S. Schael, *Nucl. Instr. Meth. A* **581** (2007) 151-155
- [89] H. Gast, P. von Doetinchem, T. Kirn, G. Roper Yearwood, and S. Schael, *Proc. 30th International Cosmic Ray Conference, Mérida, Mexico, July 2007, Vol. 2*, 293-296
- [90] H. Gast, T. Kirn, G. Roper Yearwood, and S. Schael, *Nucl. Instr. Meth. A* **581** (2007) 423-426
- [91] P. Picozza et al., PAMELA – A payload for antimatter matter exploration and light-nuclei astrophysics, *Astropart. Phys.* **27** (2007) 296-315
- [92] M. Casolino et al., *J. Adv. Space Res.* (2007), doi:10.1016/j.asr.2007.07.023
- [93] P. Papini et al., *Nucl. Instr. Meth. A* **588** (2008) 259-266
- [94] V. Malvezzi, *Nucl. Instr. Meth. A* **588** (2008) 250-254
- [95] S. Straulino et al., *Nucl. Instr. Meth. A* **556** (2006) 100-114
- [96] M. Boezio et al., *Astropart. Phys.* **26** (2006) 111-118
- [97] R. Battiston, *Nucl. Instr. Meth. A* (2008), doi:10.1016/j.nima.2008.01.044
- [98] G. Roper, Development of a high resolution tracking detector with SiPM readout, graduate thesis, RWTH Aachen, April 2007
- [99] G. Roper, PhD thesis in preparation, RWTH Aachen
- [100] H.S. Ahn et al., *Nucl. Instr. Meth. A* **579** (2007) 1034-1053

Bibliography

- [101] A.D. Panov et al., *Adv. Space Res.* **37** (2006) 1944-1949
- [102] A. Yamamoto et al., *Nucl. Phys. B (Proc. Suppl.)* **166** (2007) 62-67
- [103] R.L. Golden et al., *Nucl. Instr. Meth. A* **306** (1991) 366-377
- [104] S.W. Barwick et al., *Nucl. Instr. Meth. A* **400** (1997) 34-52
- [105] M. Ave et al., *ApJ* **678** (2008) 262-273
- [106] M. Hof et al., *Nucl. Instr. Meth. A* **454** (2000) 180-185
- [107] S. Agostinelli et al., *Nucl. Instr. Meth. A* **506** (2003) 250-303
- [108] R.L. Gluckstern, *Nucl. Instr. Meth.* **24** (1963) 381-389
- [109] R. Greim, *Lineare Silizium-Photomultiplier-Arrays*, graduate thesis (in German), RWTH Aachen, September 2008
- [110] B. Dolgoshein et al., *Nucl. Instr. Meth. A* **563** (2006), 368-376
- [111] M. McClish et al., *Nucl. Instr. Meth. A* **567** (2006), 36-40
- [112] P. Buzhan et al., *Nucl. Instr. Meth. A* **567** (2006), 353-355
- [113] D. Renker, *Nucl. Instr. Meth. A* **567** (2006), 48-56
- [114] BICRON catalogue, Saint Gobain Ceramics & Plastics, Inc., 2005
- [115] V. Balagura et al., *Nucl. Instr. Meth. A* **564** (2006) 590-596
- [116] V. Balagura, private communication
- [117] N.L. Johnson and S. Kotz, *Urn models and their application*, Wiley 1977
- [118] C.W. Fabjan and F. Gianotti, *Calorimetry for Particle Physics*, CERN-EP/2003-075
- [119] R. Wigmans, *Calorimetry*, Oxford University Press, 2000
- [120] C. Berger, *Elementarteilchenphysik*, Springer, 2002
- [121] R. Barlow, *Statistics: A Guide to the Use of Statistical Methods in the Physical Sciences*, Wiley VCH 1994
- [122] J.D. Jackson, *Classical Electrodynamics*, 3rd edition, John Wiley & Sons, 1999
- [123] B. Dolgoshein, *Nucl. Instr. Meth. A* **326** (1993) 434-469
- [124] V. Egorytchev et al., *Nucl. Instr. Meth. A* **453** (2000) 346-352
- [125] C.W. Fabjan and W. Struczinski (sic!), *Phys. Lett. B* **57** (1975) 483-486
- [126] P. v. Doetinchem et al., *Nucl. Instr. Meth. A* **558** (2006) 526-535
- [127] S. Fopp, *Entwicklung und Bau eines auf Proportionalkammern basierenden Übergangsstrahlungsdetektors für das AMS-02-Weltraumexperiment*, PhD thesis (2004), RWTH Aachen
- [128] Geant4 Physics Reference Manual
- [129] J. Apostolakis et al., CERN-LCGAPP-2007-02
- [130] G. Folger et al., *Eur. Phys. J. A* **21** (2004) 407
- [131] B. Beischer et al., *Nucl. Instr. Meth. A* **583** (2007) 485-493
- [132] A. Andronic et al., *Transition radiation spectra of electrons from 1 to 10 GeV/c in regular and irregular radiators*, *Nucl. Instr. Meth. A* **558** (2006) 516-525
- [133] J. Apostolakis et al., *Nucl. Instr. Meth. A* **453** (2000) 597-605
- [134] V.M. Grichine, *Nucl. Instr. Meth. A* **484** (2002) 573-586

- [135] V.M. Grichine, S.S. Sadilov, Nucl. Instr. Meth. A **563** (2006) 299-302
- [136] V.M. Grichine, Phys. Lett. B **525** (2002) 225-239
- [137] J. Orboeck, The final 20-Layer-Prototype for the AMS Transition Radiation Detector: Beamtests, Data-Analysis, MC-Studies, PhD thesis (2003), RWTH Aachen
- [138] V.M. Grichine, S.S. Sadilov, Nucl. Instr. Meth. A **522** (2004) 122-125
- [139] W.W.M. Allison, J.H. Cobb, Ann. Rev. Nucl. Part. Sci. **30** (1980) 253-298
- [140] L. Gatignon, The West Experimental Area at the CERN SPS, CERN SL-2000-016 EA
- [141] R.O. Duda and P.E. Hart, Comm. ACM **15** no. 1 (1972) 11-15
- [142] V. Blobel, Nucl. Instr. Meth. A **566** (2006) 14-17
- [143] GNU Scientific Library, <http://www.gnu.org/software/gsl/>
- [144] J.D. Sullivan, Nucl. Instr. Meth. **95** (1971) 5-11
- [145] S. Chatrchyan et al. (CMS collaboration), JINST **3** (2008) S08004
- [146] L. Borrello et al., CMS note 2003/020
- [147] M. Friedl et al., Nucl. Instr. Meth. A **488** (2002) 175-183
- [148] M. Axer et al., Nucl. Instr. Meth. A **518** (2004) 321-323
- [149] Kuraray Co Ltd, Scintillation Materials
- [150] Gamma Medica - Ideas (Norway) AS, <http://www.ideas.no>
- [151] P. Azzarello, Tests And Production Of The AMS-02 Silicon Tracker Detectors, PhD thesis, Université de Genève, 2004
- [152] M. Cristinziani, Search for Heavy Antimatter and Energetic Photons in Cosmic Rays with the AMS-01 Detector in Space, PhD thesis, Université de Genève, 2002
- [153] A. Kounine et al., AMS-2 DAQ software organisation, xDR and JINx nodes, European Organization for Nuclear Research draft, unpublished AMS document
- [154] R. Greim, PhD thesis in preparation, RWTH Aachen
- [155] M.S. Turner and F. Wilczek, Phys. Rev. D **42** (1990) 1001-1007
- [156] M. Kamionkowski and M.S. Turner, Phys. Rev. D **43** (1991) 1774-1780
- [157] E.A. Baltz and J. Edsjö, Phys. Rev. D **59** (1998) 023511
- [158] E.A. Baltz et al., Phys. Rev. D **65** (2002) 063511
- [159] J. Lavallo et al., A&A **479** (2008) 427-452
- [160] G.L. Kane et al., Phys. Lett. B **536** (2002) 263-269
- [161] D. Hooper et al., Phys. Rev. D **69** (2004) 103509
- [162] D. Hooper and J. Silk, Phys. Rev. D **71** (2005) 083503
- [163] H. Baer et al., [arXiv:hep-ph/0312045](http://arxiv.org/abs/hep-ph/0312045), latest version available at <http://www.hep.fsu.edu/~isajet>
- [164] P. Gondolo et al., JCAP **0407** (2004) 008
- [165] G. Bélanger et al., Comput. Phys. Commun. **176** (2007) 367
G. Bélanger et al., Comput. Phys. Commun. **174** (2006) 577
G. Bélanger et al., Comput. Phys. Commun. **149** (2002) 103
- [166] D.N. Spergel et al., ApJ Suppl. Ser. **170** (2007) 377-408

- [167] J. Edsjö and P. Gondolo, Phys. Rev. D **56** (1997) 1879
- [168] Tevatron Electroweak Working Group, arXiv:0803.1683v1
- [169] G.W. Bennett et al., Phys. Rev. D **73** (2006) 072003
- [170] L. Baudis, submitted to Proc. SUSY07, arXiv:0711.3788v1
- [171] Z. Ahmed et al., arXiv:0802.3530 (UCLA 2008 DM conference)
- [172] J. Angle et al., Phys. Rev. Lett. **100** (2008) 021303
- [173] E. Behnke et al., Science **319** (2008) 933
- [174] H.S. Lee et al., Phys. Rev. Lett. **99** (2007) 091301
- [175] T. Sjöstrand, Comp. Phys. Comm. **82** (1994) 74-89
- [176] Tevatron Electroweak Working Group, arXiv:hep-ex/0703034v1
- [177] P. Brun et al., Phys. Rev. D **76** (2007) 083506
- [178] M. Lattanzi and J. Silk, astro-ph:0812.0360v1
- [179] H. Baer et al., JCAP08 (2004) 005
- [180] Y. Ajima et al., Nucl. Instr. Meth. A **443** (2000) 71-100
- [181] R. Barlow, MAN/HEP/04/02, arXiv:physics/0406120
- [182] R. Battiston, Proposal for an ASI - DLR research program on Astroparticle Physics from LDB at the North Pole, talk given at 1st workshop on science and technology through long duration balloons, Rome, Italy, June 2008
- [183] L. Bergström et al., JCAP05 (2006) 006
- [184] F.W. Stecker et al., Astropart. Phys. **29** (2008) 25-29
- [185] A.W. Strong et al., ApJ **613** (2004) 962-976
- [186] F. Donato et al., Torino U. preprint DFTT 06/2007, arXiv:0803.2640v1
- [187] S. Orito et al., Phys. Rev. Lett. **84(6)** (2000) 1078
- [188] K. Yamato et al., Phys. Lett. B **632** (2006) 475-479
- [189] S. Profumo, arXiv:astro-ph/0812.4457v1
- [190] E.A. Baltz et al., JCAP07 (2008) 013
- [191] M. Cirelli et al., arXiv:hep-ph/0809.2409v3, to appear in Nucl. Phys. B
- [192] I. Cholis et al., arXiv:astro-ph/0811.3641v1
- [193] P. Yin et al., arXiv:hep-ph/0811.0176v2

Acknowledgements

First and foremost, I would like to thank Professor Stefan Schael who supervised the work for this thesis during the past four years. He let me play a major role in the development of the PEBS project, for which he is the driving force. In countless meetings and discussions, he inspired and motivated me by his passion for physics. He also gave me the opportunity to attend several international conferences and schools which proved to be invaluable and truly memorable experiences.

Professor Christopher Wiebusch kindly agreed to serve as the second referee for this thesis.

The smallness of the PEBS group in Aachen is more than compensated for by the talents of the gifted individuals forming part of it. Dr Thomas Kirn was always available for enlightening discussions about detector physics and beyond. Because of his guidance and experience, the testbeam measurements at CERN were both successful and enjoyable. Gregorio Roper has the power to work magic with any equipment that comes his way. I am especially indebted to him for the hard work he did in preparing and conducting the testbeam measurements described here and for the discussions about the analysis of the data gathered there. Roman Greim put a lot of effort into the preparation of the 2008 testbeam and has a very patient ear for discussions about almost any subject.

Dr Jan Olzem is a source of knowledge in so many areas, from physics to computing and far beyond, and he is never reluctant to share it copiously. The collaboration with him in the early stages of the work for this thesis was as efficient as it was pleasant. Dr Thorsten Siedenburg is exactly the right person to ask when you have run out of ideas. Admirably, he never gives up searching for the answer to a problem. Philip von Doetinchem calculated the expected atmospheric backgrounds for PEBS. Over the years that we have worked together, starting our theses at the same institute at almost the same time, he has become a close and trusted friend.

Michael Wloch and Waclaw Karpinski and their respective teams in the mechanical and electronics workshops provided most of the hardware for the testbeam measurements described here. In addition, together with Arndt Schultz von Dratzig, they turned the wild ideas of the physicists into an actual design for PEBS.

Bastian Beischer and Niko Zimmermann are extremely talented and resourceful students who contributed to many different aspects of this work.

I am deeply indebted to Dr Vladik Balagura. His short visit to Aachen brought a huge boost to the ECAL design, as well as to the ECAL simulation and analysis. He taught

me a great deal about calorimetry and inspired me with his keen analytical thinking.

It is a great pleasure to thank Dr Giovanni Ambrosi and Dr Philippe Azzarello for their kind hospitality during my visit to Perugia. They repeatedly allowed us to use their equipment and taught me how to operate the beam telescope used in the 2008 testbeam.

Professor Volker Blobel allowed me to use his software for robust parameter estimation and patiently answered many questions related to it.

Dr Chan Hoon Chung did an earlier analysis of the cosmic-ray positron fraction data in Aachen and shared his insights in cosmic-ray propagation and SUSY codes with me.

Although not directly involved with PEBS, Dr Chan Hoon Chung, Dr Alexander Furgeri, André Goerres, Dr Sonia Natale, Dr Jan Olzem, Dr Andrei Ostapchouk, and Dr Georg Schwering helped to make the testbeam campaign a success, by helping with the organisation or by spending many hours on shifts at CERN.

Dr Thomas Kress, Dr Michael Bontenackels, and Christoph Kukulies permanently kept the computing facilities in Aachen in excellent shape. Without the impressive batch cluster maintained by them, the results in this thesis would have taken so much longer to obtain.

Dr Georg Schwering is the capable head of administration of the institute. I do not remember any of my stupid questions that he did not answer patiently.

Thanks to my officemates over the years, Jan, Hendrik, Georgos, Roman and Katja, the office was always a warm and happy place.

Roman, Philip and especially Jan and Thomas read the manuscript of this thesis carefully and improved it substantially.

I owe a lot to the people I studied with, especially Klaus, Max, Martin, Philipp, Philip, Stefan and Katja. The countless hours we spent discussing and solving problems shaped my view of physics and, in fact, the world. Thank you for all the fun.

I cannot hope to repay with words what my family, Hans-Peter, Marlies and Frauke, and what my future family, Astrid, did for me over the years. I could always count on their unwavering support.

Lebenslauf

Persönliche Daten

Name	Henning Gast
Geburtsdatum	24. März 1979
Geburtsort	Düsseldorf

Ausbildung

seit 12/2007	wissenschaftlicher Mitarbeiter am I. Physikalischen Institut B der RWTH Aachen
seit 12/2004	Promotion am I. Physikalischen Institut B der RWTH Aachen, Stipendiat im Graduiertenkolleg „Elementarteilchenphysik an der TeV-Skala“
12/2004	Diplom in Physik, Thema der Arbeit: „Untersuchung der kosmischen Höhenstrahlung mit dem AMS01-Detektor im Weltraum“
09/1999 - 12/2004	Studium der Physik an der RWTH Aachen
07/1998 - 04/1999	Wehrdienst, 2./JaboG 33 in Büchel
1998	Abitur
1989 - 1998	Georg-Büchner-Gymnasium, Kaarst
1985 - 1989	Grundschule Lichtenvoorder Straße, Kaarst-Büttgen